Author:
Mauleon Amieva, Abraham

Title:
The phase behaviour of active colloidal rollers

The Phase Behaviour of Active Colloidal Rollers

Abraham Mauleon Amieva

School of Physics
University of Bristol

A dissertation submitted to the University of Bristol in accordance with the requirements of the degree of Doctor of Philosophy in the Faculty of Science.

March 2020

Word count: 48,447

Abstract

Active matter systems are those able to continuously consume energy from the environment in order to drive themselves out-of-equilibrium. This leads to fascinating behaviours not attainable at thermal equilibrium. Some of the hallmarks of such systems are the self-propulsion of individuals, and the emergence of collective phenomena, such as swarming, flocking, clustering, and phase separation in the absence of attractive forces. Moreover, such phenomena occurs in a wide range of living systems at different length scales, from the cell cytoskeleton, tissues, and bacterial colonies to larger scales such as fish schools and bird flocks.

Artificial active materials, consisting of active particles, vibrated grains, or even synthetically modified living systems, provide suitable model systems to test the behavior of active matter, and to investigate the physical principles behind. In this sense, much of the active behaviours rely upon the interactions in the system, such as the alignment interaction that promote coherent flows, as in flocks. Thus, we describe a population of interacting and motile colloidal particles, that exhibit phase transitions between passive and active states, i.e. swarms and polar flocks. Our system displays a rich and exotic phase behavior, including passive and motile crystallites, an active gas, and polar bands. We find that at low motility, *competing passive and active interactions* leads to the melting-like and behavior of active crystallites. On increasing the motility, the role of the interactions is reversed, and promotes the onset of flocking.

Furthermore, we introduce strong confinement to promote the self-organisation of structures with finite size. In a circular confinement, we observe swarming and coherent circular motion as the population increases. We show the formation of self-powered *microgears*, that consist of multilayered structures. Such microgears exhibit controllable mechanisms of rotation, from rigid-body-like to slipping behaviour. This opens the way of assembling and controlling micro devices, such as gearboxes.

Finally, the active motion on non-spherical spherical particles, e.g. *colloidal molecules*, is considered. We use fused spheres to determine the dynamics of dumbbells and trimer particles, which results markedly different from that of single spheres. One one hand, the circular in dumbbells leads to the dynamical aggregation into clusters. On the other, trimers exhibit a combination between in-plane diffusion and out-of-plane jumps.

ACKNOWLEDGEMENTS

There is a long list of people to acknowledge for their invaluable support and help throughout these years of PhD. First and foremost, I would like to express my sincere gratitude to Paddy Royall and Jeroen van Duijneveldt for their incredible support as supervisors. It has been a great pleasure to learn from both of them, and to have the opportunity to work within their research groups. I also would like to thank Tannie Liverpool and Majid Mosayebi for their interest and important collaboration to our research, which made possible the simulations of our experimental system. In addition, I thank Mike Allen and Anton Souslov for their interest and their help building models to describe our experiments, and to Ian Williams and Jens Eggers for their useful comments and suggestions.

In the context of daily work, I thank James Hallett and Francesco Turci, whose support was important during the first years of my studies. I also thank Ioatzin Ríos de Anda, Josh Robinson, Jun Dong, Peter Crowther, Max Meissner, Nick Wood, Azaima Razali, Rattachai Pinchaipat, Kate Oliver and Chris Brasnet for welcoming me into the office, and to the recent and former members of the group, Yushi Yang, Fergus Moore, Nariaki Sakai, Siân Fussell, Levke Ortlieb, Ben Carter and Max Kloucek. It has been a great experience to work, learn and share experiences with them.

Bristol has been one of the best decisions I have ever made, and one of the reasons is the Bristol Center for Functional Nanomaterials (BCFN), to which I am proud to belong. I thank Annela Seddon and Terry McMaster for their invaluable support, and for giving me the opportunity to be a BCFN student. I am also very grateful to be part of the University of Bristol. Deciding Bristol for a PhD has been a remarkable personal and professional experience in my life, one I will carry forever. Last but not least, I would like to thank Paul Bartlett and Olivier Dauchot for their valuable comments and suggestions to the present work.

Financially I acknowledge CONACYT, EPSRC and ERC for providing the necessary funding for my PhD studies. I also deeply thank Paddy Royall for securing additional funding for the last months at the end of my studies.

Dedication

Estos años que he tenido fuera de México, lejos de mi familia y amigos, por un lado me han servido para confirmar que todo lo que me proponga esta a mi alcance, y por el otro me han hecho valorar todo el cariño y apoyo que he recibido. Principalmente agradezco a mis padres por su constante amor y esfuerzo para brindarme las mejores oportunidades, a pesar de las adversidades. Ustedes son el más grande ejemplo, y siempre estaré en deuda con ustedes. A mi hermana, quién a pesar de ser menor que yo, me ha dado las más grandes lecciones de madurez y cariño. Estoy muy orgulloso de la persona que eres, y sabes que no importa donde este, siempre contarás conmigo. A los tres los amo.

A Andrea, con quién he vivido las mejores experiencias de los últimos 6 años, y quién es una constante fuente de cariño, motivación y apoyo. También quiero agradecer a esas personas especiales, mis primos Diego y Andrés, con quienes he crecido y compartido grandes experiencias. Sin duda su visita a Bristol es una de la razones por la cuales seré recordado aquí. A mi abue y a mi tía Lucha, quienes desde pequeño me llenaron de cariño. A mis amigos Germán y Axel, quienes a pesar de la distancia siempre tengo presentes, y a los que considero parte de mi familia.

Sin duda, Bristol me ha brindado de grandes experiencias personales, junto con nuevas amistades. Teo, Marcos, Ioatzin, Fer, Sel, Pili, Evelyn, Dany, Nadia gracias por compartir esta aventura conmigo.

Finalmente, quiero agradecer a una persona especial. Desafortunadamente él ya no está aquí y no podrá leer esto, ni podrá verme terminar mis estudios de doctorado. Muchas gracias por todo tío Angel. Insiste, persiste, resiste, subsiste y triunfa!

Author's declaration

I declare that the work in this dissertation was carried out in accordance with the requirements of the University's Regulations and Code of Practice for Research Degree Programmes and that it has not been submitted for any other academic award. Except where indicated by specific reference in the text, the work is the candidate's own work. Work done in collaboration with, or with the assistance of, others, is indicated as such. Any views expressed in the dissertation are those of the author.

SIGNED: ..... DATE: .....

Table of Contents

List of Tables

Table **Page**

List of Figures

Figure **Page**

CHAPTER 1

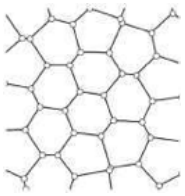

INTRODUCTION

1.0.1 Thesis Structure and Outline

In the present work, we describe the use of self-propelling colloids as a model system for active matter. Before showing our key findings, we detail the features of previously investigated models. Chapter 2 gives a general overview to active matter systems. First, we describe the characteristic self-propulsion of active agents. Later, the collective phenomena arising in active systems in discussed. We refer to the onset of collective motion characterised by flocking models, and the phase separation exhibited by active particles. Finally, we summarise the some of the most relevant experimental models of active matter.

In Chapter 3 we focus on the description of the model used in our experiments. This corresponds to the self-propulsion of particles due to the application of an external electric field, the so-called *Quincke rotation*. This chapter also describes the significant experimental realisations prior this work. Chapter 4 gives the important details of colloidal suspensions, such as interactions, colloid stabilisation and charging, and the

induced electro-hydrodynamic effects from the electric field application. These later are followed by the experimental details in Chapter 5. The preparation of charged colloidal suspensions, experimental mounting and microscopy are discussed.

In Chapter 6 we show the phase behaviour of Quincke rollers, from numerical simulations and experiments. Here, different phases are observed with changing the density and strength of the electric field. We describe the different phases by mean of competing active and passive interactions. The local structure and active behavior are characterised using a range of static and dynamic order parameters. In addition, we show the coalescence and breaking of motile aggregates.

Using the same system, in Chapter 7 we show the role of strong circular confinement. Dynamical behavior, from swarming to coherent flow are observed in Quincke rollers as the confined population is increased. Moreover, we show the self-organization of hierarchical structures to form microgears of controllable behavior. Rigid-body rotation and slipping behaviour results from modifying the number of particles comprising the rotor and the electric strength.

Chapter 7 describes the use of non-spherical particles subjected to Quincke rotation. We show that the dynamics of small particles made of fused spheres are significantly different to the random walks observed in active spheres. Finally, this thesis concludes with Chapter 9, which summarises the main findings from Chapters 6, 7 and 8. In addition, possible further developments using these model systems are proposed.

1.0.2 Disclaimer Regarding Computer Simulations and Diffusion Model for Trimer Particles

This thesis presents results from colloidal experiments, accompanied in Chapter 6 with results from numerical simulations. We find that these provide details not easily accessible in experiments. Here, the numerical simulations are based in a modified

version of the model introduced in Ref [4]. The simulations using LAMMPS Molecular Dynamics for a system of attractive Quincke rollers were performed by Majid Mosayebi [1]. No claim of their ownership or authorship is made by the author of this thesis. The results from numerical simulations and experiments, presented in Chapter 6, are analysed by the author of this thesis.

Chapter 8 describes the motility of trimer particles. We find that the motion of particles of triangular shape is significantly different from the one in spheres. From experimental observations, Michael Allen[2] derives a discrete model to account for the trimer dynamics. Appendix B details the first attempt of such model. We expect further development to relate more closely to the experimental observations.

[1] majid.mosayebi@bristol.ac.uk
[2] m.p.allen@bristol.ac.uk

CHAPTER 2

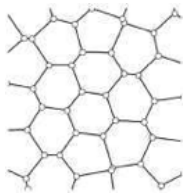

ACTIVE MATTER

"Are birds smarter than nerds?"

TONER, TU AND RAMASWAMY, 2010

2.1 Introduction

Active matter systems consist of a collection of units, each one able to store and convert surrounding energy into a net motion, e.g. self-propulsion. These systems are inherently far from equilibrium but they are distinct from those that are externally driven by boundaries (e.g. sheared systems) as in active systems energy is injected at the level of the single units [5–7]. Moreover, expressions of active matter phenomena are observed at different length scales. In this sense, nature provides a wide range of fascinating systems, whose behaviour is not observed in equilibrium systems. Figure 2.1 shows a few examples of living systems that fall into the category of active matter.

In addition to the characteristic self-propulsive motion, collective phenomena emerge from the interactions in a population. Common examples are the formation of colonies

[8–10], swarming of insects, [11–16], and the flocking of birds [17–23] observed in many species. Hence, the study of the mechanisms behind the interactions and collective phenomena of self-propelled units may provide an understating of the behaviour featured by living systems across length scales. For this, conventional non-equilibrium statistical mechanics [24] must be adapted to active matter to provide the tools for the investigation of fundamental laws and principles in such systems. This has encouraged significant growth of the field, which encompasses diverse disciplines, such as non-equilibrium statistical physics [25, 26], soft condensed matter [7, 27], biology [28], software engineering [29, 30], robotics [31], and medicine [32, 33].

In this introductory chapter we compare the particle motion due to active forces against the motion observed in thermal equilibrium. This is followed by the description of relevant models that account for the behaviour of living swimmers, i.e. bacteria. Later, we focus on the collective phenomena exhibited by active systems. We discuss two relevant topics: the transition towards collective motion, and emergent phase separation observed in self-propelled active systems. We close this chapter with a list of experimental realisations of active matter systems investigated analytically and with numerical simulations.

2.2 Particle Motion

2.2.1 Brownian Motion

First, the *passive* motion observed in thermal equilibrium is presented, with the aim of establishing a framework for the motion observed in active matter systems [27]. Let us begin from the passive case, by revisiting Brownian motion. First observed in 1827 by Robert Brown under a microscope, and described in 1905 by Einstein [35], Brownian (passive) motion arises from collisions between a suspended particle and the molecules

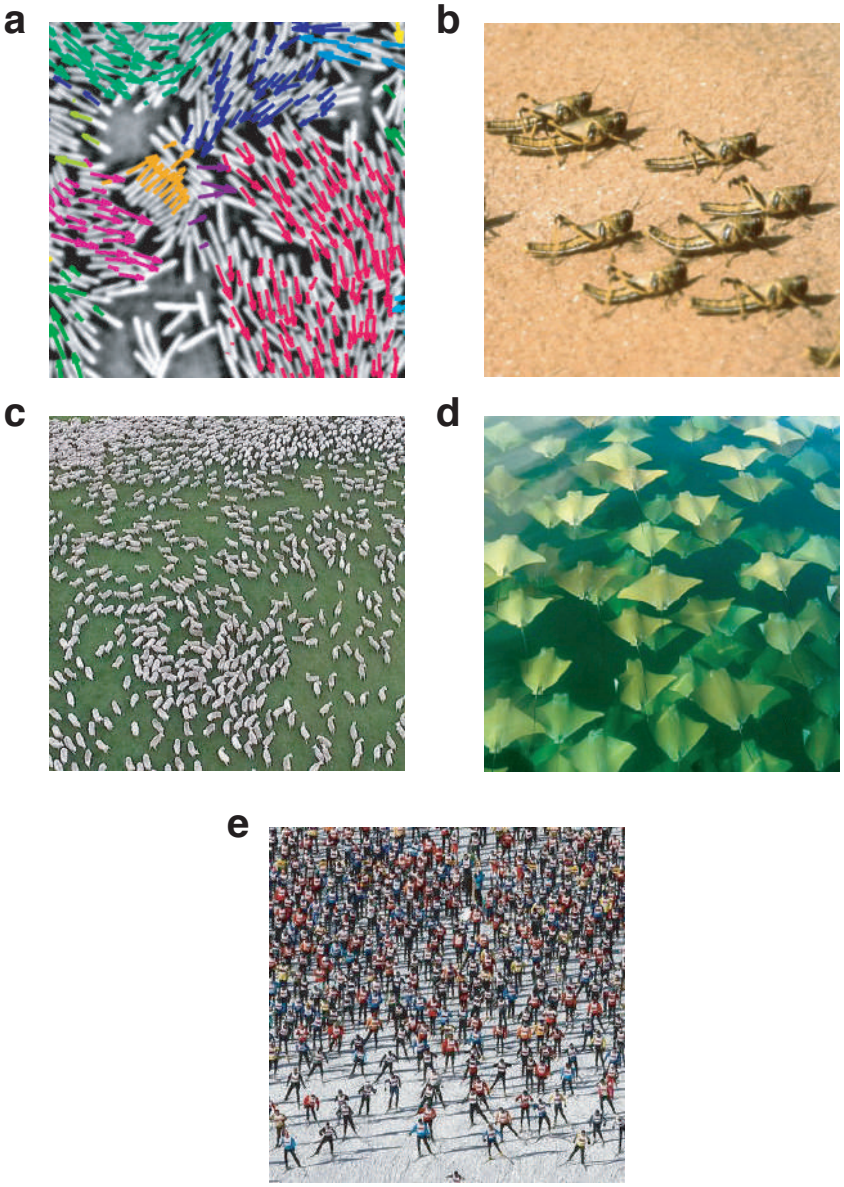

Figure 2.1: **Various types of collective behaviour across different length scales. a.** Collective motion in bacterial suspensions of *Bacillus subtilis colonies* leads to local alignment and colony displacement. Figure reproduced from Ref. [34]. **b.** Polar front observed in a collection of locusts as they perform migration. Source: Google. **c.** Aerial view of sheep forming a wave when forced to move. Image taken from Google. **d.** Three-dimensional school of rays. Reproduced from Ref. [22]. **e.** Polar front resulting from a population of skiers. Image obtained from Google.

of the surrounding media. Consider a spherical particle of radius R and mass m moving with a velocity $\mathbf{v}$ in a fluid of viscosity $\bar{\eta}$. Treating the fluid as a continuum, the particle experiences a hydrodynamic drag force $\mathbf{F}_d = -\gamma\mathbf{v}$, where γ is the so-called Stokes drag $\gamma = 6\pi\bar{\eta}R$, which is dependent of the specific viscosity $\bar{\eta}$ of the media. Brownian motion can be captured by Newtonian dynamics with the inclusion of all the forces acting on a sphere: (i) frictional force from the fluid viscosity, (ii) a random force, with zero mean value, accounting for the collision with the fluid, and (iii) a force due to an external potential $U(\mathbf{r})$ [36]. The particle motion is given by the Langevin equation,

$$\frac{\mathrm{d}\mathbf{r}}{\mathrm{d}t} = \mathbf{v}; \qquad m\frac{\mathrm{d}\mathbf{v}}{\mathrm{d}t} = -\gamma\mathbf{v} - \nabla U(\mathbf{r}) + \boldsymbol{\eta}(t) \tag{2.1}$$

where the *stochastic* velocity reads $\boldsymbol{\eta}(t) = \gamma f_{\mathrm{random}}(t)$. Ornstein and Uhlenbeck [37] described that the stochastic force is of Gaussian distribution, with independent components, and $\delta-$correlated time dependence,

$$\langle\boldsymbol{\eta}(t)\rangle = 0; \qquad \langle\boldsymbol{\eta}_i(t)\boldsymbol{\eta}_j(t')\rangle = 2D_n\delta_{i,j}\delta(t-t'); \quad \text{where} \quad i,j = x,y,z, \tag{2.2}$$

with the components $\eta_i(t)$ having a noise intensity D_n that relates to the translational diffusion D_t through the fluctuation-dissipation theorem,

$$D_n = D_t m^2 = \frac{k_B T}{6\pi\eta R} \tag{2.3}$$

where k_B is the Boltzmann constant and T is the absolute temperature. Rewriting the Langevin equation, by means of the particle diffusion D_t and noise $\boldsymbol{\eta}(t) = \sqrt{2D_t}\boldsymbol{\xi}_i(t)$, gives

$$\frac{\mathrm{d}\mathbf{v}}{\mathrm{d}t} = -\frac{\gamma}{m}\mathbf{v} - \frac{\nabla U(\mathbf{r})}{m} + \sqrt{2D_t}\boldsymbol{\xi}_i(t). \tag{2.4}$$

With $\nabla U(\mathbf{r}) = 0$ and Eq. 2.3, the integration of Eq. 2.4 gives the mean squared displacement (MSD) [38], $\langle(\Delta\mathbf{r})^2\rangle$, with initial time $t = 0$,

$$\langle(\Delta\mathbf{r})^2\rangle = \langle[\mathbf{r}(t) - \mathbf{r}_0]^2\rangle = 6D_t = \frac{k_B T}{\pi\eta R}t, \tag{2.5}$$

in three dimensions, with a general form $\langle(\Delta\mathbf{r})^2\rangle = 2dD_t t$, in d spatial dimensions. Brownian motion is a random stochastic process, with particles in the dilute regime exhibiting zero average displacement for every time interval. However, the mean squared displacement (MSD), is notably different to zero.

Considering small particles, i.e. micro-swimmers, overdamped dynamics result from the ratio of inertia over the viscous contribution given by $\bar{\eta}$ in the media [39]. The difference between inertial and viscous forces in a fluid is quantified by the Reynolds number,

$$\mathrm{Re} = \frac{v_f L}{\nu} \tag{2.6}$$

where v_f is the fluid velocity, L is a linear dimension, and ν is the kinematic viscosity of the fluid. For a micro-swimmer the magnitude of this ratio is $\mathrm{Re} \ll 1$ [40]. Assuming overdamped dynamics, the evolution of the position is given by the Langevin equation,

$$\frac{\mathrm{d}\mathbf{r}}{\mathrm{d}t} = \mathbf{v} = -\frac{\nabla U(\mathbf{r})}{\gamma} + \sqrt{2D_t}\boldsymbol{\xi}_i(t). \tag{2.7}$$

For a particle with position $\mathbf{r}_0$ at initial time t_0 the probability to find the same particle at $\mathbf{r}$ at time t is given by the Fokker-Planck equation,

$$\frac{\partial P(\mathbf{r}, t\,|\,\mathbf{r}_0, t_0)}{\partial t} = \frac{\partial}{\partial\mathbf{r}}\left[\frac{\nabla U(\mathbf{r})}{\gamma}P\right] + D_t\frac{\partial^2 P}{\partial\mathbf{r}^2}, \tag{2.8}$$

that describes the time evolution of the distribution function of the Langevin equation. For harmonic potentials $U(\mathbf{r})$, and at long times cales, the stationary solution of the Fokker-Planck becomes independent of the initial distribution, and obeys the equilibrium Maxwell-Boltzmann distribution,

$$P(\mathbf{r}) \propto \exp\left[-\frac{U(\mathbf{r})}{k_B T}\right], \tag{2.9}$$

that leads to a stationary state, as long as the fluctuation-dissipation theorem is satisfied.

2.2.2 Active Brownian Particles

Having described the Brownian motion in equilibrium, we now consider the effect of additional self-propulsion forces. Note that a particle with motion far from equilibrium requires additional sources of energy to achieve such a self-propulsion [41]. In active particle systems, the continuous energy supply eliminates time reversal symmetry, which is only possible with detailed balance in steady state. Then it is established that the persistent active motion of a particle is based on energy consumption, which allows the emergence of phenomena shown in Fig. 2.1.

A model that accounts for active motion in the presence of stochastic forces, is known as the *active Brownian particle* (ABP) model [42–44]. Similar to Brownian particles, ABPs perform random walks. Moreover, they are equally susceptible to the external fields $U(\mathbf{r})$. The hallmark of the ABP model is the use of *internal* energy that pumps particles in a given direction. In other words, active Brownian particles take energy from the environment, in order to store it as an internal energy reservoir. The stored energy is then converted into kinetic energy, leading to dynamics markedly different to particles in equilibrium [44]. Following Brownian motion (Eq. 2.1), a space-dependent potential $U(\mathbf{r})$ is added to the Langevin equation of motion,

$$\frac{\mathrm{d}\mathbf{r}}{\mathrm{d}t} = \mathbf{v}; \quad \frac{\mathrm{d}\mathbf{v}}{\mathrm{d}t} = \mathbf{F}_d - \nabla U(\mathbf{r}) + \boldsymbol{\eta}(t), \tag{2.10}$$

with $\mathbf{F}_d$ as a dissipative force, where a non-linear friction $\gamma(\mathbf{r},\mathbf{v})$ is introduced as a function of the particle position and velocity,

$$\mathbf{F}_d = -\gamma(\mathbf{r},\mathbf{v})\mathbf{v}. \tag{2.11}$$

The internal energy that pumps ABPs can be thought as a negative friction, that results in self-propulsion in a given direction [41, 45, 46]. The γ coefficient turns non-linear and position dependent. Note that amplified velocities appear in regions where the friction γ is negative. The Brownian motion of particles consists of stochastic forces with noise amplitude D_t and δ-correlated time dependence. On the other hand, for polar particles [45], with a preferred direction of motion in two dimensions, active fluctuations are introduced. Assuming a homogeneous space, i.e. $\gamma(\mathbf{r},\mathbf{v}) = \gamma(\mathbf{v})$, and neglecting external forces, $\nabla U(\mathbf{r}) = 0$, the motion follows

$$\frac{\mathrm{d}\mathbf{r}}{\mathrm{d}t} = \mathbf{v}; \quad \frac{\mathrm{d}\mathbf{v}}{\mathrm{d}t} = -\gamma(\mathbf{v})\mathbf{v} - \boldsymbol{\eta}(t), \tag{2.12}$$

where the first term accounts either for the friction or propulsion, as the $\gamma(\mathbf{v})$ coefficient turns positive or negative respectively. For a polar particle,the direction of motion is defined by a head-tail axis, with unit vector $\hat{\mathbf{n}}_h(t) = (\cos\theta(t), \sin\theta(t))$, where the time dependent orientation angle $\theta(t)$ is defined with respect to a reference axis [45]. For a particle experiencing a negative friction $-\gamma(\mathbf{v})$, the evolution of the position and orientation is given by $\frac{\mathrm{d}\mathbf{r}}{\mathrm{d}t} = \mathbf{v}(t) = v(t)\hat{\mathbf{n}}_h(t)$, with $v(t)$ as the velocity along the head orientation. Considering the time evolution on $v(t)$ and $\theta(r)$,

$$\frac{\mathrm{d}v}{\mathrm{d}t} = -\gamma(v)v + \hat{\mathbf{n}}_h \cdot \boldsymbol{\eta}(t), \quad \frac{\mathrm{d}\theta}{\mathrm{d}t} = \frac{1}{v}\hat{\mathbf{n}} \cdot \boldsymbol{\eta}(t), \tag{2.13}$$

where $\hat{\mathbf{n}}(t) = (-\sin\theta(t), \cos\theta(t))$ is the unit vector. Note that the orientation θ diverges with $v = 0$ for point-like particles. This can be avoided using finite size particles with possible reorientation at $v = 0$ [45]. For Brownian motion, the passive fluctuations develop from the media in which the particle moves, and the direction of motion is independent of the random force $\boldsymbol{\eta}_p(t) = \sqrt{2D_t}\boldsymbol{\xi}_i(t)$. In contrast, the active fluctuations consist of independent stochastic processes in the direction of motion and in the velocity. Overall, for small particles we find contributions from both passive and active fluctuations, $\boldsymbol{\eta}(t) = \boldsymbol{\eta}_p(t) + \boldsymbol{\eta}_a(t)$, with

$$\boldsymbol{\eta}_a = \sqrt{2D_v}\,\xi_v(t)\hat{\mathbf{n}}_h + \sqrt{2D_\theta}\,\xi_\theta(t)\hat{\mathbf{n}}_\theta, \tag{2.14}$$

where D_v and D_θ are the velocity and angular noise amplitudes. Thus, active fluctuations are purely out-of-equilibrium. Considering additive noise terms from the active fluctuations, the equations of motion for an ABP follow,

$$\frac{\mathrm{d}v}{\mathrm{d}t} = -\gamma(v)v + \sqrt{2D_v}\,\xi_v(t), \qquad \frac{\mathrm{d}\theta}{\mathrm{d}t} = \frac{1}{v}\sqrt{2D_\theta}\,\xi_\theta(t), \tag{2.15}$$

with decoupling between v and θ. Here, D_θ relates to the rotational diffusion, given by

$$D_r = \tau_r^{-1} = \frac{k_B T}{8\pi\eta R^3}. \tag{2.16}$$

The inverse of the rotational coefficient τ_r^{-1} is the characteristic time scale for a particle to undergo rotational diffusion. Similar to Brownian motion, the solution to the stationary velocity probability from the Fokker-Planck equation can be derived,

$$P(v) \sim v^{\frac{D_t}{D_t+D_v}} \exp\left(-\int^v dv' \frac{\gamma(v')v'}{D_v + D_t}\right). \tag{2.17}$$

A clear difference between motion in passive and active particles is given by the trajectories shown in Fig. 2.2**a**. For a passive particle, the mean value $\langle r_i \rangle = \langle r_j \rangle$, vanishes to zero due to symmetry in the stochastic processes. Notably, the mean value over the ensemble is non-zero for ABPs, having motion along some preferred orientation (usually fixed by the initial orientation) and with a persistence length, given by $l_p = v\tau_r$ [27]. Altogether, the self-propulsion properties modeled in the ABP bring different dynamics, accounting for the active contributions and fluctuations at different time scales. This is well represented by the mean square displacement, which for an ABP in two dimensions is transformed from the usual Ornstein-Uhlenbeck random walk [37] to the following expression,

$$\langle(\Delta r^2)\rangle = 4D_t t + \frac{v^2\tau_r^2}{3}\left[\frac{2t}{\tau_r} + \exp\left(\frac{-2t}{\tau_r}\right) - 1\right]. \tag{2.18}$$

which exhibits multiple crossovers. For an ABP, at short times scales the motion is diffusive and proportional to the Brownian motion diffusion coefficient D_t. At intermediate time scales, the motion becomes ballistic, i.e. $\langle(\Delta r^2)\rangle = 4D_t t + v^2 t^2$, and again diffusive at long time scales as rotational diffusion leads to a random persistent walk [27, 45, 47].

2.2.3 Phenomenological models

Microswimmers

At macroscopic scales, living systems are well known for forming large populations performing collective phenomena, such as crowds (Fig. 2.1). On the other hand, at the microscale a vast number of self-propelled organisms is found, from bacteria [48–50], spermatozoa [51, 52], and protozoa [53, 54]. The propulsion mechanism in these organisms depends either on cilia or flagella powered with molecular motors [55–59]. Even though, the motion of such microorganisms can be described by means of the

equations introduced in Sec. 2.2.2, other models have been proposed, among which a notable one is the *squirmer* model [39, 60]. This model was originally implemented to describe the swimming of organisms like *Paramecia* or *Opalina* at low Reynolds number. For this, a spherical particle with a deformable envelope can be considered for the sequential (metachronal) waving of cilia. This envelope is prescribed as a tangential surface velocity field $\mathbf{v}_s$ [61], illustrated in Fig. 2.2**e**, and given by every squirmer as,

$$\mathbf{v}_s = B_1(1+\beta\mathbf{n}\cdot\hat{\mathbf{r}}_s)[(\mathbf{n}\cdot\hat{\mathbf{r}}_s)\hat{\mathbf{r}}_s - \mathbf{n}], \tag{2.19}$$

where B_1 is a bulk constant that sets the swimming speed $v_0 = 2B_1/3$, $\mathbf{n}$ is the swimming orientation, and $\hat{\mathbf{r}}_s$ is the unit vector pointing from the sphere centre of mass $\mathbf{r}$ to the surface. The dimensionless squirmer parameter β, describes the nature of the swimmer. For $\beta < 0$ the microswimmer is referred as a *pusher* (tensile), *puller* (contractile) with $\beta > 0$, and *neutral* with $\beta = 0$ [62, 63]. These descriptions relate to the far-field fluid flow induced by the type of swimming (see blue lines in Fig. 2.2**f**). Pusher and puller swimmers act as force dipoles, with fluid flows pointing outwards and inwards along the direction of motion $\mathbf{n}$ respectively. On the other hand, a neutral squirmer acts like a source dipole, with flow streamlines similar to those in a magnetic field. Additionally, when compared to self-propelled particles, i.e. Janus spheres described later in Sec. 2.5, where the hydrodynamic perturbation decays usually with $1/r^3$, the force dipoles observed in either pullers or pushers decay with $1/r^2$ [64].

Typical examples of living squirmers are *Chlamydomonas reinhardtii* algae (puller), *E. coli* and *Bacillus subtilis* bacteria (pusher), and *Paramecium* (neutral), and the main difference between these is the anatomic location of the molecular motors. The induced flow fields for the different types of squirmers are illustrated in Fig. 2.2 f, and can be determined analytically, numerically [65, 66] and experimentally by adding tracer beads [67, 68]. As expected, different types of swimming behaviour lead to different collective

motion in large populations, where polar order is observed for long-times in neutral and contractile swimmers solely [69]. However, flocking enhancement results with puller-pusher mixtures, where pushers acquire an effective alignment [70]. Additionally, the rheological properties [71, 72] of squirmer suspensions have been tested, where an activity-induced thickening is observed in suspensions of contractile swimmers [73], and an extreme in suspensions of tensile swimmers [74] due to negative yield stress [75–77].

Run and tumble

Similar to the stochastic dynamics find in the ABP model, biological swimmers, i.e. *E. coli*, perform a persistent random walk. These fall into the category of *run and tumble* particles (RTP) [78]. Their distinction relies on the dynamics, where the motion consists of periods of persistent (linear) walks, named *runs*, with sudden reorientation events, called *tumbles*, occurring with a random rate τ_t. During the runs, the motion exhibits constant velocity $\sim v_0^2/\tau_t$, which is large compared to the typical velocities of particles undergoing Brownian motion. The hallmark of the motion in RTPs is found in the shape of the random walk, where the direction completely decorrelates with tumbles. This is in contrast with ABPs, whose direction smoothly decorrelates due to rotational diffusion D_r [79–81]. Figure 2.2 c shows a schematic comparison between RTP and ABP dynamics.

Even though the swimming direction is randomized by discrete tumbles in RTP, they are similar to ABP in the sense that particles have a constant external force $\mathbf{F}$ acting along the swimming direction $\hat{\mathbf{n}}$. Ideal ABP and RTP particles exhibit unperturbed angular dynamics from the interaction with neighbours, since the particles do not exert torques on one another.

Non-spherical bodies

The models above describe the motion for spherical particles, which are largely used in colloidal experiments and numerical simulations [82]. However, most of the examples in

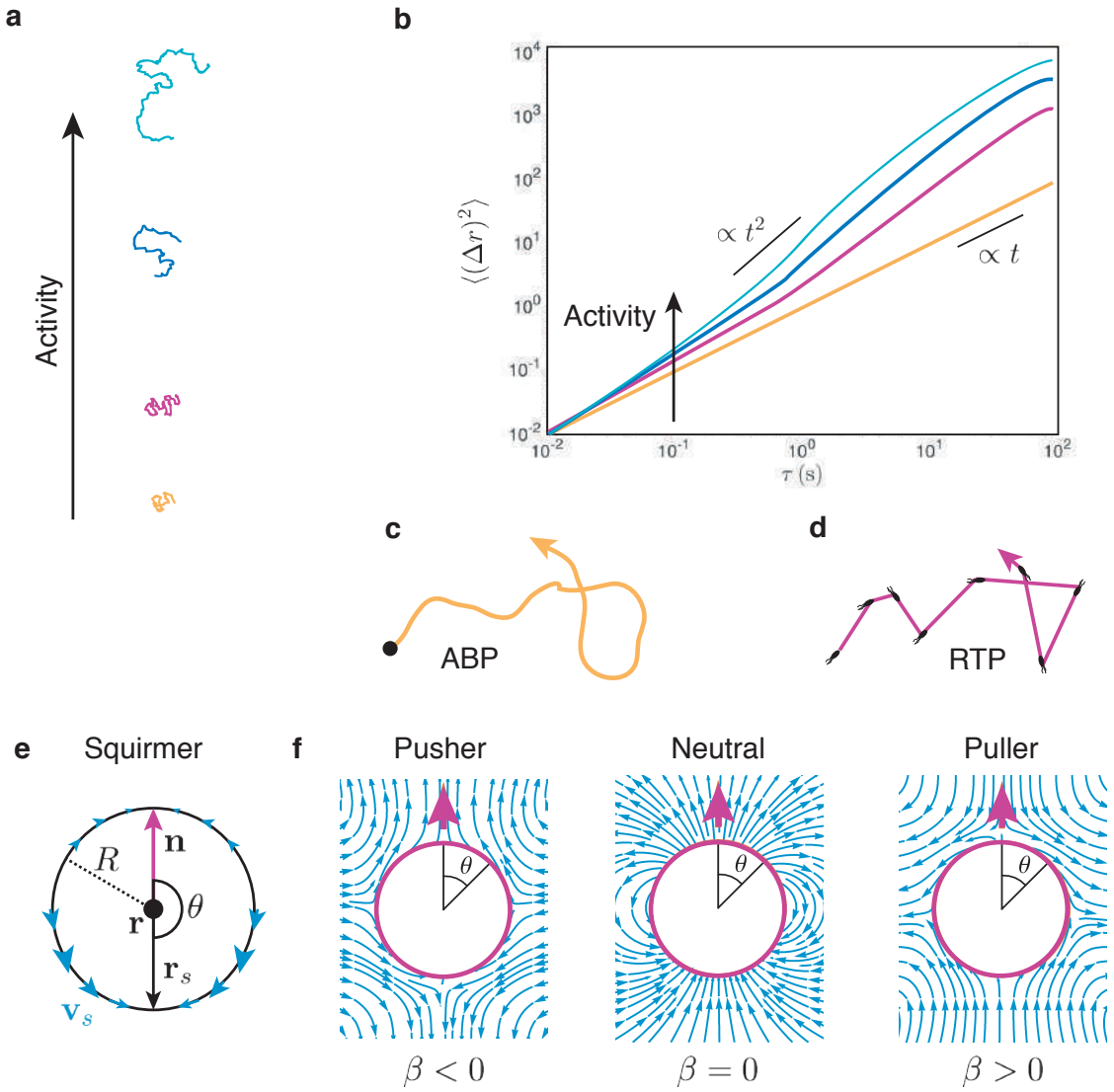

Figure 2.2: **Active Particle Dynamics. a.** Schematic representation of four particle trajectories as the activity increases. **b.** Mean square displacement for the trajectories shown in **a**. Arrow indicates the increase of the activity. Reproduced from [27]. **c** and **d** exemplify the difference between ABP and RTP trajectories. Figure from Ref. [80]. **e.** Illustration of a squirmer of radius R swimming with direction $\mathbf{n}$. Blue arrows along the surface indicate the asymmetric velocity field $\mathbf{v}_s$, which magnitude depends on the polar orientation θ of $\mathbf{r}_s$. Reproduced from [63]. **f.** Different types of squirmers given by the parameter β. Red arrows indicate $\mathbf{n}$, and blue lines represent the resultant flow stream. Pusher and puller squirmers act like force dipoles, whereas a neutral one is a source dipole.

nature deviate from spheres to elongated or rod-like shapes, with most micro-swimmers, e.g. *E. coli* and *spermatozoa*, falling into this description. On the other hand, spheres offer a good benchmark to investigate the dynamics of non-spherical bodies. Thus, the equation of motion of a sphere reads

$$\gamma \frac{\mathrm{d}\mathbf{r}}{\mathrm{d}t} = F\hat{\mathbf{n}} + \boldsymbol{\xi}(t), \tag{2.20}$$

with F as an effective force on the particle. When the orientation $\hat{\mathbf{n}}$ does not change, $\hat{\mathbf{n}}(t) \equiv \hat{\mathbf{n}}(0)$, the self-propulsion speed is given by $v_0 = F/\gamma$, and the particle trajectory is recovered with $\mathbf{r}(t) = \mathbf{r}(0) + v_0 t\hat{\mathbf{n}}(0)$. Considering the anisotropy of the body, the equations of motion for a non-spherical particle follow,

$$\mathbb{H} \cdot \mathcal{V} = \mathbf{K} + \boldsymbol{\xi}, \tag{2.21}$$

where $\mathbb{H}$ is a hydrodynamic friction tensor, that consists of a 6×6 (in three dimensions) or 3×3 (in two-dimensions) symmetric matrix, relating translation and rotation on the particle due to drag forces $\mathbf{F}$ and torques $\mathbf{T}$ [83]. $\mathcal{V}$ is a generalised velocity, $\mathcal{V} = [\mathbf{v}, \boldsymbol{\omega}]$, considering the velocity $\mathbf{v}$ and translational angular velocity $\boldsymbol{\omega}$, $\mathbf{K} = [\mathbf{F}, \mathbf{T}]$ is a generalised force and torque acting on the particle, and $\boldsymbol{\xi}$ is a δ-correlated random vector [84]. In the simple case, linear trajectories are recovered if $\boldsymbol{\omega}$ and $\boldsymbol{\xi}$ are equal to zero. For an isolated non-spherical particle, the size reduction turns in strong rotational diffusion D_r, and the motion approximates to that of ABPs. On the other hand, circular [85, 86] and helical [87] motion is observed in two and three dimensions respectively with $\boldsymbol{\omega} \neq 0$.

Motion in external fields

Active particles are characterised by their self-propulsion in the absence of external torques and forces, which requires the conversion of energy into motion. On the other

hand, non-equilibrium motion can be considered in the presence of external fields, i.e. gravity or external fluid flows. In addition to this self-propulsion force, other existing forces can be added, such as interparticle body interactions [88–90] or external forces from, e.g. confinement [85, 91–93] or gravity [94, 95]. These body and external forces can be added to the effective driving forces and torques, with the assumption that the active motion remains unperturbed. However, this assumption is not always true, as indicated by experiments. Note that the motion of rod-like particles is disturbed by the application of an external electric field, as observed in Ref. [96]. In this case, the rods are driven by electrophoresis, and the effect of applying the external field is the perturbation of surrounding ions. For this specific case, it is also noted that the concentration of ions alters the particle propulsion [97].

Motion under gravity results when the characteristic density of a particle ρ_p is larger than that of the dispersing medium ρ_l. This results in sedimentation due to the gravitational field $\mathbf{g}$ acting with an acceleration g along the $\hat{\mathbf{z}}$ direction. The sedimentation force is then given as $\delta m\mathbf{g} \sim (\rho_p - \rho_l)\mathbf{g}$, where δm is the mass buoyancy of the particle. The effective motion under gravity is given by the Langevin equation,

$$\frac{\mathrm{d}\mathbf{r}}{\mathrm{d}r} = v_0\hat{\mathbf{n}} + \frac{\delta m}{\gamma}\mathbf{g} + \sqrt{2D_t}\boldsymbol{\xi}. \tag{2.22}$$

Interestingly, it is shown in experiment using spherical [98] and asymmetric particles [86] that self-propulsion competes against sedimentation due to gravitaxis, and that the interplay between gravity and circular motion leads to complex trajectories in asymmetric particles.

2.3 Collective Behaviour

Individual self-propulsion itself is a characteristic not observed in conventional systems at equilibrium. For particles consuming local energy, persistent motion is observed along a random walk set by the particle orientation. The result of increasing the population is the emergence of collective or *social* behaviour that depends on the interactions among the neighbours. There are many examples of collective organisation in the living world, with some of the most obvious and interesting being the migration of groups of animals (Fig. 2.1). Among these we find flocks of birds, schools of fish, where the apparent interaction comes from a social context. On smaller scales, other mechanisms for the interactions are at play, like the forces exerted between cells, or the biochemical signals exchanged within a cell colony [99]. In both cases, the collective phenomena results without centralised control, where a coherent global state is given by the local neighbour-neighbour interactions [100–103]. In this sense, many studies have been devoted in the recent decades for the understanding of such interactions. This through combining analytical models with numerical simulations and the use of living and man-made experimental models.

Considering a system of many identical units, the type of interactions might be rather simple, e.g. attractive or repulsive, a combination of these [22], or in some cases topological interactions [104, 105]. Notably, the type of interactions determine how the information spreads through the system. Physically this can be captured by forces acting on particles within a certain range of interaction. Unlike the use of external fields, that impose a net orientation for the particle motion, here the local interactions, e.g. alignment interactions due to spontaneous symmetry breaking, lead to collective motion. In this regard, some models give rise to social behaviour (see Fig. 2.3) as a consequence of different metric extensions, which result in repulsion, attraction and alignment [106]. Alternatively, measurements made in flocks of birds suggest that the

extent of interactions is rather given by a topology regardless of distance. In other words, the information exchange is set by the number of neighbours, and not by the metric distance between them (see Fig. 2.3). In general, minimal models have been implemented to account for these observations, where long-range interactions [104], or metric-free interactions dominate [107].

Understanding the nature of the interactions is relevant, since the type of motion and collective phenomena is affected by the way individuals interact. Focusing on the many body alignment, a collection of particles moving with a constant velocity v_0, reorient themselves to the orientation of the neighbour within a certain range. A variation of this same model implements topological interactions, set by the number N of neighbours around one particle regardless of their separation. Alignment can be of two types: for a polar particle with a preferred direction of motion the alignment is ferromagnetic for polar particles, and nematic for particles of uniaxial director, such as in elongated bacteria aligning through steric interactions [108]. Alternatively, elongated particles exhibit nematic alignment [109]. Figure 2.3 shows the scenarios that promote interactions, along with a representation of polar and nematic alignment of particles.

In the following subsections we introduce a set of collective phenomena that have been the subject of debate in the literature. First, we discuss a minimal model in which an order-disorder transition arises from the alignment interactions in self-propelled active systems. This model proves suitable for the description of *active polar matter*, e.g. bird flocks [17]. Moreover, the coarse-graining of the microscopic details of such a minimal model leads to the derivation of continuum dynamical models [18]. Later, we present a dynamical aggregation process that leads to a non-equilibrium phase separation in motile particles. Finally, we summarise a list of experimental realisations of active matter models, displaying self-propulsion and collective behaviours via various mechanisms.

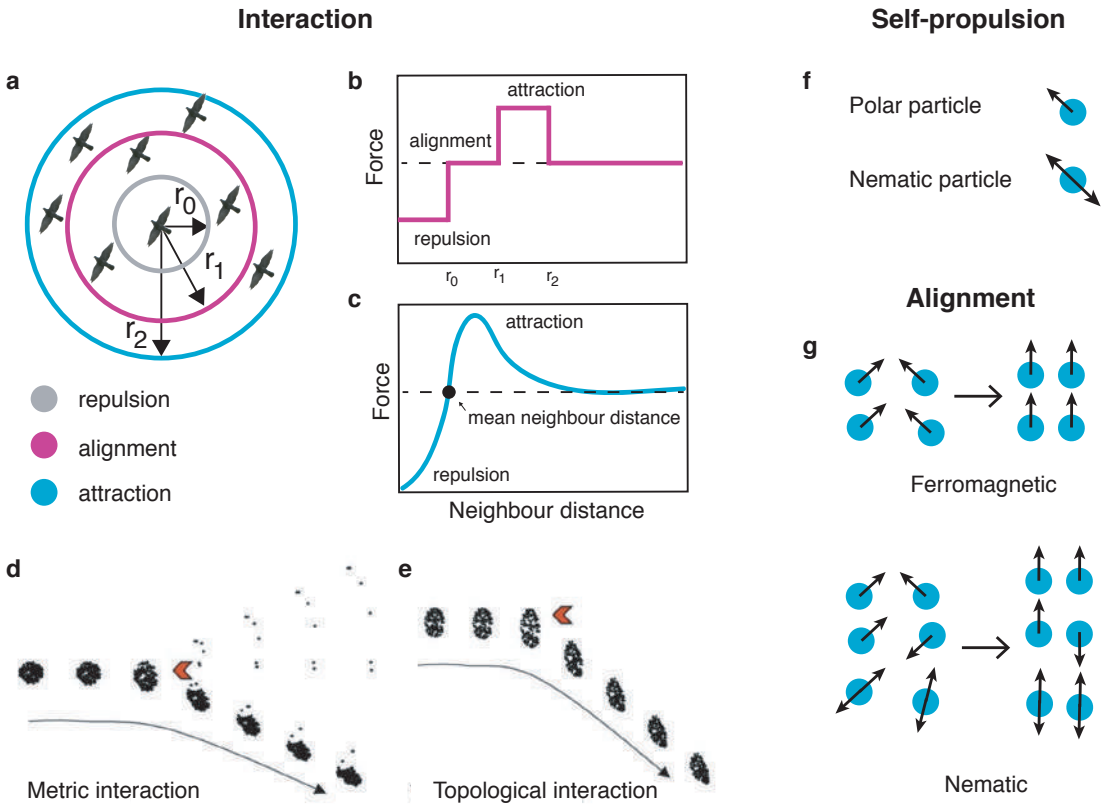

Figure 2.3: **Interactions, self-propulsion and alignment. a.** Contributions from repulsion, alignment and attraction to the different regions of behaviour, delimited by r_0, r_0 and r_0 respectively. **b** and **c** show the attractive and repulsive forces as function of the distance between neighbours. In **b** we observe that the range of alignment interactions is given by $r_0 < r < r_1$. **c** shows the short range repulsion and attraction with larger separations. Dot indicates the mean over the nearest neighbour distance at force equal to zero. Figure reproduced from [110]. **d** and **e** show a comparison between a system interacting by distance ranges described in **a**, and a system with topological interactions under external perturbation indicated by orange arrows. **d** displays the distortion of the flock, whereas **e** shows a collective response to an external perturbation. Reproduced from [104]. **f.** Self-propulsion is polar or nematic. **g.** Alignment interactions can result of ferromagnetic type or nematic [111].

2.3.1 Vicsek Model

In order to address the questions for universal laws governing the collective behaviour of active systems, different models have been proposed. A pioneer minimal model was introduced in 1995 by Vicsek [17], in which dynamics and a non-equilibrium phase transition are introduced for an active system (see Fig. 2.4), e.g flocking birds [112]. The model consists of a collection of N point particles performing self-propulsion with fixed speed and noisy alignment interactions on an inert substrate. This could be treated as a non-equilibrium extension of the XY model, where the speed alignment interaction is analogous to a ferromagnetic alignment of spins. For every ith particle, the evolution of the position in two dimensions ($d = 2$) at every time step Δt follows,

$$\mathbf{r}_i(t+\Delta t) = \mathbf{r}(t) + \Delta t \mathbf{v}_i(t+\Delta t), \tag{2.23}$$

with $\mathbf{v}_i(t+\Delta t)$ being the particle velocity with a fixed magnitude v_0 and randomly distributed orientation $\hat{\mathbf{n}}_i = (\cos\theta, \sin\theta)$, where θ in two dimensions,

$$\theta_i(t+\Delta t) = \arg\left[\sum_j n_{ij}(t)\hat{\mathbf{n}}_j(t)\right] + \eta\boldsymbol{\xi}(t) \tag{2.24}$$

with $\boldsymbol{\xi}(t)$ as δ-correlated zero average noise that has an analogous role as temperature in stochastic systems (see Eq. 2.2). This so called white noise has a uniform distribution, $\eta \in [-\pi, \pi]$, which sets a scale for the noise, where $\eta = 1$ being the maximum noise amplitude dominating the system [113]. In Eq. 2.24, we have the neighbour matrix n_{ij} which sets the the connection between particles,

$$n_{ij}(t) = \begin{cases} 1, & |\mathbf{r}_i(t) - \mathbf{r}_j(t)| < R_0 \\ 0, & |\mathbf{r}_i(t) - \mathbf{r}_j(t)| > R_0 \end{cases} \tag{2.25}$$

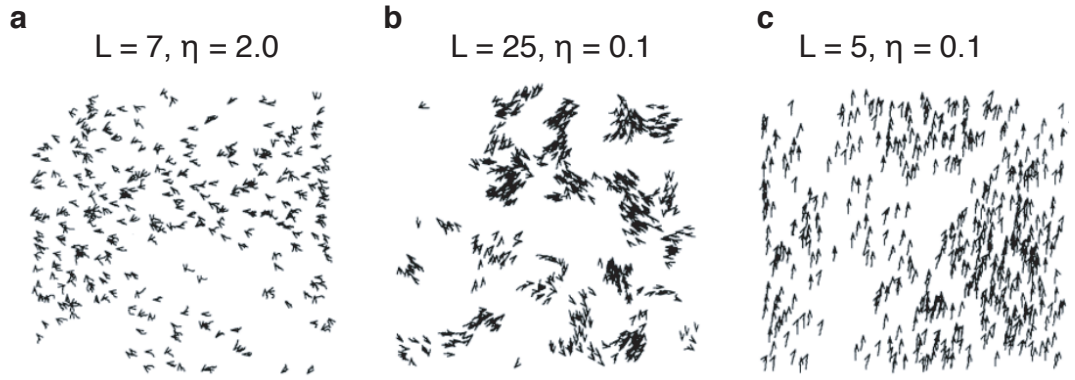

Figure 2.4: **Various states of the Vicsek model. a.** random motion with some correlation for a system with high density (L = 7) and noise ($\eta = 2.0$). **b.** Colony formation with coherent motion in random directions for L = 25 and $\eta = 0.1$. **c.** Polar order motion with L = 5 and $\eta = 0.1$. Lines in **a**, **b** and **c** represent twenty time steps. $N = 300$ and $v_0 = 0.03$ for all cases. Reprinted from [17].

where the criteria for selecting neighbours is local by means of a *metric* interaction set by a region of radius R_0, rather than *topological*, where the particles align with their nearest neighbors regardless of their distance (see Fig. 2.3 for a schematic representation). Expressing time and space in units of $\Delta t = 1$, and R_0 = 1, the model depends on three control parameters:

(i) the density of particles $\rho_0 = N/V$, with V as the system volume. Assuming periodic boundary conditions we get $V = L^d$, having L as the linear size of the system, and d the number of dimensions.

(ii) the noise amplitude η,

(iii) the magnitude of the velocity $|\mathbf{v}| = v_0$.

Note that, in this phenomenological model the only conserved quantity is the total density ρ_0 [1]. Note that momentum is not conserved, as particles propel on a dissipative

[1]Density is conserved since birth and death (in the case of birds) events are neglected here.

substrate that dissipates momentum. This kind of substrate can be seen as a viscous medium. We refer to this class of systems as *dry* active matter [7].

A hallmark of the model is the transition observed between a state of low density (high noise) to a coherent state of high density (low noise). Isotropic motion is recovered from Eqs. 2.23 and 2.24 since the orientation is not predefined. Nonetheless, the alignment contribution from Eq. 2.24 promotes a net polar motion that results in global order. We proceed to describe the characteristics of the homogeneous polar state.

Emergence of homogeneous collective motion

As described previously in the Vicsek model, spontaneous symmetry breaking results as a kinetic phase transition from disorder to polar order, i.e. $\langle \mathbf{v} \rangle = 0 \rightarrow \langle \mathbf{v} \rangle \neq 0$. As shown by Vicsek and by other numerical results [114, 115], flocks of particles with ferromagnetic-like alignment interactions form a homogeneous phase with long-range order. This expression of collective behaviour is not attainable for a two-dimensional spin system in equilibrium, as shown by Mermin, Wagner and Hohenberg [116, 117]. Spontaneous symmetry (rotational invariance) breaking to form long-range order, with $\langle \mathbf{v} \rangle \neq 0$, can not occur. For the XY model, spin wave fluctuations result in short-range interactions solely [116]. Therefore, the main distinction between the equilibrium and its active counterpart is the non-equilibrium nature of the latter. In other words, we have self-propelled particles able to "communicate" better than spins on a lattice. We now describe some of the main aspects that contribute to formation of the homogeneous polar phase.

Symmetry breaking and polar order — Isotropic motion is recovered from Eqs. 2.23-2.24 since the particle does not posses an initial preferred direction. Nevertheless, ferromagnetic alignment emerges from the polar contribution of Eq. 2.24. In addition, a global order develops if the alignment interactions overcome the noise contribution. The

collective motion is further characterised with the polar order parameter,

$$\Pi = \left\langle \left| \frac{1}{N} \sum_{i}^{N} \mathbf{n}_i(t) \right| \right\rangle_t , \tag{2.26}$$

which is analogous to the magnetisation parameter in spins. The overall value of Π is dependent of the control parameters ρ_0, η and v_0. $\langle ... \rangle_t$ denotes a time average, and the modulus gives a scale of order, from isotropic states with $|\Pi| = 0$, to collective motion with global polar order $|\Pi| = 1$. Considering finite size effects, for the isotropic phase we have $|\Pi| \sim 1/\sqrt{N}$, since the orientation vectors $\mathbf{n}$ do not cancel each own.

Control parameters — Numerical results of the Vicsek model for a large system with finite-size scaling [114, 115] show a transition from a disordered to an ordered state. Fixing both density ρ_0 and speed v_0, we have the noise amplitude η as the main control parameter. Hence, for a noise amplitude below a certain threshold η_c we obtain polar order ($|\Pi| \approx 1$) as the system undergoes spontaneous symmetry breaking. It is important to note that the critical noise η_c depends on the density and speed, thus, $\eta_c(\rho_0, v_0)$. It is this threshold that sets the onset of collective motion, which is mapped using the order parameter in Eq. 2.26.

Alignment and self-propulsion — Particles experience self-propulsion as indicated in Eq. 2.23, and they are able to continuously update their position and orientation, leading to alignment interactions through the connectivity neighbour matrix n_{ij}. To note that the neighbour-neighbour interactions are not static, and their change in time is non-trivial. For polar point-like particles, the alignment is due to ferromagnetic interactions. Other models explore rod-like particles [111], where the alignment results to be nematic, due to steric interactions [13, 108, 118]. Figure 2.3 f-g, captures the difference between ferromagnetic and nematic alignment in polar and apolar particles.

On the other hand, the alignment interactions can be thought by means of information propagation that promotes collectivity, while noise destroys it. Continuing with the idea of information propagation, for a fixed range of interaction $R_0 = 1$ and density $\rho_0 \ll 1$, a dilute gas of particles results, and the rare interactions emerge from instantaneous collisions between particles i and j. Thus, each particle needs to travel certain distance l_i between collisions. This "free" path scales as $l_i \sim 1/\rho_0$, meaning that the information can only propagate through the system if l_i is larger than the particle persistence length l_p. This latter corresponds to to the distance that a particle travels before decorrelation of the orientation. On increasing alignment, these two distances become comparable $l_i \sim l_p$. Moreover, l_p is inversely proportional to the noise variance, $l_p \sim v_0/\eta^2$, thus,

$$\eta_c \sim v_0 \rho_0^{1/d}, \quad \eta_c \sim \sqrt{\rho_0}, \quad \text{with } d = 2, v_0 = 1. \tag{2.27}$$

Giant density fluctuations — As mentioned before, a phase with long-range polar order emerges with the decrease of the noise amplitude. Even though this phase is globally homogeneous, it exhibits anomalous density fluctuations. For a system in equilibrium, short-range correlations result in density fluctuations characterised by $\Delta N \propto \langle N \rangle^a$, with $a = 0.5$. On the other hand, for a system with long-range correlations exhibiting global order the exponent is $a = 0.8$, a hallmark of the large density fluctuations (see Fig. 2.6**b**) [115].

Beyond the Vicsek model

After the pioneering work described in the previous section, many different approaches of Vicsek-like models have been proposed. Overall, the main ingredients remain the same: self-propulsion, alignment interactions and rotational noise. For instance, different implementations focus on the role of noise and how it is introduced to the system [114, 115, 119–121]. In addition, large systems and finite-size scaling effects are

explored [114, 115, 122–124]. The different approaches discriminate the contribution from the interactions, e.g. metric-free interactions as in Fig. 2.1**a** [104, 125], and the effects on the nature of the order-disorder phase transition [107]. In addition, nematic interactions of rod-like particles [107, 108, 126, 127], and inelastic collisions [128] can be added to develop analogs of the Vicsek model. Also, with the aim of studying the macroscopic phenomenology, coarse grained continuum models have been established [129, 130]. We now proceed to describe model developed from a model of ferromagnetism in statistical mechanics.

2.3.2 Active Ising Model

Following the description of the phenomenological Vicsek model, the emergence of a polar homogeneous phase with long-range order, in contrast with a spin system in equilibrium [116]. This however, is only achieved in large systems in numerical simulations [115]. To overcome the high computing power needed to render these observations, the active version of the well established Ising model [131] is introduced by Solon and Tailleur [124]. We briefly present the original model, followed by the description of its active counterpart.

Among models of spins on a lattice, e.g. the above mentioned XY model, the Ising model is the simplest model to analyse phase transitions and the characteristics of ordered phases [38]. The model considers a lattice of d dimensions, each with a set of adjacent sites, and a discrete variable σ_i represents the spin at site i, $\sigma_i \in [+1, -1]$. The spin interactions between sites i and j are through neighbour exchange, so the Hamiltonian is

$$H = -\frac{1}{2}\sum_{ij} J_{ij}\sigma_i\sigma_j - \sum_i h_i\sigma_i, \tag{2.28}$$

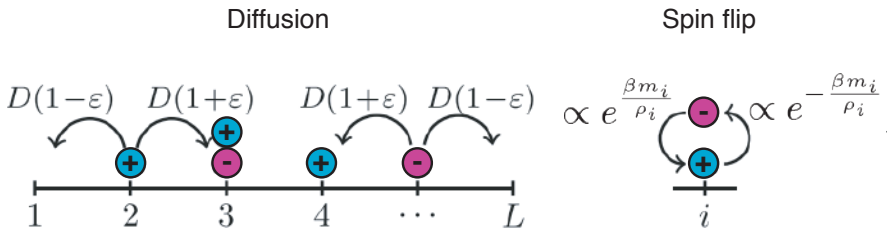

Figure 2.5: **Active Ising model.** Illustration of the hopping between lattice sites (left), and spin flip rate of locally aligned particles (right). Reproduced from Ref. [132].

where h_i represents an external magnetic field at site i. Here, J_{ij} is the spin interaction, given by

$$J_{ij} = \begin{cases} J, & \text{if } i \text{ and } j \text{ are adjacent sites} \\ 0, & \text{otherwise} \end{cases} \tag{2.29}$$

The interaction J_{ij} defines the spin pair coupling, with $J_{ij} > 0$ and $J_{ij} < 0$ resulting in ferromagnetic and anti-ferromagnetic interactions respectively. The ferromagnetic class corresponds to our previous description in Fig. 2.3**g**, where all the coupled spins have the same orientation. Here, the anti-ferromagnetic phase occurs at high temperature with $\langle \sigma_i \rangle = 0$. In the opposite case, at low temperatures the ferromagnetic phase emerges, $\langle \sigma_i \rangle \neq 0$, and $\langle \sigma_i \rangle \in [+1, -1]$. Hence, a critical temperature T_c sets the overall magnetisation m, with $m = 0$ and $m = \langle \sigma_i \rangle$ for $T > T_c$ and $T < T_c$ respectively.

In order to tackle the numerical limitations in flocking systems, a lattice-based model is introduced. Here, the active Ising model is conceived as a simpler version to analyse numerically and analytically the observations in the Vicsek model. As above, the main features of the active Ising model are the particle self-propulsion and local alignment [124, 132].

This model considers particle motion on a two-dimensional lattice of $L_x \times L_y$ sites i, and periodic boundary conditions. Particles are allowed to diffuse in the two-dimensional

plane, with the condition that self-propulsion occurs in one direction solely. Additionally, the continuous rotational symmetry considered in the Vicsek model is replaced by discrete rotational symmetry, and there are no excluded volume interactions between the particles. Similar to the early Ising model, each particle carries a spin $\sigma_i \in [+1, -1]$, and the local density and magnetisation are given by, $\rho_i = n_i^+ + n_i^1$ and $m_i = n_i^+ + n_i^-$ respectively, where $n_i^\pm$ is the arbitrary number of particles with spin ± 1.

The novelty here, is that particles are allowed to diffuse by hopping to adjacent neighbour sites, and to flip their spins. Both processes have characteristic rates that account for alignment and self-propulsion. For a particle at site i and spin σ_i the spin flip rate,

$$W(+\sigma \to -\sigma) \propto \exp\left(-\sigma\beta\frac{m_i}{\rho_i}\right), \tag{2.30}$$

where $\beta = 1/T$ is an inverse temperature. Particles with spin $+\sigma_i$ have a spin rate of $\exp(-\beta)$ if the particles on the same site i have the same spin value, and the rate varies to $\exp[\beta(1-2/\rho_i)]$ if particles have spin $-\sigma_i$. The alignment interactions are only local, i.e. for particles without hopping local alignment with neighbours at the same site i occurs. For the diffusion, each particle hops with a rate $D(1+\sigma\epsilon)$ to the right, and $D(1-\sigma\epsilon)$ for hopping to the left. Self-propulsion is given by the ϵ parameter, so that self-propulsion vanishes with $\epsilon \to 0$ and particles only diffuse on the lattice. Figure 2.5 illustrates the diffusion and spin mechanisms. Having the self-propulsion contribution on the diffusion we obtain different regimes controlled by ϵ: complete self-propulsion with $\epsilon = 1$, self-propulsion $\epsilon \in [0, 1]$, weak self-propulsion $\epsilon \sim 1/L$, and diffusive $\epsilon = 0$.

Clearly this differs with the Vicsek model, in the sense that particle motion is suppressed with $v_0 = 0$. In the absence of self-propulsion, the Vicsek dynamics resemble the equilibrium XY model. For the Ising model, the control parameters to map the phase behaviour are the self-propulsion ϵ, the average density $\rho = N(L_x L_y)$, and the

temperature $\beta^{-1} = T$, which takes the role of noise in the Vicsek class.

Similar to the previous model, a collective motion emerges with the spontaneous breaking of discrete symmetry. At low densities, a homogeneous gas is obtained with the local magnetisation $\langle m_i \rangle \approx 0$, with increasing temperature. Opposite, at lower temperatures with large densities, particles synchronise their displacement in a collective manner to form a polar liquid, where $\langle m_i = m_0 \rangle \neq 0$, with m_0 as the global magnetisation. Note that at intermediate densities, phase separation takes place with polar liquid in the form of bands traveling (either left or right) through an isotropic gas, akin to the Vicsek class. With fixing the self-propulsion ϵ and the magnetisation m_0 we have the density ρ_0 varying the shape of the polar liquid, usually named polar liquid droplet or heteroclinic cycles [124, 132, 133] (See Sec. 2.4.1 for more details).

2.3.3 From Microscopic to Large Scales

From our previous description of the Vicsek model [17], we find the analogy between a dynamical flocking system and an equilibrium ferromagnet, where the velocity $\mathbf{v}_i$ of every ith particle (bird) takes the role of a magnetic spin on the ferromagnet. The results from numerical simulations show flocking in ferromagnetic systems that posses short-range interactions, complete rotation invariance, and non-zero temperature. This is however not attainable for a two-dimensional equilibrium spin system as shown by Mermin, Wagner and Hohenberg [116, 117], where spontaneous symmetry breaking (also breaking of rotational invariance) to form long-range order, with $\langle \mathbf{v} \rangle \neq 0$, can not occur. Thus, the main distinction between the equilibrium spin system and the Vicsek model is the motion, which in the Vicsek class violates the Mermin-Wagner theorem [18]. On the other hand, solving numerically the equations of motion for the many particle system could be computationally expensive [114, 115], and one could wonder about the large scale behaviour of the flock. Therefore, many efforts have been devoted to establish

continuum approximations, in order to describe the macroscopic characteristics on a macroscopic scale [129, 130].

Thus large flocking systems, composed of many interacting individuals, can be treated as a fluid. Given the motion of simple fluid, described by the equations of motion over every molecule or constituent, the coarse graining of the fluid properties yields the continuum equations. This is achieved by means of the Navier-Stokes equations,

$$\rho\left(\frac{\partial \mathbf{v}}{\partial t} + \mathbf{v}\cdot\nabla\mathbf{v}\right) = -\nabla P + \bar{\eta}\nabla^2\mathbf{v} + \mathbf{f}, \tag{2.31}$$

and

$$\nabla\cdot\mathbf{v} = 0 \tag{2.32}$$

for an incompressible Newtonian fluid, Eq. 2.31 gives the fluid velocity field $\mathbf{v}(\mathbf{r},t)$, and the fluid density ρ and viscosity $\bar{\eta}$. P is the pressure field of the fluid, and $\mathbf{f}$ represents an external force acting on the fluid. This latter quantity is equal to the viscous drag forces, $\mathbf{f}+6\pi\bar{\eta}R\mathbf{v}=0$. Overall, the equation shows balance between contribution from inertia (on the left hand side) and viscosity $\bar{\eta}\nabla^2\mathbf{v}$. As before, the Reynolds number is defined as the ratio of the advection in the momentum $\rho\mathbf{v}\cdot\nabla\mathbf{v}$, to the contribution from viscous forces $\bar{\eta}\nabla^2\mathbf{v}$. As we previously described in Sec. 2.2.1, for microscale bodies $\mathrm{Re} << 1$. Therefore, the viscous contribution dominates over inertia, and we can neglect the $\rho\mathbf{v}\cdot\mathbf{v}$ term in Eq. 2.31.

In the case of suspensions, the dynamics of the particles and the fluid are coupled. For particles, the dynamics are entirely determined by the distribution of positions and velocities at time t. Equivalently, to the velocity field and particle positions in the fluid at time t. Thus, the fluid dynamics in Eq. 2.31 reduce to,

$$\nabla P + \eta \nabla^2 \mathbf{v} + \mathbf{f} = 0, \tag{2.33}$$

known as the Stokes equation, with incompressibility, $\nabla \cdot \mathbf{v} = 0$.

As described by the Navier-Stokes equations, the microscopic parameters are coarse-grained into hydrodynamic fields, such as the fluid velocity field $\mathbf{v}(\mathbf{r}, t)$. The different fields that build the continuum frame explicitly come from the degrees of freedom at the particle level. In dry systems, only the number density $\rho(\mathbf{r}, t)$ is conserved, as the particles move on a frictional substrate. The continuum density field is obtained from the particle position $\mathbf{r}$ distribution, and given by,

$$\rho(\mathbf{r}, t) = \sum_i \delta(\mathbf{r} - \mathbf{r}_i(t)). \tag{2.34}$$

Additionally, thinking of order-disorder phase transitions, a polarisation vector field can be defined from the particle orientations $\hat{\mathbf{n}}$,

$$\Pi(\mathbf{r}, t) = \frac{1}{\rho(\mathbf{r}, t)} \sum_i \hat{\mathbf{n}}_i(t) \delta(\mathbf{r} - \mathbf{r}_i), \tag{2.35}$$

out of which the velocity field is declared for particles with constant speed v_0, $\mathbf{v}(\mathbf{r}, t) = v_0 \Pi(\mathbf{r}, t)$. These equations are of the simplest form, and their evolution depends on the microscopic dynamics. Many implementations take this coarse graining approach to formulate the hydrodynamic equations of microscopic models [118, 125, 126, 129, 130, 134–139], including different phenomenological systems, such as active nematics [140–143], gels [144–146], and bacterial suspensions [147, 148]. Bertin *et al.* [129], introduce a Vicsek-like model considering binary collisions that promote alignment. Here, a Boltzmann-like derivation is implemented to obtain the hydrodynamic equations, which can be resolved numerically [139]. Importantly, this leads to the formulation of

relatively simple hydrodynamic equations [125, 134, 135, 138]. Furthermore, the study of the linear stability in the hydrodynamic equations allows to investigate the phase behaviour for the Vicsek-like models, and to explain the emergence of an inhomogeneous phase. With this in mind, we proceed to describe a pioneering model of flocking in a continuum version.

2.3.4 Toner and Tu Field Theory

In order to address the previously mentioned issues regarding flocking, one could derive from kinetic models a different approach, e.g. hydrodynamics. This is achieved by means of coupling the dynamics of all flocking components at the microscopic level into a coarse-grained description. Thus, the large scale properties of the flock can be accessed by such a continuum model.

For a polar flocking system, the continuum framework is introduced by Toner and Tu [18, 19]. At a large scale, the population is considered as fluid. This realisation is possible by means of the Navier-Stokes equations 2.31,2.32, with symmetries and conservation laws. For this model, the only symmetries are rotational and translation invariance. If the space through which a flock travels is considered to be statically homogeneous, and that the system lacks translational order, there is not symmetry breaking and translation invariance is neglected [20]. On the other hand, rotational invariance implies that the flock constituents lack a director, and all the directions are equivalent in space. Thus, the result is an isotropic ferromagnet. Additionally, the only conservation law is the conservation of constituents: for a flock of birds, birth and death events are not considered. To contrast with the Navier-Stokes equations, there is no conservation of momentum either, as the particles move on a frictional substrate. In addition, the system lacks Galilean invariance[2]. Having the symmetries and conservation laws clarified, we

[2]Galilean invariance is broken with the coarse-graining procedure when deriving stochastic equations. The equations of motion do not remain for a moving system as invariance is broken [149].

identify the coarse-grained hydrodynamic variables, which result to be the same of those in a simple fluid, e.g. the velocity field $\mathbf{v}(\mathbf{r},t)$, and density $\rho(\mathbf{r},t)$. To account for the slow spatial variations, the hydrodynamic description is truncated at second order in gradients,

$$\begin{aligned} &\frac{\partial \mathbf{v}}{\partial t} + \lambda_1(\mathbf{v}\cdot\nabla)\mathbf{v} + \lambda_2(\nabla\cdot\mathbf{v})\mathbf{v} + \lambda_3\nabla(|\mathbf{v}|^2) = \\ &\alpha\mathbf{v} - \beta|\mathbf{v}^2|\mathbf{v} - \nabla P + D_B\nabla(\nabla\cdot\mathbf{v}) + D_t\nabla^2\mathbf{v} + D_2(\mathbf{v}\cdot\nabla)^2\mathbf{v} + \boldsymbol{\eta}, \end{aligned} \tag{2.36}$$

where the λ terms on the left hand side in Eq. 2.36 represent the convective derivatives of the velocity field $\mathbf{v}$ in the Navier-Stokes equations. In the case of Galilean invariance, $\lambda_1 = 1$ and $\lambda_2 = \lambda_3 = 0$. For a non-equilibrium flock, momentum in not conserved and all the λ terms are non-zero phenomenological parameters determined by microscopic details [7].

The phase transition from an isotropic state to an ordered flock is observed with the change of the α term. The velocity relaxes to zero with $\alpha < 0$, resulting in an isotropic state. In contrast, spontaneous breaking of the rotational invariance is obtained with $\alpha > 0$ that forms the polar ordered state. Together, the α and β terms give the magnitude of the local velocity by $v_0 = \sqrt{\alpha/\beta}$ for an ordered phase with non-zero mean velocity value. Further terms, $D_B, D_t,$ and D_2 are diffusion or viscous terms, that in a sense account for the elastic properties of the flock by means of localised velocity fluctuations spreading due to neighbour coupling. Importantly, none of these coefficients are scalar coefficients, but instead are microscopic functionals of the density ρ and velocity $\mathbf{v}$ fields. To account for noise, the $\boldsymbol{\eta}$ term with δ-correlation is introduced. Finally, the pressure,

$$P = P(\rho) = \sum_{n=1}^{\infty} \sigma_n(\rho - \rho_0)^n, \tag{2.37}$$

to account for steric repulsion among particles. This sets the local number density $\rho(\mathbf{r})$

finite, to conserve the mean density ρ_0 in Eq. 2.38. Here σ_n is a coefficient in the pressure expansion. Finally, density is conserved by the continuity equation,

$$\frac{\partial \rho}{\partial t} + \nabla \cdot (\mathbf{v}\rho) = 0. \tag{2.38}$$

Overall, the hydrodynamic description above establishes the framework to study large scale systems, where long-range ordered phases in the form of linear waves propagate anisotropically [20]. Similar to the Vicsek bands, the waves are well captured by the continuum approach, and are equally subjected to density fluctuations.

2.4 Phase transitions

Previously, in Sec. 2.2.2 we described the self-propulsion exhibited by active constituents. Far from equilibrium, self-propelled particles show interesting dynamical properties, which are often observed in a broad range of micro-swimmers, e.g. bacteria and protozoa. Furthermore upon increasing the population, we observe the emergence of collective phenomena, in which complex and social interactions (for living systems) arise. To address the question of a universal law governing such social interactions, many models have been proposed, from kinetic models of self-propelled particles [17, 124, 150, 151], to hydrodynamic-field considerations [5, 19, 19, 129, 130].

In this section we address the phase transition to collective motion observed in polar flocking systems. We later describe the motility induced phenomenological phase separation in self-propelled particles. For both cases, minimal models discussed here address these phenomena.

2.4.1 Onset of collective motion in polar active matter

We start by recalling the phenomenology of the Vicsek model [17, 150], as a minimal model consisting mainly of particles displaying self-propulsion and alignment. It describes point particles moving in a continuous plane with constant speed v_0 and orientation $\hat{\mathbf{n}}_i$, which is updated for every discrete time step Δt (see Sec. 2.3.1 for more details). A hallmark of the system is the spontaneous symmetry breaking to achieve a transition (initially described as an order-disorder transition) between an isotropic state with $\langle \mathbf{v} \rangle \approx 0$, to a homogeneous polar state with long-range order, $\langle \mathbf{v} \rangle \neq 0$. The nature of this kinetic phase transition relies on the constant absolute velocity of particles moving on a dissipative (frictional) substrate. Therefore, momentum is not conserved, and these systems fall in the category of *dry* active matter, where only the number density $\rho(\mathbf{r}, t)$ is conserved.

Some characteristics of the homogeneous phase are as follows,

(i) It posses long-range alignment correlations.

(ii) Anomalous density fluctuations are present, compared with those which follow the central limit theorem[3] with $\delta N \propto \langle N \rangle^{\alpha}$, with $\alpha = 0.5$. For the homogeneous polar bands observed in the Vicsek class we have $\alpha = 0.8$ (Fig. 2.6**b**), measured numerically [115], $\alpha = 1.6$ for active nematics [109]. Giant density fluctuations are also observed experimentally in motor-filament and vibrated systems. [152–154]

(iii) In two-dimensions, the long-range order breaks the continuous symmetry, and violates the Mermin-Wagner theorem, that states the symmetry breaking is not achieved by a system with short-range interactions [116].

[3] This ensures a normal distribution, regardless of the shape of the population N distribution at different system sizes.

We now focus on the transition from disorder to homogeneous polar order. Numerical simulations in two dimensions [17, 122, 150] show a non-equilibrium phase transition from an isotropic to a state with long-range order, providing the first insights into the nature of active polar matter. In the original Vicsek description, the transition is pictured as continuous. In contrast, numerical simulations performed by Chaté *et al.* illustrate large systems with finite-size scaling in two dimensions, where the transition is depicted as discontinuous [114, 115]. When decreasing the noise amplitude η, high density ordered bands emerge from nucleation and propagate through a disordered gas (see Fig. 2.6**c**). This results from the development of an inhomogeneous state, e.g. the system separates into regions of low and high density and order. These fractions correspond to regions with poor and high alignment respectively, and lead to long-wavelength instabilities [129, 134]. This incurs perturbations in either the isotropic or polar homogeneous state, resulting in phase separation. Confirmation of this is given by the hysteresis observed between the disordered state and the inhomogeneous state. On decreasing the noise intensity, the homogeneous polar phase develops.

In addition, other Vicsek-like models [22, 119, 121] describe the nature of the transition to be crucially dependent on how the noise is introduced to the system. Aldana *et al.* [119], show that noise included separately[4] to the direction leads to the Vicsek observation of a continuous transition. On the other hand, including the noise contribution directly[5] to the direction results in a first order transition, as pointed out in Refs. [114, 115].

In general, the numerical analysis of the Vicsek model is hard because of finite size effects. Moreover, the interactions in the inhomogeneous phase require very large time scales in order to study the ordered bands. Therefore, continuum models by means of hydrodynamic equations are proposed. In this sense, Bertin *et al.* [129, 134, 138]

[4]The noise is added after the sum of every contribution from all particles.
[5]The noise is included directly to the contribution of each input.

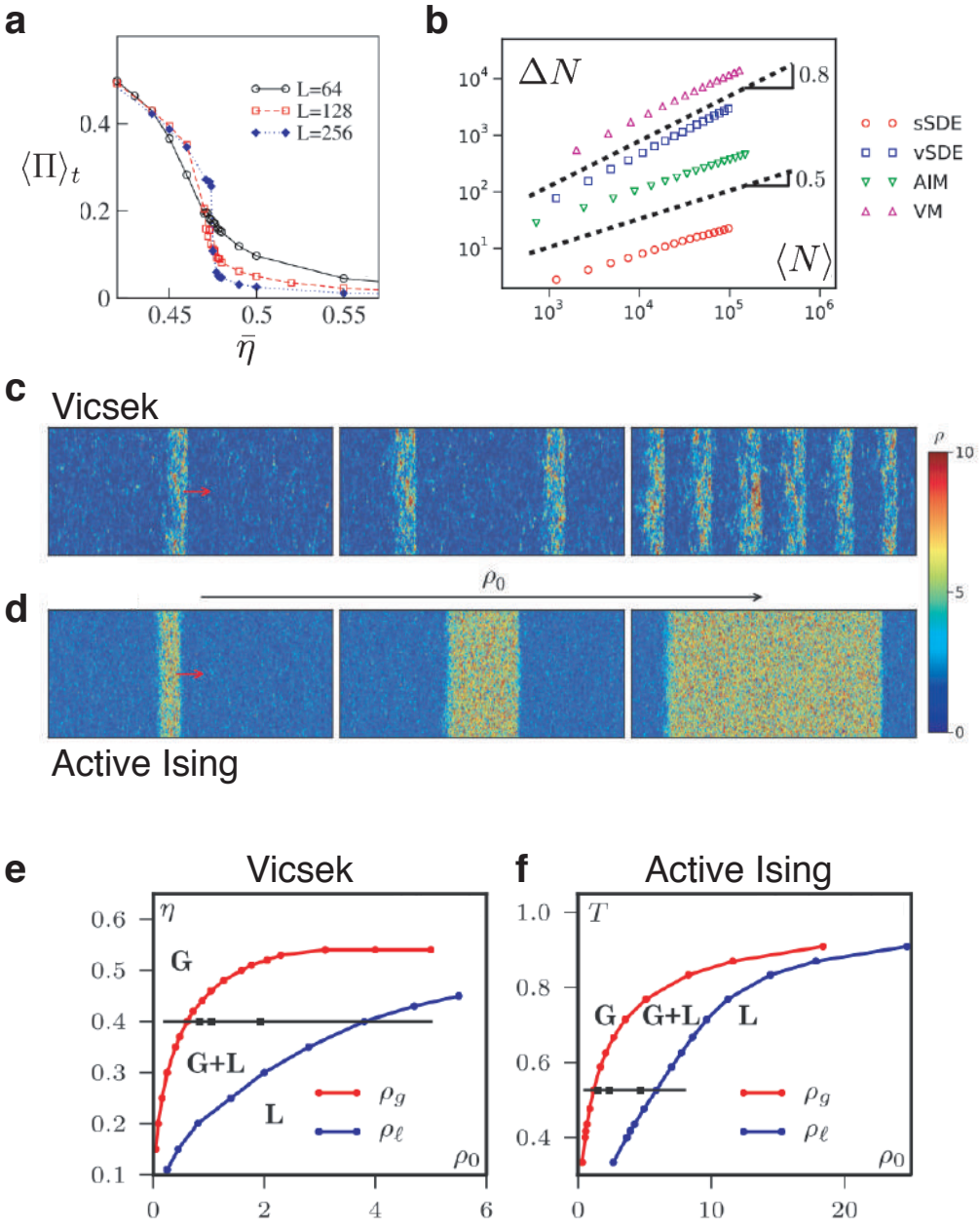

Figure 2.6: **Onset of collective motion: Inhomogeneous phases. a.** Polar order as a function of noise amplitude $\bar{\eta}$. Reproduced from Ref. [115]. **b.** Density fluctuations ΔN as function of the number of particles N. VM: Vicsek model, AIM: active Ising model, vSDE and sSDE are the vectorial and scalar stochastic equivalents for VM and AIM respectively. Taken from Ref. [132]. **c.** Smectic array of bands observed in the Vicsek model. **d.** High density bands result in the active Ising model with the increase of density. **c** and **c** are reproduced from [155] **e** and **f** are the corresponding phase diagrams of the Vicsek and active Ising models respectively. Black horizontal lines represent regions from the snaps show in **c** and **d**. **e** and **e** from [132, 151]

propose a simple model consisting of binary collisions among particles. The proposed model is constructed by means of the Boltzmann equation, making it possible to derive hydrodynamic equations in the low density limit, while remaining consistent with the previously discussed Toner and Tu model [5, 18, 19]. The equations successfully account for the phase diagram of the Vicsek model, and in particular retain the presence of the inhomogeneous phase. The model derived by Bertin *et al.* allows many inhomogeneous solutions, in contrast to the Vicsek model [17].

A different approach is the use of the active Ising model (see Sec. 2.3.2), introduced by Solon *et al.* [124, 151]. In this model the main components of the Vicsek model are retained, self-propulsion and local alignment. The main distinction here is the absence of continuous rotational symmetry, which is replaced by a discrete symmetry. Following the early Ising model [131], particles here are treated as spins able to self-propel in two possible directions (left or right), unlike the Vicsek model, where motion is observed in non-arbitrary directions of the plane. Moreover, the difference in symmetry between these two models leads to significant changes of the solved states. In the homogeneous ordered phase, the active Ising model displays short-range correlations with normal density fluctuations ($\alpha = 0.5$).

The active Ising model shows a transition to collective motion similar to the equilibrium liquid-gas transition. This is in contrast to the development of a ferromagnetic order-disorder transition. On the other hand, it is temperature that controls the demixing, similar to the noise in the Vicsek-like models. At the onset of collective motion, we have that the inhomogeneous phase separates into an isotropic gas and a polar liquid. In a canonical fashion, the temperature-density phase diagram solved by Solon and Tailleur, differs from the typical diagram observed in equilibrium. For the active system, the phase diagram lacks of a critical region, as a consequence of the different symmetries between the polar liquid and the disordered gas. Therefore, criticality is set at infinite

density $\rho_0 \to \infty$ and finite temperature (see Fig. 2.6**f**).

The main distinction between these flocking models reflects in the density profiles observed at the inhomogeneous phase. In the Vicsek model, well defined traveling bands result at the coexistence region, showing a periodic distribution in space. In Ref. [115], these periodic bands are defined as a smetic phase (Fig. 2.6**c**). This description is now corrected following the Active Ising liquid-gas transition, and the bands are considered as liquid regions. For the Vicsek model, the inhomogeneous phase displays micro-phase separation (Fig. 2.6**e**) between periodic bands of finite size and a disordered gas. On the other hand, the active Ising model exhibits full phase separation, with domains of comparable size with increasing ρ_0 (see Fig. 2.6**d**).

In general, the deterministic hydrodynamic descriptions above support the development of banding, with different solutions [127, 129, 130, 138, 156, 157]. Caussin *et al.* [158] show that many of these hydrodynamic equations allow liquid-gas phase and micro-phase separation solutions. The three types of bands are:

(i) *Periodic fractions* — With the variation of the gas density and the band propagation speed, periodic density waves form smectic arrays (see Fig. 2.6**c**) akin to the numerical observations in the microscopic implementation of Vicsek model [114, 115], and the gas-liquid micro-phase separation described previously [132, 151, 155]. Hydrodynamic and experimental realisations also support this solution [127, 159, 160].

(ii) *Solitary propagations* — Here, the periodic array diverges and solitonic polar structures appear. Often, asymmetry is observed in the propagating band, with a sharp front and a vanishing tail [114, 156, 160, 161]. Experimentally, a model system (described later in Chap. 3) reproduces this behaviour [4].

(iii) *Polar liquid* — This corresponds to complete phase separation between a disordered gas and polar liquid propagating with high velocities. Solution of the active Ising

model promotes liquid bands of such a profile (see Fig. 2.6**d**). [124, 132, 151, 155]. For this model, density fluctuations result to be normal, with $\alpha = 0.5$ [132].

Furthermore, active nematic systems display a phase diagram similar to the ones for the Vicsek and active Ising models [138]. Moreover, a phase separation is also exhibited in particles with nematic interactions, where liquid and gaseous fractions are observed [109, 162]. a Analytical and numerical results show that models of self-propelled particles with local aligning interactions exhibit a transition to collective motion characterised within the liquid-gas transition framework [132].

In summary, minimal models predict a transition to collective phases in systems of self-propelled particles. Many approaches lead to the onset of collective motion as an inhomogeneous phase, where a disordered gas fraction coexists with a ordered polar liquid. Different models result in distinct liquid fractions of different properties, such as in the local polar or nematic alignment, and anomalous or normal density fluctuations. These characteristics tune the inhomogeneous regions, where micro-phase separation is observed for the Vicsek model [17, 115, 132], full phase separation in the active Ising model [124, 132, 133], and a chaotic phase in active nematic systems [109, 111, 126, 162].

2.4.2 Motility Induced Phase Separation

Overall, the minimal models discussed in previous sections show the emergence of collective behaviour. For the transition to ordered states, we find inhomogeneous regions where two states coexist, as described in Sec. 2.4.1. In this section, we focus on a different phenomena, where the self-propulsion exhibited by particles, e.g. particles discussed in Sec. 2.2.2, also leads to the formation of an inhomogeneous phase. As before, particles self-propelling can interact via typical forces, i.e. repulsion, attraction, or alignment. We refer to a liquid-gas phase separation of self-propelled particles, that occurs even with repulsive interactions [79, 80, 89, 90, 163–166].

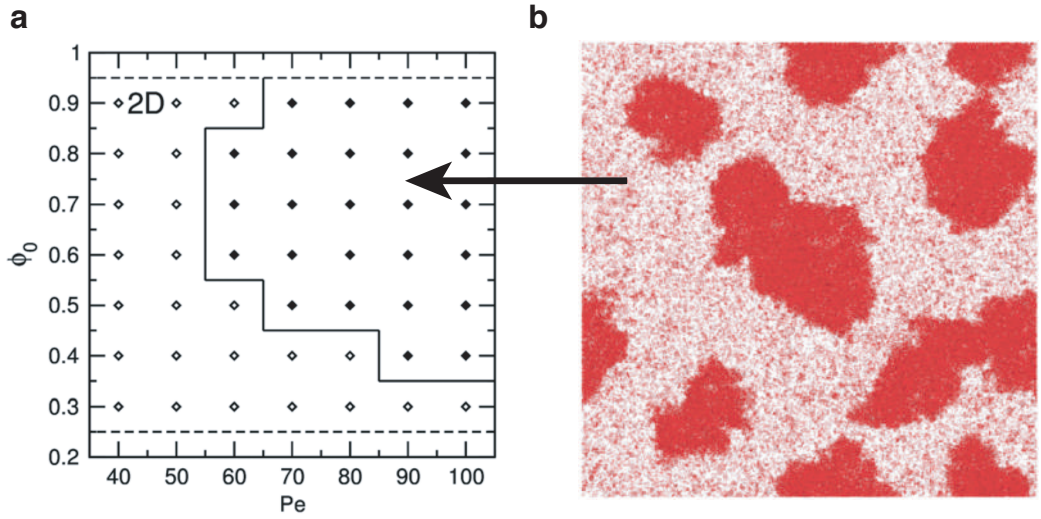

Figure 2.7: **Motility induced phase separation. a.** Phase diagram of ABPs showing the density ϕ versus Péclet numbers that characterise the active motion. Open symbols indicate a state of homogeneous density, whereas phase separation results in the regions indicated by the filled symbols. Solid and dashed lines represent the spinodal and predictions of the binodals at high Pe respectively. Reproduced from Ref. [174]. **b.** Numerical simulations of smooth spheres show phase separation beyond critical density and activity [89].

Introduced analytically by Cates and Tailleur [79], the phenomena where self-propelled particles phase separate between dense and dilute fractions is known as *Motility Induced Phase Separation* (MIPS). The main characteristic for the development of MIPS is a density-dependent velocity. The change of density promotes the emergence of slow (dense) and fast (dilute) regions. Even though this behaviour is not reproduced with passive particles, MIPS is similar to the equilibrium phase-separation between a liquid and gas in the sense of coexistence. Therefore, various suggestions have been developed to link this non-equilibrium phenomenology to thermodynamics, by means of pressure and free energy [80, 165, 167–170]. Interestingly, it is shown that for mixtures of passive and active particles, phase separation develops [171, 172], even with low densities of active particles [173].

Consider active particles self-propelling with velocity $v(\rho)$, where ρ is the local density.

High densities lead to an overdamped regime of increased collisions, therefore speed is reduced. A phase separation is observed if the propulsion speed $v(\rho)$ drops quickly enough with the increase of density. The separation is analogous to liquid-gas equilibrium phase separation, consisting of dense regions of slow motion that coexist with a dilute gas of fast particles. With non-aligning repulsive active Brownian articles (introduced in Sec. 2.2.2), the addition of hard-sphere [89, 164, 166, 174, 175] and soft [90, 163] interactions leads to a phase separation. In the overdamped regime, the interparticle collisions increase with the density, promoting slow down [163, 174]. We have that $v(\rho)$ decreases almost linearly with

$$v(\rho) = v_0[1 - \rho/\rho^\star], \tag{2.39}$$

where v_0 is the speed in the dilute regime, and $\rho^\star$ is the characteristic density for close packing at which the speed vanishes completely [89, 163, 166, 174]. Thus, MIPS develops with $\rho \leq \rho^\star$. The decrease of motility is attributed to the collisions that particles experience before being able to reorient given a characteristic time scale $\tau_r = [D_r(d-1)]^{-1}$. In this sense, the long time dynamics of active Brownian particles are similar to run and tumble particles (described in Sec. 2.2.2). Furthermore, the prediction in Eq. 2.39 is independent of the dimensionless Péclet number, given by

$$\mathrm{Pe} = \frac{3v_0\tau_r}{\sigma}, \tag{2.40}$$

which characterises the ratio of the active persistence length $l_p = v_0\tau_r$ to reorientation governed by thermal processes. Here, $\sigma = 2R$ is the particle diameter. The dimensionless Péclet number is of the same order of the ratio of the active speed to a critical threshold v_0/v_0^c, where

$$v_0^c \equiv \sqrt{\frac{8dD_t}{\tau_r}}, \tag{2.41}$$

which is set by the translational diffusion D_t. Importantly, MIPS is not observed if $v_0 \leq v_o^c$.

In many experimental systems hydrodynamic interactions can not be neglected, e.g. in squirmers [168, 176], Pe governs two main characteristics of the active suspensions for which MIPS develops: the persistence length l_p, and the bare translational diffusion D_t. However, it is observed that long-range hydrodynamic interactions suppress the motility induced phase separation [176]. On the other hand, numerical results show that phase separation develops with $\mathrm{Pe} \leq \mathrm{Pe}_c$, having $\mathrm{Pe}_c \simeq 55$ for $d = 2$, and $\mathrm{Pe} \simeq 125$ in three dimensions [89, 163, 166, 174, 177]. No coexistence is observed with $\mathrm{Pe} = \mathrm{Pe}_c$, predicting a critical point. Therefore, phase diagrams for $d = 2$ and 3 can be obtained, having non-zero translational diffusion. However, it is already established that $\mathrm{Pe} \sim v_0/v_0^c$, meaning that MIPS should develop even at low motility, i.e. $\mathrm{Pe} = 1$.

This discrepancy between this relation and numerical results is given by a factor of 50, an indication that the non-zero diffusion D_t is not responsible for the absence of MIPS at $\mathrm{Pe} < \mathrm{Pe}_c$. Unlike experiments, numerical simulations with zero value of D_t can be set arbitrarily [90, 163], yielding results akin to those where D_t is set thermally. In order to address such a discrepancy, kinetic approaches [89, 90, 163, 164, 166, 169, 177, 178] can be established by means of a vapour density ρ_v of particles at the surface of a liquid domain. Here, particles are able to join or escape from the dense domains with some rate. For the coalescence we have the rate to be of order $\rho_v v_0$, and $\kappa D_r/\sigma$ for the departure, with κ being a dimensionless fitting factor that accounts for the many escaping particles. This departure rate involves the rotational diffusion D_r since reorientation is needed in order to escape from the local region. In addition, continuum expressions derived from this approach [90, 163, 164] yield phase behaviour akin to the theoretical framework

[80]. Nonetheless, this does not offer a complete picture for which MIPS vanishes below a critical Pe_c, distinct from the analytical deduction.

Following the idea of a liquid-gas phase separation akin to equilibrium, thermodynamic and mechanical approaches [93, 179–185] have been proposed. For systems in thermal equilibrium the thermodynamic and the mechanical pressure are equivalent. Opposite, this is generally not satisfied with active particles, since the pressure can be altered by the interaction between particles and a confining wall [167]. Neglecting the particle-wall interaction, the mechanical pressure follows

$$P = P_0 + P_I + P_D \tag{2.42}$$

which relates to bulk correlations and results to be a state function for active Brownian particles [186]. The ideal pressure P_0 represents the flux of momentum in the bulk [93, 167, 181, 182], while P_I is an *indirect* pressure that couples self-propulsion and interaction forces between particles. On the other hand, P_D is the *direct* contribution to pressure in absence of activity, $v_0 = 0$. Importantly, P_I dominates at intermediate densities and holds for the propulsion slow-down due to collisions. In the absence of self-propulsion P_I vanishes. In addition, the sum of the ideal and the indirect contributions yields the *swim pressure* P_s,

$$P_s = \frac{v_0 v(\rho)}{2D_r}\rho \equiv \frac{\rho}{2}\langle \mathbf{r}\cdot\mathbf{F}^s\rangle, \tag{2.43}$$

where $\mathbf{F}^s = v_0\mathbf{n}$ is propulsion force, and $v(\rho)$ is the density dependent speed in Eq. 2.39 [93, 167, 180]. P_s is akin to a kinetic pressure. Nonetheless, the particle speed in equilibrium systems is solely controlled by temperature, whereas the swim pressure depends on the actual particle mean speed, which is indirectly controlled by density. Shown by Solon *et al.* [186], a phase separation due to self-propulsion emerges from the

contribution of P_s at high Pe. Neglecting the contributions from external torques, e.g. presence of a wall [167], equations of state can be derived from bulk correlations far from a wall [186]. However, when compared to a thermodynamic construction, e.g. Maxwell construction[6], the coexistence boundaries approaches differ.

Results from numerical simulations show the full phase diagram for active Brownian particles in two-dimensions [187]. The approach of a mechanical pressure is recalled by means of the swim force $\mathbf{F}^s$. Motility induced phase separation holds between the dilute and close-packing density regimes, at high Pe in agreement with previous observations [89, 169, 174, 177]. Furthermore, the presence of an equilibrium two-dimensional melting [188–193] is shown for density regions near close-packing and low activities $\mathrm{Pe} \to 0$. Additionally, analytical and numerical approaches suggest an analogous to equilibrium classical nucleation theory by means of free energy and nucleation rates [170, 194], as well as a negative tension that leads to a stable phase separation of ABPs [195].

2.5 Realisation of Active Systems

As above, living systems that exhibit interesting phenomena (see Fig. 2.1), such as motility and interaction among individuals, are of a higher complexity to that achieved in physical models. Therefore, as experimentalists, we aim to have better control over the many parameters in order to gain a better understanding of the nature of such complex behaviours. For this reason, a large effort has been devoted to the artificial realisation of active matter systems. Colloid synthesis provides the tools to develop new experimental models that exhibit similar behaviour to those observed in numerical simulations and analytical results. Nowadays, it is possible to find a range of models whose active behaviour rely upon different mechanisms, i.e. local chemical reactions

[6] Maxwell construction sets the stability in equilibrium by means of a thermodynamic pressure, different from the mechanical pressure considered here.

[96, 196–200] or an external magnetic field [201–204].

We mention some of the most notable artificial experimental systems that manage to reproduce the interesting phenomena discussed above.

2.5.1 Vibrated Disks

In order to gain access to the collective motion exhibited by propelled units, synthetic routes different from swimming devices where hydrodynamics are not desired [62], systems of macroscopic vibrated particles can be of use. Consider a set of dry and inert particles forming a monolayer on a flat surface to which vertical vibrations are applied. Through this method, elongated particles have been used in order to study transitions from isotropic to nematic states [205]. Persistent and coherent motion can be found in chain-like [206], polar [207, 208], and apolar [152, 205, 209] rod-like particles. Here, the experimental realisation of active nematics in liquid crystals take place [152, 205]. However, minimal models show that apolar particles experiencing nematic alignment interactions are not prone to display long-range polar order [111, 118, 126]. Note that, polar rods exhibit density fluctuations distinct from flocking models [17, 18], meaning that long-range order is not observed.

Experiments conducted by Deseigne *et al.* [153], show the persistent motion of polar disks, and the onset to large collective motion. Here, the disks develop motion from the asymmetric friction with the substrate, given the non-symmetrical mass distribution in the disks. The vibrational amplitude Γ emitted to the surface and the disk area fraction ϕ are taken as control parameters. Note that the interaction between disks results hard-core repulsive. At low disk densities, rare collisions due to motility are observed, and individual motion shows random-walk dynamics (Fig. 2.8**b**). Upon decreasing the amplitude Γ, disks display an enhanced directed motion, with a persistence length interrupted by the system size. In contrast, increasing the amplitude results in vanishing

motion, where Γ controlling the disk angular diffusion akin to noise in the Vicsek model [17] (See Sec. 2.3.1). Notably, polar disks are distinct from the particles introduced in Sec. 2.2.2, in the sense that in active Brownian particles orientation and velocity are decoupled, whereas for vibrated disks of asymmetric mass they are not [210].

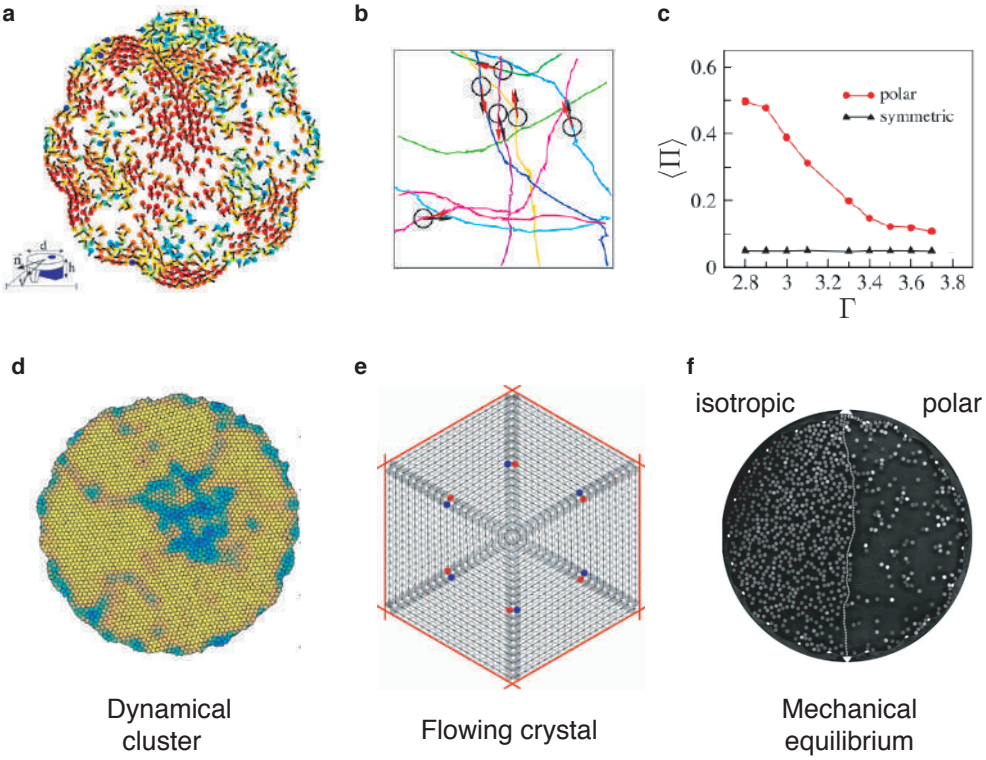

Figure 2.8: **Vibrated Disks. a.** Collective motion of polar disks. **b.** Reconstructed trajectories of the self-propelled disks. Arrows indicate velocity **v** and orientation **n**. **c.** Polar order measured for polar versus passive isotropic disks. **a-c** Reproduced from Ref. [153]. **d.** Crystallisation in dense phase of self-propelled disks, $\phi = 0.84$ from [211], and **e.** flowing crystal at larger ϕ [212]. **f.** Mechanical pressure between isotropic and polar disks separated by a flexible wall [213].

Focusing on the collective dynamics, with increasing the disk area fraction, and with a suitable vibration amplitude, some degree of polar alignment develops from collisions. High amplitudes of the vibration yield a disordered phase with isotropic disk motion. Collective dynamics develop in form of large jets and swirls with fixing ϕ and decreasing Γ. However, the emergent collective motion is not preserved for long times, and long-

range order does not develop due to the finite size from confinement. That is to say, the absence of periodic boundary conditions results in difference to the observations using numerical simulations of the same system [160, 210]. Also, the homogeneous ordered phase results difficult to obtain experimentally, due to the system physical dimensions, and due to the finite amplitude Γ, which at low values shows motility deterioration.

Moreover, experimentally this system of vibrated polar disks exhibits giant density fluctuations, and shows the onset of collective motion characterised by the polar order parameter Π [153, 214]. Numerically, for the same system [160], the emergence of collective motion is in agreement with the Vicsek-like models [17, 114, 115], and further from the transition it displays a homogeneous phase with long-range order as described by hydrodynamic approaches [5, 18, 19]. Interestingly, mixtures of polar rods and passive disks display circular coherent rod flow along the system boundary, even with low rod concentrations. Here, the motion of the rods induces a flow of homogeneous beads, akin to an active swimmer to the surrounding fluid. As a result, the polar rod interactions over large distance are given by the bead displacement [215]. Nonetheless it is unclear if the nature of the interactions, presumably from short-range collisions, can be interpreted as an effective alignment as indicated by the Vicsek-like descriptions.

Beyond the transition to collective motion, this system is an elegant and well controlled approach to investigate the dynamic properties in high density phases, e.g. the transition to crystallisation, activity induced melting [211], and the rheological properties of active crystals [212], compared to passive disks. Moreover, the mechanical pressure exerted on a flexible membrane by isotropic and self-propelled disks can be explored experimentally. As expected, an equilibrium equation of state is recovered for the passive disks, whereas pressure is not a state variable for polar disks. This results in good agreement with the previous observations from analytical and numerical results [167], since it is shown that orientation is strongly coupled to the velocity dynamics [213].

Therefore, the membrane–disk and disk-disk exerted torques can not be neglected.

2.5.2 Actin Filaments

In living microorganisms, the cytoskeleton gives the cells their shape, and provides mechanical support to perform essential activities, such as swimming or cell division [216]. In eukaryotic cells, the cytoskeleton consists of actin filaments, intermediate filaments, and microtubules involved in cilia and flagella movement [217]. Protein molecular motors, such as myosin, bind to the filaments in the cytoskeleton in order to promote cell movement by hydrolyzing adenosine tri-phosphate (ATP) as a fuel. Remarkably, the components in this systems can be exploited to study fluctuations and turbulence in active systems [159, 218–226].

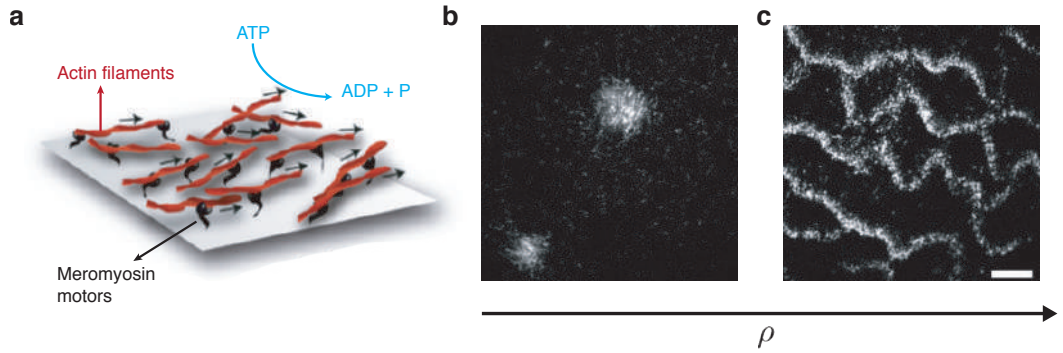

Figure 2.9: **Driven filaments. a.** Schematic representation of a motility assay of immobilised molecular motors driving actin filaments in the presence of ATP. **b.** Homogeneous cluster and **c.** polar waves with increasing the filament density ρ. Arrow indicates direction of motion. Scale bar is 50 μm.

By setting the components in a planar geometry akin to motility assays (see Fig. 2.9 **a**) fluorescent and non-fluorescent actin filaments can be propelled by myosin motors in the presence of ATP. This system of filaments driven by arrays of molecular motors on a substrate falls into the category of dry active matter, since momentum is exchanged between the filaments and the substrate. Carried by Schaller *et al.* [159] performed

experiments of driven filaments which exhibit an onset to collective motion, by adjusting the filament density ρ as control parameter. Low concentrations of filaments lead to isotropic motion, while ordered structures, in form of motile clusters, vortices and waves emerge upon increasing the density ρ. Above a critical density $\rho^\star$, an inhomogeneous phase of polar density waves and disordered filaments, reminiscent of the observations in models of active polar matter discussed in Sec. 2.3.1, and reproduced numerically [227]. Note that, giant density fluctuations are observed in the inhomogeneous phase [154], and that a homogeneous phase with coherent polar motion is not observed, leaving the full order-disorder experimental transition incomplete.

2.5.3 Colloidal Particles

Starting from the pioneering work of Jean-Baptiste Perrin, colloidal dispersions have been of great use for the study of condensed matter physics. Nowadays, colloids of different shape, size, composition and functionality can be used as building blocks to study interesting processes, such as self-assembly [82, 228, 229]. Specifically, suspensions of spherical colloids act as nearly hard spheres [230, 231], for which crystallisation [232–235], glassy and arrested structures [236–239] can be explored experimentally.

In this sense, colloids play a crucial part in the fabrication of artificial micro-swimmers that exhibit some of the attractive characteristics find inherently in microorganisms, e.g. self-propulsion [27, 63]. For this to happen, it is important to understand the dynamics of biological swimmers in order to reproduce such a behaviour. Here we describe the use of particles powered with catalytic processes. As before, microorganisms, such as bacteria, exhibit symmetry breaking that leads to self-propulsion. In this sense, artificial self-propulsion is achieved with a device fabricated by Whitesides *et al.* [240], where asymmetric catalytic reactions performed by the chemically powered swimmer allow propulsion at a liquid-air interface. Self-propulsion in bulk, first demonstrated by Paxton

et al. [196], develops from a similar concept of catalytic particles powered by a fuel in the solvent. Nowadays we can find several methods to produce swimmers of various kinds, including devices containing biological macro molecules, such as DNA in a flagella-like chain [201].

In this section we mention some of the examples that constitute a class of self-propelled particles, in addition to the different mechanisms of motion.

Janus particles

Particles of this kind fall into the category of phoretic swimmers, where the origin of the self-generated motion occurs at the particle surface. Self-propulsion develops as a result of an interfacial process, where thermal, electric or chemical gradients are produced. The surface of Janus particles is composed of two materials of different properties, one acting as an inert material and the other performing a process to develop a gradient. This process leads to a slip velocity field at the particle surface, and motion due to thermophoresis, electrophoresis or diffusiophoresis occurs [63, 241]. The simplest approach to produce Janus particles is by coating one-half of the particle surface with a functional material or chemical functional groups [242].

Conventionally, three different methods can be employed in order to produce Janus particles. Half-coating can be achieved by masking techniques, such as vapor deposition and particle trapping at an interface, which exposes only a desired part of the surface [243]. A second approach is the use of a phase separation technique. This involves having a mixture of two or more incompatible components. Here, polymeric-inorganic hybrids with a wide range of polymers can be achieved [243, 244]. Thirdly, self-assembly techniques can be of use to produce asymmetric particles by using block co-polymers, where components of different nature can demix and be adsorbed at the particle surface [242, 245]. Alternatively, electrochemistry processes can be employed to manufacture two-component metallic rods [196]. Furthermore, lithography and glancing angle deposition

methods can be used to fabricate particles of complex shapes, such as the L-shaped and chiral self-propelled particles [86, 203].

Active droplets

Distinct from the phoretic mechanisms exploited with Janus particles, self-propulsion can be promoted through Marangoni stresses that take place in the presence of a surface tension gradient at the interface between two phases. The system consists of aqueous droplets suspended in a non-aqueous phase, such as oil, and stabilised by surfactant molecules at the oil-water interface. Here, the propulsion emerges as a self-sustained process in the presence of bromine contained inside the droplet. This causes halogenation of the C = C double bonds at hydrophobic chain in the surfactant molecules. As the surfactant gets brominated it gets weaker, creating a tension gradient. This class of self-propelled particles have been investigated both experimentally [14, 246] and theoretically [247]. In addition, Izri and collaborators [248] show the emergence of self-propulsion in water droplets, only when the surfactant concentration is above the critical micelle concentration (CMC). Additionally, the same principle that generates Marangoni effects can be applied to non-spherical objects, i.e. micro-fabricated gears [249]. Gears are placed at the liquid-air interface, and local heating promotes a temperature gradient. Hence, the change in surface tension results in gear rotation controlled by temperature.

In general, the self-propulsion mechanisms either rely upon local conversion of energy, such as the catalytic devices in [196, 240], or upon the application of an external field, i.e. an oscillating artificial flagella in the presence of a magnetic field [201]. Both internally and externally driven particles can be mapped to an extent by models of self-propelled particles, e.g. active Brownian particles (in Sec. 2.2.2). Nonetheless, microscopic details from one or another might lead, for example, to distinct hydrodynamic interactions [27, 62]. We now mention the different strategies that can be employed in order to obtain

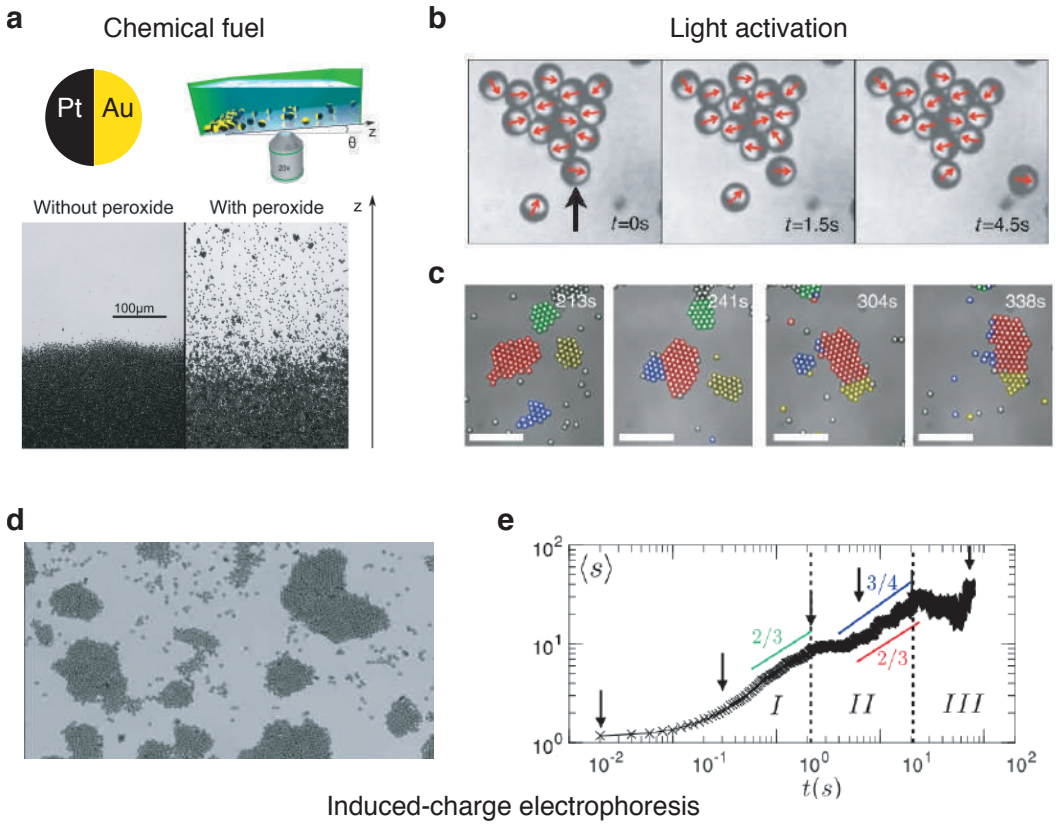

Figure 2.10: **Activation and clustering of Janus particles. a.** Artificial Janus particles powered by a chemical fuel. Particles sediment when subjected to gravity and in the absence of fuel. Self-propulsion and dynamic clustering due to phoretic interactions are observed in the presence of hydrogen peroxide [98]. **b.** Light activated Janus particles self-propelled due to the local demixing of the solvent. Self-trapping is observed since reorientation lag hinders the escape from clusters [250]. **c.** Living crystals of colloids able to locally decompose a chemical fuel when illuminated [251]. **d.** Large scale clustering in a system of Janus particles activated by induced-charge electrophoresis. Clustering is separated in three regimes, as indicated in **e.** MIPS is interrupted due to local alignment in different domains [252].

active self-propelled particles out of colloidal particles.

Chemical fuels — Here we focus on the artificial swimmers employing fuels in a solvent, and that have been explored experimentally [98, 196–198, 240, 253], and analytically [241, 254, 255]. Many systems of this kind are based on the previously described Janus particles, where diffusiophoresis occurs due to self-generated gradients.

These Janus particles can be composed of different material combinations, which include a catalyst. Alternatively, Janus particles are also powered by enzymes deposited on spheres [256]. First observations on metallic rods [257], i.e. platinum-gold (Pt-Au) and nickel-gold (Ni-Au), point to self-propulsion when suspended in solution containing hydrogen peroxide (H_2O_2) [196, 258]. However, it has been observed that the addition of ions, from salt or surfactants, to the peroxide solution has great effects on the self-propulsion [97]. Similar observations in hydrophobic Janus spheres points to the increase of particle aggregation with high salt concentrations [259].

In particles containing metallic caps, the platinum decomposes through oxidation of peroxide as, $2H_2O_2 \rightarrow 2H_2O + O_2$, creating a chemical gradient. In this sense, previous research shows the use of dielectric spheres (polystyrene, silica, PMMA, etc.) with metallic caps [198, 240, 253], to characterise the emergent directed motion in a hydrogen peroxide aqueous solution. Palacci *et al.* [253] employ Janus colloids in a solution with a chemical fuel to characterise the active dynamics against sedimentation. In the absence of fuel, colloids sediment due to gravity. In contrast, Janus spheres are able to self-propel against gravity, even with low concentrations of hydrogen peroxide. Notably, dynamical clustering is observed as the Janus particles are subjected to the sedimentation profile [98]. The dynamic clusters result from phoretic interactions, as fuel consumption leads to long-range chemical gradients (Fig. 2.10**a**), decaying with $1/r$ [241]. Thus, the interaction between Janus colloids result from chemical clouds generated by neighbours [260].

In addition, Ginot *et al.* [261] show the dynamics of active clusters by means of kinetic aggregation and fragmentation. Dynamical clusters are also obtained when the metallic catalyst, e.g. platinum or palladium, is replaced with anti-ferromagnetic cubes of hematite. Thus, the local decomposition of hydrogen peroxide is possible only when violet or blue light is shone to the colloids, opposite to the normal Brownian diffusion observed with normal illumination. This results in self-propulsion, which is in competition against

the phoretic interactions that promote the formation of so called *living crystals* [251] (Fig. 2.10 **c**). Furthermore, it is shown that different concentrations of the peroxide lead to the increase of an effective adhesion between the colloids [184].

Light activation — Unlike the self-generated chemical gradients by decomposing a fuel, thermophoretic processes rely upon temperature gradients upon local heating. Conventionally, high power lasers can be of use to heat the metallic components on Janus particles. The resulting self-thermophoresis is then controlled externally by adjusting the laser power [262, 263]. Remarkably, symmetric particles distinct from the previously described Janus particles can be manipulated using a spatially controlled asymmetric light input. Thus, the induced interactions lead to collective patterns of self-thermophoretic active particles [264]. Another approach is the use of critical liquid mixtures, by which the use of high power inputs can be overcome. Here, Janus particles are locally heated with lower light intensities. This promotes local liquid-liquid demixing as the local temperature reaches the critical point at the Janus coated surface. As a result, diffusiophoretic motion arises instead of thermophoresis [7], as shown experimentally [265, 266] and described analytically [267, 268].

A notable contribution employing the same system is given by Buttinoni *et al.* [250], in which MIPS emerges in light-activated particles. Carbon-coated Janus particles are dispersed in a lutidine-water critical mixture. With sufficient enough particle density, the system undergoes phase separation between particle clusters and a dilute phase. Unlike particles powered by hydrogen peroxide, where the nature of clustering is from phoretic attraction [98, 251, 253, 261], here the local demixing does not affect the environment since spinodal decomposition is reversible (Fig. 2.10**b**). This points to a different explanation for the dynamical clustering, where particle self-trapping induces aggregation. As discussed for Janus particles, a slip velocity arises at the particle surface

[7] The particle motion is purely Brownian below the critical temperature at which liquid-liquid separation occurs, even when illumination is applied.

from the self-generated gradient. Hence, the net direction of motion is given opposite to the gradient flux [241]. In other words, the swimming orientation is set perpendicular to the equator made between the inert and the active sides of the particle (see Fig). Therefore, the nature of the self-trapping relies on rotational diffusion, where the time taken by a particle to change its orientation and escape is given by a characteristic time scale $\tau_r = D_r^{-1}$. As a different approach, self-assembly into small clusters is based on light-absorbing and non-absorbing spheres dispersed in the same critical mixture [269]. In contrast with Janus particles, the absorbing particles generate symmetric heating under illumination, and attract neighbours due to phoretic interactions [260], where the self-propulsion of particles emerges from the interaction of absorbing and non-absorbing particles.

External fields — Various approaches to trigger self-propulsion rely upon the application of external fields, such as magnetic and electric fields. Synthetic objects are able to undergo physical deformation to achieve motion. In Ref. [201], Dreyfus *et al.* fabricate a flagella-like device, able to self-propel in a beating manner [270], under magnetic stimuli. Alternatively, controlled swimming in particles with chiral motion is achieved by employing rotating magnetic fields [203]. In addition, paramagnetic colloids can be use to assembly worm-like structures that propel in the presence of an elliptically polarized rotating magnetic field [271]. Experiments carried with magnetic Janus particles show assembly and rotation of highly ordered structures upon increasing the magnitude of a rotating magnetic field [272, 273].

Furthermore, collective phenomena, in form of flocks, vortices and unstable fronts, is observed for ferromagnetic [274] and anti-ferromagnetic [275] rollers under uniaxial alternating and rotating magnetic fields respectively. Anti-ferromagnetic cubes of hematite spin and form a cohesive chiral fluid where time-reversal symmetry is broken, in contrast with simple fluids [276]. With this system controlled by a rotating magnetic

field, the emergence of an odd viscosity [277, 278] in colloidal chiral fluids is shown. In addition to the use of magnetic fields, electric fields can be of use to induce electrophoresis, which results in motion perpendicular to the direction of the field. For a Janus particle half-coated with a metallic layer, the application of a uniform ac field generates a charge gradient, where the polarisation is of different magnitudes for the different sides of the Janus particle. This resulting self-propulsion is known to occur as induced-charge electrophoresis. [279, 280].

A rich phase behaviour using a system of induced-charge electrophoresis is shown by Yang *et al.* [280]. Here, the electric field frequency controls the dielectric response of the Janus colloids, that exhibit the formation of an isotropic gas, swarms, chains and long-scale polar waves. Low frequencies yield weak dipolar interactions due to high charge screening, that ultimately result in an isotropic gas. As the field frequency is increased, ionic screening is reduced and Janus spheres can interact via dipolar interactions. Following the same system, van Der Linden *et al.* [252] show experimentally large-scale cluster formation (Fig. 2.10**d**), compared to previous observations with chemically powered colloids [250]. Remarkably, alignment and excluded volume interactions are investigated simultaneously on an aggregating system. Here the dynamics lead towards full phase separation as aggregation and cluster size increase rapidly. This process is however interrupted by alignment interactions at long time scales. The aggregation mechanisms are given in three different regimes:

(i) At short time scales, the dynamics are dominated by aggregation of isolated spheres into small clusters, and the mean cluster size $\langle S \rangle$ increases rapidly, as shown in Fig. 2.10**e**. This regime is the onset of the phase separation in a MIPS fashion (Sec. 2.4.2).

(ii) The intermediate dynamics are characterised by an aggregation-breaking regime, that ultimately reduces aggregation. Here, domains of local alignment and high

order form, and the combination of both leads to cluster motion.

(iii) Full phase separation is interrupted at long time scales by frequent breaking events. This is a result of the different alignment between domains. Aggregates reach a regime where structural ordering competes with the stresses generated by misalignment.

Overall, this system allows one to investigate the combination of different interactions [281], such as alignment interactions that dominate in Vicsek-like models [17, 124, 132], and the short-range repulsion in active Brownian particles that develop MIPS [79, 80, 89, 163].

The experimental realisations introduced in the previous subsections offer partial validation to the theoretical framework, in addition to the exhaustive results from numerical simulations. Here we observe a transition to collective behaviour in polar systems, i.e. driven actin filaments [159], vibrated grains [153, 160], and electrophoretic Janus particles [280], where the alignment interactions arise through different processes. In addition, the cluster formation and emergence of phase separation in motile particles has been explored in different systems [98, 250, 251, 261]. It is important to emphasise that in experiments many parameters play a significant role. For example, the contribution from excluded volume, alignment, repulsion, attraction and hydrodynamic interactions.

Having introduced different models, we focus on a system of rolling colloids, which self-propulsion mechanism relies upon the application of a dc electric field E. We refer to Quincke rotation, where a transition to homogeneous polar phases is shown by Bricard *et al.* [4, 282]. In addition, MIPS is also investigated using dense phases of rolling colloids [283]. With the aim of exploring the rich behaviour of non-equilibrium active systems, we use a system driven by the so-called Quincke rotation. In the present work, we investigate the contribution from control parameters, i.e. density ϕ and field magnitude E, over the systems. We later present the behaviour of microscopic assemblies under

strong confinement. Finally, we describe the different different dynamics resulting in non-spherical particles under Quincke rotation.

CHAPTER 3

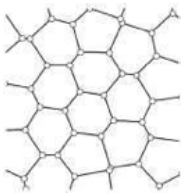

QUINCKE ROTATION

"Keep rollin' rollin' rollin' rollin"

by LIMP BIZKIT.

Motivated by emergent flocks and the many other fascinating expressions of collective phenomena in nature, several analytical and numerical methods have been proposed. In this field, many studies have been devoted to the experimental realisation of the behaviour observed in living systems and described by analytical models. As an example, the nature of flocks and the transition to collective motion through alignment interactions have been studied. In addition, living and man-made experimental models have been used to corroborate such phenomena. However, the interactions, e.g. phoretic interactions, contribute to observed behaviour [98, 251], but remain hard to control.

Models of active polar matter show features introduced in Vicsek-like models, such as the onset of collective behaviour due to alignment (see Sec. 2.3). We refer to those systems of vibrated polar grains (Sec. 2.5.1) [153, 214] and filaments driven by molecular motors 2.5.2) [159]. In both cases, a transition to polar order is observed, with the

alignment interactions presumably arising from collisions, that might be difficult to capture theoretically. On the other hand, for the motility induced phase separation, first described analytically [75, 80], we find that in experiments with Janus particles, clustering develops with different types of interactions [98, 250, 251, 261]. The different mechanisms of active motion, from the local conversion of energy to the application of external fields, results in distinct phenomenology. In this sense, electrophoretic Janus particles show aggregation, followed by interruption of phase separation as in MIPS due to alignment and cluster fragmentation [252] (2.5.3).

In this chapter we focus on the description of a system of rotating colloids, where a transition to homogeneous collective motion [4, 282], and phase separation induced by motility [283] have been investigated previously. We refer to the Quincke electro-rotation in colloidal suspensions of dielectric particles. We describe the mechanism of electro-rotation, followed by the coupling between rotation with translation that leads to the self-propulsion of colloids [4].

3.1 Particle Electro-rotation

First observed in 1896, by Georg Hermann Quincke [284], spontaneous rotation is exhibited by spherical spheres when dispersed in weakly conductive liquids and subjected to a strong and uniform electric field. This electro-hydrodynamic mechanism is known as *Quincke rotation*. The mechanism consists of having an insulating sphere of diameter $\sigma = 2R$, suspended in a liquid of conductivity s_l, viscosity η, and dielectric permittivity of ϵ_l. Consider a uniform electric field, with amplitude E and direction $\hat{\mathbf{z}}$, applied to the suspension. The charge distribution decreases in the liquid bulk as charge develops at the liquid-particle interface, where the discontinuity of conductivities and permittivities lead to a non-zero charge distribution. For a small section at the interface, we have the charge distribution,

$$Q_s = (\mathbf{E}_l \epsilon_l - \mathbf{E}_p \epsilon_p) \cdot \hat{\mathbf{r}}|_{r=R} \tag{3.1}$$

where $\mathbf{E}_i$, with $i = p, l$, is the electric field in the particle and in the liquid respectively. Following Maxwell's equations the resulting charge distribution is dipolar, given by $\mathbf{P} \equiv \int \mathrm{d}^2 s Q_s \hat{\mathbf{r}}_s$. We have the electric fields for the particle and the liquid,

$$\begin{cases} \mathbf{E}_p = \mathbf{E} - \frac{\mathbf{P}}{4\pi\epsilon_0 R^3} & r < R, \\ \mathbf{E}_l = \mathbf{E} - \frac{1}{4\pi\epsilon_0}\left(3\frac{\mathbf{P}\cdot\mathbf{e_r}}{r^3}\mathbf{e_r} - \frac{\mathbf{P}}{r^3}\right) & r > R, \end{cases} \tag{3.2}$$

where $\mathbf{e_r}$ is the radial unit vector. Here the resultant fields are the sum of the applied field $\mathbf{E}$, and the field generated by a sphere of uniform polarisation $\mathbf{P} = \frac{4}{3}\pi R^3 \mathbf{P}_0$, where $\mathbf{P}$ is the total dipole moment (see Fig. 3.1**a**).

The first condition that has to be satisfied for Quincke rotation to occur relates the relaxation times of both the liquid and the particle,$\tau_i = \frac{\epsilon_i}{s_i}$. If the charge relaxation is larger in the liquid than that of the particle, i.e. $\tau_l > \tau_p$, the charge distribution at the liquid-particle interface forms a dipole $\mathbf{P}$, with the same direction as the field $\mathbf{E}$. This scenario brings a stable situation, where no rotation is exhibited (Fig. 3.1**a**). On the contrary, for $\tau_p > \tau_l$ the dipolar charge distribution results opposite to the direction of the applied field $\mathbf{E}$, that leads to spontaneous symmetry breaking as shown in Fig 3.1**b**.

Above a critical field amplitude E_Q, spontaneous rotation of the particle perpendicular to $\mathbf{E}$ results with angular velocity ω. As the sphere experiences rotation, the dipole moment tilts, producing an electrostatic torque $\mathbf{T}^{\mathrm{E}} = \frac{\epsilon_l}{\epsilon_0}\mathbf{P} \times \mathbf{E}$, which tends to amplify the initial rotation. Importantly, a steady rotation is only achieved if a resistant viscous torque $\mathbf{T}^{\mathrm{H}} = \mu_r^{-1}\boldsymbol{\omega}$ is balanced, $\mathbf{T}^{\mathrm{H}} + \mathbf{T}^{\mathrm{E}} = 0$, with $\mu_r = (8\pi\eta R^3)^{-1}$. Therefore, we find the steady state in competition between charge advection at the interface due to the electrostatic torque, and the transport of ions between the interface and the liquid that relaxes the torque towards zero, $\mathbf{T}^{\mathrm{E}} \to 0$.

For a Quincke roller we have that the total polarisation is of two components, $\mathbf{P} = \mathbf{P}^{\mathrm{s}} + \mathbf{P}^{\mathrm{d}}$, where $\mathbf{P}^{\mathrm{s}}$ and $\mathbf{P}^{\mathrm{d}}$ are the static and dynamic contributions respectively. Here, the static component,

$$\mathbf{P}^{\mathrm{s}} = 4\pi\epsilon_0 R^3 \frac{\epsilon_p - \epsilon_l}{\epsilon_p + 2\epsilon_l}\mathbf{E}, \tag{3.3}$$

is the instantaneous part from the permittivity discontinuity at the liquid-particle interface. On the other hand, the dynamic $\mathbf{P}^{\mathrm{d}}$ component corresponds to the charge transport in the liquid. Following charge conservation $\partial_s Q_s + \nabla_s \cdot \mathbf{j}_s = 0$, with the surface current $\mathbf{j}_s = s_l \mathbf{E} + Q_s \boldsymbol{\omega} \times R\hat{\mathbf{r}}$ at the surface we obtain the evolution of the dipole moment,

$$\frac{d\mathbf{P}}{dt} = -\frac{1}{\tau}\Big(\mathbf{P} + 2\pi\epsilon_0 R^3 \mathbf{E}\Big) + \boldsymbol{\omega} \times \Big(\mathbf{P} - 4\pi\epsilon_0 R^3 \mathscr{P}^{\infty}\mathbf{E}\Big) \tag{3.4}$$

where $\mathscr{P}^{\infty} = \frac{\epsilon_p - \epsilon_l}{\epsilon_p + 2\epsilon_l}$, and $\tau = \frac{\epsilon_p + 2\epsilon_l}{s_p + 2s_l}$ is the so-called Maxwell-Wagner time [285], which gives the characteristic timescale for a dipole to relax. As mentioned before, once that $\tau_p > \tau_l$ is satisfied, and when the field amplitude exceeds a critical value,

$$E_Q = \left[4\pi\epsilon_l R^3 (\mathscr{P}^0 - \mathscr{P}^{\infty})\mu_r \tau\right]^{-\frac{1}{2}}, \tag{3.5}$$

with $\mathscr{P}^0 = \frac{s_p - s_l}{s_p + 2s_l}$. There are two stationary solutions to Eq. 3.4. The first is the non-rotating scenario where the dipole relaxes according to τ. This is unstable when $E > E_Q$, where the second solution corresponds to steady particle rotation with,

$$\omega = \frac{1}{\tau}\sqrt{\left(\frac{E}{E_Q}\right)^2 - 1}\,. \tag{3.6}$$

Here, the polarisation is constant, but as the particle rotates the dipole orientation of $\mathbf{P}^{\mathrm{d}}$ forms a finite angle with respect of the applied field $\mathbf{E}$. Notably, the angular velocity does not depend on the particle size.

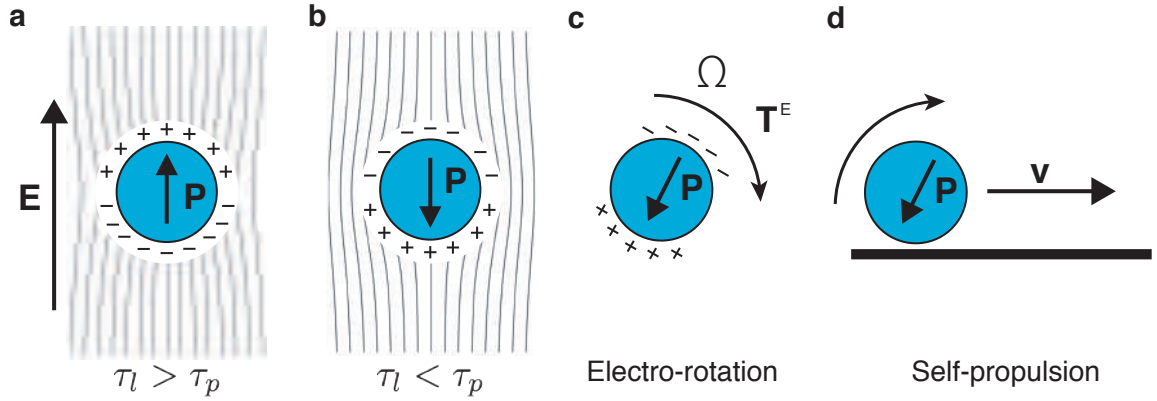

Figure 3.1: **Quincke electro-rotation and self-propulsion of particles. a.** A stable scenario arises if the liquid charge relaxation time is longer than in the particle. No rotation emerges here. **b.** The opposite case brings an unstable situation where the orientation of the induced dipole **P** is opposite to **E**. **c.** Any infinitesimal deviation of **P** results in an electrostatic torque $\mathbf{T}^{\mathrm{E}}$, and the particle rotates with an angular velocity ω. **d.** Particle rotation couples with net translation that triggers self-propulsion near a substrate. The particle travels without a preferred orientation with speed v_0.

Briefly summarising, Quincke rotation of particles spontaneously emerges when an external field E overcomes an amplitude threshold E_Q. This also requires having the particle charge relaxation τ_p higher than the one of the liquid τ_l, which promotes spontaneous breaking of the rotational symmetry. Any angular deviation of the resulting polarisation from the charge distribution at the particle-liquid interface promotes an electrostatic torque $\mathbf{T}^{\mathrm{E}}$. This process results in competition with charge relaxation and advection. On one side, the charge relaxation given by a characteristic timescale τ promotes the cancellation of $\mathbf{T}^{\mathrm{E}}$, by aligning **P** and **E**. On the other hand, the electrostatic torque $\mathbf{T}^{\mathrm{E}}$ contributes to charge advection that ultimately tilts the dynamic component $\mathbf{P}^{\mathrm{d}}$ of the total polarisation **P**. Once the viscous torque $\mathbf{T}^{\mathrm{H}}$ from the liquid is balanced, and the particle exhibits steady rotation with ω perpendicular to the field orientation **E**.

3.1.1 Experiments using Quincke Rotation

Much work has been devoted to the theoretical description of this phenomenon [284, 286–288], including the hydrodynamic and dipole interactions [289, 290]. This is followed by experimental realisations in the field of suspensions, where a system of particles undergoing Quincke rotation is suitable to study Lorenz chaos [291] and complex particle deformation. For instance, viscous droplets subjected to Quincke electro-rotation exhibit deformation into ellipsoids as they rotate [292–296]. Lemaire *et al.* [297] show interesting rheological and conductive properties of particles in suspensions performing such a electro-rotation mechanism.

In addition, Quincke rotation can be combined with external shear flows, i.e Couette and Poiseuille flows, with the effective viscosity on the suspension decreasing as Quincke rotation occurs in the same direction of the flow [297–299]. When subjected to external flows, Quincke rollers respond as classical spins in the presence of a magnetic field, and exhibit alignment of their direction with the external flow [300]. Moreover, it is also observed that the spontaneous electro-rotation promotes the increase on effective electric conductivity as the suspension is subjected to the external electric field [301, 302]. In addition, it is shown in Ref. [2] that the critical amplitude E_Q and rolling speeds are disturbed by the experimental conditions, i.e. humidity and separation between electrodes. Having introduced the mechanism of electro-rotation, we proceed to describe the coupling between rotation and translation. For a particle near a surface, such a coupling results in self-propulsion due to Quincke electro-rotation.

3.2 Self-propulsion due to Quincke Rotation

The application of an external DC field triggers spontaneous rotation of dielectric particles due to Quincke electro-rotation. When dispersed in a bulk liquid, the particle

experiences slip rotation without a net translation. In order to obtain self-propulsion, particles are allowed to sediment and perform Quincke rotation near a surface, e.g. one of the electrodes used to apply the external field E. In the lubrication regime [303], where the separation δ between the surface and the particle is small compared to the particle radius $R \gg \delta$, the particle rotation couples with translational motion. Thus, the Quincke rollers moving with speed v_0. Here, two aspects need to be considered. First, the presence of a surface implies that the system falls into the category of *dry* active matter, due to the momentum exchange between the particle and the surface. Second, the surface disturbs the electric field besides modifying the liquid hydrodynamics. Bricard *et al.* provide in Ref. [4] a model to describe the motion of Quincke rollers, where rotational $\boldsymbol{\omega}$ and translational $\mathbf{v}$ velocities give the mobility matrix,

$$\begin{bmatrix} \frac{1}{R}\mathbf{v} \\ \boldsymbol{\omega}_{||} \\ \omega_z \end{bmatrix} = \mathscr{M} \cdot \begin{bmatrix} R\mathbf{F}^{\mathrm{e}}_{||} \\ \mathbf{T}^{\mathrm{e}}_{||} \\ \mathrm{T}^{\mathrm{e}}{}_z \end{bmatrix}, \tag{3.7}$$

where $\mathbf{F}^{\mathrm{e}}$ and $\mathbf{T}^{\mathrm{e}}$ are the electrostatic and force and torque respectively, with the in-plane $\mathbf{P}_{||}$ and $\mathbf{P}_z$ components. The resulting mobility matrix $\mathscr{M}$ follows,

$$\mathscr{M} = \begin{bmatrix} \mu_t \mathbf{I} & \tilde{\mu}_t \boldsymbol{\Lambda} & 0 \\ -\tilde{\mu}_r \boldsymbol{\Lambda} & \mu_r \mathbf{I} & 0 \\ 0 & 0 & \mu_\perp \end{bmatrix}, \tag{3.8}$$

with $\boldsymbol{\Lambda} = \left(\begin{smallmatrix} 0 & 1 \\ -1 & 0 \end{smallmatrix}\right)$. Here, $\mu_r = (8\pi\eta R^3)^{-1}$ and $\mu_t = (6\pi\eta R^3)^{-1}$ are the hydrodynamic coefficients in the absence of the surface. In order to calculate these coefficients, the gap δ between the particle and the surface is assumed to be small. Hence, in the lubrication regime we have that these coefficients depend logarithmically on δ [303–306]. Ultimately, we can think in the net translation as induced by the electrostatic torque

with $\mathbf{v} = R\tilde{\mu}_t \mathbf{T}^{\mathrm{e}} \times \hat{\mathbf{e}}_z$. Combining Eq. 3.7 with the evolution of the dynamic polarisation in Eq. 3.4, the motion of a single roller follows,

$$\mathbf{v} = -\frac{\epsilon_l}{\epsilon_0} R\tilde{\mu}_t E \mathbf{P}_{||}. \tag{3.9}$$

The full picture for the particle motion under Quincke rotation is then given by two steps,

(i) Quincke electro-rotation emerges out of spontaneous symmetry breaking. The particle rotates without a preferred direction.

(ii) Net translation results from coupling rotation with non-slip motion in the presence of a surface. From Eq. 3.9 it is noted that the external amplitude affects the velocity magnitude,

$$v_0 = \frac{R\tilde{\mu}_t}{\mu_r \tau} \sqrt{\left(\frac{E}{E_Q}\right)^2 - 1} \tag{3.10}$$

From the first step it can be inferred that an isolated particle undergoes a random walk, since the initial perturbation that triggers rotation is not of preferred direction. Importantly, when rotation is converted into translation, the direction of motion is opposite to the charge dipole.

Beyond isolated particles, the interactions between rollers have to be taken into account in order to establish a microscopic model describing the dynamics of larger populations. In this sense, the interactions result from two contributions, electrostatics and hydrodynamics [290]. For a roller in motion, it carries surface charge from $\mathbf{P}$, and distorts the local electric field. Additionally, as the particle rolls it yields a flow field in the surrounding liquid, inducing hydrodynamic interactions. Importantly, the individual

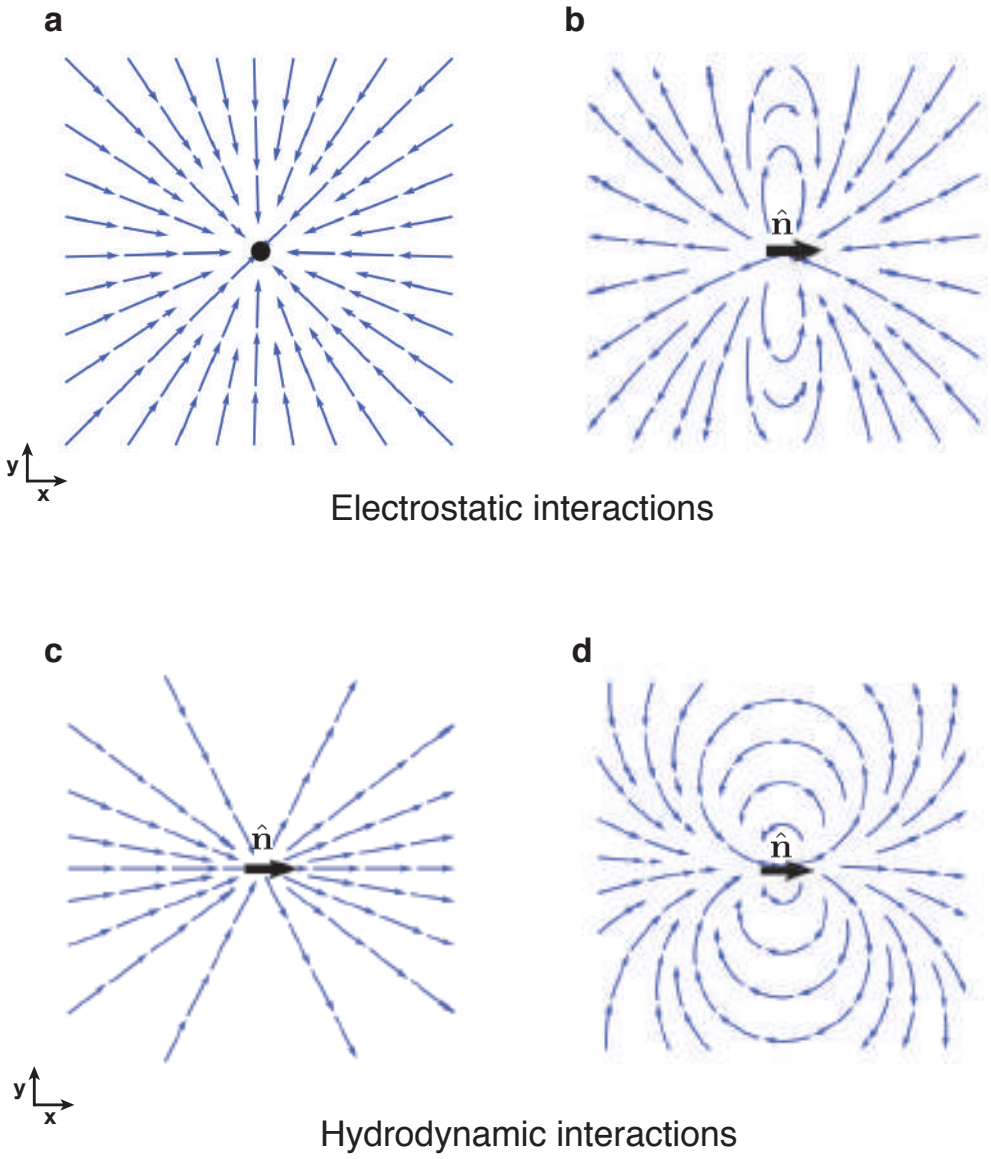

Figure 3.2: **Roller Interactions.** Electrostatic interactions are shown in **a** and **b**. **a** The dipole contribution proportional to P_z results in radial electrostatic repulsion in plane. **b** A second contribution from the in-plane $P_{||}$ yields alignment or anti-alignment interactions dependent on the particle position. Hydrodynamic interactions are illustrated in **c** and **d**. **c**. At short length scales hydrodynamic interactions promote alignment. **d**. Long range hydrodynamic interactions have a dipolar symmetry and promote alignment or anti-alignment.

self-propulsion does not have a preferred direction, different to the in-plane components of the electrostatic and hydrodynamic fields. To quickly summarise the effect of such interactions,

(i) The electrostatic field emerges from the dipole charge distribution at the particle surface. This is given by two components: The first contribution is from P_z, which yields electrostatic repulsion regardless the particle orientation. The second contribution comes from the in-plane polarisation $P_{||}$, that yields an interaction depending on the particle position. This results either in alignment, or anti-alignment between two rollers.

(ii) Hydrodynamic interactions promote alignment between rollers at short distances, due to an anisotropic radial shear induced by the roller . On the other hand, at large distances the long-range hydrodynamic interactions decay with $1/r^2$, promoting alignment or anti-alignment between rollers depending on their relative positions.

Furthermore, having the previous interactions as pairwise additive gives the following equations of motion for roller i,

$$\frac{\mathrm{d}\mathbf{r}_i}{\mathrm{d}t} = v_0 \hat{\mathbf{n}}_i \tag{3.11}$$

$$\frac{\mathrm{d}\theta_i}{\mathrm{d}t} = -\frac{1}{\tau}\frac{\partial}{\partial \theta_i}\sum_{i\neq j}\mathscr{H}_{\mathrm{eff}}(\mathbf{r}_i - \mathbf{r}_j, \hat{\mathbf{p}}_i, \hat{\mathbf{p}}_j) + \sqrt{2D_r}\,\xi_i(t), \tag{3.12}$$

where the zero mean Gaussian noise $\xi_i(t)$ is of variance $\langle \xi_i(t)\xi_j(t')\rangle = \delta(t-t')\delta_{ij}$, and accounts for the rotational noise. Importantly, the roller i has a motion with speed v_0, and its orientation is susceptible to change when interacting with roller j. Here, the effective coupling from electrostatic and hydrodynamic interactions are are included in the potential,

$$\mathscr{H}_{\text{eff}}(\mathbf{r},\hat{\mathbf{p}}_i,\hat{\mathbf{p}}_j) = -A(r)\hat{\mathbf{p}}_i\cdot\hat{\mathbf{p}}_j - B(r)\hat{\mathbf{r}}\cdot\hat{\mathbf{p}}_i - C(r)\hat{\mathbf{p}}_j\cdot(2\hat{\mathbf{r}}\mathbf{r}-\mathbf{I})\cdot\hat{\mathbf{p}}_i, \tag{3.13}$$

with $\hat{\mathbf{r}}\equiv\mathbf{r}/r$, and the coefficients $A(r)$, $B(r)$ and $C(r)$ account for the microscopic parameters,

$$A(r) = 3\tilde{\mu}_s\frac{R^3}{r^3}\Theta(r) + 9\left(\frac{\mu_\perp}{\mu_r}-1\right)\left(\mathscr{P}^\infty+\frac{1}{2}\right)\left[1-\left(\frac{E_Q}{E}\right)^2\right]\frac{R^5}{r^5}\Theta(r), \tag{3.14}$$

$$B(r) = 6\left(\frac{\mu_\perp}{\mu_r}-1\right)\sqrt{\left(\frac{E}{E_Q}\right)^2-1}\left[\left(\mathscr{P}^\infty+\frac{1}{2}\right)\left(\frac{E_Q}{E}\right)^2-\mathscr{P}^\infty\right]\frac{R^4}{r^4}\Theta(r), \tag{3.15}$$

$$C(r) = 6\tilde{\mu}_s\frac{R}{H}\left(\frac{R}{r}\right)^2 + 3\tilde{\mu}_s\frac{R^3}{r^3}\Theta(r) + 15\left(\frac{\mu_\perp}{\mu_r}-1\right)\left(\mathscr{P}^\infty+\frac{1}{2}\right)\left[1-\left(\frac{E_Q}{E}\right)^2\right]\frac{R^5}{r^5}\Theta(r). \tag{3.16}$$

where H is the characteristic separation between two surfaces, i.e. the electrodes. Here, the screening over finite range interactions is given by Θ, where $\Theta = 1$ if $r \le \frac{H}{\pi}$, and $\Theta = 0$ otherwise. Briefly, the role of these coefficients on the interacting potential is as follows,

(i) The two terms in $A(r)$ (Eq. 3.14) correspond to the short-range hydrodynamic and electrostatic coupling, which turn into the alignment of roller i in the direction of j. This coefficient is the only contribution to alignment, and notably, this is similar to the alignment interactions between spins in the **XY** model.

(ii) The electrostatic repulsive coupling is given by $B(r)$, where repulsion arises due to alignment in a monopolar field. As in Eq. 3.14, the interactions are of finite range, and screened by Θ.

(iii) The coefficient $C(r)$ also incorporates hydrodynamic and electrostatic interactions, but different to $A(r)$ this contribution does not yield alignment interactions. It

also accounts for non-screened long-range hydrodynamics that decay with $1/r^2$. However, this contribution turns to be small since $\frac{R}{H} \ll 1$.

Overall, this model accounts for particles self-propelling at a constant speed, and interacting through short-range alignment. Later on, in Chap. 6 we present results from implementing this microscopic model into numerical simulations, along with experiments using Quincke rollers.

3.3 Collective Motion due to Alignment

As mentioned above, some of the experiments using the Quincke electro-rotation of particles focus on the rheological and conductive properties of colloidal suspensions [297–299, 301, 302]. Moreover, dense suspensions of Quincke rollers have been of great use for the investigation of flocking in polar active matter [4, 282, 283, 307]. In contrast with some of the systems discussed in Sec. 2.5, where collective motion arises predominantly from collisions, here the interactions are well understood by means of electrostatic and hydrodynamic coupling.

Starting from the dilute regime, above the field threshold E_Q, colloids start to move with constant speed and with a random initial direction as Quincke rotation emerges from spontaneous symmetry breaking without a preferred direction. Under sedimentation, the rotation couples with net translation, that follows the direction of the initial perturbation. The result is an active gas, with an isotropic velocity distribution. To investigate the collective behaviour, a suspension of rollers can be confined to periodic geometries, e.g. a racetrack, such as in Ref. [4] (Fig. 3.3**a**). A transition to an ordered polar phase, akin to the one in Vicsek model (Sec. 2.4), is observed with the roller area fraction ϕ as control parameter.

Experimentally, above a critical area fraction ϕ_c the system exhibits an onset to

collective motion in form of polar bands due to velocity-alignment interactions. We note that the density profiles of such bands are distinct to those observed in the polar arrays formed by actin filaments [159]. Moreover, similar profiles result in bands of aligning spins [115]. Phase separation occurs as a flock travels through an isotropic phase with area fractions above a critical density ϕ_c. With increasing area fraction, the length of the bands along the channel is enhanced, and eventually a homogeneous phase with global order develops (Fig. 3.3**a**). The transition from isotropic to polar order is characterised by the order parameter $\mathbf{\Pi}$ in Eq. 2.26, where the modulus of the mean orientation is considered. It is noted that such a polar order vanishes with presence of arbitrary obstacles. These suppress the homogeneous phase with the increase of the obstacle density, resulting in sub-diffusion and dynamical trapping of the colloidal rollers [308, 309]. Figure 3.3c shows the flock distortion controlled with the obstacle density. In contrast with phoretic particles able to interact with obstacles [257], rollers experience enhanced rotational diffusion from the repulsion with obstacles.

Remarkably, it is shown for polar liquids that the existence of longitudinal and transverse velocity correlations couples with giant density fluctuations [283], distinct to the previous observations in Ref. [4]. This is now in agreement with the fluctuations in other flocking models (see Sec. 2.4.1) Also, the effect of density on the dynamics leads to speed enhancement on increasing the colloid area fraction [307], as the self-propulsion speed increases linearly with ϕ. Note that the previous model is Ref. [4] lacks this density dependent effect. In addition, experimental observations of clusters reveal that during alignment, the in-plane dipole-dipole interactions promote larger rolling velocities, reiterating the density-dependent dynamics [310].

In Ref. [307] it is shown that the transition to homogeneous flocks can be extended to the phase separation due to motility (discussed in Sec. 2.4.2), with the increase of area fraction to $\phi \approx 0.5$. Figure 3.3**b** shows jamming into active solids, that exhibits coexistence

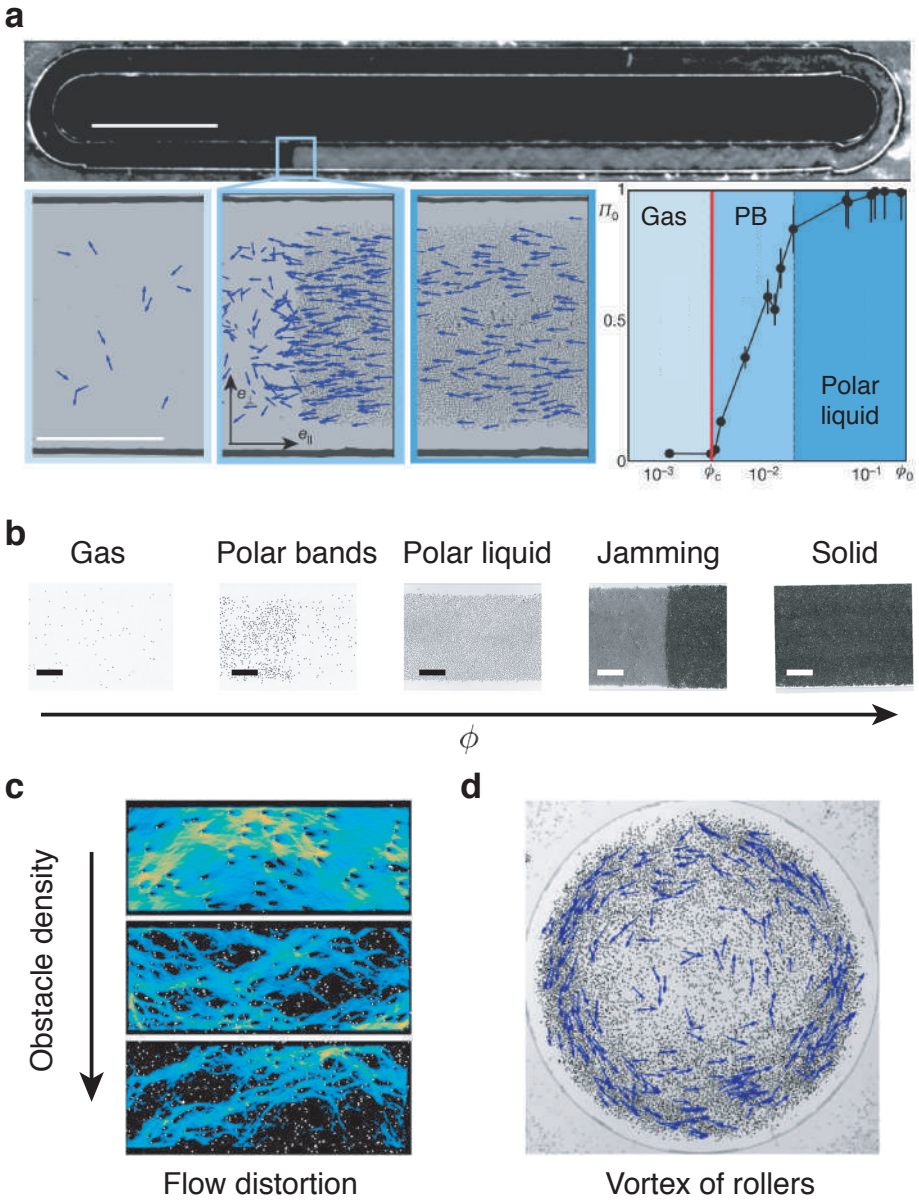

Figure 3.3: **Quincke rollers. a.** Transition to an ordered polar liquid with increasing the roller area fraction ϕ. Reproduced from [4]. **b.** Additional increase of ϕ produces jamming and phase separation between a polar liquid and a solid [283]. **c.** The introduction of obstacles to the system disturbs the polar fraction [308]. **d.** Coherent vortices emerge when rollers are confined to circular regions. Arrows indicate the direction of motion. From [282].

with a homogeneous polar flock. Here, the mechanism leading to phase separation is different to that in active Brownian particles [89, 166, 250], where for Quincke rollers it depends on the slowing down of the rolling motion. It has been suggested that the lubrication interactions, acting on rollers as viscous torques $\mathbf{T}^{\mathrm{H}}$, increase logarithmically as two particles approach one another. Thus, lubrication frustrates the electrostatic torque $\mathbf{T}^{\mathrm{E}}$ and the collective flow resulting from alignment interactions. This points towards the existence of an upper critical density, at which viscous forces overcome the in-plane alignment that enhances the rolling speed. In contrast, we show in Chapter 6 that viscous forces lead to the formation of finite size clusters, without suppressing the motility from Quincke rotation.

Moreover, with the area fraction $\phi \simeq 0.55$, the collective motion vanishes locally into active solids, which constantly coarsen on one side and melt on the other. Such a steady propagation is simply explained by the motility suppression at high density, and by the releasing of particles to join the polar fluid at solid-liquid interface. Notably, the steady motion leads to the propagation of an active solid through a less dense fluid. This in contrast with the MIPS observed in non-interacting particles, where aggregates of finite size are formed [80, 89, 98, 163, 250]. Nonetheless, clusters of finite size are not observed in suspensions of Quincke rollers confined to a racetrack (Fig. 3.3**a,b**). At much higher densities, e.g. $\phi \approx 0.7$, a homogeneous solid phase forms with motility vanishing to zero. Markedly, the system exhibits a flocking transition from isotropic gases to a polar fluid, and a freezing transition of the fluid into an active solid, both as first-order dynamical transitions.

Modification of the boundary conditions promotes swarming and flowing vortices (Fig. 3.3**d**)when colloids are confined to circular geometries [282]. Similar to the emerging polar bands (PB) in Fig. 3.3**a**, a transition from a isotropic gas to a steady vortex is set by a critical area fraction. Interestingly, the resulting vortex corresponds to a heterogeneous

phase, in contrast to the polar fluid in [4]. Above the critical density ϕ_c, the system phase separates into a dilute fraction at the centre, with the density increasing towards the boundary. The local fraction at the centre results close to ϕ_c. On the other hand, a dense fraction near the boundary shows the emergence of vortex motion. The latter develops from the alignment interactions leading to azimuthal flow. To note that the behavior of emergent vortices is not dependent on the confinement size. Regarding the polar order $\mathbf{\Pi}$, it shows bifurcation when measured azimuthally, since the spatial average vanishes in a steady vortex. On the other hand, repulsive interactions result between the colloids and the geometrical boundary due to a toroidal flow induced by the electric field E. This prevents the evaporation and condensation of rollers at the boundary, different to cells [311], vibrated disks [153, 208] and self-phoretic colloids [257].

Karani *et al.* [312] show the emergence of motile clusters from tunable Quincke rollers, through the application of electric pulses of duration and separation set by the characteristic rotation τ_r and translation τ_t timescales. In addition, run-and-tumble and Lévy flight-like dynamics result, in contrast to the conventional directed motion with a persistence length. Collective dynamics emerge in the form of swarms and clusters of different dynamics. These swarms exhibit long-range velocity correlations, along with polar order. When modifying the pulse width, a collection of different dynamical clusters emerge. By increasing the pulse width, rotating clusters form, presumably from electrostatic and hydrodynamic interactions. Polar clusters with long-range orientational order are observed with the increase on the pulse separation and by tuning the width between small and intermediate values. Finally, disordered clusters result from having both pulse separation and width increased, where the aggregates lack of orientation order.

In Chapter 6, we show the aggregation of Quincke rollers into highly-packed clusters. In addition to the very dynamic behavior, we note that such clusters posses high

structural order. Moreover, we present a phase transition from motile clusters to an inhomogeneous phase, that exhibit similar features to the onset of polar motion in the Vicsek-like models (Sec. 2.4.1).

CHAPTER 4

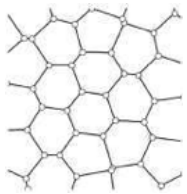

COLLOIDAL SUSPENSIONS

"The beauty of a living thing is not the atoms that go into it,
but the way those atoms are put together"
CARL SAGAN

4.1 Introduction

Colloidal dispersions consist of heterogeneous mixtures of solid (or liquid, or gas) phases dispersed in a medium when is treated as a continuum. Typically, gas bubbles, liquid droplets and solid particles can be dispersed in a gas, plasma, liquid or solid continuum medium [82]. Dispersions of this kind are ubiquitous in industry and in nature, ranging from everyday products such as milk, beer and paint.

The different combinations between the dispersed phase and medium yield various types of dispersions, which describe most of the microscopic models introduced in Sec. 2.5. We focus on colloidal suspensions of solid particles dispersed in a liquid. The size of a colloidal particle can range from the nano to the microscopic scale. These dispersed

particles are big enough to be observed using microscopy, in contrast to the size of atoms and molecules, but small enough to undergo Brownian motion [82, 313]. In the absence of self-propulsion, particles of such size exhibit Brownian motion (Sec. 2.2.1), with diffusion D_t is set by their size. For a small particle of radius $R \approx 100$ nm in an aqueous medium, its diffusion constant $D_t \approx 2\,\mu\mathrm{m}^2\mathrm{s}^{-1}$. On the other hand, particles in the order of micrometers show a diffusion D_t decreasing by an order of magnitude, along with rapid sedimentation.

If of a suitable size, individual colloids are identified and resolved in space-time in order to investigate their dynamics. For a passive particle, the dynamics are set by Brownian motion, or by some out-of-equilibrium mechanism, i.e. shearing. In addition, colloids are susceptible to interparticle interactions. Thus, colloids are typically treated as *big atoms*, and they constitute experimental models to investigate both equilibrium and non-equilibrium phase behaviour. In the present chapter we introduce colloidal suspensions as model systems. In addition we discuss the relevant interactions, and the charging mechanisms developing when dispersed in specific medium.

4.2 Colloids as Model Systems

Suspensions of spherical colloids exhibit phase behaviour akin to atoms and molecules. This behaviour depends on the interactions between the suspended particles, that unlike atoms, can be tuned. The simplest model that can be mapped to colloids is that of hard spheres. This widely studied model consists of monodisperse particles that interact only when in contact. Hard spheres lack both long range attraction and repulsion, and overlap between particles in not allowed. Hence, the interaction potential is either zero if the separation between spheres is greater than the particle size, or infinite if they overlap. Remarkably, the phase behaviour in hard spheres depends solely on one control parameter, the volume fraction,

$$\phi = \frac{\pi\sigma^3}{6}\frac{N}{V} \tag{4.1}$$

where N is the total number of particles, and V is the system volume.

Pusey and van Megen [230] first demonstrated experimentally that sterically stabilised poly(methyl methacrylate) (PMMA) spherical particles suspended in liquids with characteristic dielectric properties exhibit behaviour near to hard spheres. The combination of numerical simulations and experimental microscopy techniques, i.e. confocal microscopy, is useful to resolve the hard sphere diagram, where by controlling the volume fraction ϕ, different phases are observed. At low values of ϕ the system forms a fluid which freezes with $\phi_{\mathrm{f}} = 0.494$. Monodisperse spheres melt at $\phi_{\mathrm{m}} = 0.545$, resulting in crystal-fluid phase separation. The increase of volume fraction ϕ can result in a non-equilibrium state of slow dynamics, where the crystallisation is suppressed and a glass state is recovered at $\phi_{\mathrm{g}} \geq 0.58$. At this value of the packing fraction, crystallisation is still favourable, but at longer timescales than those accessible in experiments. In addition, frustration of the crystallisation can be achieved by introducing polydispersity to the system [314]. Larger values of the packing fraction lead to random-close packing with $\phi = 0.64$, and maximum close-packing at $\phi = 0.74$

In two dimensions, the analog for hard spheres is a system of disks with same interactions. Hard disks interact only at contact, with no long-ranged attraction or repulsion. Similar to the three dimensional problem, the phase behaviour is dependent of a single parameter, the area fraction, given by

$$\phi = \frac{\pi\sigma^2}{4}\frac{N}{A}, \tag{4.2}$$

where A is the total area of the system. Decreasing the number of dimension from three to two might seem simpler scenario. Nonetheless, the phase behaviour of hard disks was

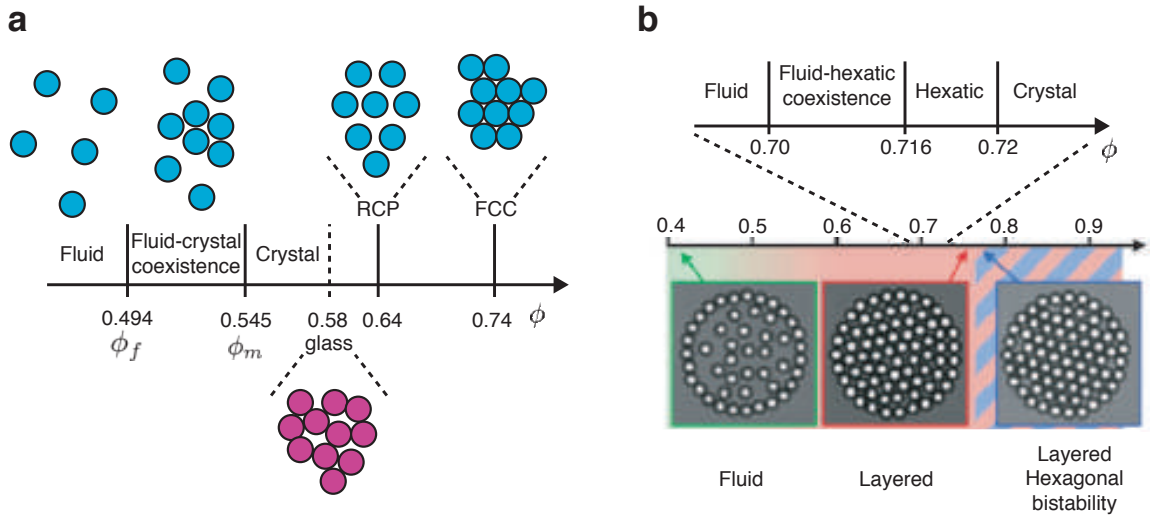

Figure 4.1: **Hard spheres and disks. a.** Phase diagram for hard spheres particles controlled by the packing fraction ϕ. Reproduced from [82] **b.** Phase diagrams for hard disc in bulk (top) [191] and under confinement (bottom) [315].

debated for decades, specifically the nature of the two-dimensional melting. The main distinction between the melting in three and two dimensions relies upon the preclusion of the long-ranged translational order in two-dimensional crystals. The controversy of such melting process is to do whether the transition is of a first order or a continuous one between a fluid and a solid.

Kosterlitz-Thouless- Halperin-Nelson-Young (KTHNY) [188–190] proposed the melting theory, with a continuous transition with an intermediate phase in between. This process consists of destroying both positional and orientational ordering through the formation of topological defects. Here, positional ordering is given by the symmetry of the systems under translation, while orientational ordering refers to the symmetry under rotation. For a two-dimensional solid, the positional order is quasi long- ranged, and orientational order is long ranged, and the most efficient packing is hexagonal for monodisperse disks. Moreover, this intermediate phase exhibits quasi long-range orientational and short range positional order.

This phase is known as the *hexatic* phase, and is characterised by the algebraic decay of orientational correlations, while the translational correlations decay exponentially. The topological defects that give rise to the melting take the form of five-fold and seven-fold coordinated disks. Together, they form dislocations arising in pairs, which displace neighbour particles in a finite region. Once formed, dislocations can unbind from each other, and disturb the positional correlations. The second stage of the melting process, is given by the unbinding of the five-fold and seven-fold coordinated regions, which yields isolated disclinations that disrupt both the positional and orientational order. Overall, the KTHNY theory suggests a continuous melting with a two-stage process to break the translational and orientational orders. In contrast, melting in three dimensions is characterised by the breaking of both types of order by a first-order transition.

After numerous attempts with experiments and numerical simulations, an alternative mechanism for the melting of disks in two dimensions is given by Bernard and Krauth [191]. Using numerical simulations of a large system, an intermediate hexatic phase is found in agreement with the KTHNY scenario, but the transition occurs in two steps. The transition between the solid and the hexatic is continuous as depicted by KTHNY. Interestingly, the liquid-hexatic transition is of first order, in contrast with the previous description. The resulting phase diagram (Fig. 4.1**b** top) is given by a fluid coexisting with the hexatic phase at $0.7 \leq \phi \leq 0.716$, a confirmation of the liquid-hexatic first order transition. The hexatic phase is then observed solely within a narrow the range $0.716 \leq \phi \leq 0.72$. With an area fraction $\phi \geq 0.72$ a hexagonal solid forms, and the hexatic-solid transition follows the KTHNY continuous scenario. Experimentally, Thorneywork *et al.* [193] corroborate the first order liquid-hexatic transition and the continuous hexatic-crystal. Their system consists of a tilted monolayer of hard disks, which results in a gradient on the area fraction. Here the coexistence is given at $0.68 \leq \phi \leq 0.70$, which is measured at the interface between the hexatic and the liquid. At $0.70 \leq \phi \leq 0.73$ the

hexatic phase is observed, with the crystal formation at $\phi = 0.73$, which result in good agreement with the simulations in Ref. [191].

In addition, work by Williams *et al.* [315] explores the two-dimensional behaviour of confined hard disks. The system consists of disks manipulated by optical tweezers and confined to a circular region. Using spheres of the same nature, a colloidal corral can be built and held under individual optical traps. Additionally, the optical manipulation allows to place other spheres in order to populate the interior. For this system, direct control over the area fraction, thus over the phase behaviour, is possible with placing a specific number of particles N. It is shown that the phase behaviour is sensitive to the nature of the confinement compared to bulk behaviour [191, 193], where layered ring-like structures form along hexagonal structures at $\phi \geq 0.77$. An illustration of the phase diagram of confined hard disks is given in Fig. 4.1**b** In the present work, we explore the behaviour of self-propelled particles confined to similar geometries.

4.3 Interactions

As discussed previously, alignment interactions play a role in the emergence of collective motion in flocking spins (Sec. 2.3.1). On the experimental side, colloids experience different types of interactions, which can be summarised as attractive or repulsive. Despite their non-equilibrium behaviour, active particles are often subjected to the same interactions of those in equilibrium, with their dynamics being strikingly different. In this section we describe the relevant interparticle interactions, and the mechanisms for colloidal stabilisation against attractive forces.

4.3.1 Van der Waals

Van der Waals forces result from the attractive interaction between the electric dipoles in atoms or molecules. These present permanent or temporary dipole moments of which

electric fields emerge and polarise neighbour atoms. The effective interactions due to these forces results pairwise additive, with the dipole-dipole interactions described as London dispersion forces, and the attraction given by van der Waals forces. The corresponding potential for two particles is dependent of the separation r between these,

$$U_{\mathrm{vdW}}(r) = -\frac{A_H}{12}\left[\frac{\sigma^2}{r^2-\sigma^2} + \frac{\sigma^2}{r^2} + 2\ln\left(\frac{r^2-\sigma^2}{r^2}\right)\right] \tag{4.3}$$

where A_H is the Hamaker constant. Its value depends on the dielectric properties of the particle and the suspending medium. For materials of similar dielectric constants at a specific frequency spectrum, the Hamaker constant vanishes to zero, thus, the decreasing attraction from van der Waals forces.

Colloidal particles in a suspension are susceptible to van der Waals forces. An approach to counter act the attraction depends on the matching of the refractive index between the particle and the media. However, complete suppression of the van der Waals forces is not achieved by this approach, given that the polarisability is frequency dependent, together with the finite range of frequency accessible using refractive index matching. Aggregation due to van der Waals attractive forces is favourable given the reduction of interfacial energy and the surface area compared to the isolated particles. At very short separations, the interaction due to van der Waals is strong and results in permanent aggregation. In addition of refractive index matching, other approaches rely upon inducing repulsive interactions to prevent irreversible aggregation.

4.3.2 Excluded Volume Interactions

Attraction due to van der Waals forces is short ranged, which means that typically repulsion is needed for distances much shorter that the particle size. Steric repulsion can be achieved experimentally on colloids with the use of adsorbed or grafted block co-polymers stabilising the surface.

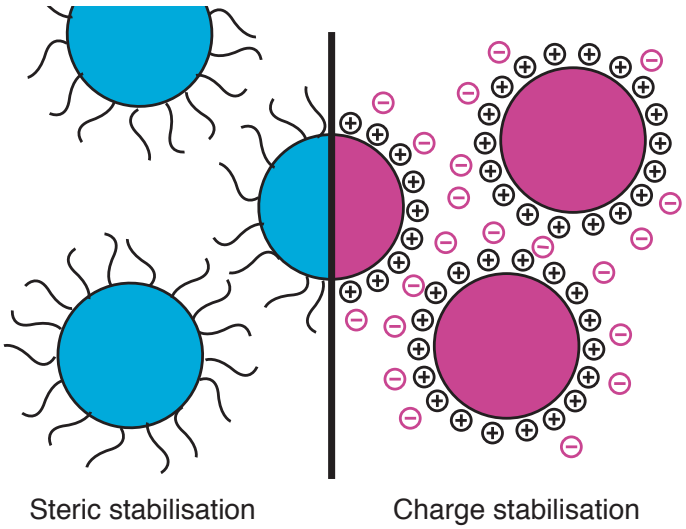

Figure 4.2: **Colloidal stabilisation.** Blue particles on the left are stabilised via steric repulsion due to the adsorption or bonding polymer chains on the surface of the particles. Pink spheres on the right are charged and stabilised by ions in the double layer.

In a suitable suspending medium, the stabilising polymer chains extend creating a volume exclusion, that allows particles to approach neighbours without aggregating, regardless of the van der Waals forces. Polymer layers from different particles occupy the same space, creating an osmotic pressure that increases dramatically with steric hindrance and configurational entropy competition between chains [316]. Therefore, the range of repulsion is set by the polymer extension. These stabilising layers take different configurations depending on the polymer density at the particle surface. With low polymer density, mushroom-like structures form, where the chains exhibit less extension and are able to occupy a larger space close to the particle surface. Alternatively, a single chain can be attached to multiple points on the surface by adsorption on different sites. On the other hand, high polymer concentrations result in brush-like arrays (Fig. 4.2 left), where the configurational entropy decreases with the polymers being unable to occupy the surrounding space.

In numerical simulations, this can be implemented via well-know potentials in systems of self-propelled particles, e.g. active Brownian particles (Sec. 2.2.2). To account

for the volume exclusion from stabilising layers, soft or hard interparticle potentials can be used. A truncated and shifted Lennard-Jones potential yields the Weeks-Chandler-Anderson (WCA) potential [317], which is typically used to model nearly hard-core or soft-core repulsion. This potential reads,

$$U(r) = \begin{cases} 4\epsilon\left[\left(\frac{\sigma}{r}\right)^{12} - \left(\frac{\sigma}{r}\right)^{6}\right] + \epsilon & \text{with } r < r^{\star} \\ 0 & \text{if } r \geq r^{\star} \end{cases} \tag{4.4}$$

where ϵ is the depth of the potential, $r^{\star} = 2^{1/6}\sigma$ is the distance cutoff dependent of $\sigma = 2R/2^{1/6}$. The cutoff is chosen in such way that the interaction force diverges when two particles approach as $r^{\star} < 2R$. Alternatively, a hard-core repulsion is achieved by increasing the separation along the bond direction when two particles overlap [251].

4.4 Charging in Colloids

A second approach to hinder aggregation relies upon surface charge. There are several processes through which a particle acquires charge. For instance, chemical groups at the surface can be ionised with a change of pH in the solvent. This section summarises the charging mechanisms that stabilise particles from aggregation and promote charge in colloids. This latter is important for the observation of colloids performing Quincke electro-rotation, as shown in Chapters 6-8.

4.4.1 Charge Stabilisation

When suspended in a solvent, colloids often experience spontaneous charging at the liquid-particle interface. The mechanisms behind the emergent surface charge rely upon the adsorption of charged species, or the dissociation of surface groups. Particles with equal sign of charge repel each other, counter acting the attraction from van der Waals

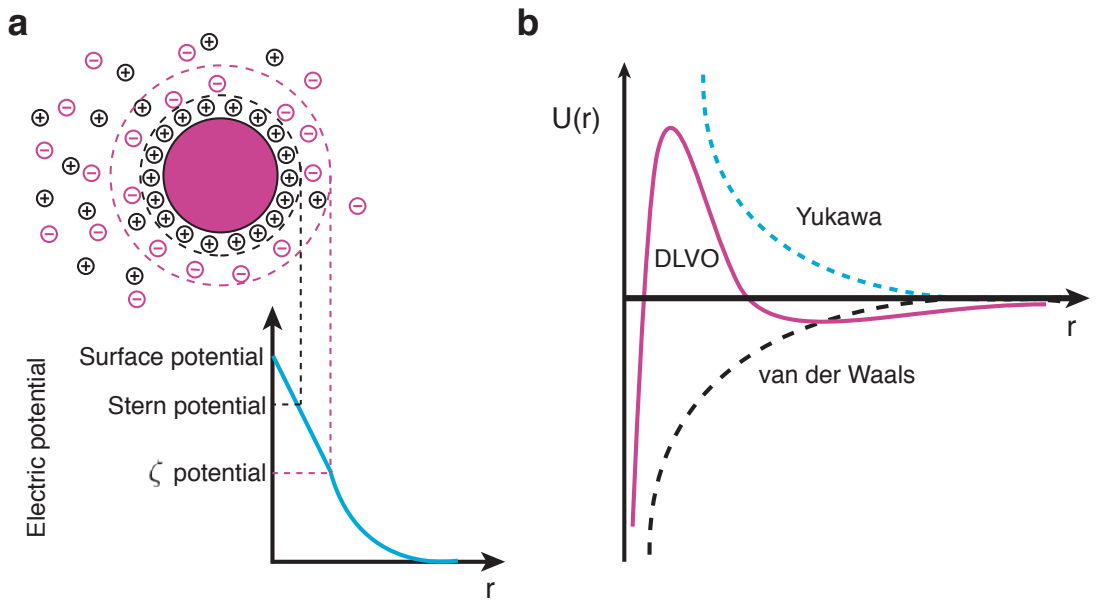

Figure 4.3: **Electric double layer. a.** Illustration of the electric double layer formed by the static Stern layer and diffusive layer. **b.** Schematic representation of the DLVO potential, which results from the sum of the attractive van der Waals and repulsive Yukawa potentials.

forces (Fig. 4.2 right). Once charge develops at the interface, an equal number of counter charges neutralise the charge at the surface. The result is a cloud of ions that forms around the colloid, due to balance between electrostatic attraction and diffusion. Here, the first layer of ions neutralising the surface charge is known as the Stern Layer. The remaining charges in the cloud give rise to a diffusive layer, where the concentration of ions around the colloid decrease outwards. Both contributions, the Stern layer and the diffusive cloud form the electric double layer, illustrated in Fig. 4.3**a**. The presence of such a double layer generates an electric potential, which decays linearly across the Stern layer, and exponentially with larger distances from the particle surface. The separation between the Stern layer and exponentially decaying potential is characterised by the zeta potential ζ [82] (Fig. 4.4**a**).

If counter charges from the solvent do not form an electric double layer, colloids exhibit Coulombic-like repulsion between each other. On the other hand, charges in the

solvent screen the colloid charge, which result in interactions described by the Yukawa form of the Debye-Hückel equation,

$$U_Y(r) = \epsilon_Y \frac{\exp[-\kappa(r-\sigma)]}{r/\sigma} \tag{4.5}$$

with ϵ_Y as the contact potential in the Yukawa form, which reads,

$$\epsilon_Y = \frac{Z^2}{\left(1+\frac{\kappa\sigma}{2}\right)^2} \frac{\lambda_B}{\sigma} k_B T \tag{4.6}$$

where Z is the particle charge given in elementary charge units. Here, $\kappa = \lambda_D^{-1} = \sqrt{4\pi\lambda_B\rho_{\text{ion}}}$ is the inverse Debye screening length, that is a good approximation to the diffusion layer thickness. Therefore, the repulsive potential decays exponentially with this characteristic length scale λ_D, where ρ_{ion} is the monovalent ionic number density, and

$$\lambda_B = \frac{e^2}{4\pi\epsilon_0\epsilon_l k_B T} \tag{4.7}$$

where e is the elementary charge and ϵ_l is the dielectric permittivity of the dispersing liquid. Here, λ_B is the Bjerrum length, which gives the range of the Coulombic interactions comparable to the magnitude of the thermal energy $k_B T$. One way of controlling the range of separation between colloids is by changing the ion concentration in the solvent, which ultimately modifies the Debye length λ_D. Typically, salt is added to the suspension in order to tune the Debye length in such way that the repulsion occurs only at short ranges. This approaches hard sphere interactions, as the very short-range repulsion from screening allows the particles to approach each other.

Both contributions from van der Waals attraction and repulsion from charging are well described by the DLVO theory, after Derjaguin-Landau-Verwey-Overbeek. The total interaction potential reads,

$$U_{DLVO}(r) = U_{\mathrm{vdW}}(r) + U_Y(r) \tag{4.8}$$

where $U_{\mathrm{vdW}}(r)$ and $U_Y(r)$ are the potentials in Eqs. 4.3 and 4.5. This potential is illustrated in Fig. 4.3**b**, along the attractive and repulsive contributions.

4.4.2 Charge in Non-polar Solvents

As stated previously, colloids exhibit a degree of charging that strongly depends on the properties of the immersing medium. The most common dispersing medium is water, given its high polarity that facilitates charge dissociation. In contrast, a non-polar medium is characterised by having a low relative dielectric constant $\epsilon_l \sim 2$, where the thermodynamics of charging depend on the Bjerrum length λ_B in Eq. 4.7. This length characterises the separation at which Coulombic interactions are equal to the thermal energy. In other words, if the separation between two oppositely charged ions is smaller than λ_B, the electrostatic attraction overcomes the random thermal forces.

For colloids in non-polar solvents this has important implications. First, the Bjerrum length is around two orders of magnitude larger in a non-polar medium compared to water, meaning that large liquid shells form around the ions in order to prevent recombination. Thus, the concentration of free charge carriers is very small since the solvation energy for an ion scales with $\lambda_B/2R_{\mathrm{ion}}$, where R_{ion} is the ionic radius. In other words, the screening of charge in an oil is very low, therefore the electrostatic interactions become extremely long-ranged. In addition, the capacitance of the double layer is around two orders of magnitude smaller than the corresponding to aqueous environments. Nonetheless, a small charge on a colloid is enough to develop an appreciable surface potential when dispersed in a non-polar medium. Markedly, the resulting surface potentials are comparable to those charged colloids in aqueous systems [1].

While the charging mechanisms are well understood in polar solvents, the case for non-polar liquids is more complex, and in many cases is determined by the nature of the particle surface. In order to facilitate charging in non-polar media, surfactants can be added to the colloidal suspensions. Reverse micelles form with the polar part of the surfactant molecules creating a shell that stabilises charge carriers. In the absence of these surfactant additives no charge is expected, regardless the application of external electric fields. Markedly, the range of electrostatic interactions is determined by the ionic strength of micelles. It is shown by Hsu *et al.* in Ref. [1] that the conductivity of the medium increases linearly with the addition of surfactant.

Nonetheless, measurements of the conductivity indicate that the fraction of ionised micelles is independent of the surfactant concentration, where the majority of micelles are non-charged. Moreover, non-charged micelles result in dynamical equilibrium with a small fraction of ionised micelles. The number density of ions ρ_{ion} shows a linear dependence on the concentration of reverse micelles, and is independent of surfactant concentration. It is suggested that the charge mechanism results from the competition between entropy and electrostatic interactions, where the Bjerrum length λ_B and the micelle core radius R_c give the ionisation as $\sim \lambda_B/2R_c$. If $\lambda_B \gg R_c$ only a small fraction of micelles acquire monovalent charge. When λ_B and R_c are comparable the micelles are able to become multiply charged.

Listed below are some other mechanisms for charging that have been proposed using micelles [318],

(i) Adsorption isotherms indicate a preferential adsorption of ions or charged micelles on the particle surface.

(ii) Dissociation of ionic groups from the particle surface, followed by charge stabilisation with micelles.

(iii) Surfactant aggregates are adsorbed at the surface in the vicinity of surface groups. This is followed by the ion exchange and disorption of ions into charged micelles.

Charging of Colloids by Reverse Micelles

For particles dispersed in a non-polar liquid, typically sodium di-2-ethylhexyl sulfosuccinate (AOT) surfactant is added. AOT corresponds to a surfactant with a sulfonate group on its polar part, along two hydrocarbon tails. This surfactant forms reverse micelles containing about 30 molecules above a critical micelle concentration (CMC), which is about 1 mM in dodecane [1]. However, the CMC values are different for every solvent used, and differ again with the presence of humidity. In this sense, AOT is highly hygroscopic and rapidly hydrates from moisture in the environment. Thus, values of the CMC for AOT in cyclohexane can range between 0.225mM and 5.7mM.

Employing a single-particle optical microelectrophoresis (SPOM) technique [319], Bartlett *et al.* investigate the charging of sterically stabilised particles in non-polar liquids. Briefly, the SPOM technique consists of measuring the electrophoretic mobility of optically trapped particles placed between two electrodes where an AC field is applied. The key advantage of this technique is the level of sensitivity and accuracy that can be accessed in terms of surface charge in the presence of inverse micelles. In order to compare the effect of AOT on charging, other additives can be of use, such as $Zr(Oct)_2$ [zirconyl 2-ethyl hexanoate], and PHSA-PMMA ([poly(12-hydroxystearic acid)-*g*-poly(methyl methacrylate)]) copolymer. Here, particles acquire a net negative charge when employing AOT, positive with $Zr(Oct)_2$, virtually uncharged with the PHSA-PMMA copolymer [318]. Measurements using SPOM reveal a similar charging mechanism, where negatively and positively charged micelles are simultaneously adsorbed on the sterically stabilised particles.

As above, in the absence of micelles, the particle electrophoretic mobility is small as the particles are virtually uncharged. The addition of surfactant promotes the formation

of reversed micelles, thus, particle charging as the micelles ionise. Also, electrostatic screening develops as the Debye length λ_D vanishes. In agreement with Hsu *et al.* [1], Roberts *et al.* [318] show that for micelles of AOT, $Zr(Oct)_2$ and PHSA-PMMA copolymer, the surface potential is independent of the concentration of micelles. The proposed charging mechanism relies upon the decoration of the particle surface with micelles, where oppositely charged and uncharged micelles compete to occupy the same binding site at the surface. The competition process reads as follows:

(i) Once in the low dielectric liquid, the surfactant molecules form a random mixture of positively and negatively ionised and uncharged micelles.

(ii) Micelles can undergo short range attractive interactions from depletion mediated by the solvent or interpenetration of the surfactant tails. Similar attractions can result between the micelles and the polymer chains that sterically stabilised the particle surface.

(iii) The surface of the particle has N_b binding sites that are decorated randomly between positive or negative micelles. This is controlled by the number of available micelles per particle. Also, the charge on the particle is dynamic and can fluctuate as micelles can be adsorbed and exchanged. Assuming equilibrium energetics, the difference in free energy between free and adsorbed micelles is either positive ΔG^+, negative ΔG^- or neutral. Assuming that $\Delta G^+ < \Delta G^-$, positive micelles are more strongly adsorbed, leads to a net positive surface potential Φ on the particle. Thus, electrostatic repulsion increases with more positive particles, followed by the adsorption of oppositely charged micelles. Ultimately, the charge on the particle results from the competition between micelles for the available binding sites.

For sterically stabilised PMMA spheres, it has been found that the surface coverage with micelles is low, and that the magnitude of the surface potential remains despite

the concentration of micelles and particle size. For the case of adding PHSA-PMMA copolymers to the suspension, charge does not develop since adsorption at the particle surface is not expected, as this copolymer is identical to particle stabilising layer. On the other hand, a net positive surface charge develops with $Zr(Oct)_2$ micelles, and negative with AOT. This presumably results from the interactions between micelle tails and the steric layer coating every particle.

Surfactant Adsorption

Focusing on sterically stabilised PMMA particles charged solely with AOT micelles, and expanding the range of surfactant concentration, Kemp *et al.* [320] propose a different mechanism of charging combining SPOM and conductivity measurements with small-angle neutron scattering (SANS) for small particles. To characterise the charging mechanism a radial scattering profile $\rho(r)$ prior to charging and after the adsorption of surfactant is shown in Fig. 4.4**b**. Here, ρ_{p} corresponds to the scattering density profile of the particle, and $\delta\rho_{\mathrm{s}}$ is the profile obtained for the stabilising PHSA layer. The adsorption of the surfactant within the PHSA layer is modeled by a band of scattering density $\Delta\rho$. Additionally, conductivity measurements are performed in order to characterise the charge fluctuations. AOT added to low dielectric solvents shows a profile with three different regimes, depending on the surfactant concentration.

In the absence of particles, the conductivity increases with a square root dependence at low concentrations of AOT. This regime characterises from the dissociation of sodium from the surfactant molecules, as $\mathrm{Na-AOT} \rightleftharpoons \mathrm{Na^+ + AOT^-}$. The second regime corresponds to concentrations around the CMC, where both dissociation of surfactant monomers and charging micelles occur. The last regime shows linear dependence of the conductivity to the surfactant concentration. Employing PMMA spheres of radius $R = 425$ nm, SPOM measurements indicate that the particles gain large surface potentials with AOT micelles. When exploring a wider range of surfactant concentration c_{S},

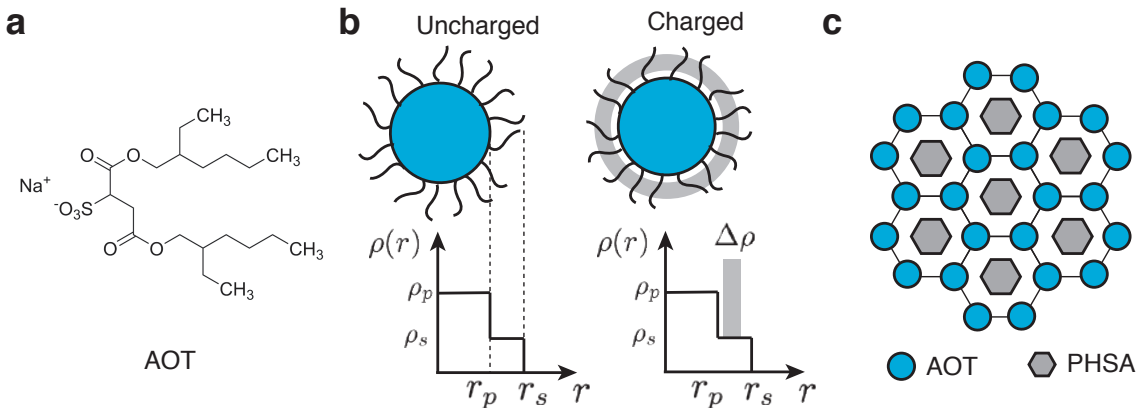

Figure 4.4: **Particle charging in a non-polar solvent. a.** Molecular structure of AOT surfactant. **b.** Radial scattering profiles for an uncharged and charged particle. Grey halo represents the adsorption of AOT within the PHSA layer, which increases the density in the profile by $\Delta\rho$. c. Packing of the AOT molecules within a hexagonal lattice made of PHSA chains at the particle surface. Reproduced from [320].

the surface potential Φ exhibits three regimes akin to conductivity.

For concentrations c_S below the CMC, the particles do not present a response to the electric field. For the second regime, above the CMC, a finite surface potential develops and increases with c_S. In this regime, a linear dependence in the magnitude of the surface potential with respect of the AOT concentration is expected. Nonetheless, the surface potential Φ increases slowly with a weak power law dependence on c_S. In contrast to the previous charging mechanism in Ref. [318], this suggest that particles charge differently from the suggested micelle adsorption mechanism. For the last regime, the surfactant concentration is high and the surface potential becomes independent of c_S, as it saturates. Interestingly, comparable values of Φ result from mobility measurements of small (R = 0.46 nm) and large (R = 1830 nm) particles, corroborating a size independent charge mechanism.

Results from SANS on small particles reveal that AOT surfactant molecules are adsorbed deeply inside the polymer stabilising layer at the particle surface (See. Fig. 4.4**b**). This suggests that charging relies upon ionised molecules instead of adsorbed

micelles [318]. To obtain stable particles against van der Waals aggregation, regions smaller to $400\,\text{Å}^2$ are covered with PHSA polymer chains. Each chain coverage is about $94\,\text{Å}$, so one could assume a hexagonally packed array of chains, leaving enough space to accommodate species of radius around $6.5\,\text{Å}$ between three chain neighbours. On the other hand, AOT molecules have a cross-sectional area of about $55\,\text{Å}^2$ and a horizontal radius $R_m \approx 15\,\text{Å}$. It is the suggested that AOT molecules can be packed vertically between PHSA polymers, as sketched in Fig. 4.4**c**. The charging mechanism is proposed of two steps, as follows:

(i) AOT molecules are deeply absorbed within the stabilising layer on the particle surface, where the particle lacks of chemically bound surface groups.

(ii) Once packed within a hexagonal lattice of PHSA chains, the AOT molecules ionise generating a surface-bound ion and a mobile ion stabilised by reversed micelles in the liquid.

Hence, the power law dependence of the surface potential Φ on the surfactant concentration c_S is a result of this process, where isolated surfactant molecules are unable to solvate charges effectively as with micelles in solution. Once the particle acquires charge and as the surface potential Φ reaches a maximum it becomes independent from the surfactant concentration. In Chap. 5 we employ surfactant concentration comparable to the ones discussed here. Thus we assume that charging of colloids in non-polar media with AOT follows the description above.

4.5 Electro-hydrodynamics

The application of an external electric field to colloidal suspensions results in a wide range of structures, from three dimensional aggregation, hexatic-like clusters, worm-like elongated chains and random closed packed structures. Given the in-plane electrostatic

interactions for induced dipoles, repulsive behaviour is expected. Transverse motion, with respect of the applied field **E**, occurs in addition the electrophoretic deposition of particles to a surface. The transverse motion is a product of the attractive interactions, that promote aggregation via an induced electro-hydrodynamic (EHD) flow. Overall, three mechanisms for such particle aggregation have been suggested,

(i) Charged particles in a liquid and near a conductive surface generate a fluid flow due to electro-osmosis [321].

(ii) The electro-hydrodynamic flow results from the particle-induced distortion of the electric field, either AC or DC. This occurs in the vicinity of the Debye screening layer at the conductive surface [322].

(iii) The aggregation mechanism results from the electrode polarisation, which generates bulk charge densities [323].

Considering the case of polarisable particles distorting the local field. In the absence of the external field **E**, charged particles with similar ζ potential do not exhibit lateral aggregation as they repel in a Coulombic fashion. Under the application of the **E** field, the ionic cloud from the double layer is polarised, and the particles experience electrostatic repulsion from the in-plane dipole-dipole interactions. Remarkably, the applied DC or AC field is distorted by the presence of a dielectric particle near the electrode. This perturbation leads to a tangential deviation of the electric field by the diffusive layer of the particles or by the charge induced on the surface of the electrode [322, 323]. It is observed that for steady currents, the electro-osmotic flows from the diffuse layer on the particles dominate. Alternatively, tangential components of the electric field from the charge induce on the electrode arise with high-frequencies [324]. The generated electro-osmotic flow is then proportional to two components: the charge in the double

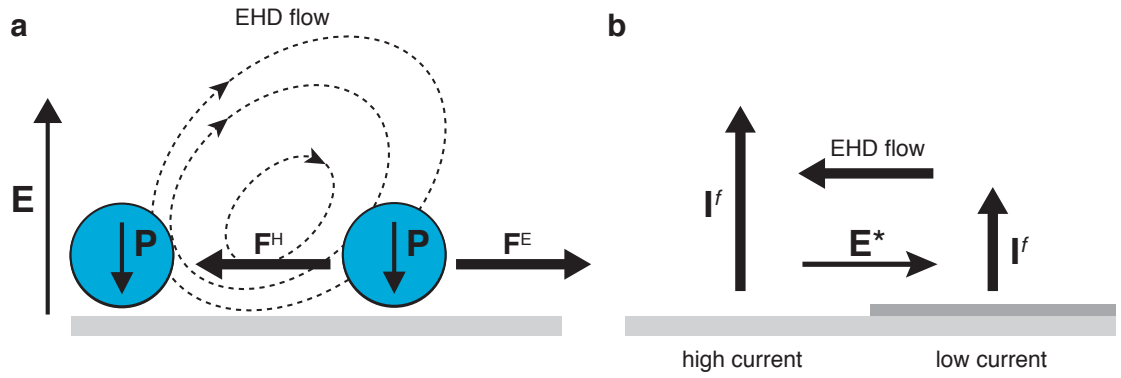

Figure 4.5: textbfElectro-hydrodynamic flows. **a.** Schematic representation of the induced attractive interactions between polarised colloids. The viscous forces from the EHD flows are counteracted by the electrostatic repulsion $\mathbf{F}^{\mathrm{E}}$. The dashed lines represent the form of the generated flow [322]. **b.** EHD flow is generated between two adjacent regions of different current $\mathbf{I}^{f}$ densities. The in-plane $\mathbf{E}^{*}$ field results from the same discontinuity [326]

layer and the tangential component of the field outside this layer, both proportional to the magnitude of the applied field $\mathbf{E}$.

In the presence of neighbours, a particle experiences a centripetal drag force from the surrounding flow generated by another particle. Such a viscous force is given by $\mathbf{F}^{\mathrm{H}} \sim 6\pi\eta R\mathbf{U}$, where $\mathbf{U} = \frac{\epsilon_l R E^2}{\eta}$ is the field dependent fluid velocity, and which balances the electrostatic repulsion $\mathbf{F}^{\mathrm{E}}$ from the dipole-dipole interactions. Employing smaller tracer beads, Yeh *et al.* [322] resolved the flow generated by individual larger particles and geometrical patterns on electrodes. In addition, Nadal *et al.* [325] determined the balance between the electro-osmotic attraction and the electrostatic repulsion using optical traps. From these measurements, it was found that both dipole-dipole repulsion and the electro-hydrodynamic attraction have the same power law dependence, E^2,on the applied field.

Most of the experimental investigations focus on the use of AC fields, with the works of Trau *et al.* [323] and Yeh *et al.* [322] showing aggregation with both AC and DC fields. Crystallisation is observed in colloids near to the electrode when a low frequency

AC field is applied, whereas at high frequencies the repulsive contribution dominates [325, 327, 328]. Interestingly, when employing an AC field, it is shown that the effect of the field frequency f on the particle ζ potential is negligible. That is to say, surface charge can be neglected in colloidal aggregation due to electro-osmotic flows [325]. However, other observations report the increase of particle separation at low frequencies [329, 330], in contrast to previous works. In this sense, Dutcher *et al.* describe in Ref. [331] a transition from random-closed packing (RCP) to an order hexatic-closed packed (HCP) state when increasing the field frequency. Increasing the frequency promotes particle separation, due to the absence of strong attractive forces. Measurements on the particle height at low frequencies reveal the diffusion enhancement that hinders crystallisation. Therefore, RCP structures form despite the aggregation rate increaseing with the reducing field frequency. Interestingly, the transition between RCP and HCP aggregates is reversible by tuning f, and shows rapid annealing properties.

For the generation of EHD flows, it is shown that the presence of dielectric particles is not the only source of tangential components of the electric field. Lateral motion of particles is also observed when they are placed between two regions of different conductivity, under the application of an external field. This is achieved by half-coating glass slides with a thin layer of indium tin oxide (ITO), where the particles move away from the non-conductive silica towards the ITO layer. An electro-hydrodynamic flow is induced from the region of low field strength towards the more conductive region (see Fig. 4.5**b**) [323].

Alternatively, lithography techniques can be of use in order to pattern electrodes with dielectric layers, where particles migrate to the regions of exposed electric field [322]. The generation of EHD flows is to do with the lateral potential gradient E^*, that results as a product of the decreasing free charge at the regions with higher current density (see Fig 4.5**b**). Thus, the surface where the EHD flow is induced can be modeled

as a flat and equipotential electrode, with varying the current density. For two parallel electrodes, the absence of current variations yields a fluid velocity equal to zero, where the osmotic pressure balances electrostatic body force. Electrochemical reactions set the flux of ions between the electrodes, resulting in a current I_f from faradaic reactions at each electrode. Here, the current density I_f is dependent on the electrode potential, ionic concentration, and electrode type. The addition of perturbations to the surface yields current inhomogeneities, and a flow with velocity proportional to the applied voltage and the variation in current density [326].

CHAPTER 5

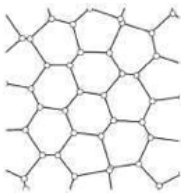

EXPERIMENTAL DETAILS

"Chemistry can be a good and bad thing.
Chemistry is good when you make love with it.
Chemistry is bad when you make crack with it"

ADAM SANDLER

As discussed in Sec. 2.5, many synthetic models have been introduced with the aim of achieving experimental realisation of the observations from numerical simulations and theory on active matter systems. Significant efforts have been devoted towards a better control and understanding of the different experimental models used. As an example, the use of different strategies to trigger particle motion, via phoretic mechanisms, molecular driving of microtubules and vibration of polar rods, are discussed in Sec. 2.4. All of these represent experiments where collective phenomena arise in the form of polar flocks or dynamical clustering. We find that many of the phenomenological observations in these systems rely upon the interactions among particles, i.e. the attractive diffusiophoretic interactions that lead to clustering in chemically fueled Janus particles [98] and light-

activated surfers [251]. In the present work, we exploit a system of Quincke rollers introduced in Chapter 3, where the interactions are well understood. In the present chapter we detail the synthesis and preparation of particles used for this work. We later described the building of confining sample cells, along the experimental set-up.

5.1 PMMA Particle Synthesis

In the present work we mostly employ colloidal suspensions of poly(methylmetacrylate) (PMMA) particles in a low-dielectric liquid. We focus on the preparation of fluorescent and sterically stabilised PMMA colloids as a model system, i.e. nearly hard spheres [236]. PMMA spheres have been studied extensively because of their attractive features, such as the wide range of particle sizes that can be prepared, from tens of nanometers to several microns, with low polydispersity. In Chapters 6 and 7 we present our main results employing such colloidal suspensions, whereas in Chapter 8 we use non-spherical particles prepared with polystyrene beads. Briefly, we describe the preparation of colloids stabilised by two different polymer chains, which provide effective steric repulsion.

5.1.1 Dispersion Polymerisation

PMMA spheres fluorescently labeled with rhodamine are prepared through a dispersion polymerisation method developed in Bristol by Antl *et al.* [332]. The spheres are coated with a comb-like structure of poly(12-hydroxystearic acid) (PHSA) to prevent aggregation. In order to form a stabilising layer, the PHSA chains bound to PMMA and poly(glycidyl methacrylate) backbone. The overall preparation is given by a two-step process: (i) nucleation and growth, (ii) and locking and stabilisation.

Nucleation and growth

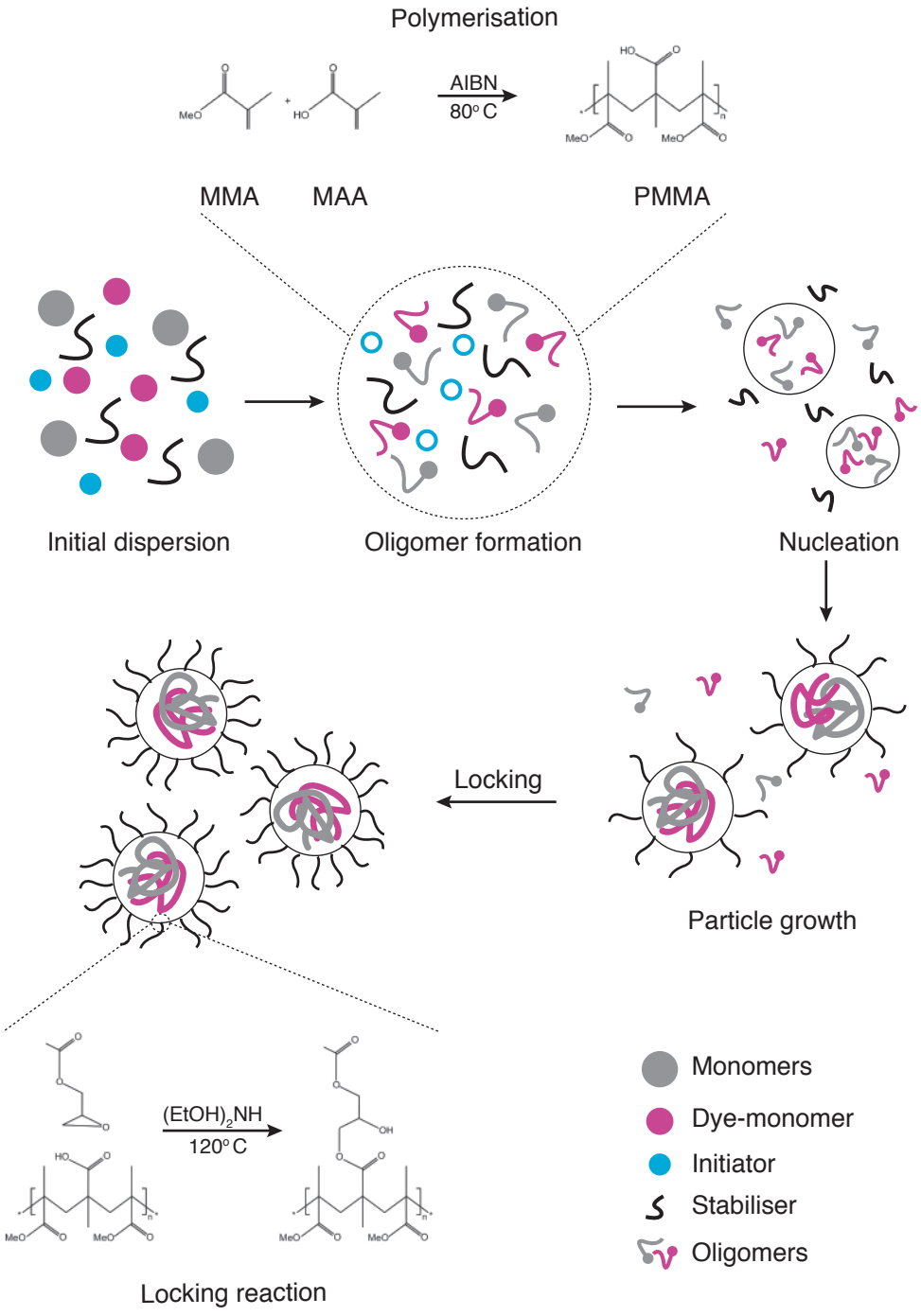

Figure 5.1: **Preparation of fluorescently labeled PMMA particles.** Particles are first prepared via dispersion polymerisation of MMA and MAA monomers. Finally, the particles are sterically stabilised with bonding PHSA through a locking reaction.

To carry out a dispersion polymerisation reaction, the solvent employed must be a good one for solubilising the reactants, but a poor one to solubilise the resulting particles. First, the methyl methacrylate (MMA) and methacrylic acid (MAA) monomers, the azobisisobutyronitrile (AIBN) initiator, hexane, together with a solution of the stabiliser in dodecane, and octanethiol are added and weighed into round bottom flask. A glass condenser is connected to the top neck of the flask, and a nitrogen source flows through the second neck. Once solubilised, the free radical initiator must be thermally decomposed. For that, the reaction is placed on a heated bath at 80°C, and the temperature is maintained throughout the process (2 hours). While heating, stirring is also carried out using a magnetic bar and setting the rotation on the hot plate to typically 200 rpm. As the reactant mixture is heated, AIBN forms free radicals and linear oligomers form as MMA and MAA begin to polymerise. These oligomers reach certain molecular weights at which solubilisation is no longer feasible, causing polymer aggregation. The resulting aggregates then become nucleation points where both more oligomers and stabiliser chains are adsorbed. Further aggregation of the solubilised oligomers result in grown particles. Dye monomers, such as rhodamine- B-isothiocyanate and aminostyrene, are added in order to fluorescently label the resulting particles.

Locking and stabilisation

After the growth of particles from nucleation of oligomers, the surface is stabilised by a locking reaction. At this stage, the PHSA chains are only adsorbed at the particle surface, but in order to fully stabilise chemical bonds have to be created. This is achieved by the esterification between the MAA carboxylic acid groups exposed at the particle surface, and the epoxide groups at the glycidyl methacrylate part of the stabiliser. For this diethanol amine is added as a catalyst at 0.2% of the total reactant weight along dodecane, and the bath temperature is raise to 120°C. In order to achieve full locking, the reaction is left under reflux for 24 hours. Once the process is complete, the particles

are washed via centrifugation at 13.6 rpm for 5 min and redispersion in dodecane at least 5 times. A representation of the preparation process process is illustrated in Fig. 5.1.

5.2 Preparation of Non-spherical Particles

So far, most analytical, numerical and experimental studies focus on the use of spherical and rod-like particles, since their dynamics and interactions are well characterised by particle resolved studies [27, 82]. In contrast, microswimmers are able to self-propel via body deformation, which implies a more complex asymmetry. As an approximation, many bodies have been designed asymmetrically, where self-propulsion can be achieved through the deformation of flagella-like assemblies [201]. In addition, particles of different geometrical shape exhibit different motion, e.g. L-shaped particles show circular motion where the clockwise or anti-clockwise direction is set by the chirality of the particle [86].

Alternatively, spherical units can be employed to fabricate particles of different shape, often called *colloidal molecules*. This can be achieved by different techniques that induce reversible or irreversible attraction on spheres. Control over the shape and number of units is achieved with the use of patterned substrates and capillary forces [333, 334]. Alternatively, attraction induced from local demixing of a solvent mixture promotes the formation of molecules that behave as migrators, spinners and rotators [269]. On the other hand, small clusters to supra-assemblies formed by smaller particles are achived with controlled evaporation [335, 336]. The latter technique relies upon dispersion of spheres in an organic solvent, which is emulsified in a continuous media, followed by heating in order to evaporate the organic phase. This leads to the local increase of sphere packing fraction, and particles stick due to van der Waals attraction.

We employ the interparticle irreversible aggregation of spherical particles. To prepare

homonuclear molecules, we use polystyrene (PS) spheres (Fluoro-Max, ThermoFischer). When dispersed in pure water, the sulfate groups in polystyrene dissociate and promote charging of particle surface. Initially, this prevents aggregation as a screening double layer forms. On the other hand and as we mentioned in Sec 4.4.2, the dissociation of surface groups is limited in non-polar solvents. We promote the lack of charge stabilisation by the drastic exchange between polar and non-polar solvents.

Commercially available PS spheres of size $\langle\sigma\rangle = 3.0\,\mu$m are dispersed in water. Particles are sedimented using centrifugation at 13.6 rpm for 5 min. The supernatant part of the medium is removed, and an equal volume of hexadecane is added, followed by sedimentation. As the liquid is removed, the packing fraction increases and particles begin to aggregate. To prevent further aggregation into bigger clusters, we add a solution of surfactant in hexadecane, and the clusters are subjected to sonication at 45°C for 1 hour. In order to remove any trace of water, particles are washed via centrifugation and redispersion in hexadecane. From this process we find a mixture of molecules composed of different number of spheres N. Some of these are shown in Fig. 5.2**c**. With the aim of gaining quantitative information, we focus on colloidal molecules with in-plane motion as they are subjected to Quincke electro-rotation. For that, we use centrifugation at low revolutions to separate small molecules from the bigger undesired ones. A method with better control is given by separation in a density gradient [335].

5.3 Particle Characterisation

Prior to experiments, PMMA spheres and PS colloidal molecules are characterised by means of size and polydispersity. For this, different techniques can be used, e.g. dynamic light scattering (DLS), which allows one to determine the hydrodynamic size of the particles in a suspension. Here we employ scanning electron microscopy (SEM) in order to image and further measure the mean size from a collection of dry and coated particles.

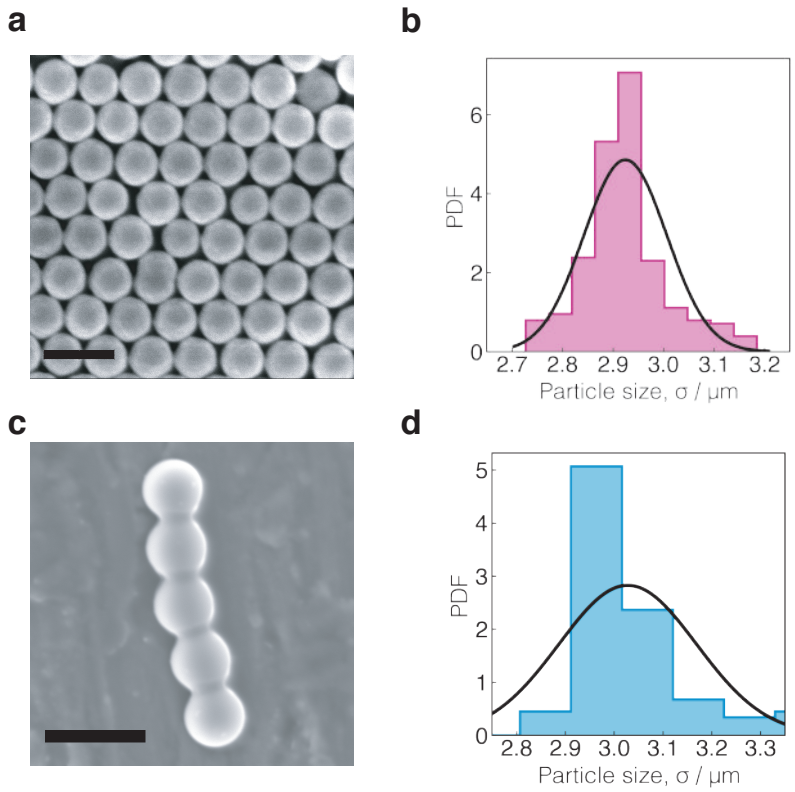

Figure 5.2: **Particle size. a.** SEM micrograph showing a monolayer of particles. Scale bar is 5 μm. **b.** Particle size distribution from measurements of SEM images. **c.** Non-spherical elongated particle made with individual PS spheres. Scale bar is 5 μm. **d.** PS sphere size distribution.

First, a small amount of the colloidal suspension in dodecane is transferred to a clean vial. Particles are sedimented via centrifugation and later redispersed in hexane. A few microliters are then deposited on a aluminum sample stub, and samples are left to dry at room temperature inside a fume hood. As the solvent evaporates, capillary forces promote the formation of two-dimensional crystalline layers of particles. Once fully dried, the samples are sputter coated with a thin platinum layer in order to enhance conductivity, as SEM relies upon the generation of secondary electrons for image reconstruction. The coated samples are then observed employing a JEOL JSM-6330F SEM microscope at a magnification that allows one to distinguish single particles for further size measurements. Images from SEM microscopy can be imported to ImageJ software,

where measurements are carried out manually over single particles. Measurements on single particles give the mean size $\langle\sigma\rangle = 2.92\,\mu$m and polydispersity,

$$s = \frac{\sqrt{\langle\sigma^2\rangle - \langle\sigma\rangle^2}}{\langle\sigma\rangle} \tag{5.1}$$

of 3.1 percent. The distribution in Fig. 5.2**a** indicates nearly monodisperse samples. The resulting particle size is of convenience for this work since particles are big enough to be resolved using conventional microscopy techniques, such as brightfield microscopy, but small enough to undergo Brownian motion in the absence of any external perturbation. We further transfer the particles to a low-conductivity medium in order to induce charging.

5.4 Sample Preparation

In order to obtain colloidal suspensions to perform experiments using the Quincke electro-rotation (Chap. 3) as a self-propulsion mechanism, particles must be transferred to a suitable media. As discussed before in Sec. 4.4.2, special additives are employed to generate charge in colloids when dispersed in low polarity liquids. Typically, surfactants are added in order to form inverse micelles that ionise and stabilise charge carriers, despite the long separation needed according the Bjerrum length λ_B [1, 318]. Compared to the charging mechanisms in polar media, i.e. water, charging in non-polar solvents is less well understood. For a system of sterically stabilised PMMA particles, it is shown via combining small-angle scattering (SANS) and electrophoretic mobility (SPOM) techniques that the presence of surfactant molecules and formation of micelles generates charge in colloidal suspensions. Typically, Aerosol-OT (AOT) surfactant is employed for this purpose, where analyses from adsorption isotherm and SANS indicate strong adsorption and packing of the AOT molecules within the stabilising layer at the particles

surface. Here we detail the preparation of charged suspensions in a low-conductivity media.

5.4.1 PMMA Dispersions in AOT/Hexadecane

We follow previous methods in the literature [2, 4, 301] in order to prepare a low-conductivity solution to disperse our previously synthesised PMMA spheres. We start from preparing a solution of AOT surfactant in hexadecane. The latter results a suitable non-polar media, given its low hygroscopicity. On the other hand, AOT surfactant consists of hygroscopic molecules that adsorb humidity from the environment. The AOT molecular structure is shown in Fig. 4.4. It consists of a polar head group and two hydrophobic tails, and above the CMC it forms reverse micelles of 1.7 nm is radius [1]. The critical micelle concentration of AOT in hexadecane is of the order of 10^{-3}mM [337], in a agreement with measurements in dodecane [320].

For a 100 mL solution at 0.15M	
AOT	Hexadecane
6.7 g	77 g

Table 5.1: Solvent and solutant quantities

Both AOT and hexadecane are obtained from Sigma-Aldrich. To prevent high concentrations of water, AOT is desiccated at 120° C in a vacuum oven during 24 hours prior dissolution in hexadecane. We weigh the AOT in a round bottom flask and adjust the liquid volume to obtain the desired concentration. The quantities needed for a 0.15M solution are detailed in Tab 5.1. We connect a flow of nitrogen to the flask in order to prevent humidity adsorption during the dissolution. At room temperature, we find AOT difficult to dissolve in the non-polar liquid. Hence, we employ an oil bath to increase the temperature to 60°C, accompanied with stirring at 100 rpm using a magnetic bar. Once fully dissolved, the AOT solution is transferred to a clean vial, previously desiccated in a

vacuum oven, and let cool at room temperature in a desiccator.

Before dispersion in the AOT solution, colloids are transferred from dodecane to hexadecane, and washed via centrifugation and redispersion for five times. For the last step, hexadecane is substituted with the AOT solution, prior to adjustments for desired volume fractions. This is achieved by a rather simple method, that consists of sedimenting particles and removing the supernatant in order to obtain a random close packing (RCP). In experiments, this value of the packing fraction ϕ_{RCP} ranges between 0.60 and 0.64 for monodisperse particles [338]. The process requires estimating the volume $V_i = \frac{m_i}{\rho_i}$ from the masses m_i and densities ρ_i of the solvent (s) and the particle (p), in other to get the volume fraction of particles,

$$\phi_p = \frac{V_p}{V_p + V_s}. \tag{5.2}$$

Assuming an initial packing fraction $\phi \equiv \phi_{\mathrm{RCP}}$, the volume of the colloids is easily deduct, and suspensions with desired packing fractions are prepared with the addition of solvent. In the present work we employ suspensions ranging from $10^{-4} - 10^{-1}$ in packing fraction. Samples are stored in individual vials inside a desiccator to prevent humidity.

5.5 Fabrication of Sampling Cells

Confinement refers to the obstruction or delimiting volume, that in this case a particle can explore. This results in significant changes in the structure, dynamics, rheology, and the phase behaviour compared to bulk properties. Thus, different behaviour arises from many contributions, such as, volume exclusion, wall-particle interactions, finite-size effects, and wetting. Controlling and understanding the properties of confined materials could lead to new routes of self-assembly [339], formation of polymorphs [340], and reaction rates [341]. For experiments and numerical simulations, typically

the confining geometries range from single walls, parallel walls, curved geometries and porous materials. Additionally, distinct confinements can be achieved with different mechanisims, starting from building physical boundaries [342], the use of external forces [315] and generation of electro-kinetic flows [286, 326]. Briefly, experiments with nearly hard spheres show layering transitions to hexagonal close packed (hcp) structures when confined in wedge cells [342]. Williams *et al.* [315] show the phase behaviour of hard disks under strong confinement using an adaptive circular boundary, yielding different phases to the ones observed in bulk [191, 193].

For active systems, the effects of confinement are similar to those mentioned above. The presence of a wall promotes the accumulation of self-propelled spheres and rods [91, 92]. This can be avoided by using a petal-like boundary that prevents aggregation against a wall, by reinjecting particles to the bulk [153, 208]. In addition, single walls and parallel surfaces of variant separation induce hydrodynamic flows that result in the formation of different structures, e.g. chains or crystals [246]. Moreover, circular geometries promote the emergence of coherent flows in bacterial suspensions [148, 343], polar microtubules [344], spinners [345] and rollers [282]. In this section we detail the fabrication of confining cells of various shapes and length scales. Our main results using different confinements are presented in Chapters 6 and 7.

To introduce strong confinement on a collection of self-propelled Quincke rollers, we follow the approach of generating electro-hydrodynamic flows by current discontinuities between two different regions [326]. These induced flows are illustrated in Fig 4.5. The result is a well controlled system, where the particles are repelled from the confining boundary, despite the absence of a physical wall. This is a convenient configuration for experiments, given that the the number density of particles is conserved. For the fabrication of these sampling cells we employ conventional lithography techniques on conductive and transparent substrates. We start by detailing the lithography process,

followed by the specifications on the geometrical confinements, and finally the assembling of the cells.

5.5.1 Electrode Patterning via Photolithography

We use conductive glass slides coated with a 370 nm layer of indium tin oxide (ITO) (ITOSOL12) provided by Solems. Slides of dimensions 2.5 mm × 5.0 mm are used to fabricate sample cells and to perform optical microscopy. The process is carried as follows,

(i) First, we clean the slides in order to remove dust and adsorbed species. The slides are placed in an acetone bath, which is sonicated for 5 minutes. The acetone is then removed, and replaced by isopropanol (IPA) before the slides get dry. Samples are sonicated for 5 min in IPA. Once the cleaning process using organic solvents is complete, the substrates are rinsed with Mili-Q water in order to remove traces. Drying is carried lout by using a nitrogen jet on the slides.

(ii) To perform the lithography process, we need to apply a photoresist layer. Typically SU-8, a negative photoresist is employed in the fabrication of microfluidic chips, where the layer is deposited on a silicon wafer. Here, we use a positive photoresist (Microposit S1818), which shows good adhesion to the ITO-coated glass slides. A layer of the Microposit resist is applied via spin coating at 2500 rpm for 45 seconds, which yields a layer thickness of about 2μm. In the case of non-uniform coating due to dust or lack of resist, Microposit is easily removed in acetone. Once coated with a uniform resist layer, the samples are transferred to a hot plate, previously set at 100°C, in order to evaporate carrying solvents and solidify the film. The coated slides are left on a hot plate for 5 minutes the ensure good adhesion.

(iii) Once a uniform film is obtained through spin coating and soft baking, exposure to UV light is needed in order to develop patterns on the film. The interaction

between the UV light and the photosensitive components of the resist promote chemical reactions which favour the removal of certain regions of the film by a photographic developer. In the case of a positive photoresist, exposed regions to a high dose of UV are removed. In order to select the regions of exposure, we design a photomask containing the desired geometries for the confinement. We use a mask aligner (MIDAS MDA-400M-6), in order to place with micrometer precision the mask with respect of our film coated slides. The UV exposure is carried out for 7 seconds with a dose of 150 mJ.

(iv) Following the exposure process, the samples undergo development in order to remove desired regions. This is achieved via submerging the slides in an aqueous-based developer that dissolves the UV chemically affected regions. For this we transfer the exposed samples to vessel containing the developer (Microsposit, MF351) for 5 seconds, followed by rinsing with Milli-Q water to stop the development. The slides are then dried using a nitrogen jet, and finally the desired features are inspected under an optical microscope. In case of feature damage, the entire process can be repeated by removing the remaining film with acetone.

5.5.2 Confining Geometries

As above, confining geometries can play a crucial role on the structural and dynamical behaviour of both passive and active systems [92, 315, 341, 342, 344]. Focusing on a system of Quincke rollers (detailed in Chapter 3), the group of Denis Bartolo has explored different confined systems, where polar [4] or whirling-like [282] behaviours emerge. One on side, one could make use of periodic designs in order to study flocking. On the order, enclosed geometries can be used to investigate the finite size effects on the system. Both approaches a readily produced employing a lithography process as described before, and ultimately depends on the design of the photomask.

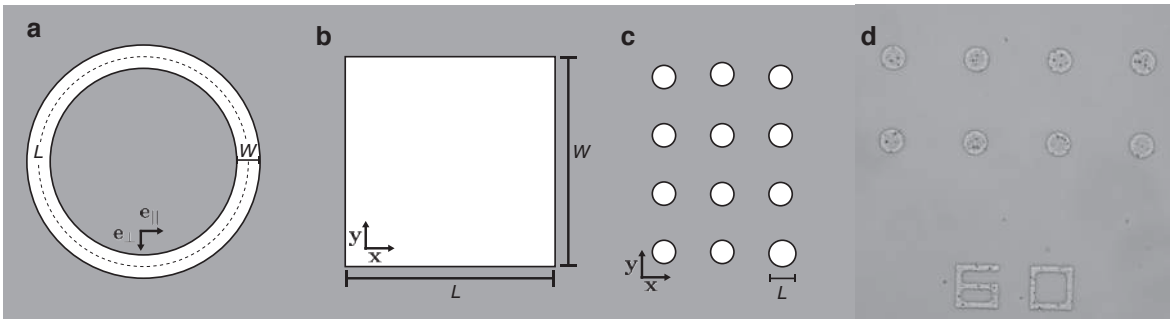

Figure 5.3: **Confining geometries. a.** Ring-like periodic track. **b.** Square geometry where finite size effects are tested. **c.** Smaller circular regions of length L = 30, 60 and 120 μm. **d.** Micrograph of a patterned electrode using photolithography.

We use the KLayout software in order to edit and visualise our geometrical designs. Alternatively, common software like Adobe AutoCAD can be used. Our final designs are sent to print on a flexible and transparent substrate by JD Photo Data. Here we provide the details on the confinement geometries we use to perform experiments with Quincke rollers. We start from the designs employed in Chapter 6, which consist of large scale experiments, followed by constrained systems in Chapter 7. As a first approach, we follow Bricard *et al.* [4], and produced a periodic geometry consisting of ring-like channel, where a flock can travel indefinitely. This geometry yields the radial constrain of the self-propelled rollers, where the direction of motion is along a curvilinear coordinate. For a ring-like channel, the relevant geometrical parameters are the channel width $W = 500\,\mu$m and length $L = 15\,$mm. On the other hand, we chose an enclosed geometry to investigate a finite size system. The easiest realisation of this is a square region of length $L = 5\,$mm. Interestingly, particle aggregation near a wall [91, 92] is not observed for any of the geometries.

Motivated by a system of hard discs confined to a circular adaptive boundary set by optically trapped particles [315, 346], we produce smaller confinement regions. Previous works show the emergent vortical motion of self-propelled [148, 282, 345] and driven units [344] constrained in this geometry. Employing the same technique to produce large

scale confinement, we fabricate circular regions of length $30\mu\text{m} \leq L \leq 120\mu\text{m}$. Images of the confining regions are shown in Fig. 5.3.

5.5.3 Cell Assembling

Following the patterning of the ITO-coated slides, the cell assembling proceeds as follows,

(i) Prior the lithography process, small orifices are created at the sides of the glass slides in order to inject the colloidal suspensions later. Patterning via lithography is then carried out.

(ii) Conductive glass slides lacking of patterns are used as counter electrodes. Prior the assembling,the slides undergo the same cleaning procedure with organic solvents.

(iii) Single layers of double sided tape of thickness $100\,\mu$m are adhered on the edges of the counter electrode.

(iv) The patterned electrode is then aligned with respect of the counter electrode, in such way that the features are positioned at the center of the cell with leaving enough space exposed for the electric connections. The two electrodes are pressed using spring clamps to ensure good adhesion.

(v) Electric connections to the ITO-coated slides are made with using conductive epoxy glue (CW2400, Chemtronics) and conductive copper tape adhered to the slides. Wires are glued to the type using the conductive epoxy to ensure electric contact.

(vi) Finally, laser cut perspex cubes are glued on top of the orifices on the patterned electrode. This to connect the polytetrafluoroethylene (PTFE) tubes used for injecting the suspension into the cell

The previous process yields cells which are of dimensions equal to the original size of the slides, illustrated in Fig. 5.4. Alternatively, slides of 5 mm × 5 mm can be cut to

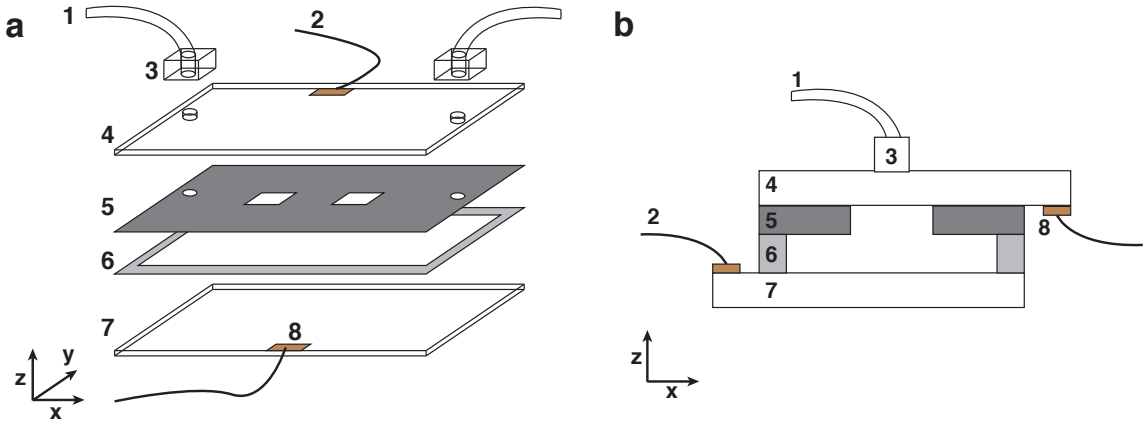

1. PTFE tubing
2. Conductive wire
3. Perspex cube
4. Patterned electrode
5. Photoresist layer
6. Double sided tape
7. Counter electrode
8. Copper tape

Figure 5.4: **Sample cell.a.** Schematic representation of the sample cell assembly. **b.** Cross-sectional representation of an assembled cell. All components in **a** and **b** are enumerated and labeled below. Figures not drawn in real scale.

produce smaller cells, in which to avoid the PTFE connections. In this case, colloidal suspensions can be loaded with the use of a micropipette near the edge of the cell, which is filled due to capillarity. Once the colloidal samples are loaded, cells are closed with micro tubing clamps or sealed with Norland 81 optical adhesive.

5.6 Experimental Mounting and Microscopy

To perform experiments using Quincke rollers, sampling cells containing colloidal suspensions are prepared in advance. Here, we describe the experimental set up and the microscopy used to image the colloids, which are later analysed employing particle tracking algorithms [347].

5.6.1 Electric Field Application

As described in Chapter 3, the Quincke electro-rotation of particles relies upon the application of a field amplitude E exceeding a threshold E_Q. This requires the use of large potentials, of the order of hundred of volts. Prior imaging the colloids, we mount the sampling cells and connect to external devices for the application of the electric field. Here, we use bench power supply (Elektro Automatik PS-2384-05B), which provides potentials ranging between $0-84$ volts. The advantage of this equipment is that it provides the option of being controlled remotely with software (Easy PS2000). We later magnify the potential from the power supply using voltage amplifier (Trek 606E-6), which yields a peak voltage of four orders of magnitude. To trigger self-propulsion due to Quincke rotation, the potentials applied here range between $80-300$ volts. Therefore, we make use of simple potential divider device in order to fractionate the potential from the power supply prior amplification. All the equipment is mounted on an optical table, and for safety reasons we prevent contact with the sample while running experiments. For this, we fabricate insulating boxes made of transparent perspex, that contain the sampling cells and allow easy connection with the voltage amplifier. Once connected, a DC electric field of different amplitudes is applied between the electrodes of the sampling cell.

5.6.2 Microscopy

Different microscopy techniques are used in order to characterise colloidal samples. For instance, SEM allows direct visualisation and measurement in order to obtain a size distribution. Real-space and time studies of colloidal suspensions are performed with using optical, fluorescent or laser microscopy. In this case, confocal laser scanning microscopy (CLSM) allows three dimensional scanning of samples, by locally exciting dye molecules in the sample and excluding the out-of-focus signal emitted. As mentioned

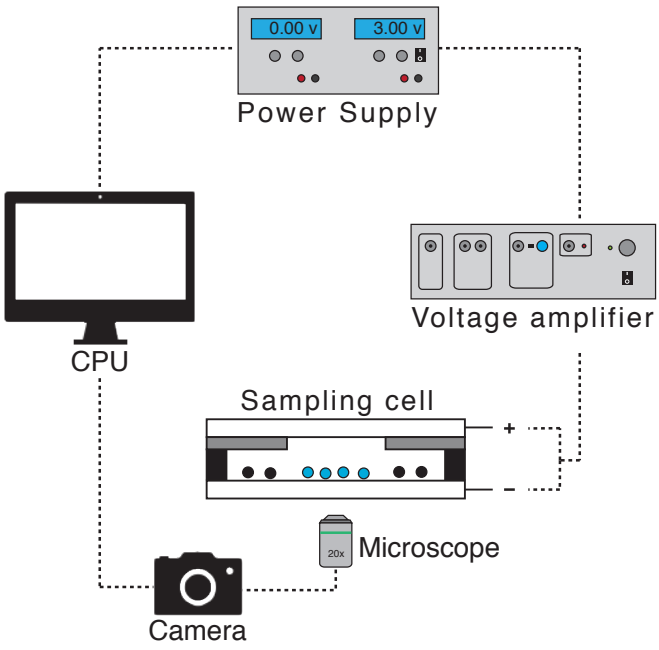

Figure 5.5: Schematic representation of the experimental set up, including all the components for microscopy and E field application. The use of the power supply (details in text) allows one to remotely control the field amplitude.

in Chapter 2, must of the experimental realisations of active systems consist of units performing self-propulsion in two dimensions, that permits the use of simpler microscopy techniques.

Conventional optical microscopy is employed in order to image our colloids. From our PMMA synthesis, we obtain spherical particles of size $\langle\sigma\rangle = 2.92\,\mu$m, and non-spherical particles which smallest unit is of $\langle\sigma\rangle = 3\,\mu$m. In both cases, particles are small enough to undergo Brownian motion, but large enough so that we can easily identify individual particles. Here, we employ brightfield microscopy (Leica DMI 3000B), and magnifications between 5-20 X allows to image the local and large scale behaviours. In addition to brightfield, fluorescent microscopy can be performed as PMMA particles are rhodamine-labeled and PS spheres are dyed with fluorescein. The confined colloids are recorded in order to investigate the spatio-temporal behaviour upon the field application. For

this, we use a monochromatic high speed camera (Basler ACE), which allows to record movies up to 1000 fps, depending on the resolution. We later show the ballistic motion in Quincke rollers, which is in agreement with the description of of various self-propelled particles [27] (see Sec. 2.2.2). Therefore, we find that windows of 1024px × 1024px yield a recording speed of 354 fps, enough to perform particle resolved studies [347]. For the smaller confined systems, windows of less resolution permit to record with speeds up to 900 fps. A full schematic representation of the experimental mounting is shown in Fig. 5.5.

5.7 Particle Resolved Studies

In order to perform quantitative analysis from experimentally recorded samples, particle tracking by means of identifying individual particles in space and time is required. Going back to the work of Perrin [348], manual measurements on sedimenting colloids first established the thermal diffusion at equilibrium. Today, the use of computer algorithms allows the identification of many objects, from single bacteria cells to dust particles in a plasma [82]. In the same way, these computational routines can be of use in order to track colloids and study processes of interest, such as crystallisation, vitrification, sedimentation and emulsion formation.

Conventional algorithms were developed by Crocker and Grier [347], where the location of particles is extracted from images by means of position coordinates in time. Hence, the linking of the the time dependent position allows to reconstruct particle trajectories and study their behaviour, i.e. random walks. The process consists of image processing in order to obtain well defined intensity peaks that account for particle positions with pixel resolution. Subpixel resolution is possible when analysing the centre of mass of surrounding pixels around a local maxima. In addition, different experimental techniques involve the use of dispersing media that optically matches the

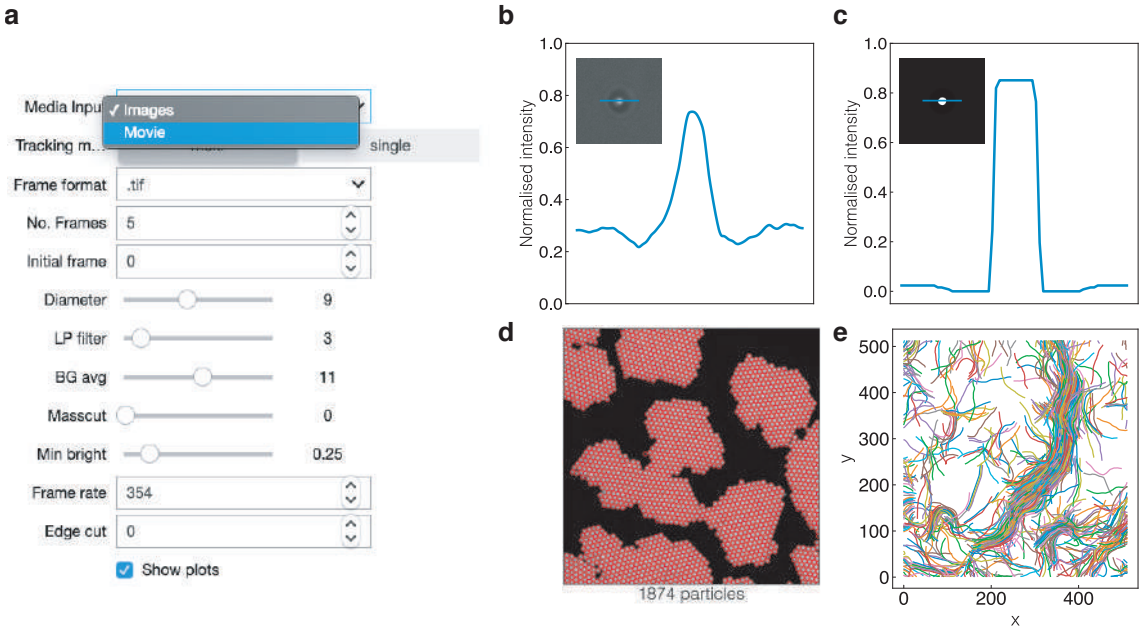

Figure 5.6: **Particle resolved studies. a.** Interactive menu where parameters to perform the particle identification are selected by the user. **b.** Intensity profile before and **c.** after image processing. **d.** Identified particles from an acquired micrograph. Particles are circled in red after discrimination. **e.** Individual trajectories are reconstructed from the time dependent locations.

refractive index of the colloidal particles [231]. Two and three dimensional positions can be investigated with the use of fluorescent particles under confocal and stimulated emission depletion (STED) microscopy. Nonetheless, in most cases this requires samples with sufficient size to be detected and low polydispersity. Recent developments provide solutions to samples of particles with different size distributions [349]. This is important for systems where polydispersity plays a role in the forming structure, e.g. a colloidal glass [350]. Alternatively, for particles of the order of nanometers or bacterial suspensions, differential dynamic microscopy (DDM) can be employed to investigate the dynamics, whether particles can be resolved individually or not [351].

In this work we make use of typical algorithms that resolve individual particle locations. For images acquired though a microscopy technique, each pixel in the array

posses an intensity value between 0 being black and 255 white. In order to identify local maxima, images are processed by means of convolution with a Gaussian kernel of a certain width. This promotes the refinement of intensity profiles across colloids and removes noise from non-uniform contrast and illumination (see Fig. 5.6**b**,**c**). For identifying real particles, first the candidates must be discriminated, and the positions are refined with subpixel accuracy later. The time dependent distribution of the particle locations are then obtained with,

$$P(\mathbf{r},t) = \sum_{i}^{N} \delta(\mathbf{r} - \mathbf{r}_i(t)) \tag{5.3}$$

where $\mathbf{r}(t)$ represents the position of the ith particle at time t, and the process run for all N particles. Having the probability $P(\mathbf{r},t)$, the motion of single particles can be obtained frame by frame. Here we use a `Python` implemented version of a previous `IDL` version [347]. This involves using different libraries, previously developed for `Python`, such as `NumPy` and `SciPy`, and in some cases the development of own algorithms. The overall process of tracking is given as follows,

(i) Single frames are loaded, and image processing is performed prior particle identification. We apply image convolution in order to reduce noise obtained from non-uniform sample illumination or contrast.

(ii) After processing, a characteristic lengthscale is chosen, which accounts for the particle size σ in pixel units. A bright pixel is then considered as a candidate for a particle if any other pixel is found within a radial profile set by such lengthscale.

(iii) In order to filter real particles from other candidates, it is assumed that particles about the same size exhibit similar brightness after convolution. Hence, a brightness threshold value can be selected, where candidates of intensity below this value are neglected. At this instance, a preliminary position of the particles is obtained.

(iv) To obtain subpixel accuracy on the particle location, the intensity of neighbour pixels is analysed. A brightness-weighted centroid is given by the brightest pixel and by intensity values in the x and y directions with δx and δy respectively. Assuming that (x_0, y_0) is the location of the brightest pixel, the refined location of the particle is given by $(x_0 + \delta x, y_0 + \delta y)$. The analysis of the intensities within the centroid is given by,

$$\mathbf{r} = \frac{\sum_i I_i \mathbf{r}_i^p}{\sum_i I_i}, \tag{5.4}$$

where $\mathbf{r}_i^p$ is the location of pixel i, and I_i is the intensity [82, 347]. Running the algorithm with the adequate parameters allows the identification of all particles in one frame.

(v) In order to reconstruct the trajectories, a sequence of frames of which particle coordinates can be extracted are needed. For two consecutive images, a particle undergoing Brownian motion has a probability of displacing that follows

$$P(\delta|\tau) = \frac{1}{4\pi D_t \tau} \exp\left(-\frac{\delta^2}{4D_t\tau}\right) \tag{5.5}$$

where δ is the distance of displacement in a time interval τ, with diffusion D_t. The same probability runs over all N particles in order to recover all the trajectories. Importantly, $P(\delta|\tau)$ maximises for the case of non-interacting particles, where the Brownian time τ_B is given by tens of seconds. With the particles subjected to Brownian motion, this condition can be addressed within a finite packing fraction. For particles diffusing ballistically, the time interval τ must be sufficiently small to recover the trajectories.

The `Python` version of the conventional tracking algorithms allows us to resolve a collection of active particles in space and time. With the aim of an interactive use, also for new users, we developed an interface of these algorithms using `Jupyter Notebooks`. This interface allows loading of images from singles frames and recorded movies, and all the parameters needed for the tracking are given as an interactive menu (see Fig. 5.6**a**). Additionally, these `Jupyter Notebooks` compute relevant structural and dynamical order parameters we use in Chapters 6,7 and 8.

CHAPTER 6

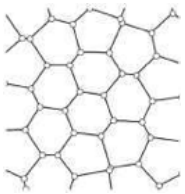

PHASE BEHAVIOUR IN ATTRACTIVE ROLLERS

"I'm nothing but a bloody amoeba"

PRINCE PHILIP, DUKE OF EDINBURGH

Motivated by the interesting collective phenomena introduced in Sec. 2.3 we perform experiments and numerical simulations of an active matter model. Our system consists of a collection of colloidal particles performing spontaneous self-propulsion due to Quincke electro-rotation (Sec. 3.1). Previous studies using this model show the emergence of collective motion, with the system undergoing a phase transition from disorder to a state of polar order with the increase of the number of rollers [4, 282, 283]. In this work, we also focus on the contribution from the applied field E, that on one a side affects the roller velocity v_0 [310], and on the other promotes different interactions. The hallmark of this work is the competition between passive and active interactions acting simultaneously on the rollers.

In the present chapter we show our main findings from experimental and numerical results using Quincke rollers. First we describe the nature of our colloidal model in the

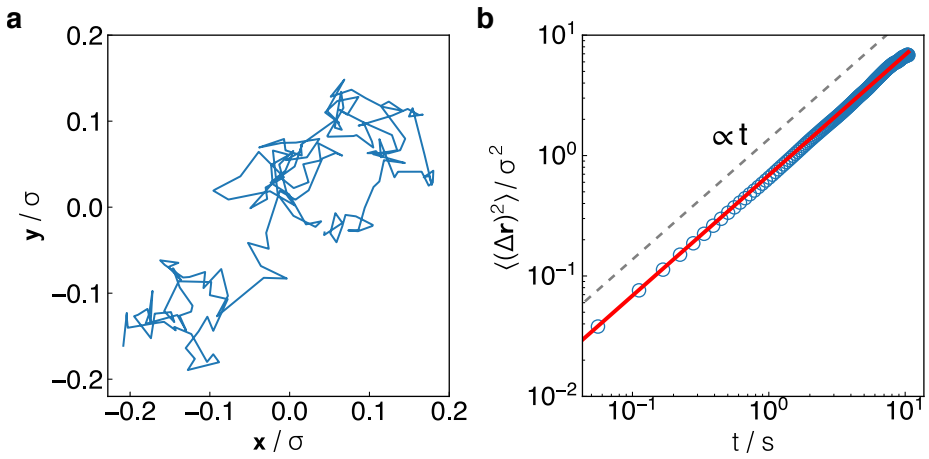

Figure 6.1: **Brownian Motion. a.** Isolated particle performing Brownian motion from collision with the solvent. **b.** Mean squared displacement for Brownian particles. Red line is a fitting to the data, and dashed line is a reference $\propto t$.

absence of an external field. Then we proceed with the characterisation of structure, as particles exhibit aggregation from induced passive interactions. By increasing the strength of applied electric field E, particles spontaneously self-propel due to Quincke rotation, where we show that the increasing density results in the onset of collective motion. We build the phase diagram, and characterise the structural and dynamical behaviour of the different phases at different values of the control parameters.

6.1 Motion in Absence of External Fields

Prior to field application to trigger Quincke electro-rotation of particles, the thermal behaviour of our colloids is determined. We use a suspension of synthesised PMMA sterically stabilised spheres (Sec. 5.4.1), in a dilute regime with $\phi \approx 10^{-3}$ in order to neglect interactions and collisions between colloids. A few microliters are injected in a simple sampling cell made with glass coverslips. Particles sediment and form a quasi two-dimensional layer due to density mismatch between the particle and the medium.

In the absence of self-propulsion, the particles behave as Brownian disks, and follow

the dynamics described in Sec. 2.2.1. We measure the particle motion from collisions with the solvent by analysing time sequences of individual colloids. In two dimensions, an isolated particle diffuses with a mean squared displacement $\langle(\Delta r)^2\rangle = 4D_t t$ (MSD), where D_t is the translational diffusion coefficient. For a Brownian particle, the characteristic timescale τ_B is the time that takes a particle in displace a distance equal to its own radius due to Brownian motion,

$$\tau_B = \frac{\pi\eta\sigma^3}{8k_BT}, \tag{6.1}$$

where η is the solvent viscosity and σ the particle size. Also, the origin of the formation of a quasi two-dimensional layer is related to the gravitational length,

$$l_g = \frac{6k_BT}{\pi\Delta\rho g\sigma^3}, \tag{6.2}$$

with the particle-solvent density mismatch represented by $\Delta\rho$. This gravitational length l_g is the height which corresponds to a change in gravitational potential energy equivalent to the thermal energy k_BT.

For PMMA particles of size $\sigma = 2.9\,\mu$m, dispersed in hexadecane we obtain diffusive motion from MSD, with $\langle(\Delta r)^2\rangle \propto t$, with translational diffusion $D_t \approx 0.02\,\mu^2 \mathrm{m}\,s^{-1}$, which is close to the value given by the Stokes-Einstein relation. Figure. 6.1 illustrates a single trajectory of a particle undergoing Brownian motion, and the resulting MSD for a collection of isolated spheres. The empirical value of τ_B is ≈ 9 s, which is comparable to the 6.5 s obtained from Eq. 6.1. We use τ_B as a reference for the subsequent timescales determined in this chapter. Regarding the gravitational length, we estimate $l_g \approx 80\,$nm using Eq. 6.2. Hence, particles sediment quickly, and form a quasi two-dimensional array near the bottom slide.

6.2 Determination of the Critical Field Amplitude

Spontaneous particle rotation is observed for dielectric particles dispersed in low conductive media. This mechanism is known as Quincke electro-rotation, discussed in detail in Chap. 3. The origin of this phenomena occurs due to the surface charge distribution and spontaneous charge symmetry breaking, controlled by the field amplitude E. Hence, E must exceed a threshold value E_Q, at which any infinitesimal perturbation of the dipole moment $\mathbf{P}$ on the particle produces an electric torque $\mathbf{T}^{\mathrm{E}}$.

As previously discussed in Sec. 6.1, the density mismatch between the colloids and the medium causes sedimentation and the formation of a quasi two-dimensional layer. Near the electrode, the electro-rotation results in non-slip motion as the friction coefficients depend logarithmically on the separation between the sphere and the surface in the lubrication regime [303, 304]. Particle self-propulsion, with a net velocity v_0, arises from the coupling between rotation and translation (see Sec. 3.2). Hence, the field amplitude at which directed motion results is given by,

$$E_Q = \left[4\pi\epsilon_l R^3(\mathscr{P}^0 - \mathscr{P}^\infty)\mu_r\tau\right]^{-\frac{1}{2}}, \tag{6.3}$$

where $\mathscr{P}^0 = \frac{s_p - s_l}{s_p + 2s_l}$ and $\mathscr{P}^\infty = \frac{\epsilon_p - \epsilon_l}{\epsilon_p + 2\epsilon_l}$ are the polarisability factors, which depend on the dielectric ϵ_i and conductivity s_i of the particle (p) and the liquid (l). μ_r is rotational frictional drag coefficient for a sphere of radius $R = \frac{\sigma}{2}$. τ corresponds to the Maxwell-Wagner relaxation time, given by $\tau = \frac{\epsilon_p + 2\epsilon_l}{s_p + 2s_l}$. For a dispersion of PMMA spheres in hexadecane, the relevant material properties are listed in Tab. 6.1 considering anhydrous conditions [2]. Using Eq. 6.3 and the values in Tab. 6.1 we obtain $E_Q = 0.7\,V\,\mu\mathrm{m}^{-1}$, which is in good agreement with the empirical value from experiments, $E_Q \approx 0.8\,V\,\mu\mathrm{m}^{-1}$. For field amplitudes higher than E_Q the sedimented colloids exhibit directed motion.

Material	Density ρ (g cm^{-3})	Dielectric constant	Conductivity s (S m^{-1})	Viscosity η (Pa s^{-1})
PMMA	1.18	$2.6\epsilon_0$	10^{-17}	NA
Hexadecane	0.77	$2.0\epsilon_0$	10^{-8}	4.3×10^{-3}

Table 6.1: Material properties for a colloidal suspension of PMMA spheres in hexadecane [1, 2]

6.3 Mapping of the Particle Velocities to Péclet Numbers

In our experiments the main control parameter is the applied field strength E. For amplitudes $E \geq E_Q$ particle motion results with velocity v_0 dependent on E. In addition, we use numerical simulations in which a wide range of area fraction and activity forces $\mathbf{F}^{\mathrm{a}}$ can be accessed. With the aim of gaining quantitative comparison, we map our experiments to the numerical results by means of an active Péclet number,

$$\mathrm{Pe} = \frac{3v_0\tau_r}{\sigma}. \tag{6.4}$$

Here, $\tau_r = D_r^{-1}$ is the characteristic timescale for the rotational diffusion. Pe quantifies the contribution of translational and rotational diffusion to the directed motion from active forces. In simulations, the contribution from the magnitude of the active force $\mathbf{F}^{\mathrm{a}}$ is straightforwardly implemented in the roller equations of motion (see Appendix A for more details of the numerical simulations).

To quantify Pe numbers in experiments, we use a dilute suspension at area fraction $\phi \approx 10^{-3}$, to avoid the contributions from interactions and collisions with other rollers. Being subjected to confinement, the escape of rollers is suppressed as the induced EHD flow (Fig. 4.5) reorients the rollers towards the central region of the confining geometry. Hence, we analyse rollers solely within central sections of our sampling cell. We explore field strengths with range $E \in [1,3]E_Q$, where we find field-dependent velocities. To

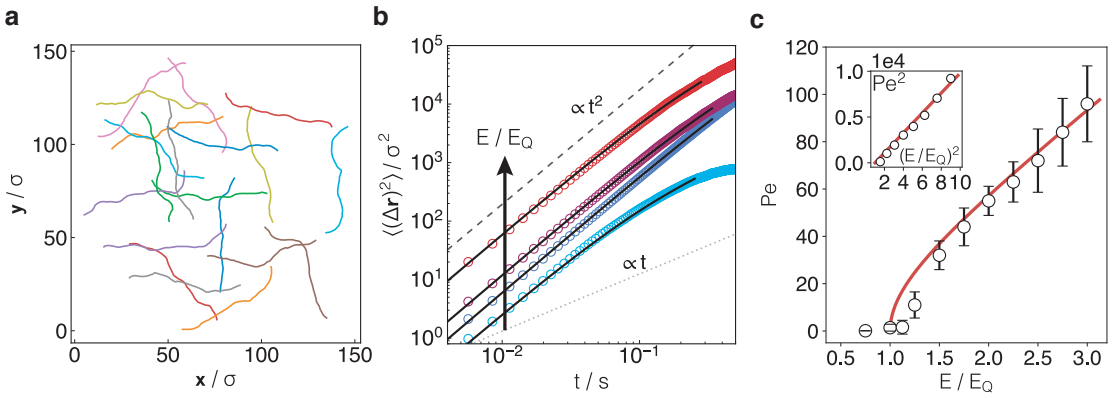

Figure 6.2: **Mapping to Péclet numbers. a.** Roller trajectories at $E = 3E_Q$. **b.** Mean squared displacement for rollers at different field strengths. Solid lines over symbols are fittings from Eq. 6.5. Dashed and dotted lines are proportional to t^2 and t respectively, and arrow indicates the increase of E/E_Q. **c.** Estimation of Péclet numbers from Eq. 6.4. Inset shows the linear dependency when squaring Pe and the normalised amplitudes. Symbols are experimental measurements, and solid lines are $\propto \frac{\sigma}{2\tau}\sqrt{(E/E_Q)^2 - 1}$, with $\tau \approx 1$ms.

extract the necessary parameters to estimate the dimensionless Pe numbers we compute the roller mean square displacement [27], and fit the data with the following expression,

$$\langle \Delta r^2(t) \rangle = 4D_t t + \frac{v_0^2 \tau_r^2}{3}\left[\frac{2t}{\tau_r} + \exp\left(\frac{-2t}{\tau_r}\right) - 1\right], \tag{6.5}$$

where D_t is previously estimated in Sec. 6.1. For a collection of Quincke rollers, we take the mean value of the velocity distribution to calculate the corresponding Pe for the applied magnitude of E. Fig. 6.2**a** are particle trajectories showing directed motion. Mean squared displacements are shown in Fig. 6.2**b**, with increasing electric strengths, where the solid lines are a theoretical fit using Eq. 6.5. Dashed and dotted lines are $\propto t^2$ and $\propto t$ respectively, where the crossover on the MSD indicates the change in motion from ballistic to diffusive. Using Eq. 6.4, the dimensionless Pe numbers are estimated for several amplitudes of E, as shown in Fig. 6.2**c**.

With the aim of establishing a quantitative comparison, Péclet values ranging as $\mathrm{Pe} \in [0, 150]$ are explored in simulations. Importantly, the threshold value set the field

amplitude at which Quincke rotation begins, with $E \geq E_Q$. For lower field strengths, $E \ll E_Q$, the small values on Pe ~ 0 weakly depend on E, and the behaviour is diffusive at long timescales.

6.4 Induced Particle Aggregation

Having characterised the passive dynamics of our colloids, we now focus on the contribution from the application of a DC field E. To observe the spontaneous self-propulsion of colloids due to Quincke rotation, the amplitude of the field E must overcome a threshold value E_Q. Below this value, E is insufficient and the colloids behave as Brownian disks. Moreover, we investigate the role of the density using colloidal dispersions with area fractions ranging from $\phi \in [10^{-3}, 10^{-1}]$. The suspensions are confined using square geometries, as detailed in Sec. 5.5.2.

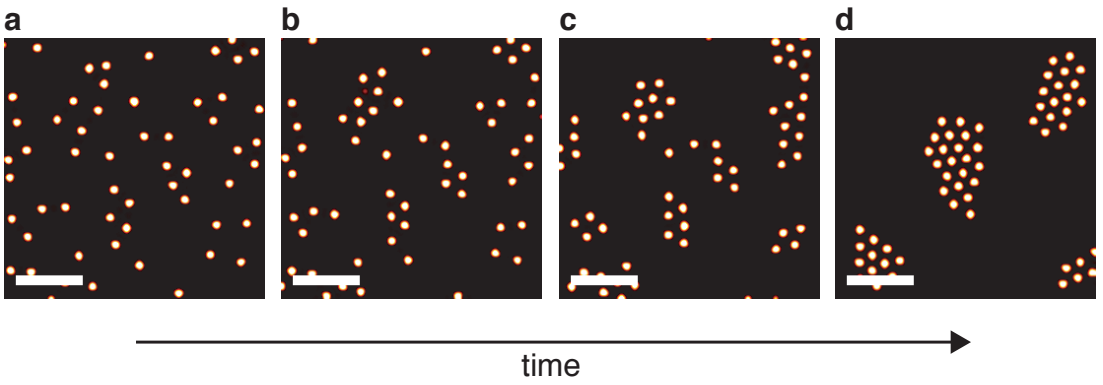

Figure 6.3: **Induced aggregation. a.** Initial particle positions in the absence of E. **b.** Application of E at low amplitude. $t = 8s$. **c.** $t = 30s$. **d.** Crystallites form after $t = 130s$. Scale bars represent $10\,\mu$m.

Crystallisation develops from particle condensation at low field strength, e.g. $E = 0.5\,V\,\mu\text{m}^{-1}$. We find this amplitude to be too low to observe Quincke rotation, i.e $E < E_Q$. As we previously discussed in Sec. 4.5, electro-hydrodydamic (EHD) flows are induced by the application of an external field. In our experiments, colloids act as a dielectric regions

that perturbs the charge distribution of an equipotential surface. These perturbations result in the tangential flow of ions, generating an electro-osmotic flow. Figure 4.5 schematically represents the generated EHD flow, which is of toroidal shape. As a result, lateral motion occurs as a centripetal drag force $\mathbf{F}^{\mathrm{H}}$ acts within the layer of colloids, and balances the repulsion from dipole-dipole interactions along $\hat{\mathbf{z}}$.

For monodisperse samples, the transverse motion yields the formation of clusters, where the aggregation time scales with E. For field amplitudes $E << E_Q$ the aggregation rate is of the order of 10^2 s, where the increase in E facilitates the condensation since the velocity U of the EHD flow is proportional to the field amplitude. Figure 6.3 shows a time sequence of the condensation process. The removal of the field makes the aggregation reversible, which shows the repulsive nature of the colloids. With an area fraction of $\phi \simeq 10^{-2}$, we find that the condensation forms hexagonal crystallites. Importantly, for lower area fractions we expect the aggregation rate to be much smaller and not comparable to the timescales of particles performing active motion. Having formed ordered aggregates at low field strengths, $E < E_Q$, we first characterise the local structure.

6.4.1 Bond Orientational Order Parameter

To quantify the local structure order of the formed aggregates we use the two-dimensional hexagonal bond orientational order parameter, $\psi_6 = \frac{1}{N}\sum_j^N |\psi_6^j|$, to characterise the local order of every j particle,

$$\psi_6^j \equiv \frac{1}{Z_j}\sum_{k=1}^{Z_j} \exp\left(i6\theta_k^j\right), \tag{6.6}$$

where Z_j is the co-ordination number of particle j, e.g. the number of neighbours, obtained from a Voronoi tessellation. k labels each neighbour, and θ_k^j is the bond angle made between particles j and k with respect of a reference axis $\hat{\mathbf{x}}$. The vertical bars on ψ_6^j denote the magnitude of the complex exponential. Importantly, the hexagonal order

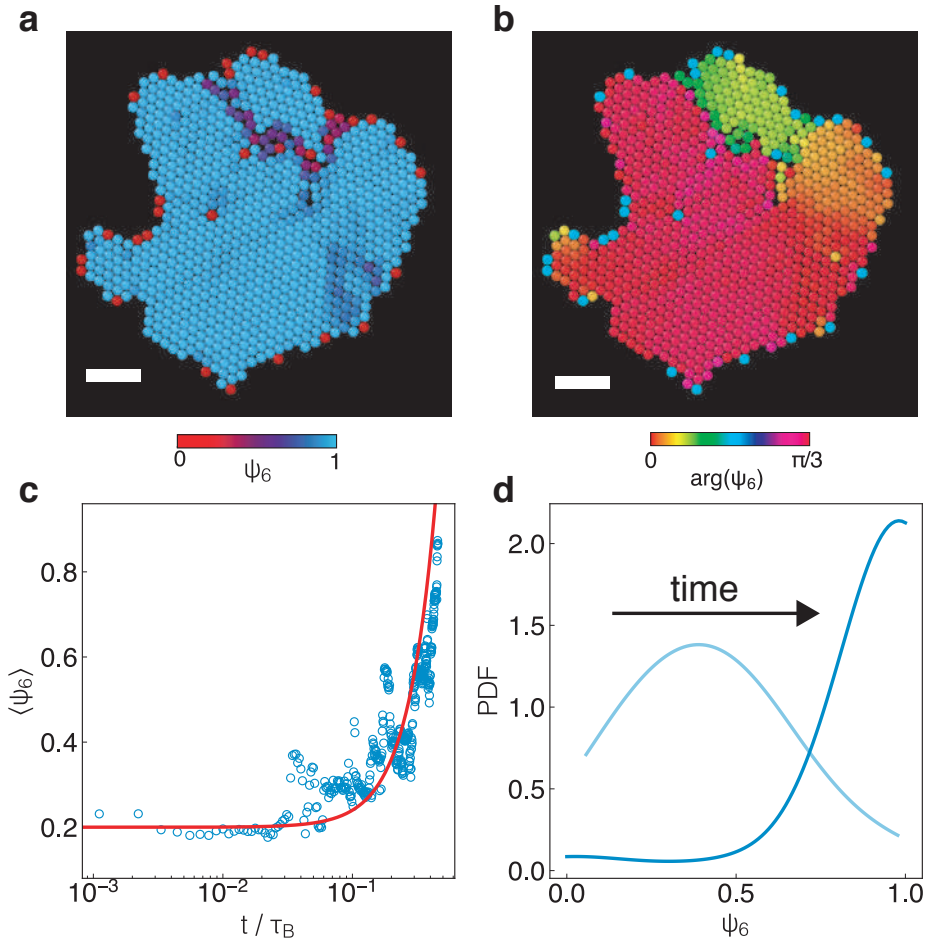

Figure 6.4: **Crystallisation. a.** Aggregation at low field strengths, $E < E_Q$. Colourbar indicates the local order characterised with ψ_6. **b.** Argument of the local ψ_6. Scale bars is 20 μm. **c.** Plot of the increase of ψ_6 in time. The red line is a guide to the eye, given by t^2. **d.** Evolution of the distribution on the hexagonal order as crystallites form.

differs from the hexatic order, where the modulus is taken as $|\langle\psi_6\rangle|$. For the hexagonal order, $\langle\psi_6\rangle = 1$ represents perfect hexagonal ordering, whereas $\langle\psi_6\rangle = 0$ is complete disorder, and $\langle ...\rangle$ indicates time average.

For colloids confined to a finite size geometry, we observe crystallite formation within the confinement region solely, as E is suppressed elsewhere. Figure 6.4**a** shows one of the crystallites obtained at $E = 0.5V\,\mu\text{m}^{-1}$. Colours in the particles indicate the local hexagonal order $|\psi_6^j|$, where light blue indicates $|\psi_6^j| \approx 1$ and red $|\psi_6^j| \approx 0$. Perfect ordering

hardly results due to the mismatch in local orientational of different domains and boundary imperfections, as shown by the argument of the local hexagonal order shown in Fig. 6.4**b**. We map the evolution of the hexagonal order for a set of forming crystallites. Figure 6.4**c** shows the increase of the global ψ_6 in time, as the particles experience lateral motion due to EHD attraction. In addition, 6.4d shows the distribution of the hexagonal order for the forming structure at $t = 0.05\tau_B$ (light blue distribution), and $t = 0.5\tau_B$ (dark blue line). From the distributions, the range of order in forming crystallites is from low values, i.e. $\psi_6 \approx 0$, to high order $\psi_6 \approx 1$. Once formed, the structures exhibit high order with $\psi_6 > 0.6$. For crystallites reaching a maximum finite size, their structure retains high order with a constant amplitude of E, thus, the high hexagonal order results from a freezing process into static structures. The removal of E promotes melting, thus the decrease on ψ_6. This is in good agreement with previous observations with the assembly of colloidal aggregates near patterned electrodes [322, 323], and to the melting-annealing process of RCP and hexagonal structures [331]. There is also the case where for a mixture of active and passive particles, self-propulsion promotes the fast annealing of crystalline structures [352].

In order to distinguish the various structures and their variations, we use the orientational order parameter ψ_6 as we map the system with varying the electric strength E and area fraction ϕ. Using numerical simulations and quantitative particle resolved studies we extract orientational and dynamical correlations, discussed in the forthcoming subsections.

6.5 Phase Transitions

Using the roller area fraction ϕ and the electric strength E as control parameters we investigate the phase behaviour of Quincke rollers. To map with numerical results, we estimate *activity* values by means of dimensionless Péclet numbers. Here we explore

area fractions $\phi \in [10^{-3}, 10^{-1}]$ and activity values $\mathrm{Pe} \in [\approx 0, 100]$. In the previous section, we show that with sufficient roller fraction, e.g. $\phi \simeq 10^{-2}$, the lateral aggregation from induced EHD flows result in crystallisation of isolated domains with $E < E_Q$ ($\mathrm{Pe} \approx 0$). For isolated colloids at lower ϕ, Quincke spontaneous rotation emerges on increasing E, with the roller speed v_0 controlled by the field amplitude.

First demonstrated by Bricard *et al.* [4], Quincke rollers exhibit an order-disorder phase transition with the increase of the roller population ϕ. As ϕ exceeds a critical roller fraction, roller-roller alignment interactions promote polar order within the liquid state formed by rollers (see also Sec. 3.3). We compare a periodic confining geometry similar to that in Ref. [4], against a square confinement, where we foresee the influence of finite size effects over the different phases. We then exploit the activity as main control parameter, and show a set of transitions from passive crystallites to a state of inhomogeneous polar order, akin to the description in Sec. 2.4.1.

6.5.1 Activity-induced Phase Transitions

In contrast to the periodicity of ring-like geometries, we use Quincke rollers confined to a square arena. For a roller fraction $\phi \geq 10^{-1}$, with the application of a field E, with magnitude below E_Q, aggregates form. This is a consequence of the lateral attraction due to the electro-osmotic flow which depends on E. As shown in the previous Sec. 6.4, the resulting clusters are of high structural order, characterised by the orientational order parameter ψ_6. The increase of the field magnitude then triggers the Quincke electro-rotation, with $E \geq E_Q$. For small populations, i.e. $\phi < 10^{-2}$, a gas state forms with the roller motion following a random walk.

With sufficient roller fraction, we observe crystallite motility upon increasing the activity $\mathrm{Pe} \approx 2$, $E \equiv E_Q$. This crystallite motility is similar to the one in Quincke rollers performing run-and-tumble dynamics [312]. The motility in the crystallites is likely

to arise from a complex interplay between interactions, where passive and active interactions are in competition [353]. On one side, the attraction from hydrodynamics and in-plane dipole-dipole coupling [310] pull colloids one to another. However, the interactions from dipole coupling and the far-field hydrodynamic can become repulsive [4]. With Quincke rotation acting on every sphere, the aggregates become dynamical structures. We term this an *amoeba* phase, since the motility leads the aggregates to constantly reshape, in a fashion reminiscent of the motion of amoebae. Figure. 6.5**a** illustrates a short time sequence of an amoebae aggregate. Rollers within the aggregates exhibit collective translation, which yields net motion and cluster rotation. For a group of individual aggregates, we follow the evolution of the orientational order, characterised by ψ_6, which shows decrease and recovery events (Fig. 6.5**b** and Supplementary Movie 1 in Appendix C.1.1).

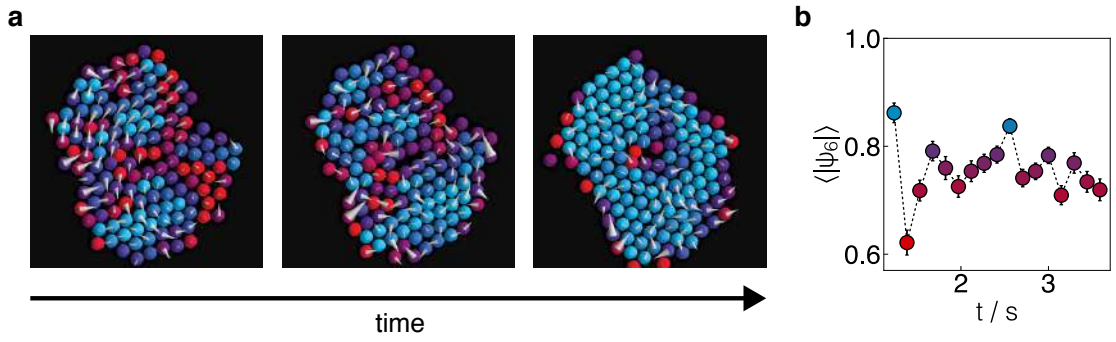

Figure 6.5: **Amoebae aggregate. a.** Time sequence for a small amoebae cluster. Colours on particles indicate the local hexagonal order, ψ_6 (see Sec. 6.4.1 for details), and arrows indicate instantaneous velocities. Pe = 2, $E \equiv E_Q$. **b.** Mean hexagonal order parameter in time for a set of amoebae aggregates similar to **a**.

For increasing activity, a transition from initially steady aggregates to travelling amoebae crystallites occurs. [354]. In addition, amoebae aggregates show coalescence and splitting dynamics, as in bacterial colonies [10], chiral spinners [355], and to the interrupted phase separation due to alignment mismatch [252]. With the activity acting on individual rollers, the amoebae aggregates are also of similarity to the mesophases

in passive systems, i.e. mermaid particle systems [356]. Here, the competition between repulsive and alignment interactions leads to the characteristic collective dynamics of the amoebae aggregates. The activity acts as a long-ranged repulsion that stabilises these structures in the presence of alignment forces. On increasing the activity, the contribution from alignment increases and leads to the breaking of the active crystallites to a state of increasing polar order [357].

Beyond the random walk dynamics obtained with small populations, an inhomogeneous phase results with the increasing area fraction, i.e $\phi \geq 4 \times 10^{-2}$. Here, an emergent roller fraction exhibits longer persistent motion, with the rest of the population undergoing a random walk. This refers to the inhomogeneous phase observed in polar matter, mentioned in Sec. 2.4.1. With alignment interactions acting on a collection of rollers, polar bands form and travel across a disordered gas. We find propagating bands akin to the slender bands in driven filaments [154]. Hence, this inhomogeneous state corresponds to the onset of collective motion as in Vicsek-like models (see Sec. 2.3.1) [17, 18], with the bands forming a liquid fraction [132]. Two important characteristics regarding the inhomogeneous state: (*i*) the emergent alignment interactions are controlled by both activity and the roller area fraction, and (*ii*) with sufficient area fraction we find the local population enough to obtain hexagonal order within the propagating bands. This last point is a novel feature of bands with polar and orientational order.

The phase diagram is rich in behaviour, as shown in Fig. 6.6. Here, the different phases are labelled as follows: crystallites formed from attractive interactions with activity $\mathrm{Pe} \approx 0$ are represented by $\mathbf{X}$. With the field amplitude exceeding E_Q, Quincke rollers performing a persistent random walk are considered an active gas $\mathbf{G}$. Competition between attractive and repulsive interactions yields active crystallites, upon increasing the area fraction. While Quincke rotation acts as a long-ranged repulsion, the induced hydrodynamic interactions drive partial demixing, thus, we refer to this as an amoebae-

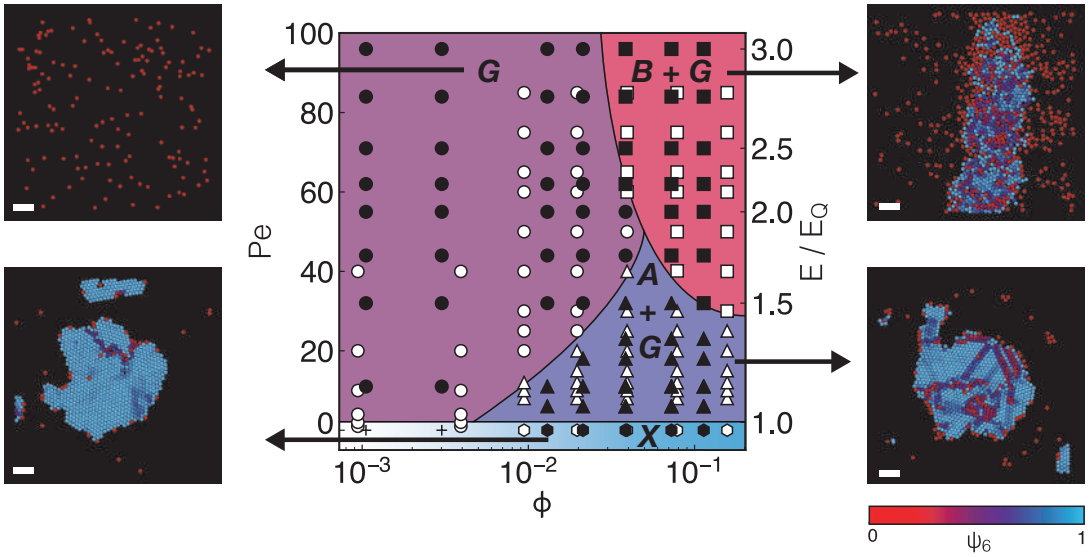

Figure 6.6: **Phase diagram of Quincke rollers with competing interactions.** The diagram shows the different phases obtained with varying the area fraction ϕ and the activity, by means of Péclet numbers and electric strength E/E_Q. Constructed from experiments (closed symbols) and numerical simulations (open symbols) on Quincke rollers. Solid lines are guides. Snapshots on the sides illustrate the different phases on the diagram as indicated by the arrows. Scale bars on images are 20 μm.

gas state, **A+G**. Moreover, with increased activity and with a sufficient area fraction, an inhomogeneous state of directed bands is observed that propagates through a disordered gas **B+G**. We note that for this inhomogeneous state, the role of activity is reversed, and leads to demixing. The formation of polar bands occurs through the alignment interactions while the rollers self-propel. Moreover, the repulsion due to the hard core of the disks leads to local order within the polar bands.

Having introduced all the phenomenological states of our system, we proceed to characterise each phase according orientational and dynamical order parameters. Starting with the orientational order parameter in previous section 6.4.1, we identify the local structure for the individual phases. This is followed by a dynamical distinction of the active and passive states.

6.5.2 Local Structure

We use the hexagonal bond orientational order parameter ψ_6 to proceed with structural characterisation of the phases shown in Fig. 6.6. As mentioned in Sec. 6.4, lateral aggregation occurs due to hydrodynamic interactions, and leads to the the formation of hexagonal crystallites. These are of finite size and exhibit domains of variable orientation, which hinder perfect hexagonal ordering. With particles joining the crystallites, the distribution of ψ_6 shows increased order (Fig. 6.4**d**). For small populations, few instantaneous collisions are observed and result insufficient to develop amoebae aggregates or structured bands. Unsurprisingly, the active gas lacks both polar and orientational order. We note a rich phase behaviour with increased density (Fig. 6.6), thus, we investigate the role of activity in structures forming at higher area fractions, i.e. $\phi \geq 4 \times 10^{-2}$.

Figure 6.7**a** shows the average orientational order ψ_6 versus Pe, where symbols are experimental measurements and solid lines are from numerical results. Overall, we find a good agreement between experiments and simulations. In the absence of activity, colloids behave as Brownian disks with no orientational order. As before, the lateral aggregation from EHD flows promotes rapid increase of the orientational order $\psi_6 \approx 0.9$, with $\mathrm{Pe} \approx 0$. In this regime, the system is composed of a collection of crystallites that lack motion. It is possible that they may be a condensed liquid (or hexatic) phase [191, 193], although this is not apparent within our data, and the transition appears first order for the sampled electric strengths. We believe this to be similar to the two-dimensional attractive systems undergoing crystallisation in equilibrium, with further activity driven transitions.

Additional increase in the activity into the amoebae phase yields the decrease on ψ_6. Nonetheless, the magnitude of the orientational order remains significantly above disorder, indicating crystal-like of the amoebae aggregates. While this state is far from equilibrium, ψ_6 exhibits temporal fluctuations consistent with a steady state (Fig. 6.5**b**),

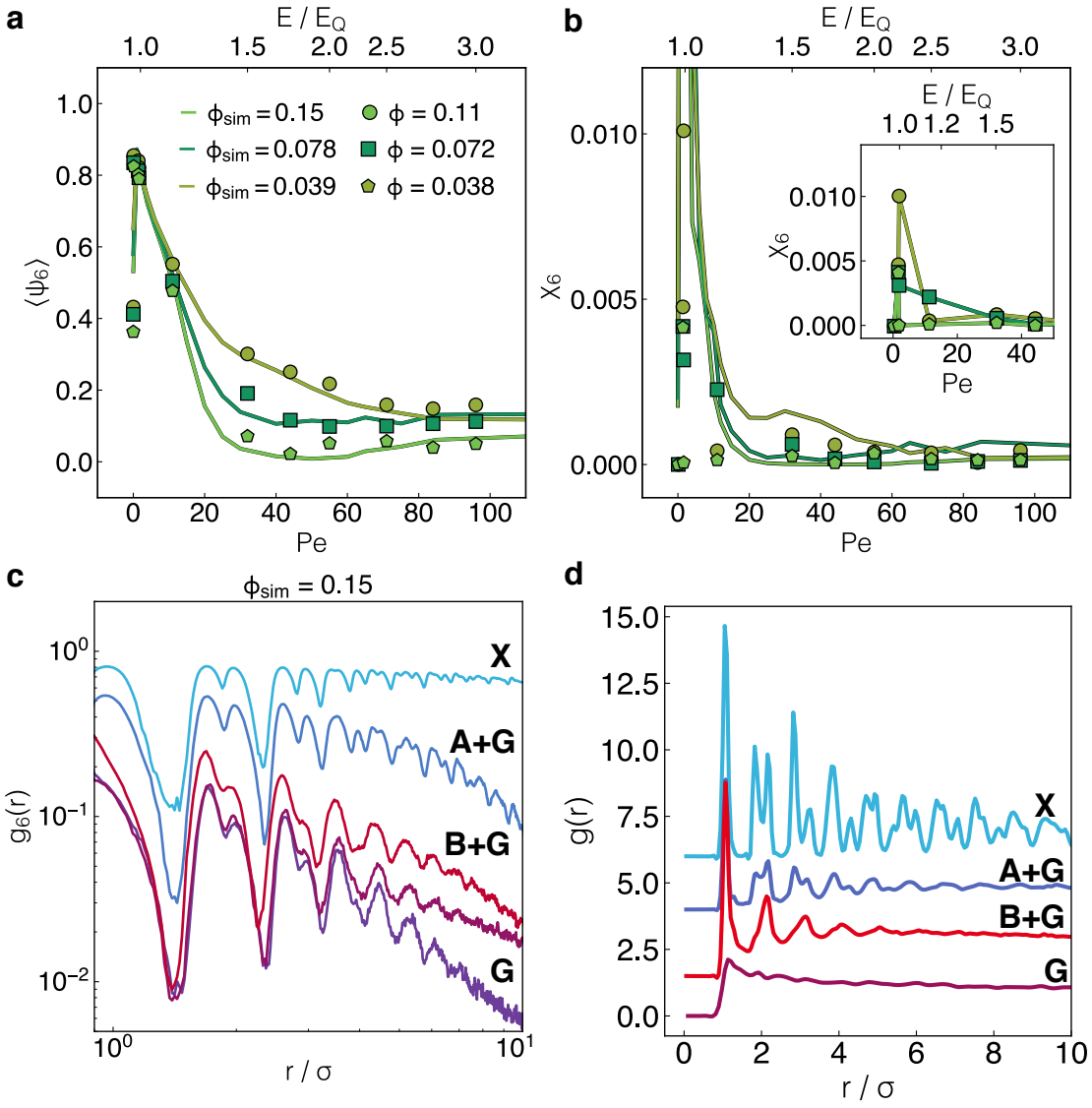

Figure 6.7: **Local structure as function of** Pe**. a.** Local order determined with the bond orientational parameter ψ_6 upon increasing Pe values. **b**. Fluctuations of the bond orientational parameter χ_6 as defined in the text. Inset displays experimental measurements where a peak develops at the transition between the crystallites and the amoebae phase. **c.** Orientational correlation functions $g_6(r)$ for Pe as indicated by the labels. Data obtained from simulations with $\phi = 0.15$. **d.** Pair correlation functions $g(r)$ from experiments at $\phi \approx 4 \times 10^{-2}$.

as amoebae aggregates reveal rotational motion. In order to distinguish between the passive crystallites and the amoebae, a dynamic order parameter seems suitable. At larger activities, $11 \leq \mathrm{Pe} < 40$, the magnitude of ψ_6, drops significantly, as the amoebae *dissolve*, apparently in a continuous fashion. Finally, with high activity ($Pe \geq 40$), upon the emergence of an inhomogeneous state with banding, a form of phase separation driven by alignment. Here, the value of ψ_6 remains low, as denser bands travel through a disordered state.

With the aim of gaining further insight into these transitions, in Fig. 6.7**b** we plot the fluctuations in the hexagonal order, as $\chi_6 = \langle \psi_6^2 \rangle - \langle \psi_6 \rangle^2$, where the average is taken over different snapshots. Again, at low Péclet numbers, we find experiments and numerical results in good agreement. However, when the motility is higher, the experiments show a faster decay towards the following active phases. Nonetheless, we find no enhancement in χ_6 around the subsequent phase boundaries, indicating that the transition is a cross-over rather than a first order-like between different phases.

To quantify the spatial correlations in ψ_6, we compute $g_6(r)$ defined as,

$$g_6(r = |\mathbf{r}_i - \mathbf{r}_j|) = \left\langle \psi_6^{i*} \psi_6^{j} \right\rangle \tag{6.7}$$

where ψ_6^i is the complex value of the bond orientation order parameter for particle i at position $\mathbf{r}_i$. At low Pe, we observe long-ranged orientational correlations in the crystal and amoebae regimes. Further decay is observed indicating aggregate finite size. The correlations are significantly shorter-ranged in the gas. For the largest Pe at the banding regime with $\phi = 0.15$, we find that the bond-orientational order parameter is correlated over a larger domain than in the gas regime. Therefore, formation of the bands not only holds the magnitude of ψ_6, but also enhances its spatial correlations. Still, high activity values show exponential deorrelation on $g_6(\mathbf{r})$.

To account for positional correlations, we compute the radial distribution function, $g(\mathbf{r})$, given by,

$$g(\mathbf{r}) = \frac{1}{\rho}\Big\langle \sum_{i\neq j} \delta(r - |\mathbf{r}_i - \mathbf{r}_j|)\Big\rangle \tag{6.8}$$

where ρ is the roller density number, and $\langle ... \rangle$ denotes time average. This returns the probability of finding a neighbour as function of distance r. In Fig. 6.7**d** four $g(\mathbf{r})$ from experimental samples at $\phi \approx 4 \times 10^{-2}$ are shown, with each line corresponding to the indicated phase label. The sharpness of the first peak on the **X** phase is usually an indicative of hard disk interactions, with the splitting on the following peaks as a characteristic of particles on a hexagonal lattice. While peaks on the crystallites are well defined, the loss of positional correlation in the active phases is indicated by the less defined peaks in the amoebae and band phases. As expected, the active gas lacks both positional and orientational ordering. Focusing on the closest correlations, the distinction between the steady and the active amoebae crystallites is the increase of crystal domains as amoebae aggregates reshape, split and coalesce. This can be also explained in terms of activity-induced topological defects in form of dislocations. On the other hand, the inhomogeneous banding phase exhibits the characteristics of a liquid.

6.5.3 Dynamical Characterisation

With competing interactions playing a role in the active crystallites, we find the magnitude of hexagonal order parameter ψ_6 to be of proximity to the one of passive crystallites. Hence, a dynamical order parameter is suitable to distinguish the crystallites from amoebae aggregates. We follow the approach taken to characterise the self-melting crystalls shown in Ref. [211]. For the dynamics, we use the self-part of the overlap function, defined as

$$Q(t) = \left\langle \frac{1}{N} \sum_{i}^{N} \exp - \left(\frac{\left[\mathbf{r}_i(t'+t) - \mathbf{r}_i(t') \right]^2}{a^2} \right) \right\rangle_{t'}, \tag{6.9}$$

with evaluating $a = \sigma$. The overlap function runs over individual roller trajectories. The results from the dynamic correlations are shown in Fig. 6.8**a**, which we fit with a stretched exponential form, $Q(t) = \exp[-(t/\tau_\alpha)^b]$, with b as the stretching exponent. From fitting the experimental samples, we extract the relaxation timescale τ_α for the different Pe numbers shown in the colour bar. The α relaxation time is shown in Fig. 6.8**b**.

Most striking in the crystal-amoebae transition is the rapid drop of the α relaxation time, with a total of five decades. This is a very substantial dynamical change for particle-resolved studies of colloids, active or passive [82]. The crystallites are effectively dynamically arrested solids, while the amoebae exhibit timescales of colloidal liquids, even though their local structure is polycrystalline (Fig. 6.7**a**). As the rollers experience an increased activity, $Q(t)$ rapidly decreases with the roller motion being ballistic (see Fig. 6.2**a**). Despite this precipitous drop in relaxation time, we find that the transition from crystallites to amoebae is apparently continuous in nature. We thus conclude that the crystallite-amoebae and amoebae-active gas transitions are both continuous, at least insofar as we can detect.

In addition to Q(t), we compute the bond orientational correlation function $g_6(t)$, defined by

$$g_6(t) = \left\langle \frac{\psi_6^{j*}(\tau)\psi_6^j(\tau+t)}{|\psi_6^j|^2} \right\rangle. \tag{6.10}$$

Similar to the overlap $Q(t)$, this correlation function allows one to distinguish crystallites from amoebae (Fig. 6.8**c**), in the same sense that a liquid is differentiated from the hexatic phase in thermal equilibrium [193]. For the crystallites, complete correlation is observed for the timescales analysed in the lab framework. The decay for the amoebae

phase seems algebraic in contrast to the rapid decay on $Q(t)$, showing liquid dynamics combined with crystalline structure. Fitting lines to the data, using the same stretched exponential form as in $Q(t)$ gives the relaxation of the orientational order, which for phases beyond amoebae we find agreement with the decay in Fig. 6.8**b**. We can conclude the increasing Pe promotes the dynamical loss of positional and orientational order.

6.5.4 Nature of the Active Phase Transitions

With Pe increasing from the passive regime, we find the transition to amoebae aggregates to be continuous at the densities considered here. This is characterised by the drop in ψ_6, along with the continuous change in the dynamics described above.

The application of higher field amplitudes yields the formation of an inhomogeneous phase, characterised by a polar fraction traveling through a disordered gas. Here, the resulting bands exhibit motion with a preferred direction. Compared to the asymmetric profiles obtained in periodic confinements [4], here the bands are of slender shape [159], with a change from smectic arrangements to solitary bands [132, 133] with increasing Pe. This state represents the onset of collective motion, and is in good agreement with the microphase separation of flocking models in Sec. 2.3.1, [17, 18]. Strikingly, a hallmark in the case of the transition to the inhomogeneous phase is the alignment interactions, characterised by the local polar order parameter,

$$\mathbf{\Pi} = \left\langle \left| \frac{1}{N} \sum_{i}^{N} \mathbf{n}_i(t) \right| \right\rangle_t , \tag{6.11}$$

which shows an increase towards complete a full polar state (Fig. 6.8**d**). We find the confining geometry playing a role, where for periodic racetracks a polar liquid [4] already forms with the densities considered here. For a square region, the finite size effects delay the emergence of the polar state, which in any case should exhibit a bifurcation similar to the dense vortices in Ref. [282].

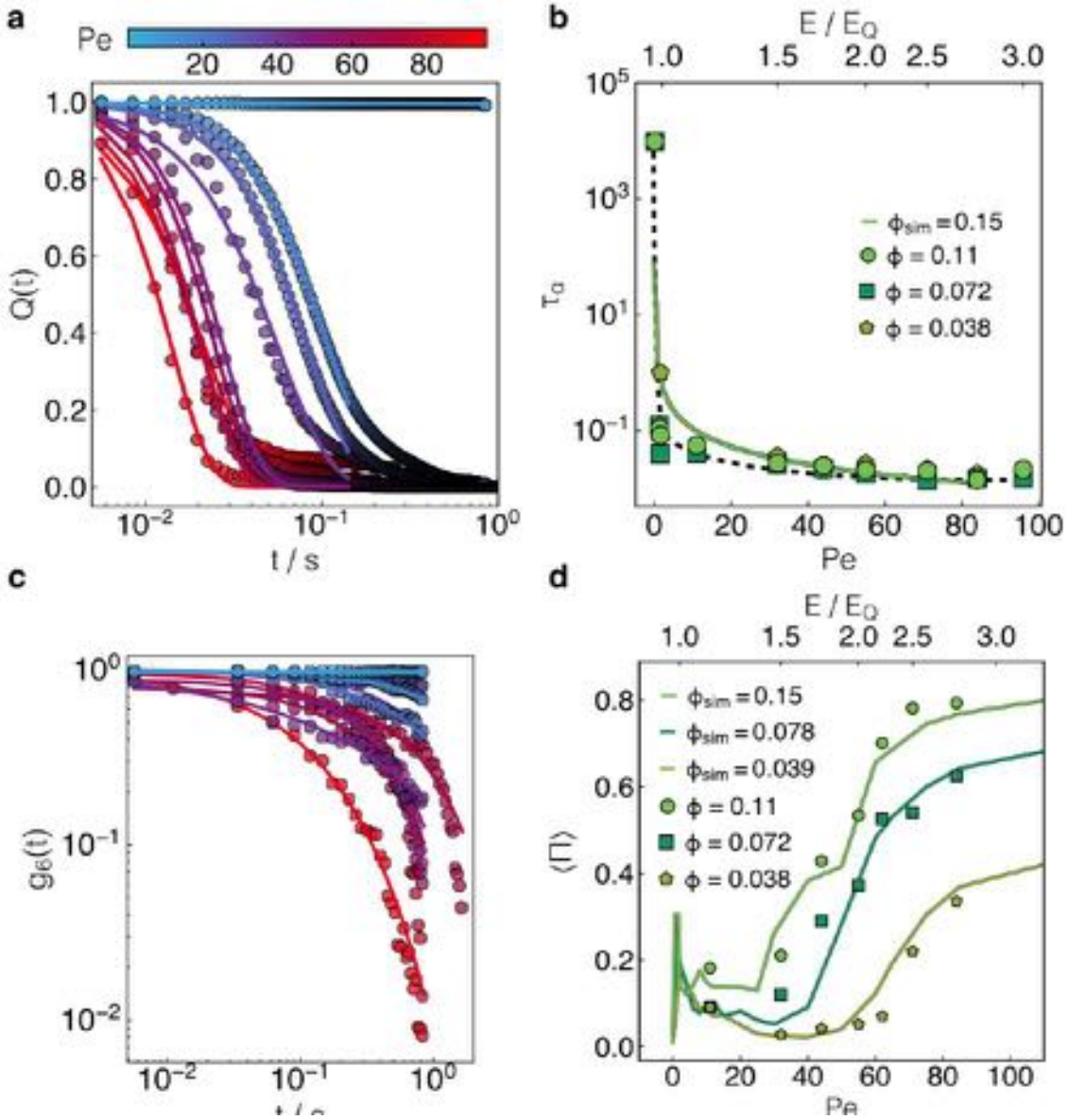

Figure 6.8: **Dynamics of the various phases. a.** Overlap function $Q(t)$ from Eq. 6.9. Symbols represent experimental data for $\phi = 0.11$, and solid lines are exponential fits as described in the text. Colour bar indicates the correspondent Pe for each line. **b.** Relaxation time τ_α from stretched exponential fitting to symbols in **a**. Symbols represent experiments, and the solid line is obtained from simulations. Dashed line is a guide to the eye. **c.** Time correlation function of the hexagonal order ψ_6 in a log-log plot, from Eq. 6.10. Symbols are experimental data and lines are stretched exponential fits. Colours indicated by colour bar in **a**. **d.** Mean polar order parameter Θ against Pe. Symbols and lines correspond to results from experiments and simulations respectively.

With the highest area fraction tested here, the emergent polar bands exhibit some degree of local order, with the bond orientational order parameter $\psi_6 \approx 0.2$. While far from complete hexagonal order, this is significantly above zero. Despite the exponential decay, the spatial correlation of ψ_6 show enhancement against the uncorrelated active gas, showing that bands are able to hold a small degree of orientational order. A close-up of one of these bands shows local hexagonal order (blue domains in Fig. 6.6), while the demixing affects the global order. Decreasing ϕ also drops the magnitude of ψ_6 towards an active gas of complete disorder.

We note that the amoebae-banding transition is continuous, as indicated by the orientational, dynamical and polar orders. As Pe increases, amoebae crystallites dissolve into the active gas, where the interplay of alignment interactions promote the increase in $\mathbf{\Pi}$. Analysis of the polar order indicates a degree of polar order in the amoebae aggregates, as local alignment develops in the trajectories. Considering the limit between amoebae and the inhomogeneous phase in Fig. 6.6 to be the point at which a preferred direction of motion is detected. We find this to be dependent on both activity and area fraction. One one side, lowering ϕ weakens the collective motion, and on the other, decreasing the activity leads to partial demixing due to the hydrodynamic attraction. For the polar order $\mathbf{\Pi}$, the numerical results show a sharp increase with the increase of Pe, an indication of banding formation, thus, the partial demixing due to the reversed role of activity. Thus, the suggested line delimiting **A+G** and **B+G**.

Regarding the inhomogeneous phase observed here, the main addition to the polar bands observed previously [4, 17, 18, 115, 132]is that the bands formed in a system of competing interactions not only display directed motion, but local orientational order due to repulsive interactions [357]. Also, for a given density, e.g. $\phi \approx 10^{-1}$, we find good control upon the transitions between the dynamic states and the passive aggregates by changing E. Details of the experimental movies showing band quenching to crystallites,

and vice versa are included in Appendix C.

6.6 Cluster Size and Density Fluctuations

As shown in the phase diagram in Fig. 6.6, a combination of passive and active phases result as function of the colloid area fraction and the activity. In agreement with previous observations on flocks [4], exceeding a critical density leads to the emergence of collective motion. Additionally, the balance with the short-range electrostatic repulsion from hydrodynamics results in passive and active aggregates when controlling E. For the range of area fractions in Fig. 6.7**a**, we map the evolution of the structural order characterised with the bond orientational order parameter ψ_6. Complete decay of the hexagonal order is not observed, as indicated by the local order in certain domains and by spatio-temporal correlations indicating a degree of order on the bands formed at the inhomogeneous state. In addition to the analysis of structure and dynamics, we show the different regimes of finite size structures, and the corresponding density fluctuations.

We analyse various aggregates forming at different area fractions. Clusters with a minimum number of rollers $n = 4$, and interparticle distance $|\mathbf{r}_i - \mathbf{r}_j| \leq 1.25\sigma$ are solely considered. Figure 6.9**a**) shows the sharp increase of the mean cluster size S with the application of the field E. This observation is in agreement with the increased order indicated by ψ_6. Within this regime, at low Pe, the mean cluster size S reaches an average value of 10^3, as the particles experience a lateral drag from the EHD flows described in Sec. 4.5. The increase in the activity yields smaller aggregates as amoebae crystallites break, and later dissolve into an active gas with varying Pe and ϕ. As polar motion arises in the inhomogeneous state, a denser fraction forms, in which according to our definition of a cluster we find different domains within the propagating bands. Importantly, all the active aggregates evolve in size with time, except for the steady crystallites at Pe ≈ 0. We consider such a dynamical evolution in our measurements in

Fig. 6.9**a**. For the lower area fraction considered here, the cluster size diverges from the numerical observations. Nonetheless, the polar order distinguishes this from the isolated rollers in the gas and we neglect this effect on the phase diagram.

Focusing on the inhomogeneous phase, in Sec. 2.4.1 we highlight the main characteristics beyond phase separation and microphase separation between two states of different polar order. Namely, density fluctuations are a common characteristic of active fluids [7, 20]. In contrast with the systems in thermal equilibrium, the long-range correlations in polar order promote anomalous giant density fluctuations in active systems. We investigate the emergence of these so called density fluctuations by taking the number N of rollers in boxes of different size l, at time t, with the fluctuations given by, $\Delta N^2 = \langle (N(t) - \langle N \rangle)^2 \rangle$.

Giant density fluctuations are numerically distinguished by the relation between the mean and the fluctuation value, which scales with $\Delta N^2 \sim \langle N \rangle^{\alpha}$, with α being the scaling exponent. For the flocking models described in Sec. 2.3.1 [5, 17, 18], the emergent homogeneous polar liquid is of fluctuations with $\alpha = 2.56$ and 3, considering metric and topological interactions respectively. Equally for a polar liquid of Quincke rollers, anomalous fluctuations are observed with $\alpha \approx 2$ [307]. In Fig. 6.9**b** we plot the density fluctuations of the different states find in our system at $\phi = 10^{-1}$.

Amoebae aggregates exhibit density fluctuations with a lower scaling exponent to $\alpha = 2$, but significantly larger to the fluctuations in equilibrium, with $\alpha = 0.5$. By increasing the activity to $\mathrm{Pe} \geq 32$, the inhomogeneous phase shows density fluctuations that compare with the value of the fluctuations in the polar liquid, with $\alpha \approx 2$. This results in agreement with the observations in driven filaments [159] and to the fluctuations exhibited by polar disks [153]. Given such a scaling exponent, the density fluctuations suggest that the inhomogeneous state can lead to a polar liquid. However, the finite size from confinement suppresses the emergence of the polar liquid, despite the developing of

alignment interactions. This suppression is observed as band reflection at the boundaries, which locally disturb the polar order.

6.7 Active and Passive Crystallites

In the absence of Quincke rotation, low field strengths below E_Q give crystallite formation in the case of sufficient area fraction. From the overlap function Q(t) and the time orientational correlation $g_6(t)$, crystallites are dynamically arrested. For monodisperse colloids, high packing results in hexagonal structures that exhibit high orientational order, as marked by ψ_6. Furthermore, the increase of Pe leads to the competition between active motion and the induced attraction, which results in the motion of amoebae crystallites. We find these amoebae aggregates to be highly dynamical, while retaining a high degree of hexagonal order.

Similar to the clusters in electrophoretic self-propelled particles that show interrupted phase separation [252], amoebae aggregates exhibit cluster aggregation and breaking events. This is due to the motility contribution that generates topological defects, namely, dislocations that may result in grain boundaries. Given the process of the breaking events, we compare amoeba aggregates to liquid droplets [358]. Both coalescence and break-off of liquid drops are macroscopic driven processes that are clearly not in a steady state. In contrast, the amoebae aggregates are apparently a non-equilibrium steady state. Furthermore, the aggregates are locally ordered. Nevertheless, one may ask if insights about the steady-state behaviour of our active system can be obtained by considering the behaviour of a driven passive system that is not in a steady state. It is noteworthy that in passive systems there is a strong asymmetry between liquid drop coalescence and the break-off dynamics, reflecting the fact that ending points of the two processes are rather different.

For the amoebae phase, it is not at all obvious if there would be symmetry between

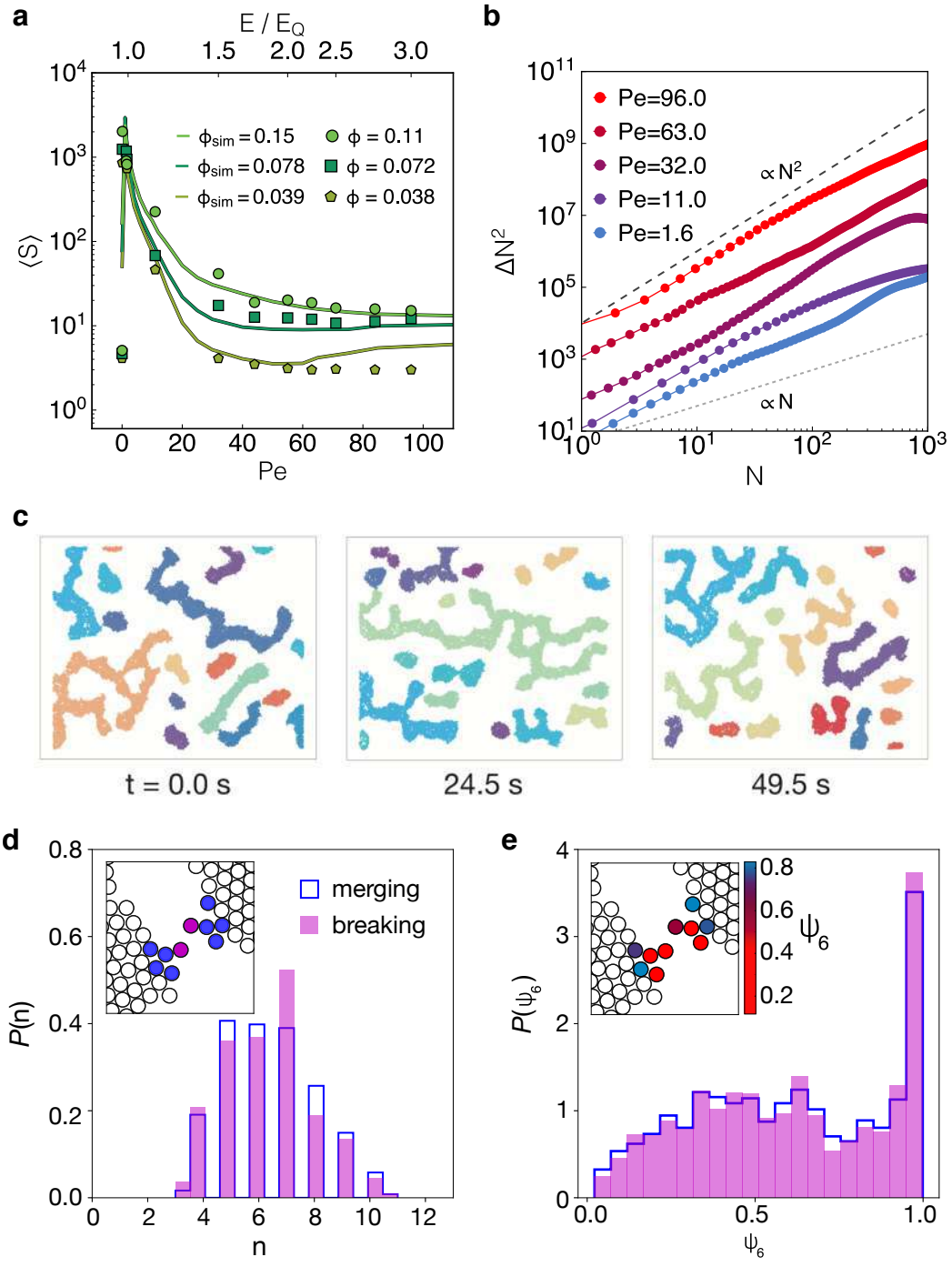

Figure 6.9: **Amoeba clusters and giant density fluctuations. a.** Mean cluster size as function of Pe. **b.** Giant density fluctuations versus the mean number of rollers N measured in boxes of size l. **c.** Time sequence of amoebae aggregates. Colours indicate individual clusters. **d** and **e** are the distributions of the n particles and ψ_6 at the cluster interface. Insets show a merging-breaking event.

the dynamics of coalescence and break-off, because it is a non-equilibrium steady state. Namely, while of course the microscopic equations of motion in this non-equilibrium system are not expected to exhibit time-reversal symmetry, we enquire whether this is apparent at the level of the coalescence and splitting behaviour in the amoebae phase. In particular, we consider whether we can distinguish to an extend the pathways by which coalescence and splitting occurs within amoebae aggregates.

We investigate the coalescence and break-off dynamics of the amoebae crystallites as follows. First, distinct amoebae clusters are identified using the same conditions as in our cluster definition. Fig. 6.9**c** illustrates a time sequence of amoebae clusters, where the different colours indicate different aggregates. Markedly, very dynamical structures display continuous reshaping, along breaking and coalescence events. To account for the morphological changes, we start from detecting the change in the number M of rollers per amoebae, and measure the nearest distance between boundary particles in different clusters. In separating the mass invariant aggregates from the growing and dividing aggregates on time, we track the contacts of link and break (see Fig. 6.9**c** inset).

We find pairs of rollers involved in both coalescence and splitting dynamic processes. We also identify the number of neighbours within a distance of 1.25σ and analyse the local orientational order ψ_6. In Fig. 6.9**d**,**e**, we plot the resulting distributions of the number n of neighbours in the neighbourhood and the local ψ_6, with time running forwards and backwards. Since the distributions, both of the number of particles n in the neighbourhood and ψ_6 appear rather similar within our statistics, we infer that our analysis does not reveal any breaking of time-reversal symmetry. This is consistent with recent work with active Janus colloids which considered aggregation and fragmentation rates [261]. Thus, we find this non-equilibrium steady state to be fundamentally different to the highly asymmetric case of droplet coalescence and break-off in driven passive liquids [358].

6.8 Inhomogeneous and Homogeneous Phases

We follow Ref. [4] and investigate the effect of different confinement geometries. Using a square geometry, polar bands and an inhomogeneous phase develop at $\phi = 0.11$ and $\mathrm{Pe} \approx 100$. These emerging bands correspond to solitary propagations [133]. Figure 6.10**a** shows a propagating band with a longitudinal extension comparable to the length of the confinement. While propagating, bands explore the entire confining space, and exhibit reflection upon reaching the confinement limit. It is worth noting that the area fraction, i.e. $\phi = 0.072$, used in square geometries is comparable to the one that leads to polar liquids in Ref. [4]. This suggests that systems of finite size hinder the development of the homogeneous polar state, with band distortion occurring for every reflection at the boundary limits.

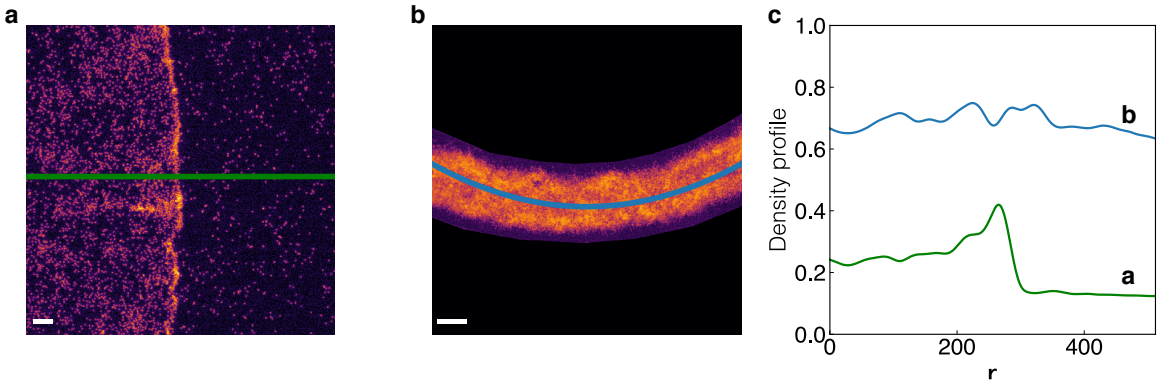

Figure 6.10: **Density profiles. a.** Polar band propagating through an active gas. $\phi = 0.072$. Scale bar is $20\,\mu$m. **b.** Homogeneous polar liquid confined to a racetrack. $\phi \approx 10^{-1}$. Scale bar is $50\,\mu$m. **c.** Density profiles measured from the normalised intensity. Line colour corresponds to the lines drawn in **a** and **b**.

In addition, we test a suspension of similar area fraction in a periodic racetrack. With $\phi \approx 10^{-1}$ and $\mathrm{Pe} \approx 100$, we find a homogeneous liquid of directed motion. This is in good agreement with the observations in Ref. [4], where polar order develops with the density exceeding a critical value. Using fluorescent microscopy time sequences, we analyse the density profiles, where dense regions are readily distinguished from the

dilute gas. For the Vicsek-like polar bands, density profiles are measured normal to the front propagation, as indicated by the green line in Fig. 6.10**a**. For the periodic case, we use a curvilinear profile to estimate the tangential density to the boundaries (Fig. 6.10**b**). Figure 6.10c, shows two different profiles corresponding to the phase separated and homogeneous states. For the polar liquid, the density estimation from intensity fluctuates, but is of constant value ≈ 0.7 across $\mathbf{r}$. On the other hand, slender bands display a sharp increase in the intensity signal, a clear indication of an interface from the phase separation. As the band propagates, the tail behind the polar front shows a smooth decrease, as expected for a solitary band [133].

A suggestion for the change in phase is to do with the nature of the confinement, where coherent flows are observed in active fluids upon confinement [148]. The confinement used in most of the previous experiments with Quincke rollers [4, 283, 300], consists of racetracks of finite width W and length L. For rollers of velocity $\mathbf{v}$, the transverse velocity component $v_\perp$ is limited by W, whereas the periodicity along L enhances the tangential component $v_\perp$. Thus, confinement of this kind promotes directed motion at sufficient ϕ, and protects the homogeneous polar liquid [300]. In contrast, a confinement of equal aspect ratio sets the velocity components (v_x,v_y) equal to L, retarding the development of a polar liquid state.

6.9 Summary and Discussion

In the present chapter we present results from experiments and numerical simulations of Quincke rollers, in which dynamics are markedly different to those in the absence of activity (Fig. 6.1**b** and Fig. 6.2**b**). We follow the previous studies that indicate a transition to states of polar order [4, 282], and solidification [283] with increased density. In addition to this latter, we investigated the phase behaviour using the electric strength E and the area fraction ϕ as control parameters. Also, the colloidal suspensions were confined to

square geometries, which significantly change the phase behaviour in contrast to periodic geometries [4, 283].

Upon the application of the field E, lateral motion into aggregation is observed (Fig. 6.3). Note that this process occurs given the generation of electro-hydrodynamic (EHD) (Sec. 4.5) flows which drags sedimented particles. With sufficient area fraction, e.g. $\phi \geq 10^{-2}$, and with field magnitude E below a threshold E_Q, condensation forming passive crystallites occurs. The resulting aggregates are characterised by having high order, as indicated by the hexagonal bond orientational order parameter ψ_6. In addition, the high order remains with constant E, given the steady behaviour of the crystallites.

The increase of the field strength to $E \geq E_Q$ leads to the onset of Quincke rotation and activity-induced phase transitions. For small populations, i.e. $\phi < 10^{-2}$, an active gas forms, with the rollers showing persistent random walks. We investigate the roller dynamics by means of the dimensionless Péclet numbers. Figure 6.2**c** shows the relation between active motion and the applied field E. In addition, we use the estimated Pe values to map our experimental observations to numerical simulations.

Looking at the density regime at which steady crystallites form, increasing the activity to $\mathrm{Pe} \approx 2$ leads to aggregate motility, similar to that in run-and-tumble rollers [312] and to aligning clusters [252]. Given the dynamical behaviour, combined with constant reshaping, we refer to these motile aggregates as amoebae. We note that the time evolution of hexagonal order shows fluctuations around high values of ψ_6. The dynamical behaviour of the amoebae aggregates seems to result from the simultaneous interplay of different interactions, i.e. alignment and repulsion [356, 357]. Moreover, coalescence and breaking of amoebae aggregates are observed with constant activity. We note that the amoeba aggregates are apparently a non-equilibrium steady state, given the similar nature of the coalescence and break-off events (ig.6.9**d,e**).

For increasing activity, the amoeba aggregates dissolve in an inhomogeneous state,

characterised by a disordered fraction, i.e. a gas, and a state of increasing polar order (Fig. 6.8**d**). We find the state in agreement with the onset of collective motion described in the Vicsek-like models [17, 18, 115, 132, 133]. In contrast with the polar liquid observed at similar densities [4], the inhomogeneous state in our system consists of solitary waves [133], similar to the slender bands in driven filaments [159] (Fig. 6.10). It is important to emphasise, that these dynamical transitions can be readily accessed by increasing and decreasing the field magnitude E. Figure 6.6 shows the phase diagram obtained from experiments and simulations of rollers with competing interactions.

Given the rich phase behaviour, we analyse the structure by means of the bond order parameter ψ_6. Figure 6.7**a** shows the relation between ψ_6 and Pe, and good agreement between experiments and simulations. The decay of ψ_6 with increasing Pe suggests a continuous transition between the crystallites and amoebae. In addition, a dynamical order parameter is needed to account the difference between the steady and dynamical states. We use the overlap Q_t, that enables to investigate the α relaxation time of each phase. Markedly, the crystal-amoebae transition shows a drop of five decades in τ_α, as shown by the relaxation times in Fig. 6.8**b**. Thus, amoeba aggregates are locally crystalline structure with the dynamics of a colloidal liquid.

For the inhomogeneous phase at high Pe, the structural order lack complete decay, as indicated by ψ_6. In addition, the spatial correlation $g_6(r)$ shows enhancement in the correlation than the gas. In contrast to the interactions leading amoeba aggregates, the role of high activity is at the onset of collective motion due to alignment. A close-up to one of the bands is shown at the phase diagram in Fig. 6.6, where the regions of high ψ_6 result from the repulsive core interactions [357]. Also, the onset of collective motion is captured in Vicsek-like models with the polar order parameter $\mathbf{\Pi}$, which increases with the emergence of polar bands (Fig.6.8**d**). Another feature of flocking systems is given by the giant density fluctuations ΔN^2. Figure. 6.9**b** shows the fluctuations of the active

phases, which relation shows $\Delta N^2 \propto N^2$ with increasing Pe.

Finally, we have shown that the Quincke roller system exhibits a rich and complex phase behaviour, with passive crystals, amoebae active crystallites, active gas and an ordered banding phase. Given the variety of static and dynamic order parameters, the nature of the transitions between these states is continuous. At low field strength, activity suppresses demixing, while the hydrodynamic interactions drive partial demixing with the formation of amoeba aggregates. At high field strength, the role of activity reverses. It drives partial demixing in the inhomogeneous state, showing polar bands of local order due to excluded volume.

CHAPTER 7

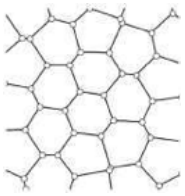

ROLLING IN STRONG CONFINEMENT

"Life is like a ten speed bicycle.

Most of us have gears we never use"

CHARLES M. SCHULZ

Colloidal dispersions are often investigated under the influence of an external field, where colloids are typically driven far from equilibrium in a controllable manner. Some of the most common approaches involve the use of either an external field, e.g. electric, magnetic, and optical fields, shearing, or confinement. Here, the relevant external contribution is the application of an electric field, combined with confinement of quasi two-dimensional layers of sedimented colloids.

The present chapter is motivated by a confined system under an optical field [315]. The later system consists of an adaptive confinement built with optically trapped colloids. Using optical tweezers, colloids are manipulated to create structures not attainable in equilibrium. In this case, a colloidal corral is made of individually trapped spheres, and which is populated with untrapped colloids. Confinement of this nature leads to a

different behaviour compared to the one observed in bulk, and when confined by planar walls. We refer to the system introduced in Sec. 4.2, and which behaviour results different from the phase diagram of hard disks [191, 193], including bistability between hexagonal and layered structures at high density N. As the systems is of finite size, the population experiences strong confinement, in this case as the population increases to $N = 48$ [315].

Furthermore, shear can be added as an external field on top of the confinement and gravity in order to obtain rotating structures. This is achieved by introducing rotation to the adaptive boundary using the same optical traps. The rotating wall exerts forces on the solvent, leading to fluid flows that affect the confined population. This gives rise to a system named the *colloidal washing machine*, which is shown in Fig. 7.1**a** [346]. Controlling the population of particles permits one to investigate the transmission of torque, determined by internal structure that could be of a solid or fluid-like nature. The dynamical behaviour is of a stick-slip mechanism akin to that in macroscopic gearwheels slipping, with the transmission mechanism governed by the rotation rate of the trapped boundary. Additionally, the local variation of the boundary radius allows engagement or disengagement of torque, giving rise to a minimal model of a colloidal clutch.

Based on this model, one would ask about the effect on structure and mechanics for a population experiencing the same forces as the boundary particles. Hence, the use of active particles seems suitable. In Chapter 6, we investigated the behaviour of Quincke rollers, where the contribution from active and passive interactions drives crystallite motility and structurally ordered bands. Taking advantage of the simultaneous interactions that promote the emergence of amoeba aggregates, we now make use of strong confinement to study the active behavior of microgears similar to that driven by optical fields [346]. Furthermore, we describe in detail a specific population used to assemble microgears whose rotational behaviour is controlled by the activity.

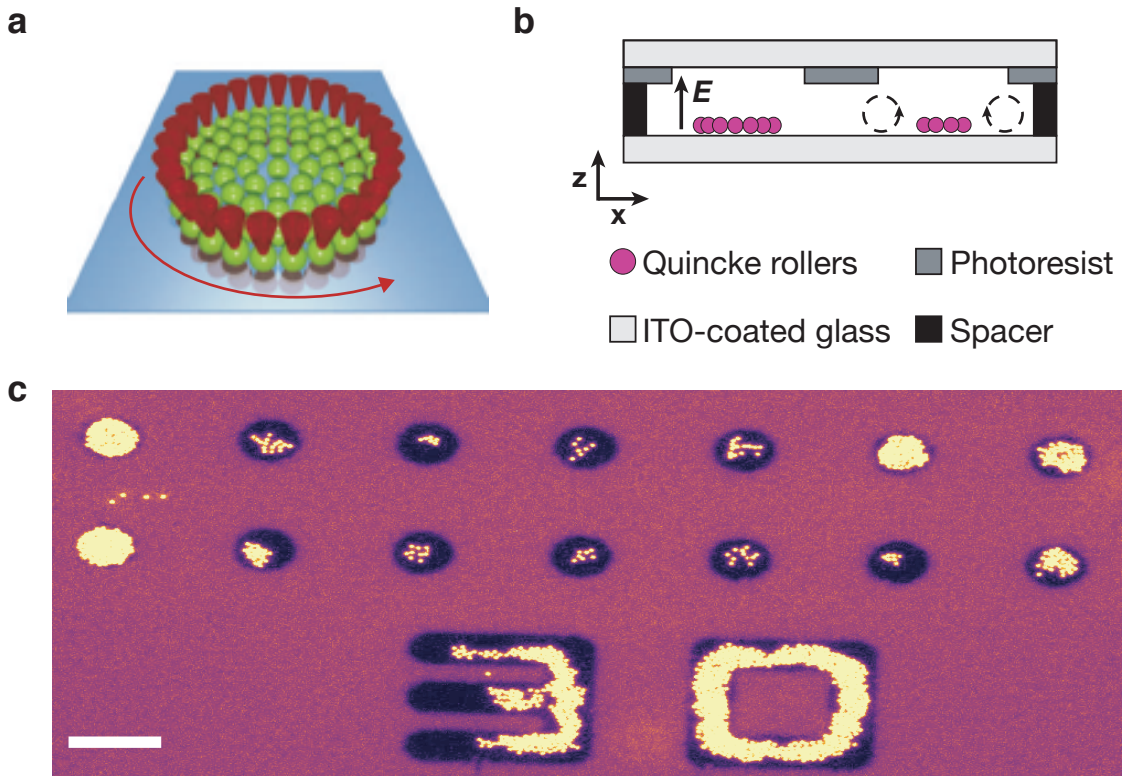

Figure 7.1: **Circular confinement. a.** Adaptive confinements can be populated with a specific number N of colloids using optical tweezers. Moreover, rotation of the boundary drives the internal population, resulting in a *colloidal washing machine* [346]. **b.** Schematic representation of the confining cell for Quincke rollers. A dielectric layer is used to localise the electric field E, whose application generates an incoming flow (dashed lines) that confines the rollers by repelling them away from the circular edge. **c.** Circular regions of radius $R_c = 15\,\mu$m (black regions) are used to confine different populations of Quincke rollers. Image shows a small section of the confinement lattice. Scale bar is $50\,\mu$m. See Supplementary Movie 1 details in Appendix C.1.2.

7.1 Circular Confinement

Planar walls are among the most common type of confinement, due to the influence of planar boundaries on the structure of colloidal suspensions [82, 342]. For the geometry considered here, strong effects from curvature are introduced, thus different structures form due to the boundary. Considering the radius of curvature to be large compared to the particle size, the local curvature is small and the difference between planar and curved

Confinement Radius, R_c (μm)	$N_{\max}$	$\phi_{\max}$	Contacts
15	85	0.8053	180
30	358	0.8479	779
60	1478	0.8751	2853

Table 7.1: Circular confinement. Most efficient packing values for circular confinements of different size, assuming particles of size $\sigma = 2.92\,\mu$m [3].

confining walls should be small. On the other hand, when lengthscales are comparable the contribution from curvature, a different packing may result. For the two-dimensional case, a curved wall is the most common expression of a circular confinement, and where a population is fully confined by a cylindrical projection of the extended circle to three dimensions. In the present chapter, a strong circular confinement is employed.

For a small circular confinement, the number N of confined units and their size with respect to the confinement must be considered. The goal is to find the most efficient way of packing the N interior particles, or finding the minimum confinement size to hold the population N without overlapping. For the confined area fraction ϕ, results from numerical simulations indicate that confinement of hard disks to a smooth curved boundary yields the adaption of the internal structure, where disks mimic the shape by forming concentric circular layers [359]. The result is for varying the population, or the confinement radius R_c, where the maximum value of N changes from its value in bulk, given by $\phi = \pi/\sqrt{12}$. For very small populations, e.g $N \simeq 1$, ϕ drops from perfect packing to values around ≈ 0.87 with $N \to \infty$. With sufficient population, the development of layers results in inhomogeneous density profiles, as single layers grow outwards in density. Therefore, the increase of N leads to pronounced layer formation, compared to the weak layering at low packing fractions.

For the lengthscales considered in our confinement designs in Chap. 5, we summarise

in Tab. 7.1 the different values of $\phi_{\max}$ when using disks of size $\sigma = 2.92\,\mu$m. Nevertheless, we expect the theoretical predictions to vary within experiments as the induced flows exert repulsion to the particles, different to the excluded volume considered here solely. Fig. 7.1**b** shows a fraction of the confining regions of size $R_c = 15\,\mu$m. Quincke rollers are confined by an electrokinetic flow within darker regions, which are exposed to the field E. Colloids outside these regions are considered as passive and we neglect their behaviour. Figure 7.1**b** shows individual confining regions of different populations, which can be indirectly controlled by adjusting the volume fraction of the injected suspension. In the following sections we show the spontaneous formation of concentric layers that exhibit a coherent flow, which is reminiscent of the transitions in bacterial suspensions and active fluids [148, 282, 344]. Also, we focus on a population of $N = 61$, where commensurate and incommensurate layered structures form due to the competition between local ordering, boundary conditions, and self-propulsion.

7.2 Motility in Strong Confinement

In the absence of self-propulsion, the strong confinement induces a decrease in motility in highly packed structures. Moreover, the nature of the confinement, e.g. planar walls, influences the type of motility between the normal and perpendicular directions. Confinement made of rough walls suppresses the local motion, giving rise to dynamical heterogeneity [82, 314]. Here, we use circular regions of $R_c = 15\,\mu$m under smooth confinement, which are comparable to the particle size with $R_c \approx 5\sigma$. We emphasize that the confinement exerted on the particles is not due to a physical wall, but rather from an electrokinetic flow generated from the current discontinuity upon the application of the electric field E [326] (Fig. 7.1**b**). In the absence of the field, particles behave as Brownian disks and are able to diffuse freely at the bottom electrode.

Upon application of the field, loose particles outside the confinement at the bottom

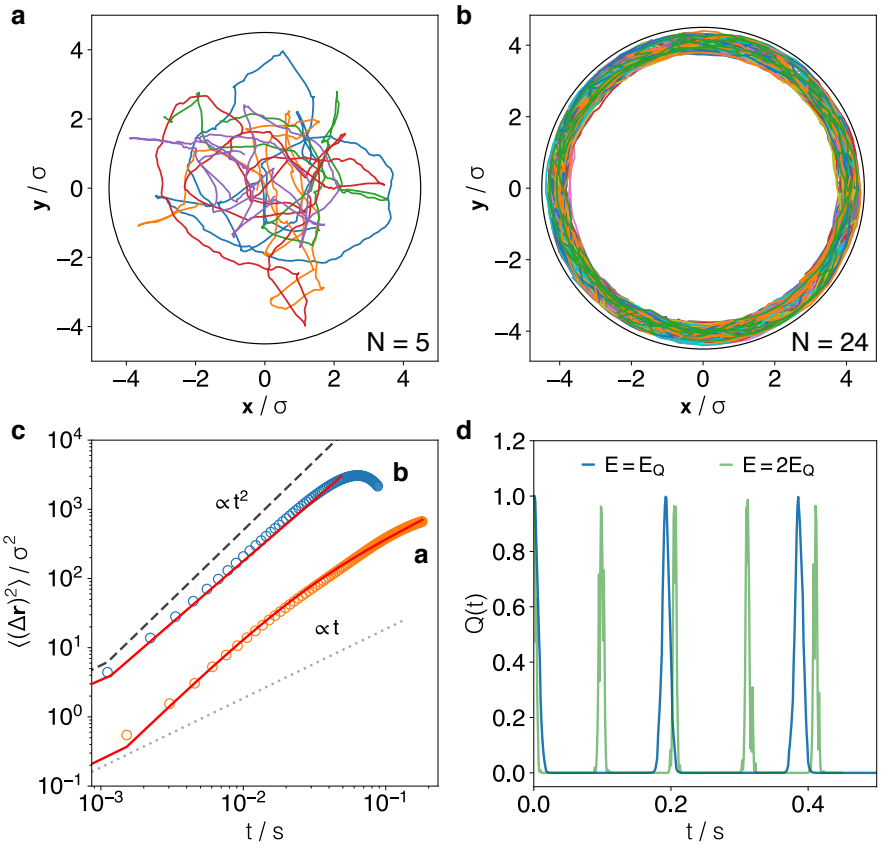

Figure 7.2: **Roller motion in circular confinement. a.** Trajectories for a population of $N = 5$. **b.** Layer formation with $N = 24$. **c.** Mean squared displacements for the trajectories in **a** and **b**, with $E = E_Q$. **d.** Overlap function $Q(t)$ for $N = 24$. Peaks indicate periodicity of the layer as rollers move tangentially with respect of the boundary.

plane are pulled laterally into the circular regions, where the induced flows hold the population. As shown in Fig. 7.1**b**, the number of confined particles N varies, depending on the local density which can be controlled indirectly by changing the packing fraction of the injected dispersion. For circular confining regions at this lengthscale, a suspension with volume fraction $\phi = 5 \times 10^{-2}$ is sufficient to populate a lattice made of confining regions. Our system is suitable to investigate the behaviour within different populations of rollers. Once confined, particles remain steady with a field amplitude E below the E_Q threshold, where single crystallites form with increasing N. We maintain the same

experimental conditions as in Chap. 6, with the confinement lengthscale being the only variation. Thus, we find E_Q to be of the same magnitude. When exceeding E_Q, spontaneous motion results, with a limited persistence length set by $2R_c$, which is significantly smaller compared to the macroscopic confinement employed before. For small populations, e.g. $N = 5$, we find a persistent random walk with an enhanced rotational diffusion $D_r \approx 10^{-2} s^{-1}$ from the torques exerted on the particles from flow at the boundary (Fig. 7.2**a**).

On increasing N, alignment acting on the population results in coherent motion. Alignment interactions promote the change of the radial density profiles, with the population forming a coherent layer flow near the boundary. For a strong confinement, one might expect that interparticle interactions and collisions slow down the dynamics, as in self-propelled hard disks [211]. On the other hand, measurements from roller velocities and mean squared displacement (MSD) indicate an improved motility from the alignment interactions, similar to observations in [310]. For a population of $N = 24$ and $E = E_Q$, a perfect layer of thickness σ forms, with the roller motion along the boundary (Fig. 7.2**b**). These layers are reminiscent to the rings formed by self-propelling Janus spheres [280]. Moreover, we find this coherent state to be the scaling down of the previously investigated vortices in Quincke rollers [282].

Having a coherent flow, we investigate the periodicity of the layer formed with $N = 24$ by means of the overlap $Q(t)$, previously used in Eq. 6.9. Fig. 7.2**d** shows $Q(t)$ against time on a linear scale. With a layer of rollers moving tangentially with respect to the boundary, the periodicity is well characterised by the recovery of $Q(t)$, displayed as peaks, which value approximates to $Q(t) = 1$, indicating further overlap. For a field strength $E = E_Q$ we measure an angular velocity $\omega = \mathrm{d}\varphi/\mathrm{d}t$ to be $\approx 33\,\mathrm{rad}\,s^{-1}$ (≈ 315 rpm), and $\omega \approx 60\,\mathrm{rad}\,s^{-1}$ (≈ 573 rpm) upon increasing the field magnitude to $2E_Q$. Being an active system, the rotation velocities displayed by ballistic layers are significantly

larger compared with a system of driven layers [346]. We later describe an assembly of a characteristic population $N = 61$, where the different layers rotate with either the same or different angular velocity ω with varying E.

7.3 Structures in Different Populations

The use of confinement in systems at thermal equilibrium and far from equilibrium contributes to the change in structure and dynamics [360]. In the case of a driven system, where confinement is achieved with optical traps [315], the behaviour is different to that of hard disks in bulk [191, 193]. The hallmark of such a system is the bistability between hexagonal and fluid-like structures in the confined population (Fig. 4.1**b**). Our system consists of confining regions of comparable lengthscale to the particle size, which might lead to similar features as in the aforementioned driven system.

For the structure, the many geometrical shapes used to confine colloids usually result in layers, which follow the shape of the confinement [359]. Layered structures develop close to the wall towards the interior, as the area fraction is increased. In Tab. 7.1, we summarise the maximum packing fraction for the lengthscales considered here. Those cases represent the most dense structures where strong layering is observed. In contrast with smooth walls, the use of a rough confinement might lead to distortion into liquid-like assemblies. Also, both particle polydispersity and binary systems suppress layering, with the resulting structures being glass-like [314]. This is not the case here as we only deal with smooth boundaries and colloids of monodisperse size.

Similar to the results in Chap. 6, the behaviour of the population of particles is controlled by the local density N, in addition to surrounding energy accessible to perform active motion. From our experimental studies, we find various deterministic structures given the number of confined units N and activity characterised by E. Single crystallites of finite size remain steady if $E < E_Q$, which is in agreement with our previous obser-

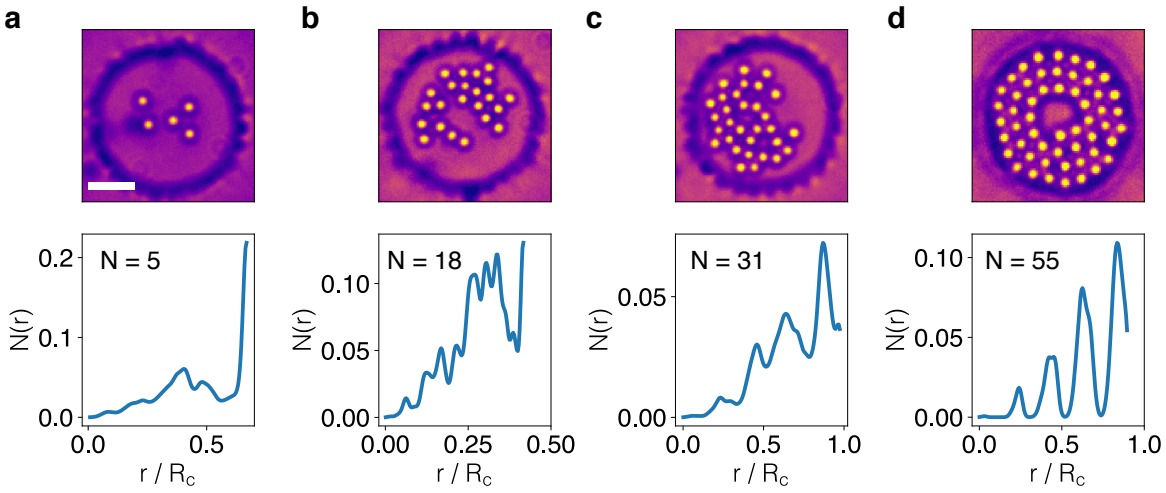

Figure 7.3: **Radial density profiles** for various roller populations. Top images show micrographs, and bottom panel are the corresponding density profiles for **a** $N = 5$, **b** $N = 23$, **c** $N = 31$, and **d** $N = 55$. Density distribution profiles $N(r)$ are normalised by the population number N. Scale bar on **a** is $10\,\mu$m.

vations in Chap. 6. For sake of simplicity, first we investigate the dynamical behaviour with increasing N and with fixed field strength, e.g. $E = E_Q$.

Small populations display swarming motion, akin to amoeba aggregates, and with the persistence length delimited by $2R_c$. Upon increasing the population number N, fluid layers spontaneously form and swirl with sufficient activity, e.g. $E \geq E_Q$. In Figs. 7.2**c**,**d**, we note the motility enhancement from alignment interactions [4, 310], and the periodicity displayed by rotating layers shown by $Q(t)$. To account for the distinct structures resulting for varying N, we start by taking the radial density profiles $N(r)$ for different populations. Figure 7.3 shows the density profiles $N(r)$ from the time dependent position $\mathbf{r}(t)$ of every roller. With small populations swarming, some preference to move towards R_c is noted. The shape of $N(r)$ corresponds to a typical fluid of low density. The increase of N, i.e. to $N = 18$, gives a first indication of fragmentation, with some of the total motion happening towards the centre. Better patterns are resolved with the increment on the roller population, as shown in Fig. 7.3**c**, a good indication of

layering with $N = 31$. As the local fraction is further increased, clear layers form (Fig. 6.10**d**), and the density profile $N(r)$ returns well defined peaks for each layer formed concentrically. For a population of $N = 55$, mimicking of the confinement shape is evident, with concentric layers forming from $r \approx R_c$ towards the centre.

7.4 Phase Diagram of Rollers in Strong Confinement

Based on the dynamical analysis performed on various wells containing different populations we distinguish two features. First, at low N, small aggregates form and swarm with sufficient field E. These are essentially amoeba aggregates of limited size. Nonetheless, the finite size of the systems due to strong confinement leads to short persistent motion, and dominating rotational diffusion. Second, as N increases, concentric layering develops due to alignment interactions. The result is layer rotation, with every roller self-propelling along the azimuthal direction, forming a state of coherent flow. This observation is consistent with previous investigations on ordered flows in confined active liquids [148, 282, 344]. Moreover, as a coherent vortex forms, alignment interactions lead to speed enhancement (Fig. 7.2) [310].

In addition, we show the different populations by means of density profiles $N(r)$ measured radially with respect of the confinement radius R_c. With low N, rollers perform swarming within a preferred location $0.5R_c \leq \mathbf{r} \leq R_c$. A density profile similar to that in Fig. 7.3**a** corresponds to a low density fluid. The increase of N leads to layer formation, as a result of copying the imposed shape from the boundary. An indication of this is given by the better resolved patterns on the profiles shown in Fig. 7.2**c**,**d**. For sufficiently large populations, e.g. $N = 55$, clear peaks are obtained in the density distribution $N(r)$, each peak corresponding to individual layers formed concentrically. Thus, for layering we identify a clear dependence of the disk population.

Following our analysis of the active and passive crystallites discussed in Chapter 6, we

use the two-dimensional bond orientational order parameter ψ_6 to further characterise the dynamical structures here.

For the different populations N, we measure the mean ψ_6, which combined with the density profiles denote different structures. We start with the passive aggregates that form due to the electro-hydrodynamic (EHD) flow upon application of E [322, 323, 325, 328]. Monodisperse disks form highly ordered arrays which pack into hexagonal structures in the bulk (see Sec. 6.4). Such structures are characterised by having a high orientational order, given by $\psi_6 \approx 1$. For passive disks under strong confinement, boundary effects might induce distortion of the local order, with particles adapting and layering with respect of the boundary. For a system confined within a colloidal corral [315], high hexagonal order is displayed within the central structure for $N = 47$. Increasing the population to $N = 49$, induces strong layering and inhibits the hexagonal order towards the boundary. Notably, the distribution of the local ordering indicates bistability between structures of high and low ψ_6 order. Concentric fluid layers correspond to structures of low hexagonal order near the boundary, whereas the high order is given by the local order on the central part (see Fig. 4.1**b**) [315].

As above, our design allows one to populate various confining wells with different N simultaneously. We emphasize that our confinement comes from the use of an electro-kinetic flow induced by boundary [326] and not a hard wall. Thus, the boundary effect on layering might be different here compared with the colloidal corral. As the population number increases, both contributions from layering and hexagonal ordering become more evident. For the various populations, we take the density N and normalise with $N_{\max}$ according the values in Tab. 7.1 for a circular confinement of radius $R_c = 15\,\mu$m.

In the absence of Quincke rotation, single crystallites form with $E < E_Q$. As before, crystallites are characterised by high ψ_6 order, vanishing with decreasing N, and equivalently for N (Fig. 7.4**a**). We focus on the highly packed assemblies, i.e. $N \geq 55$.

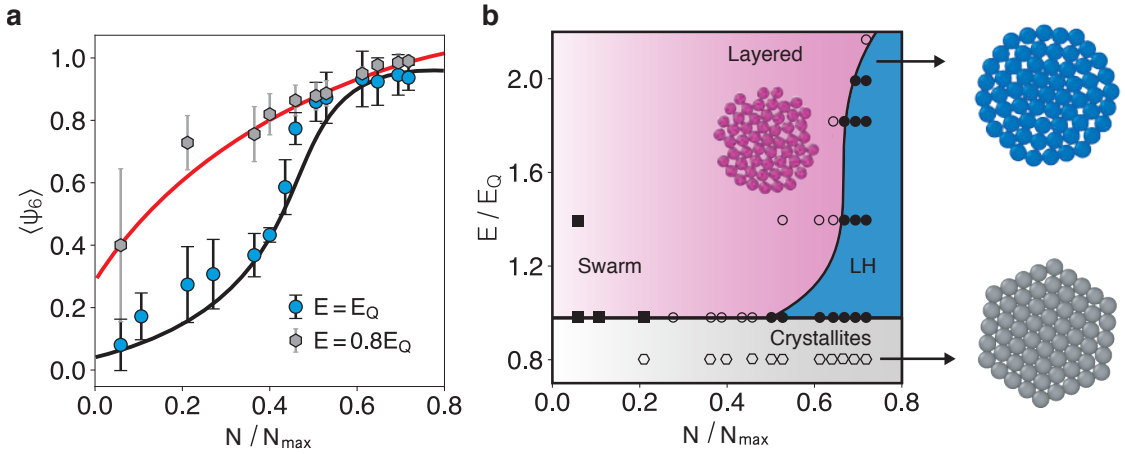

Figure 7.4: **Local ordering and phase diagram of rollers in strong confinement. a.** Mean orientational ordering characterised by ψ_6 on increasing N. Error bars are 1 s.d. Solid lines are guides to the eye. **b.** Suggested diagram according measurements of structure and motility. Different states are show: (⬡) Crystallites, (■) Swarms, (◯) Layered structures, and (●) Layered-Hexagonal bistable structures. Arrow indicate a crystallite in grey, a LH bistable assembly in blue, and a layered fluid in pink.

Despite strong boundary curvature, highly hexagonal structures form with $N < N_{\max}$. This in contrast to driven assemblies [315], where curvature suppresses ψ_6 close to the boundary. Here the hydrodynamic interactions from the EHD flows seem sufficient to hold the orientational order at $E = 0.8E_Q$ (see grey symbols in Fig. 7.4**a**). For densities of $N \geq 0.7N_{\max}$ we find almost perfect hexagonal ordering, among which a population of $N = 61$ yields a perfect hexagonal shape (see grey assembly pointed by the arrow in 7.4b). We give more attention to assemblies of this kind in the following sections.

With increasing the magnitude of the field to $E = E_Q$ aggregate motility begins, akin to amoeba aggregates. In Fig. 7.4**a** we map the change of ψ_6 with varying the density. Here, three regimes on orientational ordering are identified. At low densities, ψ_6 drops with small aggregates showing swarming. At intermediate densities, e.g. $0.25 \leq N/N_{\max} < 0.5$, the excluded volume interactions in the population lead to the increase of ψ_6, while the strong confinement induces layer development that mimics the

boundary shape. Figure 7.3 shows the corresponding density profiles indicating layering. For larger densities, the hexagonal order reaches values comparable to the passive crystallites, while competing where strong layering. Moreover, the simultaneous contributions from strong curvature and local ordering yield commensurate and incommensurate states. Thus, structural competition between concentrically layered configurations and structures of high hexagonal ordering are observed with $N \geq 0.64 N_{\max}$. We refer to these assemblies as bistable in terms of structural features.

A suggested phase diagram for Quincke rollers under strong confinement is given in Fig. 7.4**b**. The different phases are discriminated between active and passive assemblies. The increment on both N and E turn swarming arrays into layered fluid structures. Those layers form concentrically, given the strong confinement, with the azimuthal velocity controlled with the field magnitude (Fig. 7.2**d**). Increasing N yields competition between highly ordered structures and layering from confinement. Thus, bistability between highly ordered structures and fluid layers are observed. These structures are labelled as LH at the diagram in 7.4b. We focus on assemblies of high density that show competition between local order, activity and boundary conditions. The analysis on a specific population indicates commensurate-incommensurate states with all these contributions acting simultaneously on the assemblies.

7.5 Layered Structures at High Densities

Given the different phase behaviour according to the local structure and dynamics, we now proceed to analyse the layered and bistable assemblies (Fig 7.6a). At low densities, swarms have a strong contribution from rotational diffusion, and thus, Péclet numbers of low values result. In contrast, self-assembled layers exhibit vortices, whose rotational speed v_0 is controlled with $E \geq E_Q$. Using the same approach as in Sec. 6.3, we measure the roller velocity to determine Péclet numbers $N = 24$. Figure 7.5**a** compares Pe numbers

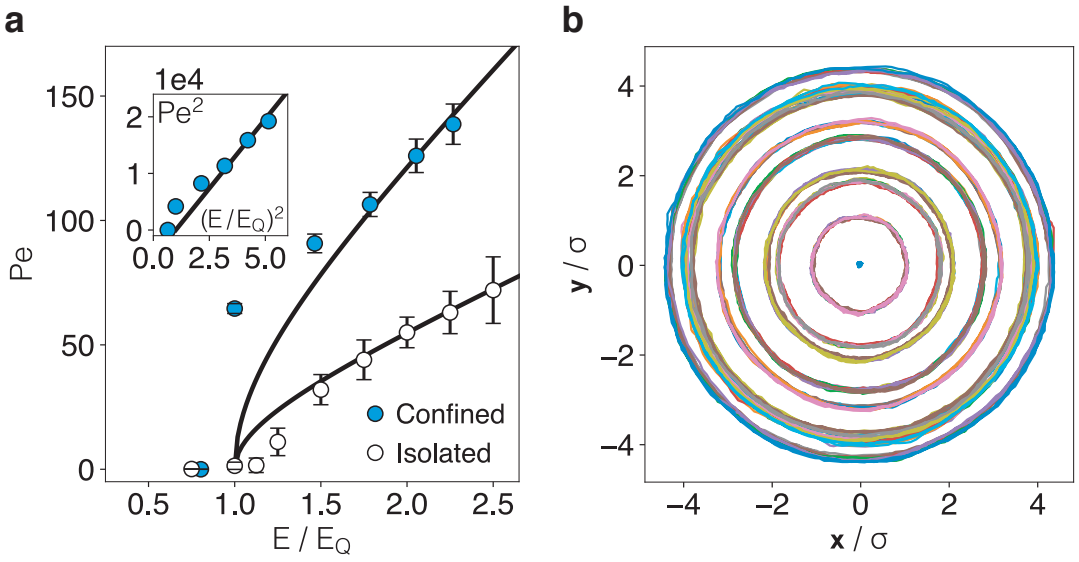

Figure 7.5: **Péclet numbers for a confined population. a.** Comparison of Péclet numbers between isolated rollers and a confined population of $N = 24$, obtained by varying the field magnitude E. Inset shows Pe^2 versus $(E/E_Q)^2$. Symbols are from experiments, and solid lines are $\propto \frac{\sigma}{2\tau}\sqrt{(E/E_Q^2 - 1)}$, where $\tau \approx 1$ms is the Maxwell-Wagner relaxation time. **b.** Experimental trajectories obtained from packed structures, i.e. bistable assemblies, where concentric layers are well defined.

for isolated particles used in Chap. 6, and the values obtained when using a confined population. It is worth noting the increase of Pe numbers when using a population of $N = 24$, which shows coherent motion [310]. As shown before in Fig. 7.2**d**, the rotational frequency on microscopic vortices are characterised by the overlap function $Q(t)$. For a single layer the angular velocity ω, and thus the frequency, is controlled with the field strength E.

In the absence of self-propulsion, steady crystallites develop (see Sec. 6.4 for details on aggregation) with increased population N. As the activity increases, concentric multi-layered assemblies form, with the rollers moving azimuthally under the influence of the circular boundary. Thus, we investigate the rotational behaviour of multi-layered structures (Fig. 7.5**b**). Akin to the colloidal layers driven by an adaptive boundary [346], we foresee a rich behaviour based on local structure and individual layer dynamics.

We start by looking at the layer structure in high density assemblies, followed by an intralayer dynamical analysis.

7.5.1 Local Structure

We analyse local structures forming with densities $N \geq 0.55N_{\max}$, in which layering and local order are more evident. Structures of different density N, at Pe = 90 ($E = 1.4E_Q$) are illustrated in Fig. 7.6**a**. By decreasing N incomplete layers are observed, mostly near the boundary as the assemblies are well packed at the interior. Further reduction of the area fraction, $N < 0.55N_{\max}$ promotes less resolved layers, with the roller motion changing between layers. For the densities considered here, well defined periodic patterns are observed from the individual roller trajectories, as illustrated in Fig. 7.5**b**.

With rollers self-propelling, e.g. Pe = 90, well defined rotating layers develop. Figure 7.6**b**. shows the corresponding density profiles $N(r)$ for the structures observed with high densities. For a population of $N = 47$, the peaks in $N(r)$ indicate the fluid layered structure, despite voids due to insufficient population. Increasing the density to $N = 55$, promotes the radial increase in population, as shown in $N(r)$. With this activity, $N = 47$ and $N = 55$ show globally high hexagonal order, given by the time average on ψ_6 (Fig. 7.4**a**). This is presumably related to the packed interior and coordination between outer layers. The increase of activity leads to the decorrelation of ψ_6, giving rise to a more evident layered behaviour (Fig. 7.5**b** and 7.7).

For denser structures, with $N \geq 0.69N_{\max}$ layer peaks in $N(r)$ are equally defined, with a characteristic split over layers $l = 2, 3$ and 4 where l is the layer index. Highly ordered samples are characterised by split peaks, indicating high ψ_6. This split is also observed in the trajectories shown in Fig. 7.5**b**, where the peaks lack definition and high ψ_6 results in rigid body behaviour. To account for the effect of having less population, the local cell area can be measured from Voronoi tessellations over all layers. With the

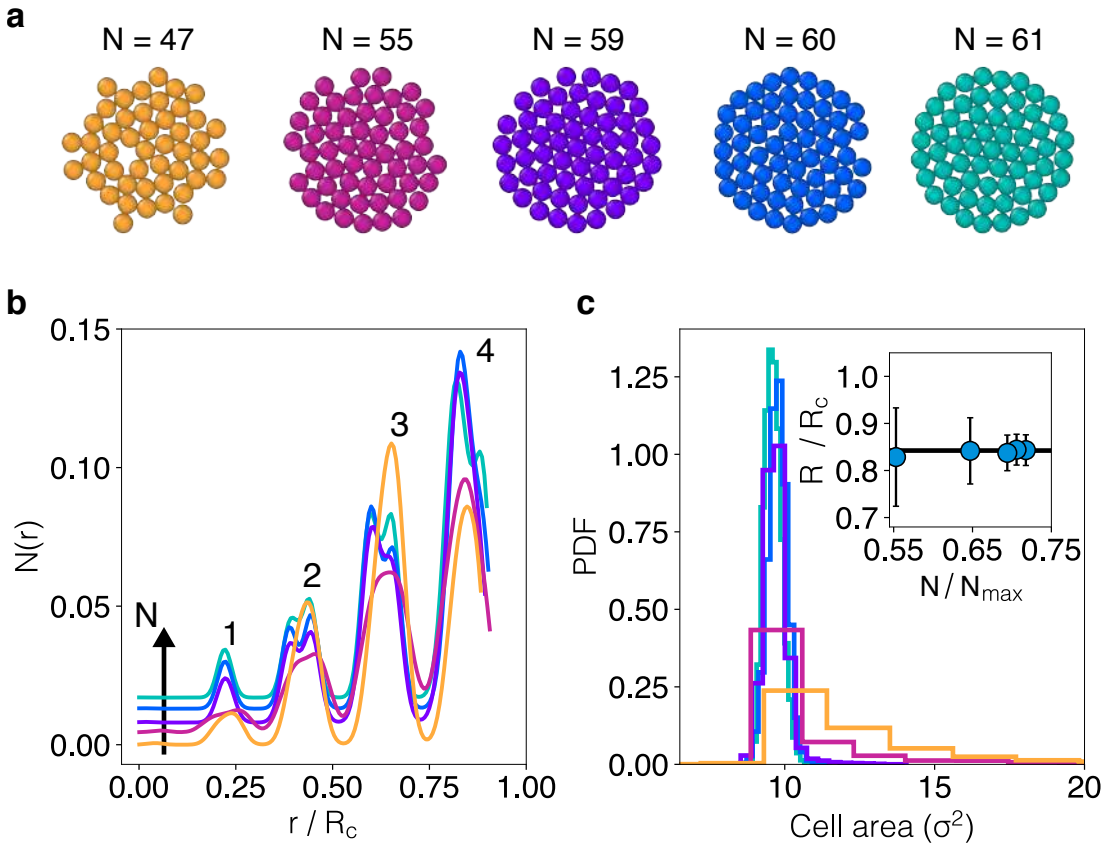

Figure 7.6: **High density layered structures. a.** Illustrations of the layered structures forming with different N. **b.** Density distribution profiles normalised by the total population N. Colors correspond to structures in **a**. Numbers over the peaks indicate the layer number. **c.** Cell area distribution of $l = 3$ obtained from Voronoi tessellation. Inset: Normalised assembly radius R.

exception of layers in $N = 61$, incomplete assemblies are observed, with missing rollers mostly at $l = 4$. Even though the interlayer separation is constant, with the structures having a similar radius R among different densities (7.6c inset), such voids might affect the local order. Figure 7.6**c** shows the normalised area distribution for the local cells at the third layer for every N. As rollers get removed from the outer layer, the cell area increases significantly, compared to the closed-packed structures at $N \geq 0.69N_{\text{max}}$.

In addition to the observations from the density profiles and void formation, we look at the local orientational ordering. For populations of $N < 0.69N_{\text{max}}$ layering is

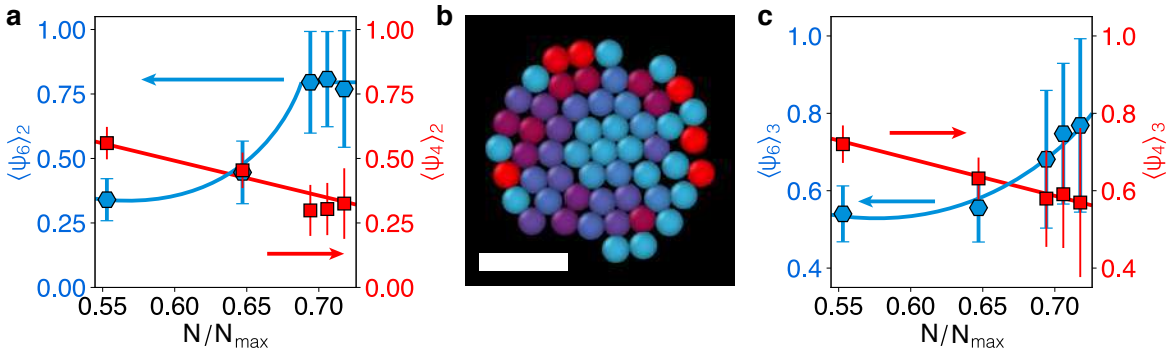

Figure 7.7: **Structural order of intermediate layers. a** and **c** correspond to ψ_6 (blue hexagons) and ψ_4 (red squares) orientational order within the second and third layers in populations with different N. Pe = 90. Arrows indicate the corresponding axis for ψ_6 and ψ_4. **b.** Local hexagonal order in a population $N = 55$. Light blue indicates $\psi_6 \approx 1$, whereas red is disorder. Scale bar is $10\,\mu$m

well defined, combined with the increase of void space. In the absence of confinement, passive and active amoeba crystallites exhibit high ψ_6 (Sec. 6.5.2). Curvature from strong confinement suppresses ψ_6, and promotes the emergence of fluid layers. The frustration on the hexagonal order might be well understood in terms of boundary-induced defects. Hence, we measure the global four-fold orientational order $\psi_4 = \frac{1}{N}\sum_j^N |\psi_4^j|$, where

$$\psi_4^j \equiv \frac{1}{Z_j}\sum_{k=1}^{Z_j} \exp\left(i4\theta_k^j\right), \tag{7.1}$$

and Z_j is the co-ordination number of particle j. Layered-hexagonal bistable structures form with Pe > 0 ($E \geq E_Q$), and consist of a core with rigid-like structure and a fluid shell. The core is given by a central roller, which motion is inhibited by an adjacent first layer, as N increases. For packed interiors, the local order results of high ψ_6 (see Fig. 7.7**b**). For a circular confinement of radius R_c, the number of layers allow one to investigate the local structure between a hexagonal core and a fluid boundary. Thus, we measure coordination order of layers $l = 2,3$ by means of both ψ_6 and ψ_4. Figures 7.7**a** and **c** show the local order on $l = 2,3$. With $N = 55$ the magnitude from four-fold coordination is higher then ψ_6, in agreement with $N(r)$ showing strong layering.

On increasing the area fraction to $N \approx 0.64N_{\max}$, both values of ψ_6 and ψ_4 are of similar magnitude, suggesting strong competition between layering and ψ_6. The middle panel in Fig. 7.7 corresponds to $N \approx 0.64N_{\max}$. On increasing the packing fraction, the contribution from hexagonal ordering becomes stronger, as indicated by the peaks split on the density profile (Fig. 7.6**b**). Equally, populations at $N \geq 0.69N_{\max}$ show increasing ψ_6. For $l = 2$, the increase is prominent with the hexagonal order extending from the core. Similarly, defects from layering decay as ψ_6 grows even at $l = 3$. Thus, rigid body behaviour combined with fluid motion is identified at high densities with Pe = 90. Later we analyse in detail the variation of Pe for a specific population.

7.5.2 Rotation Profiles

Coherent flows emerge from roller propulsion combined with alignment interactions and strong confinement (Fig. 7.5**b**). Structures of concentric layers spontaneously form with increasing N and $E \geq E_Q$. For the different states shown in the phase diagram (Fig. 7.4), analysis of density and local order leads to the determination of the structural features that play a role in the dynamics. To gain further insight we investigate the rotational behaviour of structures showing coherent motion.

Following the identification of concentric assemblies in population of high density, we proceed to analyse the individual layer dynamics. We measure the angular ω and linear velocity, $v = r\omega$, profiles for each layer forming in assemblies of variant density N. For the densities considered here, i.e. $N \geq 55$, structures with a steady central roller form. We measure the azimuthal displacement $\Delta\varphi$ for every roller taking the central coordinate of the assembly as a reference. Thus, we investigate the effects from local structure and strong layering over individual layer dynamics.

For the populations investigated previously, the corresponding profiles of the radially dependent angular velocities $\omega(r)$ at Pe = 90 are shown in Fig. 7.8**a**. It is noted that for

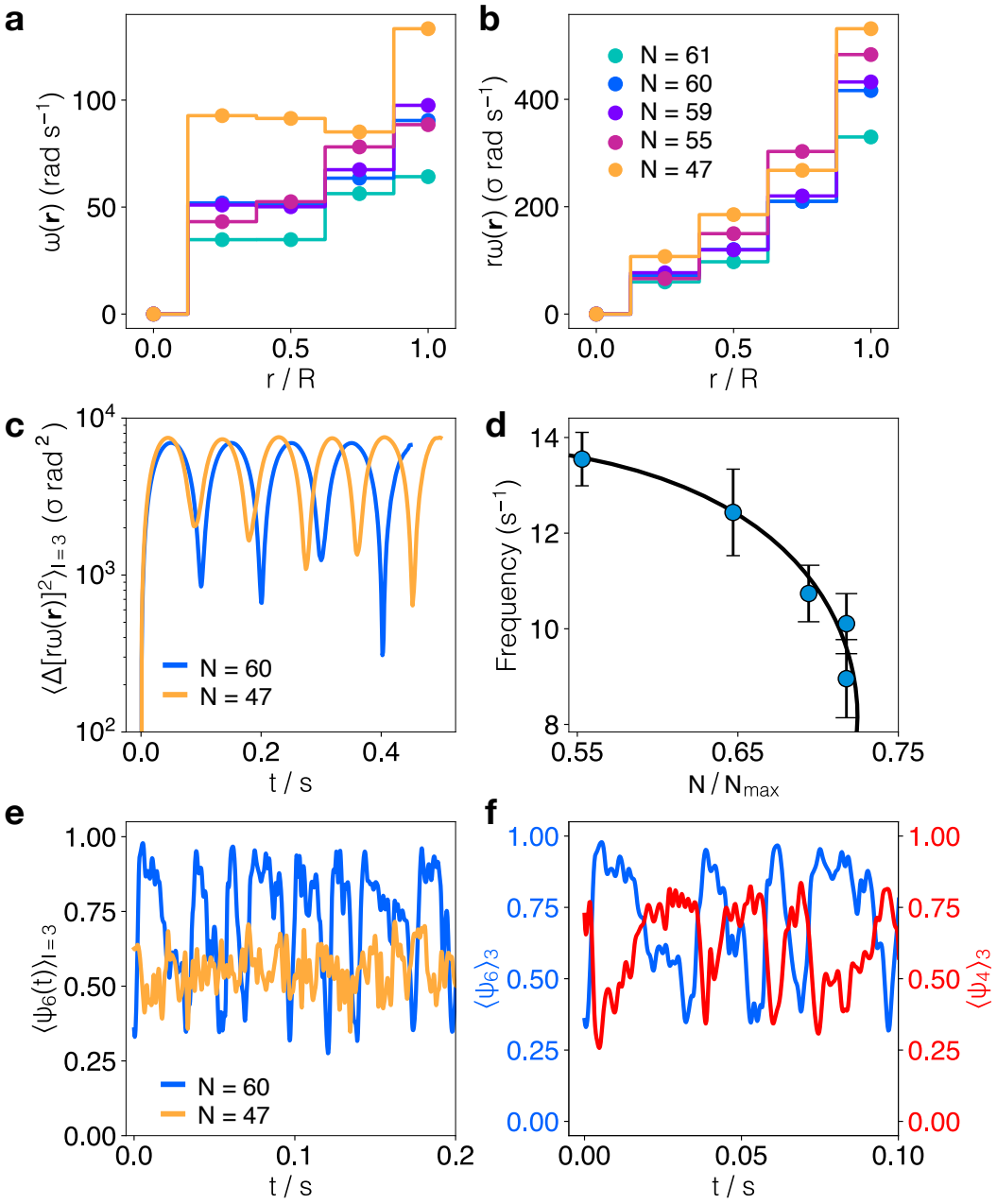

Figure 7.8: **Rotational dynamics. a** and **b** Mean angular and tangential layer velocities for the different assemblies of population N. Pe = 90. Colours compound to the populations indicated in **b**. **c.** Mean squared tangential displacement plotted on a y-log scale versus linear time, showing periodicity of $l = 3$. **d.** Rotation frequency of the same layer, extracted from tangential displacements. Solid line is a guide. **e.** Time dependent ψ_6 measured on the same layer as in **c** for $N = 47, 60$. **f.** Time evolution of ψ_6 (blue) and ψ_4 (red) for $N = 60$.

all the structures the central point at $r = 0$ corresponds to a pinned roller, whose motility is suppressed by the concentric layers. Starting with the most layered structures, with $N \leq 0.64N_{\max}$, fluid behaviour is observed with every layer slipping with respect of the adjacent layers. With $N = 47$, ω seems to be higher at the interior with respect of $l = 3$, and with voids enabling rollers to self-propel faster at $l = 4$. Similar fluid behaviour is observed with $N = 55$, with the layers slipping past one another as they rotate with different ω. For both cases, we find a good agreement between the strong layering on $N(r)$ and the velocity profiles. Thus, we can interpret this behaviour as a high shear rate between layers with densities $N \leq 0.64N_{\max}$.

On the other hand, assemblies of highest densities, $N \geq 0.69N_{\max}$ exhibit competition between layering and hexagonal order (Fig. 7.7). Rotational profiles point to rigid body dynamics, with the internal layers rotating with equal ω, while layers at $r > 0.5R$ show fluid-like behaviour. This is similar to the shear banding of colloidal glasses [361], in which fluid-like bands coexist with solid structures. In this sense, fluctuations of ψ_6 are observed at $l = 3$ from the strong competition between local order and layering from the adjacent layer at $r = R$ (Fig. 7.8**e**). The hexagonal order drops as the outermost layer develops defects, pointed by the increased four-fold order ψ_4 (Fig 7.8f)). Thus, the interchange mechanism between ψ_6 and ψ_4 may be thought of as a change from commensurate to incommensurate states between layers. For a purely layered structure, fluctuations of the orientational order ψ_6 are less pronounced with decreasing N, in agreement with the fluid-like behaviour.

To account for the local density and the position dependent rotation we show in Fig. 7.8**b** the tangential velocity profiles, given by the product between the radial position r and the layer angular velocity, $v = r\omega$. Self-propulsion of the outermost layer shows enhancement with decreasing the population, whereas the condensed layer between $0 < r < 0.5R$ displays equal behaviour for most of the populations. In addition to the

velocity profiles, we analyse the periodic behaviour by means of the mean squared tangential displacement, $\langle \Delta[r\omega(t)]^2 \rangle$. Figure 7.8**c** shows the tangential displacements of $l = 3$ in a fluid-like and LH structures, where the characteristic frequencies are appreciated. Measurements over the different structures indicate reduction on the mean frequency as N is increased. Thus, the higher rotational frequency displayed in smaller populations is readily associated with the fluidity, given by the small fluctuations of the local order 7.8e.

Combining analysis from local structure with rotational dynamics, we identify the role of layering and rigid body behaviour in the coherent flows. Overall, the effect of increasing N gives structures of high orientational order ψ_6 that compete with the strong layering imposed by the boundary (Fig. 7.6**b** and Fig. 7.7). For a given Péclet value greater than zero, Quincke rotation and alignment interactions act on the population, with the layer dynamics determined by the local structure (Fig. 7.8). Next, we proceed to investigate the role of activity for a population of given density.

7.6 Microgears with N=61, The Magic Number

The assembly and manipulation of micro-sized objects is of importance for micro-engineering and biological applications. In this sense, colloids not only offer a good model to investigate statistical physics, but also can be used as building blocks [229]. While external driving fields are commonly used for assembly and to induce actuation [346], the manipulation of micro-engineered inanimate objects can be achieved by active suspensions. Chemically fueled Janus spheres can be docked to microgears in order to exert body rotational motion [362]. Alternatively, unicellular swimming bacteria can be employed to power engineered micromotors [363, 364]. Self-assembly of spinning rotors is also possible with diffusiophoretic particles driven with light [365], or magnetically responsive Janus spheres [272].

In the previous sections we have shown the use of an active system combined with strong confinement, to self-assemble gear-like structures for which the dynamics are autonomous. The assemblies consist of a population of active Quincke rollers, able to self-propel individually. It is important to note that the assemblies here are larger hierarchical structures than those of driven rotors [365], allowing us to investigate multi-layer dynamics. In Chapter 6 we investigated the role of competing interactions acting on the rollers, and which contribution yields the formation of amoeba crystallites. The present Chapter introduces the use of strong circular confinement, which contribution results in structures of competing layered-hexagonal order (Fig. 7.7). For this, coherent motion is observed as the rollers simultaneously self-propulsion and self-assemble in layered structures. (Fig. 7.5**b**). On increasing the roller population N, packed structures of hexagonal order show internal rigid mechanics along with fluid-like behaviour near the boundary (Fig. 7.8).

Among the populations examined in the previous section, we find a population of $N = 61$ to be suitable for further investigation of the the role of activity in LH bistable structures. From the previous analysis, it is determined that concentric layers form around a suppressed roller. However, the hallmark of a population $N = 61$ is the formation of perfect concentric layers, in addition to the activity-dependent rotational behavior of microgears.

7.6.1 Activity Dependent Structural and Rotational Behaviour

Using the Péclet values determined in Sec. 7.5, we analyse the different structures resulting as the activity varies in many populations, of which $N = 61$ is the most interesting. Radial density profiles $N(r)$ are measured for different structures, with Pe values ranging between ≈ 0 to 140. In the absence of self-propulsion due to Quincke electro-rotation with Pe ≈ 0 ($E = 0.8E_Q$), samples with high orientational order ψ_6 form at the interior of

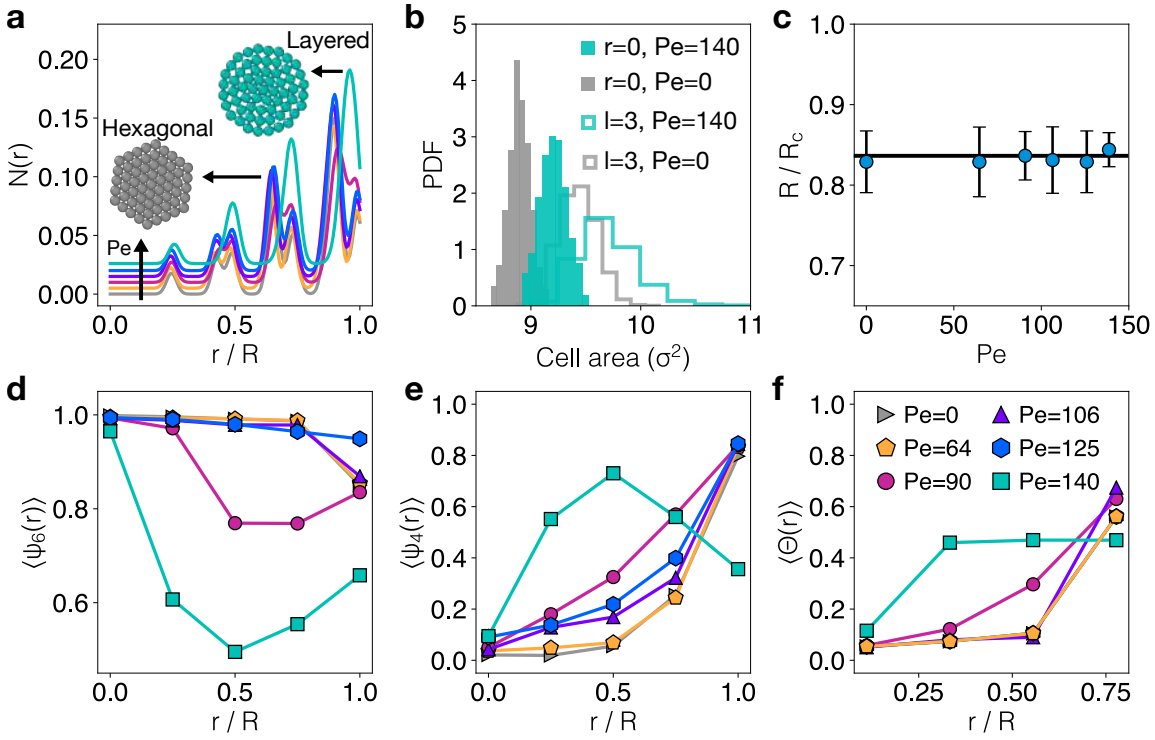

Figure 7.9: **Structure profile of N = 61. a.** Activity dependent density profiles $N(r)$. Vertical arrow indicates the increase of Pe, and colour on lines correspond to Pe = 0 (grey), Pe = 64 (yellow), Pe = 90 (pink), Pe = 106 (purple), Pe = 125 (blue), Pe = 150 (teal). Insets show layered and hexagonal structures. **b.** Cell area distributions for structures at different values of Pe. Filled histograms corresponds to the assembly centre $r = 0$, and lines to $r = 0.75R$. **c.** Mean assembly radius R, normalised by R_c. **d** and **e** Mean values on the $\psi_6(r)$ and $\psi_4(r)$ order parameters against Pe. **f.** Bond distortion parameter $\Theta(r)$ characterised between layers. $\langle ... \rangle$ in **d**, **e** and **f** indicates time average.

the confinement. Layering effects from the boundary are weak in the passive crystallites, as highly packed structures appear as a result of the EHD attractions. Crystallites are characterised by high ψ_6 in Fig. 7.9**d**, along with distinctive split peaks in $N(r)$. Passive structures remain steady when maintaining the field strength below E_Q, of which small vibrations give a Péclet value Pe ≈ 0. Thus, dynamically arrested crystallites appear within the timescales investigated in the laboratory framework.

Upon introducing activity, coherent flow is observed in samples of high density (Fig. 7.5**b**). Structures forming with different Pe values display well defined peaks in $N(r)$, of

which four concentric layers are identified (Fig. 7.9**a**), significantly less than the number of layers explored in flowing crystals [212]. With the field magnitude reaching E_Q, the roller self-propulsion emerges with Pe = 64. The yellow line in Fig. 7.9**a** corresponds to the density profile $N(r)$ of the first active assembly, which is of the same structure as with Pe = 0. This corresponds to a hexagonal crystal, where the formation of a layered fluid due to confinement seems negligible, as shown by the splitting on $N(r)$. Time average measurements of both ψ_6 and ψ_4 verify almost perfect hexagonal ordering (Fig. 7.9**d**,**e**), with the value on ψ_6 at the outermost layer decaying slightly as the structure is of finite size. The rigid body behaviour observed in the structure is confirmed by the velocity profile $\omega(r)$ in Fig. 7.10**a**, showing rotation on all layers with same angular velocity (see Appendix C.1.2 for details on Supplementary Movie 2). This rigid body rotation is given by simultaneous contribution from self-propulsion and hydrodynamic attractions, such as in amoebae aggregates (Sec. 6.5.1). Also, at this activity value, the rotating crystals are of similar rotational dynamics to those magnetically driven [272], and exhibit rotation frequencies one order of magnitude above driven micromotors [364, 365] and several above the optically driven system in Ref. [346].

The increase of activity produces structural change as indicated in Fig. 7.9. Note that with Pe = 90 the hexagonal order drops, along with a slight shift in $N(r)$. It is worth noting that the angular velocity measurements indicate two rotational regimes of the structure. Rigid body rotation is observed at the interior, whereas the outer layers exhibit slip behaviour with different ω, as shown in Fig. 7.10**a**. It is interesting to note that the competition between rigid hexagonal and layered fluid behaviour. The simultaneous decay in ψ_6 and increasing ψ_4 reflects the structural competition between neighbouring layers (Fig. 7.9**d**,**e**). Fluid layer formation at high density requires a slight layer grow, as indicated by the increase of the assembly radius R and by the shift in $N(r)$ (Fig. 7.9**a**,**c**). Thus, going from a rigid state of high hexagonal order to a LH bistable structure with

fluid layers involves a melting-like process, that can be understood in terms of bond angle breaking. To account for the bond change between adjacent layers we introduce a bond distortion parameter, given by

$$\Theta = \frac{1}{\theta^\star} \sum_{i}^{Z} |\theta_i - \theta^\star|, \tag{7.2}$$

that runs over the number Z of neighbours determined with a Delaunay triangulation. Acute angles result from a triangular lattice made by a HCP structures, hence we consider $\theta^\star = \frac{\pi}{3}$. This distortion parameter returns a scale where $\Theta = 0$ represents no angular change between neighbours and $\Theta = 1$ is complete distortion with the formation of right angled triangles. Figure 7.9**f** shows the increase of the distortion Θ between central and outer layers, in agreement with the results on ψ_4 at Pe = 90.

On increasing the activity to Pe = 106 the hexagonal order recovers, as indicated by the density profile $N(r)$ and local order ψ_6 in Fig. 7.9. This corresponds to the same hexagonal structure forming with Pe = 64. However, the angular velocities in the innermost layers show inverse rotational behaviour to Pe = 90. Here, central rigid rotation occurs with higher rates than in the slipping outer layers, as shown in Fig. 7.10**a**. Additional increasing of the activity to Pe = 125, results in a rotational behaviour similar to the one observed with Pe = 106. It is important to note the low distortion marked by Θ and fast recovery from the time average measurements of ψ_6 at Pe = 106 and 125 (Fig. 7.9**d**,**f**).

For Pe = 140 the rotational behaviour is markedly different from that of a central rigid body. The angular velocity profile in Fig. 7.10a indicates vanishing of the internal rigid rotation with complete slip behaviour, as ω decays outwards. The profile of the tangential velocity shows an inverse behaviour, with the linear velocity increasing with the layer position r (Fig. 7.10**b**). The rotational behaviour reflects on the layered structure, which displays fluid-like characteristics, with the peaks in the density profile $N(r)$ in Fig. 7.9**a**

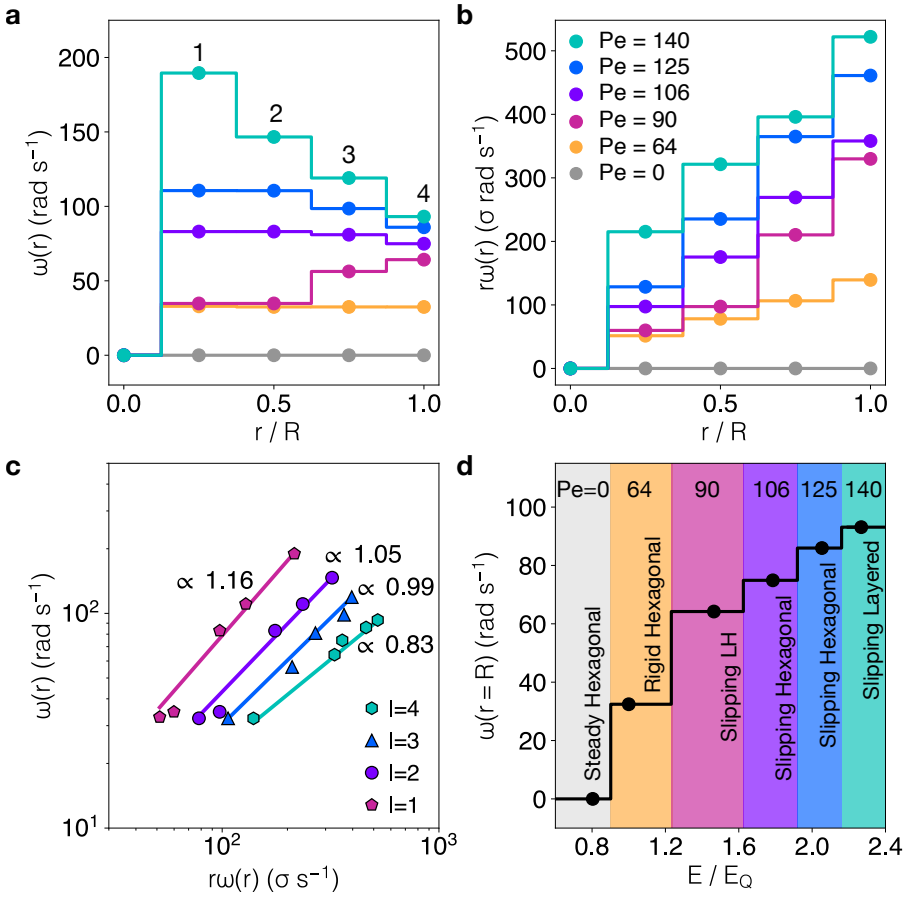

Figure 7.10: **Activity driven rotational behaviour. a.** Angular velocity $\omega(r)$ measured for every layer l at different Pe. **b.** Corresponding tangential velocities obtained from **a.** **c.** Linear relation between ω and $r\omega$ for every layer l as indicated by numbers in **a**. **d.** Angular velocities of the outermost layer against the applied field E. Different coloured regions indicate the observed behaviour with changing activity.

showing a lack of splitting, along with the increase of the assembly radius R (Fig. 7.9**c**). To corroborate the structural change at high activity, in Fig. 7.9**b** we plot the distribution of area occupied by the central roller at $r/R = 0$ and layer $l = 3$ for assemblies at different Péclet values. For Pe = 140 the area shows increment compared to the compressed structure at Pe = 0. Moreover, fluid-like behaviour is characterised by the drop in the time average measurements of ψ_6, equally with increasing ψ_4 and bond angle distortion Θ (Fig. 6.7**d-f**).

The relation between linear v and angular ω velocities is shown in Fig. 7.10**c**. Power

law fits on the measurements from profiles in Figs. 7.10**a,b** show scaling exponents increasing for the inner layers. The activity dependent behaviour is summarised in Fig. 7.10**d**, that shows the change of angular velocity at $r = R$ with the field strength E. The different regions are labelled according our measurements of structure and rotational behaviour. For Pe > 0 we find the rigid hexagonal behaviour at Pe = 64 of least complexity in contrast with assemblies exhibiting slip behaviour with higher activity.

7.6.2 Pe = 64, Rigid Body Rotation

In the absence of self-propulsion, e.g. Pe ≈ 0, the attraction between colloids leads to crystallite formation, as detailed in Sec. 6.4. For a confined population of $N = 61$, this results in the formation of a nearly perfect hexagonal structure. The increase of the electric strength, to $E = E_Q$, leads to the emergence of Quincke rotation. For rollers in bulk, the simultaneous contribution from attraction and activity leads to the motility of amoebae aggregates. When confined, the same effects result in the rigid rotation of a single amoeba at Pe = 64, as shown in Fig. 7.10**a** and Fig. 7.11**a**. For a rotating crystallite, the mean value of the hexagonal order $\psi_6(t)$ remains near perfect ordering, as indicated by Fig. 7.11**b**. Despite showing the least complex behavior compared to the rotation at higher activity, this rigid motion exhibits faster rotation than the bacteria-driven [364] and light-activated [365] rotors, with $\omega \approx 30 rad\, s^{-1}$ (Fig. 7.10**a**).

7.6.3 Pe = 90, Layered-Hexagonal Bistability

Beyond the rigid body behaviour observed at Pe = 64, the increase of activity to Pe = 90 results in the development of LH bistable assemblies. Measurements of the structure show competition between hexagonal and fluid-like behaviour, according the local order given by ψ_6 and ψ_4 (Fig. 7.9**d,e**). Moreover, the velocity profiles in Fig. 7.10**a** indicate fluid motion of the outer layers in contrast to the rigid rotation at the centre. As layers slip

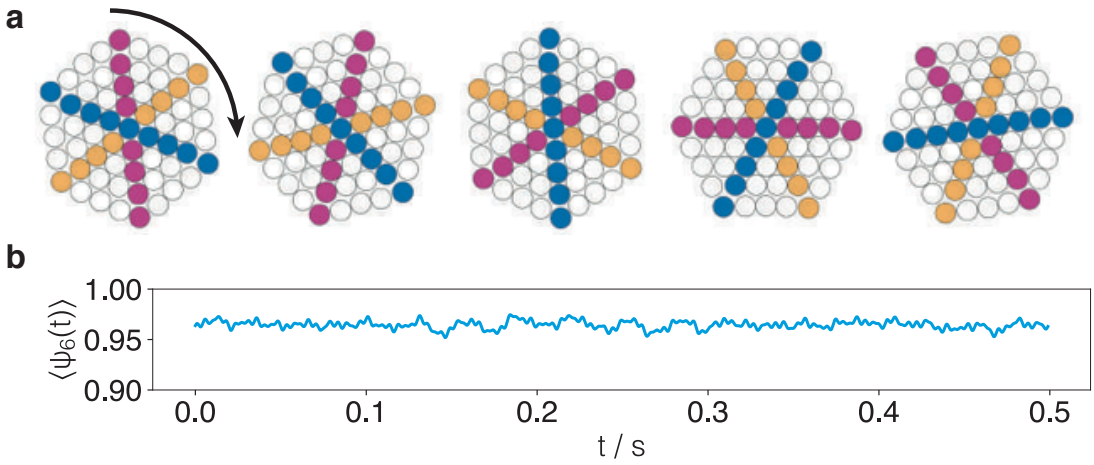

Figure 7.11: **Pe = 64, Rigid Body Rotation. a** Rotation time sequence indicated by the C_6 symmetry lines of the hexagonal crystallite. **b.** Time dependence of the mean hexagonal order ψ_6. See Supplementary Movie 2 in Appendix C.1.2

past one another, angular distortion Θ develops within neighbour layers. Nonetheless, structural fluctuations develop with slipping layers (Fig. 7.8**f**), suggesting variation between configurations.

Alternation between solid-like and layered-hexagonal configurations develops at short timescales. In Fig. 7.12**a** the two configurations are shown. The image in red corresponds to a hexagonal sample of ordered structure (Fig. 7.9). On the other hand, the slip behaviour results in LH configurations as shown on the right side of Fig. 7.12**a**. Thus, by varying between rigid-like and fluid-like behaviour a stick-slip mechanism develops, similar to that in driven colloids [346].

Structural features of the H and LH configurations are well characterised by the density profiles $N(r)$ and local ordering ψ_6 (Fig. 7.9**a**,**d**). For a time sequence showing configurational change, we analyse the fluctuations between H and LH structures at constant activity with Pe = 90. In addition, a good distinction between the hexagonal and the bistable states can be gained by means of radial density profiles $N(r)$, as in Fig. 7.10**a**. Moreover, the slip behaviour of the outer layers develops instantaneous change of the assembly radius R, measured as the distance between the central roller and

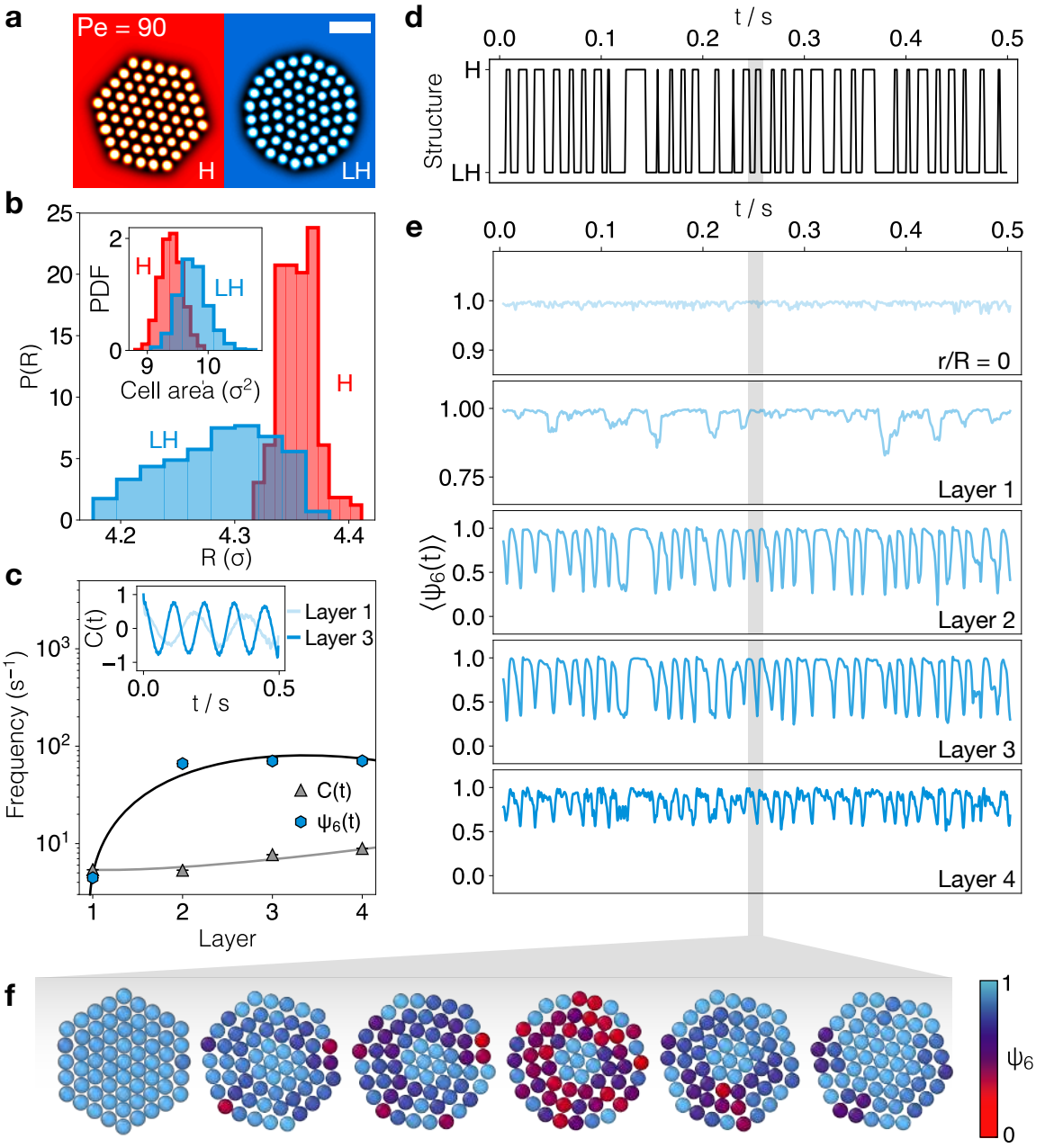

Figure 7.12: **Pe = 90, Hexagonal-Layered Bistable Rotation. a.** Micrographs of the variant structures. Left: Hexagonal (H) structure. Right: Layered-hexagonal (LH) bistable structure. Scale bar is 10 μm. **b.** Assembly radius distribution. Inset: cell area distribution for rollers at $l = 3$. Labels correspond to images in **a**. **c.** Rotational and fluctuational ψ_6 frequencies extracted from $C(t)$ and $\psi_6(t)$. Inset: Velocity autocorrelation functions $C(t)$ measured at layers $l = 1$ and $l = 3$. Lines are guides to the eye. **d.** Time variation between H and LH structures. **e.** Time average measurements of ψ_6 for each layer. **f.** Time sequence of the structures corresponding to the shade regions in **d** and **e**. Illustrations show the change of the local ψ_6. See details on Supplementary Movie 3 in Appendix C.1.2

the outermost layer. Note that H structures exhibit increased R, as illustrated in Fig. 7.12**b**. Simultaneously, slipping events on the outermost layer promote the increase of space available for rollers at layer $l = 3$. This results in contrast with the well packed hexagonal configurations (Inset in 7.12b). With these features, we identify the number of variations between H and LH dynamical structures (7.12d). To compare with the structural variations, we extract the rotation rates for each layer from the velocity autocorrelations,

$$C(t) = \frac{\mathbf{v}(t) \cdot \mathbf{v}(t+\tau)}{\mathbf{v}^2_{t=0}}, \tag{7.3}$$

displayed at the inset in Fig. 7.12**c** for layers $l = 1$ and $l = 3$. Each period is taken with $C(t)$ increasing towards $C(t = 0)$.

Periodicity in structural variations is measured by considering the time dependence of the local structure. Taking the average over all rollers at every layer we measure the dynamical order $\psi_6(t)$. Figure 7.12**e** shows the variations in local structure resolved for individual layers. As observed in Fig. 7.8**f**, each drop in ψ_6 corresponds to increasing four-fold order ψ_4, thus bond distortion between adjacent layers (Fig. 7.9**d**-**f**). For individual layers the structural variation periodicity is extracted from the decay of ψ_6. The rigid body behaviour at the interior is verified with the small fluctuations of the central roller at $r/R = 0$ and first layer. Note that variations on ψ_6 are more significant in $l = 2$, despite the rigid rotation observed with the angular velocity ω profile in Fig. 7.10**a**. This corresponds to an overtaking process of rollers being left behind by the faster-moving neighbours in outer layers. Thus, the instantaneous increase of the four-fold order ψ_4 with the third layer slipping over $l = 2$. The fluctuations of the outermost layers show coupling as rollers slip past one another. The decay events of ψ_6 indicate slipping frequencies over an order of magnitude above rotation periods, as observed in Fig. 7.12**c**.

Overtaking events developing at the outer layers distort the bonds between adjacent

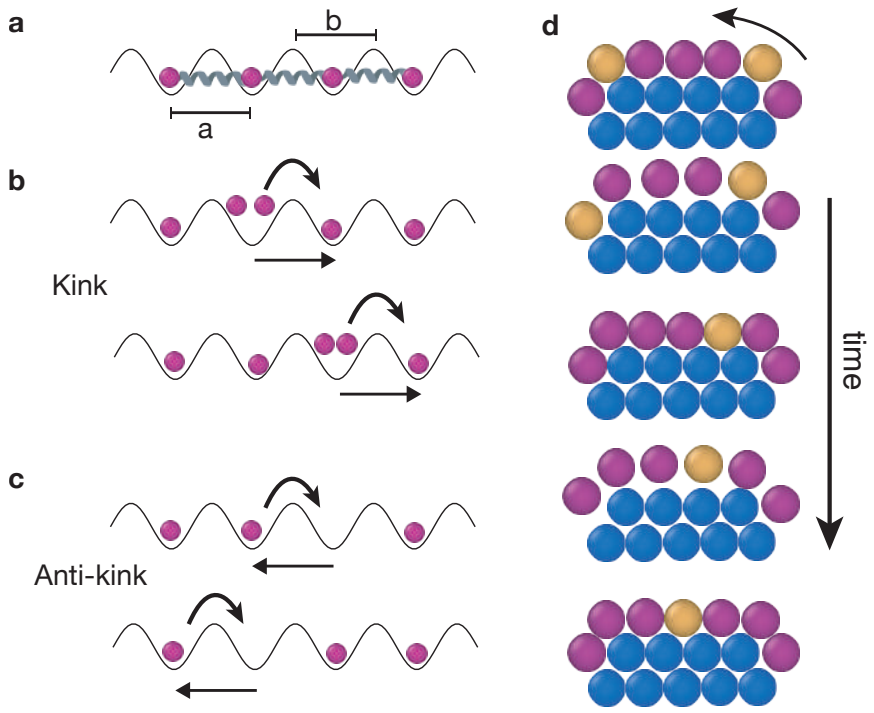

Figure 7.13: **Frenkel-Kontorova model. a.** Illustration of the 1D Frenkel-Kontorova model. Sliding particles are treated as a periodic lattice connected by stiff springs of distance a. The substrate is a periodic lattice of subspacing b. **b.** Kinks are a compression of a, and propagate according the arrows. **c.** Anti-kinks are local expansions of the chain a, and their displacement is opposite to kinks. **d.** Time sequence showing a representation of the Frenkel-Kontorova model in our system. A layer slides over a substrate of blue particles, as indicated by the yellow roller. Commensurate-incomensurate configurations result with the chain sliding.

layers, characterised by Θ in Fig. 7.9**f**. Thus, a dropping of the hexagonal order becomes evident as four-fold coordinated regions develop. By considering topology, emergence of five-fold and seven-fold coordination regions is given with increasing ψ_4. Figure 7.12**f** gives a short sequence of an assembly showing local variation of the roller orientational order ψ_6. Structures in 7.12**f** correspond to the configuration change indicated by shaded region in 7.12**d,e**. Dislocations develop over the six-fold coordinated regions (blue regions) with the outer layers showing instantaneous fluid-like behaviour. At the interior, the dominant rigid behaviour protects the hexagonal structure from the propagation of defects.

In addition to the stick-slip behaviour developed from the fluid-like nature of the outer layers, configurational change can be understood in terms of commensurability. For a one-dimensional system, the Frenkel-Kontorova model is the simplest mechanical model to investigate adsorption on periodic lattices [38]. This model consists of adsorbed species on a substrate, treated as a harmonic chain of spacing a. On the other hand, the substrate is modeled as a one-dimensional periodic lattice, which interaction with the adsorbed particles give either commensurate or incomensurate configurations. A schematic representation of the model is given in Fig. 7.13**a**. Moreover, the Frenkel-Kontorova model suggests the emergence of topological solitons, named kinks and anti-kinks. A kink develops with two particle in the same potential well, leading to local chain compression. In contrast, anti-kinks correspond to local extension of the particle chain with respect of the lattice subspacing b, resulting in empty wells [38, 366] (Fig. 7.13**b**).

Given the nature of our system, fluid-like layers slipping over internal rigid layers can be thought locally as a sliding chain on a lattice. For a rigid body at Pe = 64, commensurate conditions between the different layers are observed, indicated by the low distortion and high orientational order (Fig. 7.9**d**,**f**). Given the variantion of configurations at Pe = 90, we consider the instantaneous commensurate-incommensurate states. Competition between layering at the outside and rigid body behaviour at the centre makes the third layer as good candidate to investigate the process (Fig. 7.10**a**). Thus, we select the second layer as the locally periodic substrate.

Commensurability is observed in H structures, whereas the LH configurations lead to chain sliding. Figure 7.14**c** shows a time sequence for the varying configurations as in 7.12**d**. The corresponding structures and local deformation are shown in Fig. 7.14**a**. Distortion at the assembly centre is not detected, in agreement with the sequence in Fig. 7.12**f**, and with the local ordering observed in Fig. 7.12**e** for $l = 1$. For H configurations

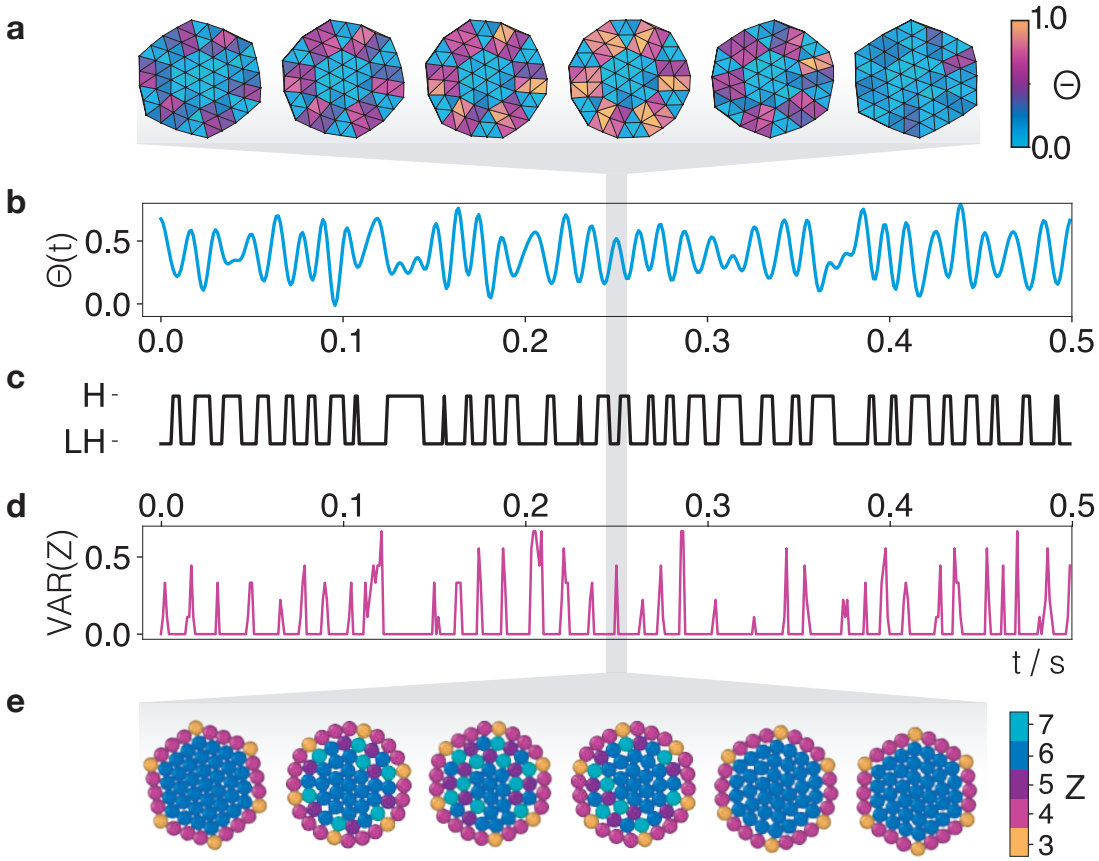

Figure 7.14: **Layer distortion. a.** Local distortion in structures indicated by shaded region. **b.** Time dependent bond-angle distortion $\Theta(t)$. **c.** Configuration change as in Fig. 7.12**d**. **d.** Fluctuations of the coordination number Z of rollers at $l = 3$. Shaded region corresponds to local dislocations in **e.** Colour on spheres indicates the local coordination number Z.

we find low distortion, indication of a commensurate state. Also, vanishing fluctuations of the coordination number Z are noted in Fig. 7.14**d**. On the other hand, the development of LH yields incommensurability, with dislocations emerging as layers slip over one another (Fig. 7.14**e** and Supplementary Movie 3 in Appendix C.1.2). Measurements of the time dependent Z fluctuations show increase of the number of dislocations with chain sliding. Moreover, the increasing angle distortions Θ between $l = 2$ and $l = 3$ suggest anti-kinks with a chain displacement of $b = \sigma$. The development of anti-kinks reduce significantly the friction between the sliding layer and the lattice [27], thus, the resulting

fluid-like behaviour of the outermost layers.

7.6.4 Pe = 106, 125. Slipping-Hexagonal

On increasing the activity to Pe = 106, 125, a slipping behaviour similar to the previously discussed case at Pe = 90 is observed. The profiles of the angular velocities ω (Fig. 7.10**a**) indicate fluid-like behaviour of the outer layers, while rigid rotation at the centre remains. However, it is important to note that with Pe = 104, 125 the velocity ω is larger at the interior, in contrast with Pe = 90. Strikingly, layered-hexagonal bistable configurations do not develop and only hexagonal structures are observed. Thus, a different approach is needed to account for the slip dynamics.

Analysis on the density profiles $N(r)$ and local orientational order ψ_6 and ψ_4 indicate similar hexagonal structures to the passive and rigid active assemblies with Pe = 0, 64 (Fig. 7.9). Thus, the time dependence of the orientational order $\psi_6(t)$ do not exhibit sharp decaying, even at the outer layers, compared to assemblies of lower population and LH bistable structures (Fig. 7.15**d**). In agreement, low bond distortion Θ is measured between the second and third layers (Fig. 7.15**f**). Hence, high commensurability is assumed throughout rotation, as dislocations are suppressed by the strong hexagonal behaviour. On the other hand, slip dynamics become evident from the difference in the velocity autocorrelation functions $C(t)$ in Fig. 7.15**d**, measured on individual layers. Thus, the dynamics are significantly distinct from rigid body behaviour, i.e. with Pe = 64.

We investigate the rotational behaviour of individual layers by means of the argument on the local orientational order $\arg(\psi_6)$. For highly ordered layers rotating with different angular velocities ω sharp changes of $\arg(\psi_6)$ occur. Figure 7.15**c** shows the variation of $\arg(\psi_6)$ for two different layers. The argument on the local orientation varies from π to $\pi/3$ with each layer performing a rotational period. At short times, the different layers show similar values on $\arg(\psi_6)$ indicating rigid-like rotation. Moreover, sharp

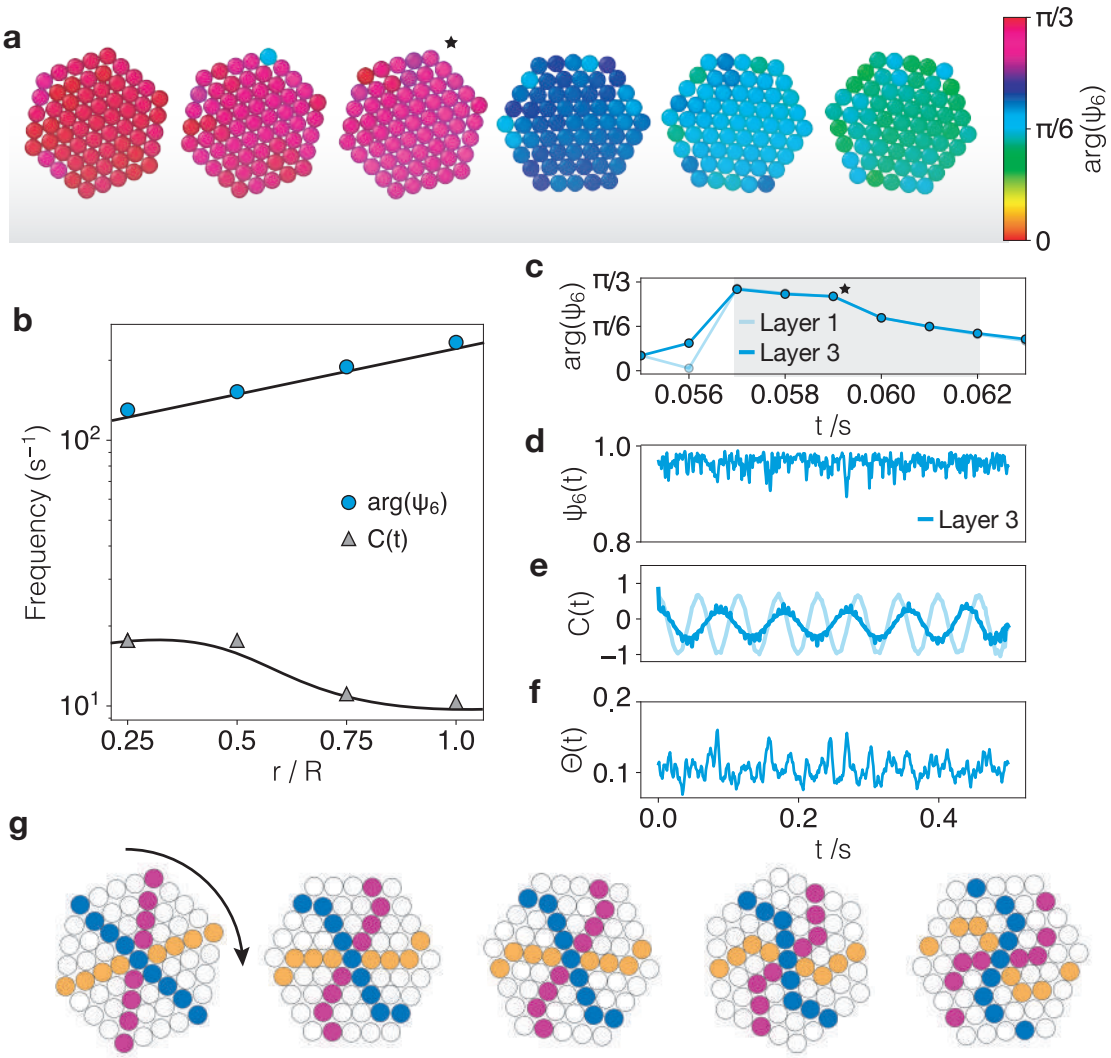

Figure 7.15: **Pe=125, Slipping-Hexagonal a.** Assembly rotation sequence showing slip behaviour. Colours indicate the local arg(ψ_6) indicated in colour bar. **b.** Rotation and change of the arg(ψ_6) frequencies calculated from **c** and **d**. **c**. Short time sequence of the time dependent arg(ψ_6) for first and third layers. The $\star$ indicates the corresponding structure in **a**. **d.** Velocity autocorrelation functions $C(t)$ for layers $l = 1, 3$. **e.** Bond-angle distortion in time $\Theta(r)$ between second and third layers. **f.** Time sequence of H structures showing simultaneous rotation and slipping. Colours indicate rollers at the C_6 symmetry lines at $t = 0$. Coloured particles are left behind as layers slip over one another. See Supplementary Movie 4 details in Appendix C.1.2.

variations are identified, as shown by $\star$ in Fig. 7.15**c**. The corresponding rotational and orientational change is indicated by the same symbol over the structure in Fig. 7.15**a**.

For single layers we measure the frequency of the arg(ψ_6) sharp variations. Figure 7.15**b** gives the frequency on rotation and orientation variations measured from signals in Figs. 7.15**c**,**d**. Sudden variations on arg(ψ_6) show larger frequencies with r increasing towards the boundary. Rotational frequencies extracted from autocorrelations $C(t)$ in Fig. 7.15**e** are in agreement with the angular velocity profiles in Fig. 7.9**a**. Nonetheless, the combination between slip behaviour and the absence of fluid layers remains unclear. Thus, the contribution from the confining eletrokinetic flow may be significant. Figure 7.15**g** illustrates a short rotation sequence of one assembly at Pe = 125. Coloured rollers indicate the structure symmetry lines at a given initial time. At short times lines persist, indicating rigid rotation. Sharp slip events become apparent with particles that are left behind in the outer layers.

7.6.5 Pe=140, Slipping-layered

In contrast to the assemblies at intermediate activities, e.g. Pe = 106, 125, complete layering is obtained with Pe = 140, as shown by $N(r)$ in Fig. 7.9**a**. Layers slipping on one another lead to the growth of the assembly radius R, thus, increasing the area accessible for rollers at individual layers (Fig. 7.9**b-c**). Moreover, fluid-like behaviour suppresses the local order with four-fold order ψ_4 and distortion Θ developing between first and second layers. We note that the internal rigid-body behaviour vanishes with individual layer rotation at different angular velocity ω, shown in Fig. 7.10**a**.

For layered structures, we compare the effect of increasing Pe. Figure 7.16**a** and b shows the variation of local order ψ_6 and coordination number Z between LH structures at Pe = 90 and full layered behaviour with Pe = 140. Internal rigid-body structure protects the local hexagonal structure from dislocations and bond distortions. In contrast, the

development of fluid-like behaviour across layers enables defect propagation towards the assembly centre. As the activity increases, we find a growing absence of commensurability with the layered behaviour dominating over the hexagonal structures (see Supplementary Movie 5 in Appendix C.1.2). This rotational behaviour is similar to the one observed with lower densities N (Fig. 7.8).

Notably, the angular velocity profile $\omega(r)$ in Fig. 7.10**a** indicates velocities growing inwards, in contrast with the rotation at Pe = 90. By suppressing the local order, the innermost layers disengage from rigid motion, and consequently, dislocations propagate towards the centre with the development of the fluid behaviour (Figs. 7.16**b** and 7.9**d-f**). We measure the time dependence of the local order characterised by ψ_6, displayed in Fig. 7.16**e** for $l = 3$. Features on the signal indicate fast variation, a consequence of the increasing slip behaviour. In agreement with this, fast oscillations develop on the measured distortion Θ, as well on the time dependent fluctuations of the coordination number Z (Fig. 7.16**f**,**g**). On the other hand, the rotational features observed in Fig. 7.10**a** agree with the periodic behaviour displayed in the autocorrelations $C(t)$. Figure 7.16 shows the frequency on structural variations characterised by the time dependent measurements of the local order ψ_6, bond distortion Θ, and local roller coordination Z. Note that the rotational timescales are comparable to the ψ_6 order variations at the innermost layers. Moreover, a degree of synchronisation between even and odd layers is indicated by the relation between the signals on local order ψ_6 and fluctuations of Z.

For the previous case of Pe = 90, we consider one of the ordered layers as a locally periodic substrate on which a fluid chain slides. This corresponds to an adaption of the Frenkel-Kontorova model [38]. Alternation between H and LH configurations results in commensurate-incommensurate states. Friction reduction between layers, thus slip behaviour, develops with instantaneous anti-kinks (Fig. 7.13). However, full layer behaviour is observed by increasing the activity to Pe = 140. We note that anti-kinks dominate as

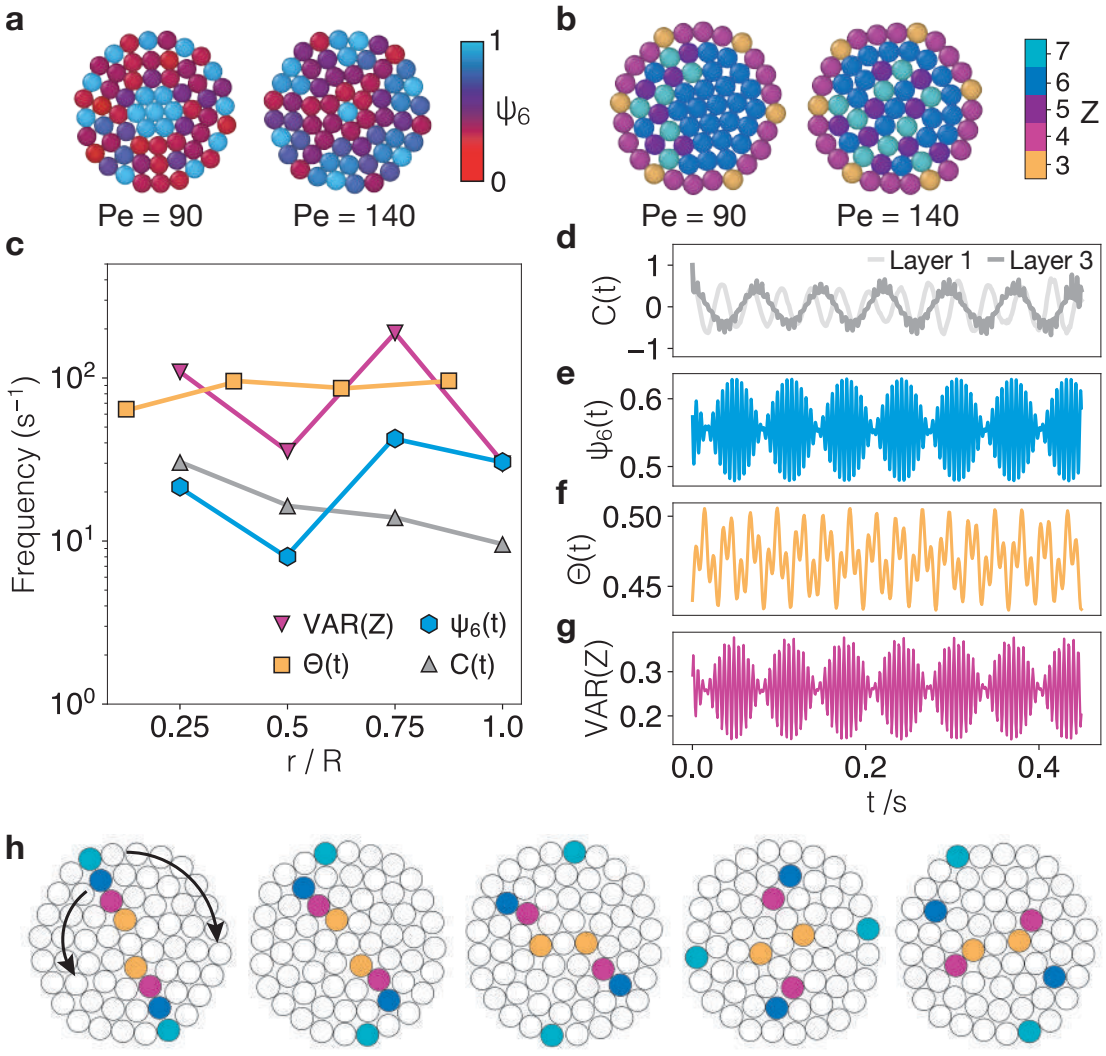

Figure 7.16: **Pe = 140, Layered behaviour. a.** Local bond orientation ψ_6 of assemblies with Pe = 90, 140. **b.** Emerging dislocations for the same structures in **a**. **c.** Comparison between variation frequency on local order ψ_6, bond distortion Θ, increasing fluctuations of Z and rotation. **d.** Velocity autocorrelation functions $C(t)$. **e.** Time dependence on the local ψ_6, **f.** bond distortion Θ, **g.** coordination number Z fluctuations. **e** and **g** are signals obtained from $l = 3$. **f** shows Θ measurements between second and third layers. **h.** Rotation sequence showing layers slipping on one another.

individual layers move at different rate. Figure 7.16**h** illustrates the rotational behaviour using trace rollers. Note that with layers disengaging from one another, the outermost layer rotates opposite to the interior. Moreover, gearwheel-like behaviour is appreciated with coloured rollers indicating the different layer rotation.

7.7 Summary and Discussion

Motivated by the optically driven system in Ref. [346] (Fig. 7.1**a**), we present the phase behaviour of Quincke rollers in strong circular confinement. Similar to our observations in Chap. 6 the system is controlled with the roller fraction N and electric strength E. Our sampling cell design permits one the study of multiple confining wells that contain different number N of rollers. Importantly, the population is held by a generated electrokinetic flow under the application of E. In the absence of activity, rollers behave as passive disks and are able to diffuse away from the confinement. Self-assembly of small crystallites results at enough density N and with the application of E below a critical strength E_Q. The formed assemblies are of similar characteristics as the passive crystals in Sec. 6.4.

On increasing the electric strength E, roller motion is observed. For different populations we detect characteristic dynamical behaviour. Under strong confinement the persistence length is delimited by the size R_c of the confinement, hence, the contribution from rotational diffusion dominates. Small populations, e.g. $N = 5$, exhibit swarming behaviour. Adjusting the population towards larger densities results in coherent motion due to alignment interactions. Using a large population, i.e. $N = 24$, spontaneous layer formation occurs, with azimuthal motion with respect to the boundary (Fig. 7.2**b** and Fig. 7.3). Varying the density N and the magnitude of the field E we investigate the phase behaviour. Figure. 7.4**b** shows the experimental phase diagram of Quincke rollers in strong confinement. At low densities, $N \leq 0.2N_{\max}$, swarming behaviour dominates with

E exceeding E_Q. On increasing the population, concentric layer structures develop.

Using an emergent layer, we estimate the Péclet numbers in Fig. 7.5**a**, by adjusting the flow velocity with the field E. For layers forming at higher densities, i.e. $N \geq 0.55N_{\max}$, we investigate the rotational behaviour of more robust layered structures. The local structure of each assembly is characterised by means of the bond orientational order parameter ψ_6 and density profiles $N(r)$ in Fig. 7.6**b**. Local hexagonal order develops on increasing N, as indicated in Fig. 7.7. Consequently, the local rotational behaviour exhibits fluid-like and rigid motion (Fig. 7.8**a**). Beyond layer formation from boundary effects and intermediate densities, layered-hexagonal structures are investigated. With high densities, $N \geq 0.69N_{\max}$, internal hexagonal order develops while the outermost layers show fluid-like behaviour.

For a population $N = 61$, we investigated the rotational behaviour of the different configurations emerging with different Pe. Moreover, the hierarchical assemblies here correspond to larger self-powered gears, compared to those in Ref. [365]. In this case, the assemblies consist of concentric multilayered structures. Moreover, different rotational regimes are identified with changing the activity. At the onset of Quincke rotation with Pe = 64, rigid-body behaviour is observed in the angular velocity profile $\omega(r)$, in Fig. 7.10**a**. In this regime, fluid-like layers are suppressed by the high hexagonal order ψ_6. Moreover, configurational change between hexagonal and LH structures results with Pe = 90. The decay of the hexagonal order promotes fluid-like behaviour of the outer layers. It is worth nothing that the angular profile in Fig. 7.10**a** shows slipping between layer rotating with different velocities ω. Figure 7.12**e** shows the time dependent order ψ_6, which corresponds to the configuration change occurring at a high rate compared to the rotation frequency for each layer (Fig. 7.12**c**). In addition, local distortion and structural defects develop with the overtaking process of layers slipping over one another (Figs. 7.14**a-e**). Thus, commensurate and incommensurate configurations may be thought as

the topological solitons described by the Frenkel-Konotorova model [38]. These solitions correspond to the local contraction (kink) and extension (anti-kink) of a chain with respect of a lattice (Fig. 7.13). On rotation, slip between layers develop anti-kinks which reduce the friction [27].

By increasing the activity to Pe = 106, 125, only hexagonal structures are observed. Nonetheless, the rotational behaviour is markedly different from the rigid-body motion at lower activity with Pe = 64. The angular velocity profiles in Fig. 7.10**a** indicate slip behaviour without development of LH configurations, as with Pe = 90. Notably, the rigid-body behaviour remains at the interior, that shows higher rotation frequencies than the outermost layers (Fig. 7.15**b**). On rotation, we identify the sharp slips accompanied with marked variations on the orientation, given by the argument of ψ_6 in Fig. 7.15**a,c**. Compared with the rotation at Pe = 90, the reverse rotation mechanism remains unclear. A possible explanation is the development of large self-propulsion at the interior, with suppression of the outer layers by the flow at the boundary.

With high activity, e.g. Pe = 140, complete fluid-like behaviour develops as the hexagonal order is suppressed by large self-propulsion. Indicated in Fig. 7.9**a**, the rotation speed is significantly different for every layer, and shows decrease with r. For the structure, the internal rigid behaviour vanishes with increased dislocations, thus, the resulting fluid-like behaviour (Fig. 7.16 **a,b**). Moreover, high incommensurability develops as layers disengage from one another and friction reduces (Fig. 7.16**h**). Having characterised the rotational behaviour of roller assemblies, it is possible to investigate the friction and mechanical properties of soft active materials. Motivated from the previously investigated driven and active microrotors [272, 346, 364, 365], our work represents an important step in the assembly of complex rotators. Moreover we expect novel designs showing an interplay between active devices, similar to the microgears we present.

CHAPTER 8

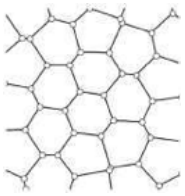

ACTIVE MOTION OF NON-SPHERICAL MOLECULES

"Jump!"

VAN HALEN

The present chapter, along with Appendix B, include details from a discrete model elaborated by Mike Allen [367].

Following Sec. 4.2, colloidal dispersions are good models to experimentally investigate the fundamental questions of statistical physics and condensed matter [82]. In this sense, stabilised poly(methyl methacrylate)]) (PMMA) colloids exhibit nearly hard sphere behaviour, as shown by Pusey and van Megen [230]. Since then, many efforts have been devoted to the investigation of condensed matter phenomena, i.e. crystallisation and glass structure, with colloids being considered as *big atoms* [313].

By considering the simplest model, spherically isotropic colloids are a good approximation to form different structures from binary crystals [234] to amorphous aggregates [350], and to test geometrically confined structures [315]. In addition to spheres, rods and platelets are widely used, leaving aside particles of different shape. Nonetheless, prepa-

ration of small clusters from spheres is achieved with compressive forces [335]. Clusters of finite size are often referred as *colloidal molecules* [228, 229, 368–370]. Similar to common molecules, colloidal molecules consist of a n number of colloidal particles bound together. Moreover, the different sizes and shapes of molecules yield distinct physical, chemical, or biological properties. For example, chirality is an important asymmetry feature that enables many relevant processes to occur, such as specific adsorption of molecules by enzymes. Colloidal molecules of similar chiral properties can be prepared by different routes, with colloids mimicking atoms [202].

Apart from the dense packing achieved by drying emulsions [335, 336], other techniques have developed controlled manufacture of hybrid colloidal molecules [269, 333]. Also, while most of the assembly of these molecules focuses on equilibrium systems, non-spherical active molecules [371] remain widely unexplored in experiments. L-shaped chiral molecules exhibit a characteristic circular motion when activated using illumination [86]. For this case, it is observed that the rotation is characterised by angular velocities increasing linearly with the illumination intensity. Alternatively, active and hybrid molecules can be fabricated using templates and capillary forces [333]. When subjected to AC fields, these hybrid molecules display reconfiguration between translational and rotational by controlling the external field [369]. Also, phoretic interactions on light-activated colloids [251] can be of use to assemble colloidal molecules locally [269]. The simplest molecule formed with this approach is a Janus dumbbell that self-propels phoretically. The assembly of more complex molecules results in different types of motion, such as in migrators, stators, spinners and rotators [269].

Studies on Quincke electro-rotation (Sec. 3.1) of particles focus mostly on spherical and elliptical objects [4, 295, 301, 372]. Many of these show how rotation can be coupled to translation when the particles sediment on a surface, thus provide model systems for active matter (Sec. 3.3) [4, 282, 283, 307]. On the other hand, numerical simulations

on asymmetric particles show self-propulsion far from a surface due to Quincke rotation [373]. Nonetheless, the experimental realisation of colloidal molecules performing Quincke rotation remains open.

In this Chapter we experimentally show the dynamics of colloidal molecules. The different molecules are previously prepared using attractive interactions on sphere monomers. We show the individual behaviour of the molecules employed here, and characterise their dynamics in comparison with spheres. Given the different types of molecule, we observe in-plane motion combined with three-dimensional dynamics for some cases. In addition, we show the dynamical formation of clusters in circular swimmers that may lead to phase separation.

8.1 Formation of Colloidal Molecules

Non-spherical molecules are prepared using attractive interactions between spherical monomers. Different to the sterically non-stabilised particles employed in Chapters 6 and 7, the monomers consists of non-stabilised polystyrene (PS) particles of size $\sigma = 3\,\mu$m, that aggregate permanently due to van der Waals forces (Sec. 4.4). More details on the preparation of the molecules are described in Sec. 5.2. Molecules of different n monomers are then separated using gravitational forces. Given the complexity that results from aggregating a large number n of monomers, we focus on smaller molecules for which active dynamics are readily investigated. Figure 8.1 shows scanning electronic microscopy (SEM) images of irreversible aggregated molecules of size $N \leq 5$. Note that different n monomers, together with different bond angles for $n > 2$ yields distinct molecules of equal n (e.g Figs. 8.1**b,c**)

Dispersions containing colloidal molecules are injected in a sample chamber, where the molecules form a quasi two-dimensional layer due to density mismatch with the solvent. In the absence of activity, colloidal molecules exhibit Brownian motion, where

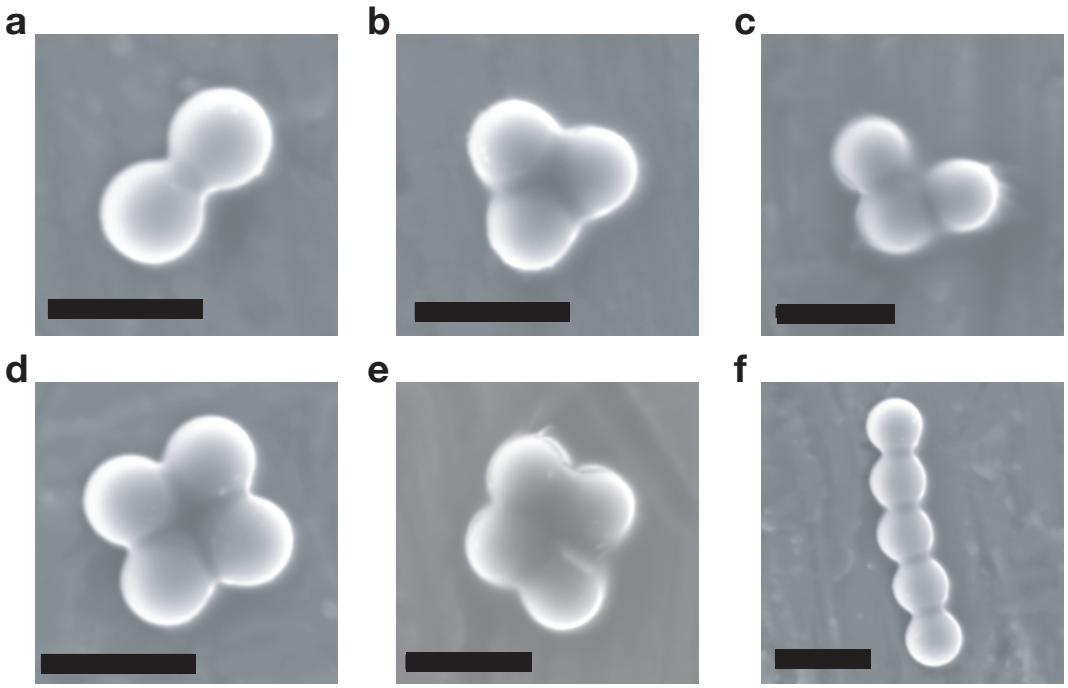

Figure 8.1: **Colloidal molecules. a.** Dumbbell. $N = 2$. **b.** Equilateral trimer. $N = 3$. **c.** Isosceles trimer. $N = 3$. **d.** Square tetramer. $N = 4$. **e.** Rhomboidal tetramer. $N = 4$. **f.** Pentamer chain. $N = 5$. All scale bars are $5\,\mu$m.

the translational and rotational coefficients can be extracted from hydrodynamic friction tensors [83]. Upon application of an external DC field E of magnitude $E \geq E_Q$, molecules exhibit active motion markedly different from that of spherical monomers. We perform particle resolved studies on dilute suspensions to investigate the dynamic behaviour of colloidal molecules under Quincke rotation.

8.2 Circular Motion in Colloidal Dumbbells

Colloidal dumbbells consist of $N = 2$ fused spheres, as shown in Fig. 8.1**a**. In contrast with homogeneous spheres, where the orientation is uncertain with respect of the direction of motion, for dumbbells we define an arbitrary orientation $\hat{\mathbf{n}} = (\cos\theta_{\hat{\mathbf{n}}}, \sin\theta_{\hat{\mathbf{n}}})$, perpendicular to the bond angle made by the centres of mass $\mathbf{r}_i = (\mathrm{x}_i, \mathrm{y}_i)$ of each sphere.

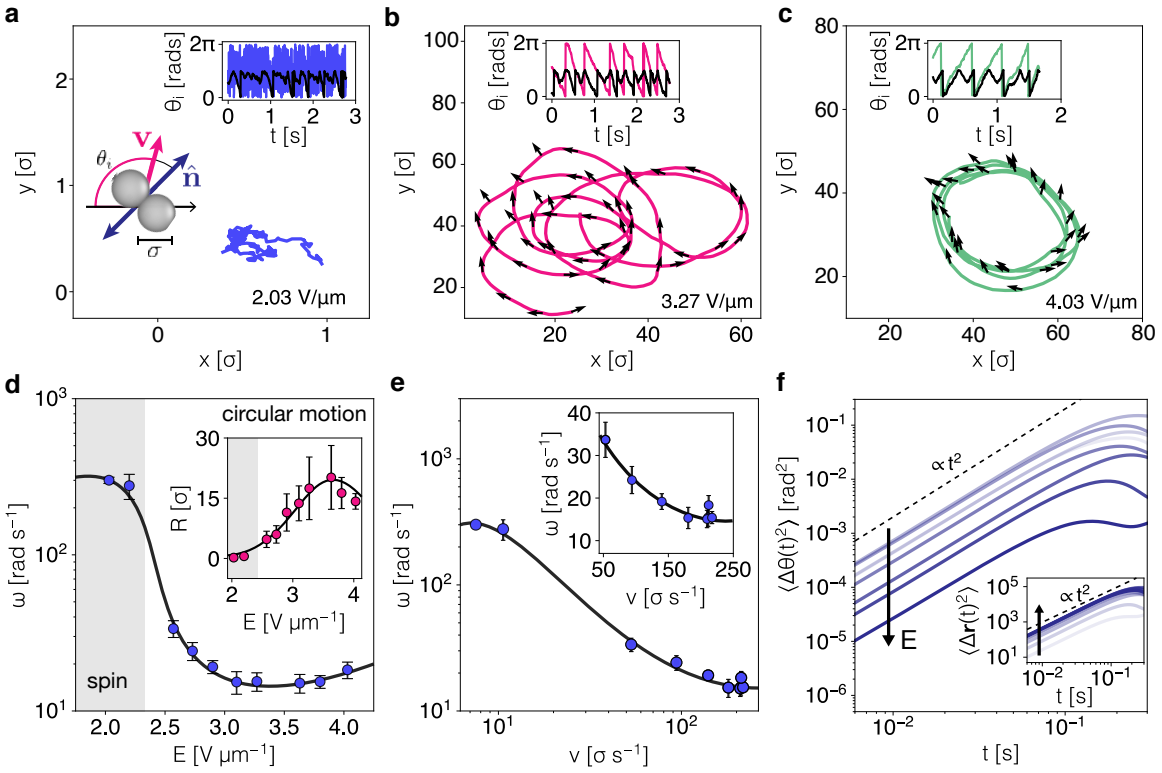

Figure 8.2: **Colloidal dumbbells. a.** The dumbbell orientation $\hat{\mathbf{n}}$ is given by direction perpendicular to the bond between the two spheres. **a-c** Show trajectories of dumbbells at different values of E. Arrows indicate the orientation $\hat{\mathbf{n}}$. Insets: Evolution of the orientation (black lines) and velocity (coloured lines) angles θ_i. **a.** Angular velocity ω against the field magnitude E.Inset: Trajectory radius R for the same values of E. **e.** Angular velocity ω versus the normalised linear velocity v. Inset shows a close-up of larger values of v. **f.** Mean squared angular displacements $\langle \Delta\theta(t)^2 \rangle$ for increasing values of E as indicated by arrow. Inset shows the linear mean squared displacement for the same strengths.

The angle θ_i indicates the angle for the orientation ($i = \hat{\mathbf{n}}$) and the displacement ($i = \mathbf{v}$) with respect a reference axis. Given the symmetry of the molecule, the orientation $\theta_{\hat{\mathbf{n}}}$ is always $\theta_{\hat{\mathbf{n}}} \in [\theta_{\hat{\mathbf{n}}}, \theta_{\hat{\mathbf{n}}} + \pi]$. The inset in Fig. 8.2**a** illustrates a dumbbell of orientation $\hat{\mathbf{n}}$ decoupling from the direction of motion given by $\mathbf{v}$. For individual dumbbells we analyse the relation between displacement $\Delta\mathbf{r}$ and orientation (Fig. 8.2**a-c**).

Using the electric strength E as control parameter, we investigate the activity dependent motion of individual dumbbells. At sufficient strengths, e.g. $E \geq 2.5\mathrm{V}\,\mu\mathrm{m}^{-1}$, the

circular motion is markedly different to the persistent random walk of spheres [27] (Sec. 2.2.2). The circular motion here results similar to the motion observed in asymmetric particles [86, 334], but different to that of directed Janus dumbbells assembled with light [269]. Also, the direction of motion, i.e. clockwise (+) and anti-clockwise(-), is not predefined as in chiral L-shaped particles [86]. Thus, self-propulsion in the form of circles may be given even by the slightest difference in the sphere size σ (see details on Supplementary Movie 1 in Appendix C.1.3). Considering a dumbbell with constant self-propulsion speed v, but with constant fluctuations in the direction of motion due to the angular velocity ω. Neglecting the interactions from electrostatic and hydrodynamic couplings, and in the absence of confining potentials, the motion for a circular swimmers is well captured by the Langevin equation,

$$\frac{\mathrm{d}\mathbf{r}}{\mathrm{d}t} = \beta\mathbf{D}\cdot\Big[\mathbf{F}^{\mathrm{a}} + \boldsymbol{\xi}\Big]; \qquad \frac{\mathrm{d}\theta}{\mathrm{d}t} = \beta D_r\Big[\mathscr{T} + \boldsymbol{\xi}_\theta\Big], \tag{8.1}$$

where $\beta = (k_B T)^{-1}$ and $\mathbf{F}^{\mathrm{a}} = F\hat{\mathbf{n}}$ is the active force that represents self-propulsion in the orientation given by $\theta_{\hat{\mathbf{n}}}$. $\mathbf{D}$ corresponds to the short time diffusion tensor that for an elongated particle reads $\mathbf{D} = D_{||}(\hat{\mathbf{n}}\otimes\hat{\mathbf{n}}) + D_{\perp}(\mathbf{I} - \hat{\mathbf{n}}\otimes\hat{\mathbf{n}})$, where $\otimes$ represents a dyadic product. The coefficients $D_{||}$ and $D_{\perp}$ correspond to the short time longitudinal ($||$) and translational ($\perp$) translational diffusion. Rotational diffusion D_r is given at the orientation time derivative in Eq. 8.1. $\mathscr{T}$ represents an effective torque promoting circular motion. $\boldsymbol{\xi}$ and $\boldsymbol{\xi}_\theta$ are white noise of zero mean Gaussian distribution and random force and torque respectively [85].

Figure 8.2**d** shows the relation between angular velocity ω and the applied field strength E, where a non-monotonic decay is observed. By decreasing the field strength, $E < 2.5\mathrm{V}\,\mu\mathrm{m}^{-1}$, spin motion is observed with each side spinning around the centre of mass $\mathbf{r}$. In this regime, small displacements of $\mathbf{r}$ are observed, as illustrated by the trajectory in Fig. 8.2**d**. Figures 8.2**b,c** show the circular motion with increasing E. Solid

lines are $\Delta\mathbf{r}$, whereas arrows indicate the orientation $\hat{\mathbf{n}}$. For the strengths in Fig. 8.2**a-c**, the evolution of the displacement and orientation angles θ_i is shown at the insets. The coupling between v and $\hat{\mathbf{n}}$ turns evident as E increases, and with the orientation $\theta_{\hat{\mathbf{n}}}$ showing values between 0 and π.

The increase of E leads to to persistent circular motion, that shows growing of the trajectory radius R. The inset in Fig. 8.2**d** shows a non-monotonic increase of R, which is in agreement with the relation between ω and the field strength E. This behaviour appears to be in contrast with the circular motion of Janus spheres, that shows a sharp decrease of R with increasing v [374]. In addition, Fig. 8.2**e** shows the angular velocity ω as function of the normalised linear velocity v. It is noted that ω depends non-linearly on v (Inset in Fig. 8.2**e**). Moreover, persistent rotation is observed even with increasing velocities v. Markedly, the dynamics significantly differs from chiral particles that show linear increase of ω with v, while the trajectory radius R remains constant [86]. In Fig. 8.2 we plot the mean squared angular displacement $\langle\Delta\theta(t)^2\rangle$, and the linear mean squared displacement $\langle\Delta\mathbf{r}(t)^2\rangle$ as an inset figure. The angular displacement increases in the spinning regime, while growing of R during persistent circular motion leads to directed behaviour.

Having discussed the emergent circular motion in colloidal dumbbells, we show how dynamical interactions arise from collisions, given the increase of the circular radius R (Inset in Fig. 8.2**d**). It is important to mention that the interactions referred here are markedly different to those leading to aggregation in spherical rollers, in Chap. 6.

8.2.1 Dynamical Formation of Tetramers

In experiments, different factors lead to the aggregation of particles into clusters, such as self-propulsion, alignment, excluded volume, attractive, repulsive and hydrodynamic interactions [27, 98, 250–252, 261]. For particles performing local conversion of energy,

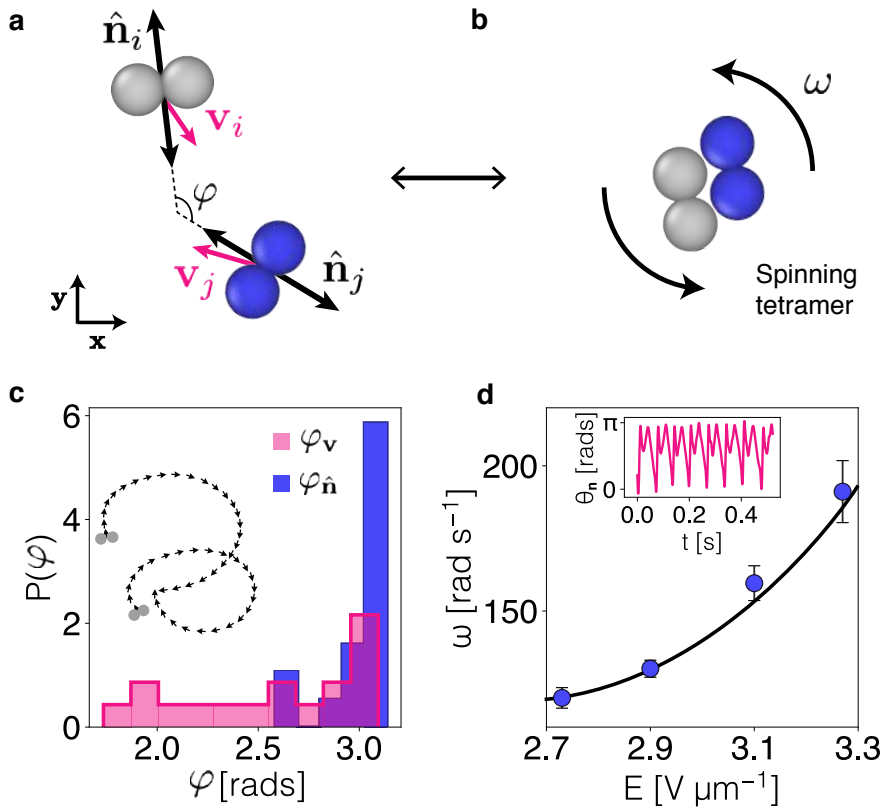

Figure 8.3: **Spinning tetramers. a.** Isolated dumbbells perform circular motion. For two colliding dumbbells we take the angle φ made between the orientations $\hat{\mathbf{n}}_{ij}$ and velocities $\mathbf{v}_{ij}$ before the collision. **b.** Tetramers consisting of two dumbbells form if alignment of the orientations $\hat{\mathbf{n}}_{ij}$ coincides with opposite displacement $\mathbf{v}$. Tetramers exhibit steady spinning motion characterised by ω. **c.** Distribution of the angle φ made between velocities and orientations for colliding dumbbells. **d.** Measured angular velocities ω for spinning tetramers observed at different magnitudes of E. Inset shows the evolution of the tetramer orientation.

the interactions are phoretic and result from the generation of a gradients, i.e. chemical, temperature and electric potential gradients [241, 260]. Moreover, competing interactions, e.g. alignment and excluded volume, lead to dynamical aggregates. In Chapter 6, we showed the formation of amoeba crystallites from competing self-propulsion and hydrodynamic interactions.

In the absence of attractive forces, dynamical aggregation is achieved with the local demixing of the media by using light-activated colloids [250]. This corresponds to the

experimental observation of motility induced phase separation (MIPS, Sec. 2.4.2), given by the self-trapping of motile particles [79, 80]. Clusters of finite size form with colliding particles, and whose orientation hinders their escape. In this section, we show the dynamical formation of clusters using circular swimmers. It is worth noting that the contribution from hydrodynamic interactions seems negligible, as the colloidal molecules lack aggregation into amoeba-like clusters at low field strengths. Moreover, the dynamical aggregation results in clusters of significantly smaller size, and it is far from complete phase separation.

Figure 8.3**a** illustrates two dumbbell molecules before a collision. Given the orientation $\hat{\mathbf{n}}$ and the velocity $\mathbf{v}$ of each dumbbell, we identify the nature of the collision. The inset in Fig. 8.3**c** shows two dumbbell trajectories exhibiting their characteristic circular motion. Note that the trajectory radius R depends on the field strength E, as shown at the inset in Fig. 8.2**b**. Thus, R must be of sufficient size to observe collisions between dumbbells. Given our measurements of R, intermediate field strengths E lead to increasing number of collisions.

For two colliding dumbbells, we measure the angle φ made between the orientations $\hat{\mathbf{n}}_{ij}$ and velocities $\mathbf{v}_{ij}$ prior to the collision. In the case of aligning, i.e. with the orientations giving $\varphi \approx \pi$, and with opposite displacements $\mathbf{v}_i + \mathbf{v}_j = 0$, the dumbbell collision leads to tetramer formation, shown in Fig. 8.3**b**. Note that, these tetramers form from dynamical clustering, and are markedly different to the rigid tetramers in Fig. 8.1**d,e**. For dumbbell forming tetramers, we measure $\varphi_{\hat{\mathbf{n}},\mathbf{v}}$. Figure 8.3**c** shows the distributions of φ, that indicate a preferential orientation $\hat{\mathbf{n}}$. For dumbbells that exhibit partial decoupling between orientation and translation (Fig. 8.2**b,c**), we find different distributions for $\varphi_{\hat{\mathbf{n}}}$ and $\varphi_{\mathbf{v}}$. The angles φ obtained from the dumbbell translation show a broad distribution with $\varphi_{\mathbf{v}} = \in \left[\frac{2\pi}{3}, \pi\right]$, and indicate partial preference towards alignment. On the other hand, $\varphi_{\hat{\mathbf{n}}}$ shows a clear preference for alignment at $\varphi_{\hat{\mathbf{n}}} \approx \pi$, which suggests the tetramer

formation as dependent on the incoming orientations $\hat{\mathbf{n}}_{ij}$.

Tetramers are of rhomboidal structure, as shown in Fig. 8.3**b**. The resulting shape frustrates reorientation, making the escape hard. Markedly, the opposite direction of motion displayed by the dumbbells in the tetramer suppresses the translational motion, and leads to steady rotation given the misalignment of the centres of mass $\mathbf{r}$. Figure 8.3**d** shows the spin angular velocity ω measured for different regimes of circular motion (Inset in Fig. 8.2**d**). On increasing E, the angular velocity ω shows a non-linear growth. Markedly, the spinning velocities of tetramers compare to those observed in single dumbbells at low field strengths E (Fig. 8.2d). Tetramers exhibit steady rotation if unperturbed. Otherwise, any perturbation from collisions with neighbour molecules disturbs the aligned orientations, and results in tetramers breaking (see Supplementary Movie 2 details in Appendix C.1.3). Nonetheless, collisions with certain incoming dumbbells result in more complex spinning molecules.

8.2.2 From Tetramers to Hexamers

Previously, we showed the formation of tetramers from the collision between dumbbells (Fig. 8.3**a,b**), which strongly depends on the orientation alignment, with $\varphi_{\hat{\mathbf{n}}} \approx \pi$. Spinning tetramers exhibit a steady rotation, and any further collision with other molecules might result in tetramer breaking and the return to circular motion of dumbbells (Fig. 8.2). However, some collisions might lead to the formation of more complex structures depending of the orientations $\hat{\mathbf{n}}$.

Similar to tetramers, the structures forming from collisions must suppress reorientation in order to prevent breaking. Thus, stable structures depend strongly on orientation. Remarkably, hexamers result from the collisions and local rearrangement between a formed tetramer and a third dumbbell (Fig. 8.4**a,b**). Hexamers are of triangular shape, as shown in Fig. 8.4**b**. This structure is stable, as self-trapping suppresses the local

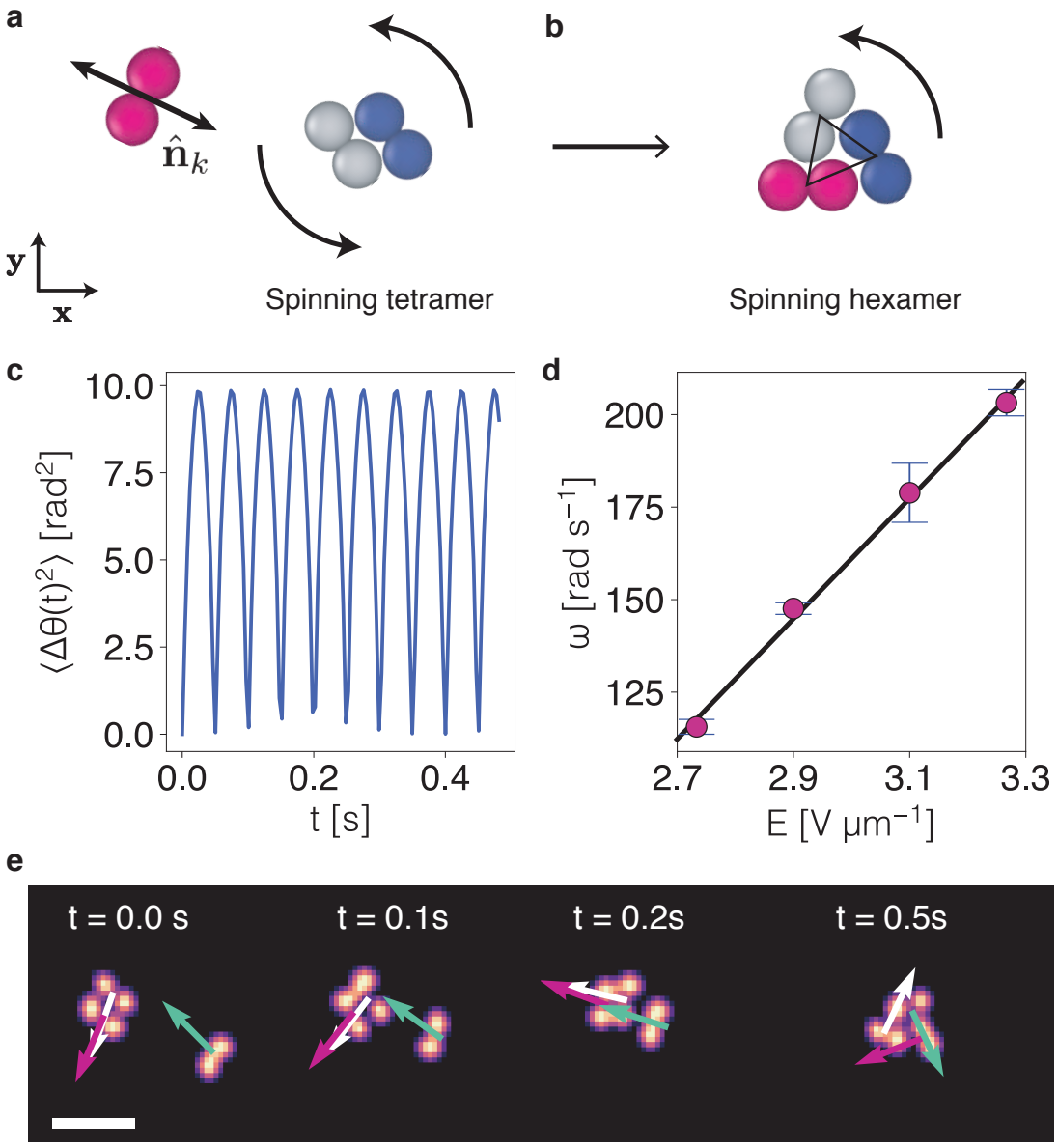

Figure 8.4: **Spinning hexamers. a.** Collision between a spinning tetramer and a third dumbbell lead to hexamer formation. **b.** Such hexamers are of triangular shape and exhibit steady rotation. **c.** Mean squared angular displacement plotted in linear scales for one sample at $E = 3.2V\ \mu\text{m}^{-1}$. **d.** Angular velocity ω versus field strength. **e.** Time sequence showing the collision and formation of a hexamer. Arrows indicate the local orientations $\hat{\mathbf{n}}$.

reorientation. Figure 8.4**e** shows the formation of a hexamer structure, given the collision of a loose dumbbell with a spinning tetramer.

Similar to tetramers, self-propulsion drives local spinning. Given the hexamer structure, the individual motion **v** is suppressed by the dumbbell in front, and self-propulsion converts to rotation Fig. 8.4**b**. Figure 8.4**c** gives the mean squared angular displacement $\langle \Delta\theta(t)^2 \rangle$ that shows the periodic behaviour of spinning tetramers (Supplementary Movie 4 in Appendix C.1.3). Note that hexamer formation strictly depends on previously formed tetramers. Thus, limited samples are found at the same regimes of circular motion (Fig. 8.2**d**).

Figure 8.4**d** shows the linear response of angular velocity ω to the electric strength E. This relation results different to the one observed in tetramers, as indicated in Fig. 8.3**d**. In addition, at low field strengths E the resulting spin motion is slightly damped. On increasing E, the angular velocity ω is similar to spinning dumbbells (Fig. 8.2**d**). Moreover, local perturbations, i.e. collisions with neighbour molecules, promote breaking of the hexamers (Supplementary Movie 3, Appendix C.1.3). Thus, dynamical formation of large clusters seems difficult as self-trapping decreases with changes in orientation $\hat{\mathbf{n}}$.

8.3 Flip Motion in Trimer Molecules

Dumbbells exhibit circular motion, as shown in Fig. 8.2. This is in contrast to the persistent random walk observed in isolated Quincke rollers. The circular motion is likely to arise from the slight asymmetry in size between two fused spheres. For molecules slightly bigger, i.e. rigid trimers (Fig. 8.1**b,c**), the motion is notably different compared with the motion of spheres and dumbbells.

For isolated trimers, we observe a combination between in-plane and out-of-plane motion. In the absence of activity, trimers sediment and the three fused spheres are in contact with the substrate. Like spheres and dumbbells, trimers are subjected to in-plane

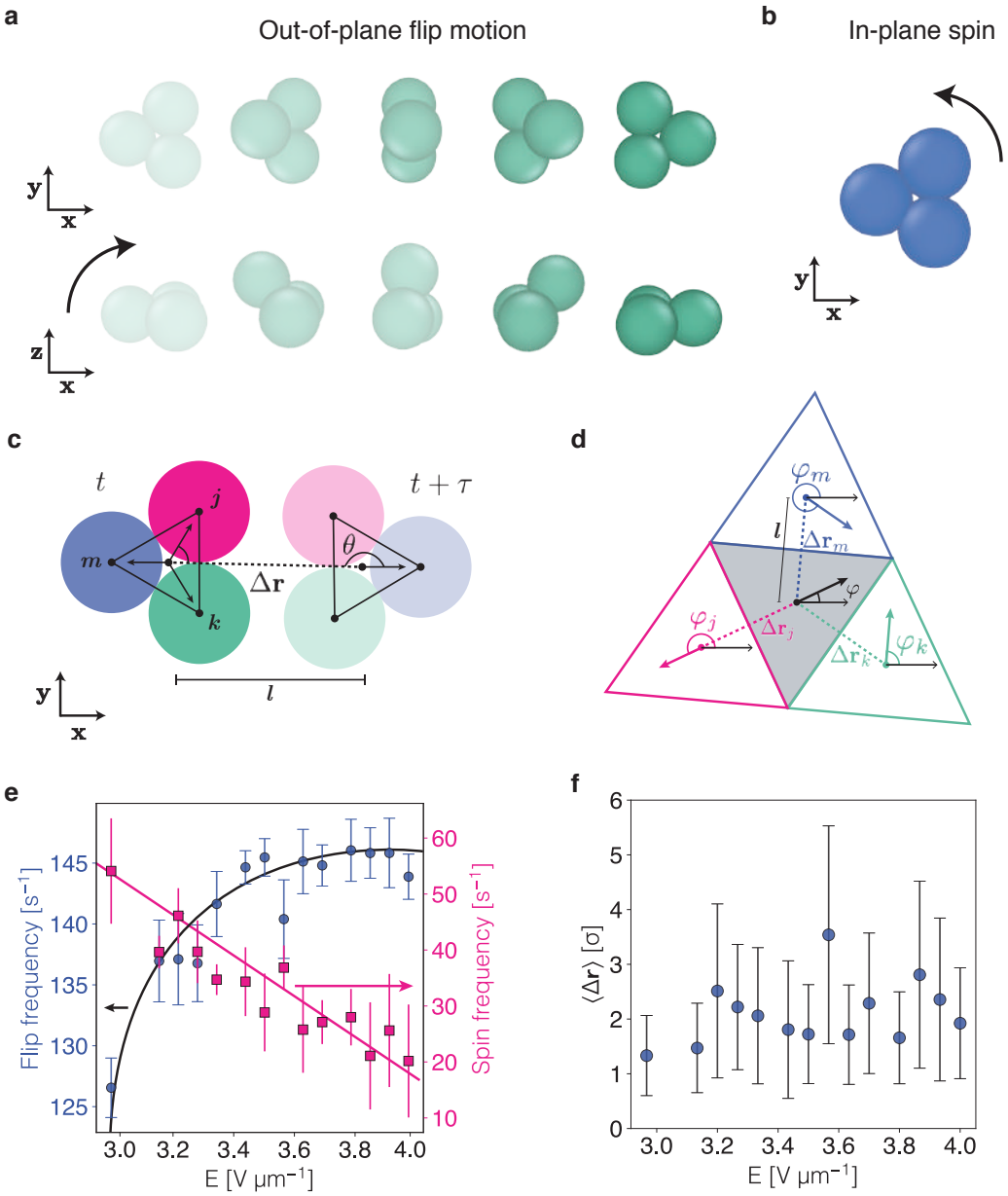

Figure 8.5: **Trimer molecules. a.** Flipping motion consists of out-of-plane jumps. Arrow indicates the flip firection. **b.** The in-plane motion is characterised by spins. **c.** A trimer can be considered as a triangle with vertices $\mathbf{r}_i$. Particle resolved studies of trimers require the evaluation over the angle θ made between the displacement of the centre of mass $\Delta\mathbf{r}$ and individual vertices $\mathbf{r}_i$. **d.** Representation of the Quincke trimers model. Grey region corresponds to the initial position $\mathbf{r}$, and every coloured triangle is the possible evolution of $\mathbf{r}$ given a flip event. The magnitude of the displacement $\Delta\mathbf{r}_i$ is given by l, and φ_i is the evolution of the orientation. **e.** Frequency of flips and spins against the applied field strength E. Arrow indicate the corresponding axis for each drawn fit line. **f.** Mean maximum displacement $\Delta\mathbf{r}$ against E.

rotational diffusion, which appears in the form of spins changing slightly the orientation (Fig. 8.5**b**). Moreover, upon increasing the field amplitude to, i.e. $E \approx 3V\ \mu\text{m}^{-1}$, the dynamics notably change, and out-of-plane jumps appears (Supplementary Movie 5, Appendix C.1.3). Given the triangular shape of a trimer, this out-of-plane motion consists of a single vertex leapfrogging over one side, as illustrated in Figure 8.5**a**. We refer to these jumps as Quincke *flips*, which discontinuously evolve centre of mass $\mathbf{r}$ and the orientation angle φ. Therefore, the active motion of trimers is a product of the combination between diffusion and Quincke flips.

A simple model describing this type of motion is given in Appendix B. Briefly, a single trimer is considered as an equilateral triangle, and its motion is effectively given in two dimensions by diffusion and flips. Each flip instantaneously rotates the triangle by an angle π over one of the edges, thus, moving the centre of mass $\mathbf{r}$ through a distance l perpendicular to the edge. Figure 8.5**d** illustrates in grey the initial position of the trimer, and the adjacent triangles are the possible next positions given a flip. An initial orientation φ is declared between one vertex and a reference axis. The in-plane diffusion evolves the position and orientation, whereas the flips discontinuously change $\mathbf{r}$ and φ. Given the geometry, the evolution of the orientation results in $\Delta\varphi \propto \frac{\pi}{3}$, that gives the change of position as $\Delta\mathbf{r} = l\left[\cos(\varphi - \Delta\varphi), \sin(\varphi - \Delta\varphi)\right]$.

In order to distinguish flips from diffusion processes, particle resolved studies need modification from conventional algorithms to reconstruct trajectories (Sec. 5.7) [347]. Similar to the model in Fig. 8.5**d**, flips discontinuously change the position. Given two consecutive frames, the initial at time t and consecutive at $t + \tau$ vertex coordinates $\mathbf{r}_{j,k,m}$ and centre of mass $\mathbf{r}$ are identified. The position displacement $\Delta\mathbf{r}$ is of magnitude l, and is used as a reference. For a flip, l usually takes values of $l \geq |\mathbf{r} - \mathbf{r}_{j,k,m}|$. To identify the leapfrogging vertex, angles θ are taken for every vertex with respect of $\Delta\mathbf{r}$. Thus, leapfrogging vertex is given by $\theta \approx \pi$. Remaining positions are readily linked with $\Delta\mathbf{r}_{j,k,m}$.

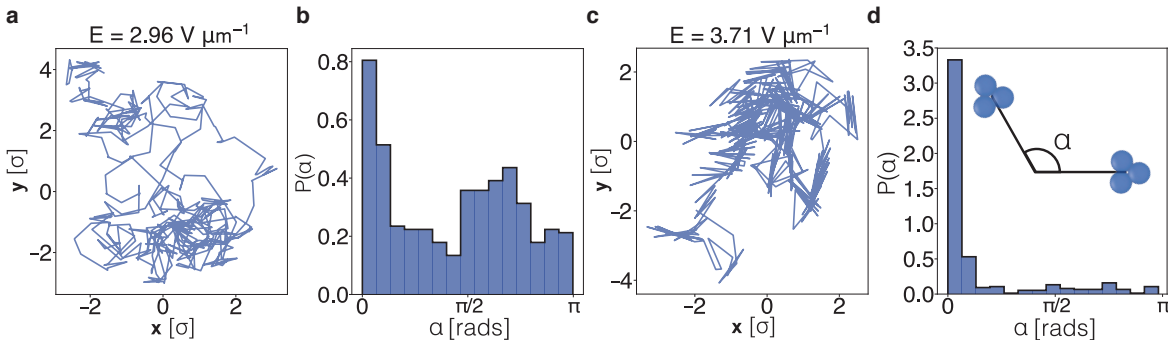

Figure 8.6: **Trimer trajectories. a.** Trajectory at lower field strengths E, and **b** resulting distribution of angles α. **c.** Trajectory of a sample at higher electric strength. **d.** Shows distribution of angles α, which are taken as illustrated by the inset.

For isolated trimers, we investigate their motion by means of spins and in-plane reorientation, and out-of-plane flips. Figure 8.5**e** shows the rate of flips and spins for different values of the electric field E. Note that the arrows indicate the different magnitude for spins and flips. Overall, flips are more frequent than in-plane rotation, by a factor of two at the lowest field magnitude tested, $E = 2.96 V\ \mu\text{m}^{-1}$. As E increases, the frequency of spins shows a linear decrease. Note that the flips become more dominant as the activity increases. Given the fast change of position $\Delta\mathbf{r}$ due to flips, the contribution from translational diffusion is less evident. Figure 8.6**a,c** shows trimer trajectories corresponding to the lowest and highest magnitudes of E tested. For a single trajectory, we take the angle α made between three consecutive positions $\mathbf{r}$, as shown by the inset in Fig. 8.6**d**. As flips overtake the in-plane reorientation, the distribution of α angles markedly shifts to $\alpha \approx 0$, an indication of a preferred leapfrogging direction.

From trajectories in Fig. 8.6**a,c**, we note that the overall displacement is comparable to the sphere size σ. For the range of field amplitudes E that we used, the trajectory sizes lack significant changes, as indicated in Fig. 8.6**f**. At low field strengths, the trajectories exhibited by trimers are reminiscent in shape to those in observed in rollers performing Lévy walks [312]. Sharp trajectories result with the increase of E, suggesting a transition

that leads to strong memory in the motion of trimers.

8.4 Summary and Discussion

In this Chapter we have shown the motion of non-spherical particles subjected to the Quincke electro-rotation mechanism employed in previous experiments (Chaps. 6, 7) [4, 282, 283, 312]. Often, these type of particles are referred as *colloidal molecules* [228, 229, 368–370]. Different methods can be used in order to prepare these so-called molecules, with control of the shape and size [333]. In addition, hybrid molecules exhibit a variety of active motion depending of the combination between active and passive particles [269]. Moreover, selective chiral properties can be investigated with the use of asymmetric active particles [86].

The colloidal molecules used here consist of n fused particles [335], as detailed in Sec. 5.2. Figure 8.1 shows a variety of colloidal molecules prepared with the use of attractive forces. Mainly, we have focused on the use of small molecules, as complexity to analyse out-of-plane motion scales with n. We first show the spinning and circular motion of colloidal dumbbells arising at different regimes of the electric strength. Local spins are observed with low amplitudes of the field E, and are characteristic of high angular velocities ω. As the field strength increases, a transition to circular emerges (Fig. 8.2**d**). Such a circular motion is likely to arise from the slight asymmetry in size between two fused spheres, and it appears in contrast to the directed motion of Janus dumbbells [269].

Moreover, the behaviour is markedly different for asymmetric particles [86] and to spheres displaying circular motion in a viscoelastic media [374]. To start, a specific direction of motion is not predefined as with the L-shaped particles in Ref. [86]. For the field strengths E investigated, we observe a non-monotonic behaviour of the angular velocity ω. This is in agreement with the change of trajectory radius R, in Fig. 8.2**d**. In

addition, the relation between linear v and angular ω velocity results non-linear, with the decrease of rotation as R grows (Fig. 8.2**e**).

Remarkably, collisions between dumbbells lead to the dynamical formation of tetramers and hexamers, given the behaviour of the trajectory radius R set by E. Self-propelled dumbbells are characterised by a predefined orientation $\hat{\mathbf{n}}$ and velocity $\mathbf{v}$, which partially decouple one to another (Fig. 8.2**a**). For colliding dumbbells, we note that the formation of tetramers strongly depends on the orientation alignment between two dumbbells, as shown in Fig. 8.3**c**. The circular motion of dumbbells is suppressed by the formation of a tetramer, in which self-propulsion and frustration leads to spinning motion. Tetramers exhibit spin velocities ω comparable to those observed in spinning dumbbells (Fig. 8.2**d**), and depend non-linearly on E.

Perturbations to the orientation. i.e. an additional collision, can lead to tetramer breaking. Nonetheless, certain collisions may result in hexamer formation. Like in tetramers, the formation of hexamers depends on the local orientations (Fig. 8.4**e**). Moreover, a hexamer requires local restructuring in a triangular shape, as shown in Fig. 8.4**b**. As before, the resulting shape suppresses the individual circular motion and self-propulsion converts to spinning (Fig. 8.4**c**). In contrast with tetramers, ω depends linearly on E. Nonetheless, small fluctuations of the local orientations lead to breaking events, thus, circular motion of individual dumbbells. Overall, the break events in tetramers and hexamers suppress demixing.

In addition to dumbbells, we have shown the motion of slightly bigger molecules, i.e. trimers made of $N = 3$ fused spheres (Fig. 8.1**b**). The dynamics of trimers characterise from an in-plane and out-of-plane motion, different from the observed in spheres and dumbbells. For the in-plane motion, rotational and translational diffusion appears, while the out-of-plane motion consists of jumps that discontinuously evolve the position and orientation. We refer to these jumps as *flips* (Fig. 8.5**d**). For the change of activity, we

noted that the rate of flips against the in-plane rotation increases with E. Figure 8.5**e** shows the growing contribution from flips with increasing E. This effect is well illustrated by the trimer trajectories, that show a transition from Levy-like walks to sharp motion (Fig. 8.6**a,c**). Moreover, trajectories exhibit memory in the direction of motion as flips dominate, indicated in Fig. 8.6**d**.

Molecules subjected to Quincke electro-rotation exhibit characteristic motion that depends on size and shape. We have shown the dynamics of small molecules, and the case of dynamical aggregation into small clusters. Nonetheless, bigger molecules and the interplay between them remains unexplored. Also, dense suspensions are of interest, given the different motion between spheres, dumbbells and trimers, which might lead to different types of collective behaviour.

CHAPTER 9

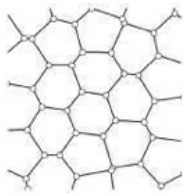

SUMMARY, CONCLUSIONS AND OUTLOOK

9.1 Thesis Overview

Broadly, this work presents the use of Quincke rollers (in Sec. 3.1) as a model system to investigate some of the phenomena in active matter systems, i.e. the onset of collective behaviour and clustering (Sec. 2.3). Moreover, we find our system useful to experimentally investigate the interplay between active and passive interactions. In Chapter 5, we detailed the preparation of colloidal suspensions, and the design of the experimental set-up employed, which together give form to our experiments. This system is employed to investigate the bulk phase behaviour of active particles with competing interactions, detailed in Chapter 6. Moreover, using the same system we show the assembly and rotational behaviour of microscopic colloidal gears in Chapter 7. Finally, in Chapter 8 the motion of colloidal molecules under Quincke electro-rotation is shown. In this final section, we summarise the main findings of the experiments described above, and propose possible aspects for future investigation.

9.2 Competing Interactions in Active Colloids

In Chapter 6 we have shown the results from numerical simulations and experiments using Quincke rollers. Using the area fraction ϕ and the electric field strength E as control parameters, we have shown the rich phase behaviour of an active system with competing active and passive interactions. The absence of activity, i.e. an electric strength below a threshold E_Q, results in a passive fluid at low densities. On increasing ϕ, the induced hydrodynamic interactions lead to the formation of highly ordered structures. These correspond to steady crystallites.

With sufficient area fraction, the competition between hydrodynamic interactions and self-propulsion, at $E \geq E_Q$, leads to amoebae-like active crystallites. We note that, while self-propulsion acts as a long-ranged repulsion, hydrodynamics drive partial demixing, thus, an inhomogeneous state. At high field strength, the contribution from activity reverses and promotes demixing. Partial separation, in form of bands traveling through an active gas is observed. Using the electric strength E as main control parameter, we have shown a series of transitions between passive and active phases.

We have used a variety of static and dynamic order parameters to characterise the nature of such phase transitions. These parameters suggest continuous transitions. Given the high order of the passive crystallites, the bond orientational order parameter ψ_6 decreases with the formation of the inhomogeneous phases, i.e. amoebae and polar bands. Nonetheless, the time-dependent overlap parameter $Q(t)$ is used to distinguish amoebae from passive crystallites. Notably, amoebae aggregates exhibit the dynamical features of a colloidal liquid, while the structural order remains. We note that these polar bands consist of denser regions in contrast with the dilute gas, and exhibit local order ψ_6 given the repulsive core of the particles. The observed transitions also reflect in the polar order, which shows an increase with the activity promoting alignment interactions in the bands. These latter, also exhibit the anomalous giant density fluctuations described

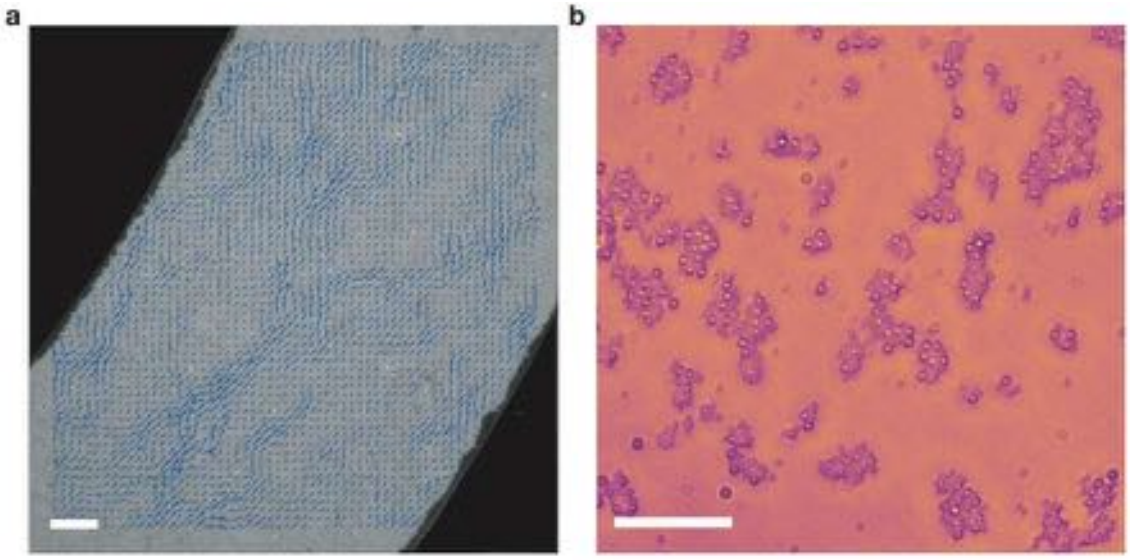

Figure 9.1: **Active solid and binary systems. a.** Active solid at $\phi \approx 0.4$. Arrows indicate the particle flow. **b.** Amoeba aggregates formed with a binary system. Big particles are $\sigma_b = 2.92$ μm, and small particles are $\sigma = 1$ μm. Scale bars are 50 μm.

in flocking models.

For amoebae aggregates, breaking and coalescence events occur from competing interactions. We have analysed the features of both events, and find a time-reversal symmetry mechanism. This in contrast to splitting and coalescence of passive droplets. On the other hand, the contribution from strong confinement leads to the formation of a polar liquid with area fractions similar to those investigated in bulk.

9.2.1 Outlook

Our experimental system permits one to investigate the *microscopic* and *macroscopic* details of active matter with competing interactions. As above, hydrodynamic interactions drive partial deximig and the formation of finite size amoebae aggregates, which exhibit high structural order. After showing the characteristics of such aggregates, the motility of highly-packed structures can be investigated. Following the observations in Ref. [283], homogeneous solids of Quincke rollers exhibit vanishing particle current. In contrast,

a partial flow is observed in a high-density amoebae, which forms an inhomogeneous solid. Figure 9.1**a** shows the flow streams, presumably resulting from defect propagation through crystalline domains.

Moreover binary systems can be considered. Using a particle suspension of two different sizes, we find that the hexagonal order observed in passive and active crystallites vanishes, as shown in Fig. 9.1**b**. Nonetheless, a more detailed analysis by means of the area fraction of each particle type is suggested. This to investigate the phase separation in active particles with different diffusivities [172].

9.3 Microgears in Strong Confinement

Following the emergence of passive and amoebae aggregates in Chapter 6, we used a strong confinement for the assembly of self-powered microgears, in Chapter 7. Using circular confining regions, we have analysed the behaviour of different roller populations N. In the absence of activity, the hydrodynamic interactions lead to the formation of small aggregates. Bouncing swarms results with low populations, e.g. $N \leq 5$, and the field strength $E \geq E_Q$. On increasing the population, spontaneous coherent flows emerge. Given the different structures and dynamics for the populations analysed, we find a periodic behaviour in rotating layers. Moreover, concentric layered structures develop with the increase of the population. At higher densities, i.e. $N \geq 59$, competition between hexagonal and layered structures appears.

For populations $N \geq 47$, we have shown the rotational behaviour, that indicates fluid-like motion with layers slipping one past another. Notably, a population $N = 61$ yields perfect concentric layers, and is a good sample to investigate the formation of hexagonal and layered configurations. In addition, microgears of different rotational behaviour are shown. As in Chapter 6, we use the electric strength E as main control parameter. With $E < E_Q$, the contribution from the hydrodynamic interactions lead to

the formation of a hexagonal crystal, that lacks layered behaviour. On increasing the field strength, the hexagonal structure remains, and rigid-body rotation ω is shown as self-propulsion due to Quincke rotation emerges.

We noted that the increase of the activity leads the alternating formation of hexagonal and LH rotating structures. While hexagonal structures exhibit rigid-body behaviour, the outer layers in LH structures show fluid-like behaviour as they slip one on another. We have shown the nature of this mechanism by means of the time dependent local structure. The hexagonal order ψ_6 shows sharp decays as LH form. This reflects in the emergence of four-fold coordinated regions, characterised by the distortion of the bond angles. In addition, the slipping mechanism generates local dislocations from the outside, which vanish at the rigid hexagonal core. This process may be thought of as a friction between adjacent layers. Using the Frenkel-Kontorova model, the slipping process in LH configurations corresponds to anti-kinks, i.e. local extension of a sliding chain on a periodic lattice. Change between hexagonal and LH configurations correspond to commensurate and incomensurate states. Overall, this change in configuration is well captured by the fluctuations of the bond-angle distortions Θ and by the emergent dislocations between layers.

Additional increase of the activity reverses the rotational behaviour. We note that the rigid core rotates faster than the outer layers. However, this process is not driven by the emergence of LH structures as before. Here, a hexagonal structure remains, and the slips are characterised by sharp changes of the argument of ψ_6. Given the dominant hexagonal order, the bond distortion is low and dislocations do not seem to emerge. However, it remains unclear what drives the slipping behaviour in this regime. A suggestion may be the interaction with the amplified electro-hydrodynamic flow that confines the population. For the highest activity value tested, we find complete fluid-like behaviour, with every layer slipping one past another at different values of ω. In contrast to LH configurations,

at high activity the rigid core vanishes and defects propagate to the centre. Moreover, layers decouple from one another, allowing different directions of rotation. In addition, the time dependent local structure and dislocations show synchrony between layers.

9.3.1 Outlook

The microgears in Chapter 7 are motivated by the driven assemblies using optical tweezers in Ref. [346]. We noted that having the Quincke rotation acting on every roller significantly increases the rotational performance of the active assemblies compared to the latter system. Moreover, our system enables to the assembly of larger microgears of active particles, in contrast with the single layered gears in Ref. [365]. Given the localisation of hydrodynamic interactions, self-assembly of even larger gears may be possible. On the other hand, we expect that this type of controllable rotational behaviour to be useful for investigating friction in analytically and experimentally active assemblies.

9.4 Active Motion of Non-Spherical Colloids

In contrast with Chapters 6 and 7, we have shown the active behaviour of non-spherical particles in Chapter 8. These consist of a number N of fused spheres, that are typically referred as *colloidal molecules*. We find the preparation of such molecules rather simple. However, a better control on size, shape and hybrid preparation is achieved with other techniques [333, 334].Given the complexity of such molecules with high N, we focused on the motion of small molecules, i.e. $N = 2,3$, under Quincke electro-rotation.

These molecules exhibit dynamics markedly different from that of the persistent random walks of spheres. Colloidal dumbbells of $N = 2$, exhibit two types of motion, which is dependent of the electric strength E. At low amplitudes of E, the dumbbells exhibit in-place spin motion, characterised by high angular velocities ω. On increasing E, a transition to circular motion appears. We noted that the circular motion of Quincke

dumbbells is significantly different from the directed Janus dumbbells in Ref. [269]. Here, the circular motion may arise from the asymmetry in size between the two fused spheres, and it characterises from the increase of trajectory radius R and reduction of ω. These observations appears reversed for the circular motion of spheres in viscoelastic media [374]. Moreover, a chiral orientation is not predefined, as in the asymmetric particles in Ref. [86].

In addition to the circular motion, dynamical clustering of dumbbells is noted. Given the shape and displacement of single dumbbells, an orientation $\hat{\mathbf{n}}$ and velocity $\mathbf{v}$ are distinguished. We noted partial decoupling between these two at different values of E. For two dumbbells colliding, the formation of dynamical tetramers appears, due to a preferred alignment of the orientations. Also, the opposite displacement of the two dumbbells, combined with geometrical frustration, leads to the formation of spinning tetramers, whose angular velocities ω are comparable to those in single spinning dumbbells. Beyond tetramers, we have shown that certain additional collisions lead to the formation of more complex hexamers. These depend on a previously formed tetramer and an incoming dumbbell with the correct orientation. As with tetramers, the local structure suppresses the circular motion and results in spinning hexamers, whose angular velocity depends linearly on E. Nonetheless, both tetramers and hexamers are susceptible to additional collision, which perturb the orientations and lead to breaking of the dynamical clusters. These breaking events suppress a possible phase separation in circular swimmers.

Beyond dumbbells, we have shown the active motion of colloidal trimers, i.e. $N = 3$. This type of motion is a combination of in-plane diffusion and out-of-plane jumps, which discontinuously evolve the position $\mathbf{r}$. We refer to these latter as *flips*. Given the symmetry, a trimer is considered as an equilateral triangle, where the in-plane rotational diffusion leads to the continuous evolution of the orientation. In contrast, a flip evolves the position $\mathbf{r}$ by a distance l, and significantly changes the orientation angle φ. For the

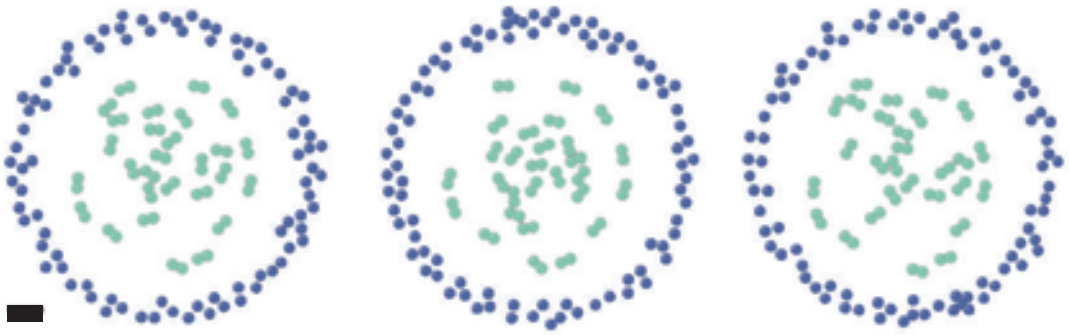

Figure 9.2: **Phase separation in dumbbells and spheres.** Spheres exhibit an azimuthal flow, while dumbbells segregate at the centre. Scale bar is 10 μm.

trimer trajectories, Lévy-like walks appear with low amplitudes of E, whereas flip events become significantly dominant over the in-plane spins with an increased E. This leads to sharp trajectories, that seem to develop memory over a preferred flip direction.

9.4.1 Outlook

While the vast majority of studies focus on the use of spheres and rod-like particles, the motion of colloidal molecules due to Quincke rotation has been shown here. As above, dumbbells exhibit circular motion and dynamical aggregation, while trimers show continuous out-of-plane flip motion. However, molecules of different size and shape remain unexplored. Moreover, dense suspensions of dumbbells and trimers are of interest to investigate the collective motion of circular swimmers and jumpers. For this, an efficient mechanism for the separation of the different molecules is needed, i.e. density gradient centrifugation [335] or the use of microfluidics.

In addition, molecule mixtures and confinement are also of interest. Figure 9.2 shows a short time sequence of a sphere-dumbbell mixture under circular confinement. We noted a phase separation between the different particles, where spheres form a coherent flow tangential to the boundary, and dumbbells segregate at the centre. However, more

analysis with different sphere-dumbbell ratios may lead to different behaviours in particles of different diffusivities. Another alternative is the use of a square confinement to investigate the change of the coherent flow and how this may affect the demixing.

9.5 Conclusions

In this work we have shown the behaviour of active particles with competing interactions, under strong confinement, and the motion of particles of different shape, which probe useful to investigate active matter systems.Active systems are characterised from featuring behaviours not observed at thermal equilibrium, i.e. self-propulsion and the emergence of collective behaviour. Many of the questions regarding these systems have been addressed with the use of analytical models, numerical simulations and experiments. Here, we employed microswimmers, powered by Quincke electro-rotation, as model system to investigate active matter phenomena. We have shown the role of competing passive and active interactions, which drive the formation of amoebae-like dynamical aggregates and polar bands. Using the same system, we have shown the self-assembly of micro devices under strong confinement, where exploiting the activity we controlled the rotational behaviour of microgears, from rigid-body to fluid-like rotation. Furthermore, we investigated the active motion of small colloidal molecules under Quincke rotation. These molecules exhibit a type of motion notably different from the dynamics observed in spheres, where Quincke dumbbells feature circular motion, and trimers show out-of-plane flips. Finally, these different experiments probe useful to studying the simultaneous role of interactions in active particles, and for the design of materials and micro size devices.

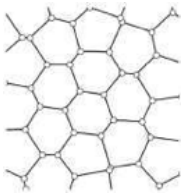

APPENDIX A

A.1 Microscopic model of effective interactions in Quincke rollers

Following Ref.[4], we consider a pairwise alignment interaction between rollers that leads to a torque on particle i

$$\mathscr{T}_i = -\frac{\partial \mathscr{R}_{\text{align}}}{\partial \theta_i};$$

$$\mathscr{R}_{\text{align}} = -\sum_{j,|\mathbf{r}_{ij}| \le r_{c1}} \left(A_1 \hat{\mathbf{P}}_i \cdot \hat{\mathbf{P}}_j + A_2(\hat{\mathbf{P}}_i - \hat{\mathbf{P}}_j)\cdot \hat{\mathbf{r}}_{ij} + A_3 \hat{\mathbf{P}}_j \cdot (2\hat{\mathbf{r}}_{ij}\hat{\mathbf{r}}_{ij} - \mathbf{I}) \cdot \hat{\mathbf{P}}_i\right) \tag{A.1}$$

where $\hat{\mathbf{P}}_i = (\cos\theta_i, \sin\theta_i)$ is the direction of motion of the ith roller, and $\mathbf{r}_{ij}$ is the separation between rollers i and j. This has the minimum number of terms required to describe the electro-hydrodynamically induced alignment interactions with the correct symmetry and whose range is set by the distance between plates in the experimental

setup. We truncate $\mathscr{R}_{\text{align}}$ at $r_{c1} = 3.0\sigma$, where σ is the particle diameter. We note that angular momentum is not conserved by these dynamics.

The electro-osmotic long-ranged attraction [325] is modelled by a truncated and shifted (at $r_{c2} = 5.0\sigma$) potential of the form

$$\mathscr{H}_{\text{attr}} = -A_4 \exp(-\kappa r)/r^2, \tag{A.2}$$

where $\kappa = 1/3\sigma^{-1}$ is the inverse screening length. The excluded volume interactions between rollers are represented by a repulsive Weeks-Chandler-Anderson (WCA) interaction of the form $\mathscr{H}_{\text{exc}} = 4\epsilon((\sigma/r)^{12} - (\sigma/r)^6) + \epsilon$, where $\epsilon = k_{\text{B}}T$ is the energy unit of the model. The WCA potential is truncated at $r_{c3} = 2^{1/6}\sigma$.

The coupling parameters in the alignment interactions are estimated to be $A_1 = 0.93k_BT$, $A_2 = 0.33k_BT$ and $A_3 = 0.48k_BT$ for our experimental conditions (see SM for more details), and we chose the attraction strength to be $A_4 = 10k_{\text{B}}T$. We verified that the qualitative phase behaviour of the model remains the same if we vary the strength of the long-ranged attraction. We note that we have parametrised A_1, A_3 from the single particle dynamics in the dilute gas phase, the attractive interactions A_2, A_4 are determined from the experimental parameters.

A.2 Simulation Details

Brownian dynamics simulations were performed by Majid Mosayebi, using a two-dimensional system composed of $N = 10000$ interacting Quincke rollers. We integrate the over-damped Langevin equations in, using the stochastic Euler scheme with a time step of $dt = 10^{-5}\tau$. In our simulations, the interparticle force on the ith roller $\mathbf{F}_i = -\nabla_i(\mathscr{H}_{\text{attr}} + \mathscr{H}_{\text{exc}})$ while the torque on the ith roller $\mathscr{T}_i = -\partial\mathscr{R}_{\text{align}}/\partial\theta_i$. The particle diameter σ, thermal energy $\epsilon = k_{\text{B}}T$ and Brownian time $\tau = \sigma^2/D_t$ are chosen as basic

units for length, energy and time, respectively. We take $D_r = 3D_t/\sigma^2$, as expected for an spherical particle in the low-Reynolds-number regime. We study the phase behaviour of the system as a function of two dimensionless parameters; Péclet number $\mathrm{Pe} = f^p\sigma/k_\mathrm{B}T$ and the area fraction $\phi = \frac{N\pi\sigma^2}{4L^2}$, where L is the linear size of the simulation box.

A.3 Microscopic model of Alignment Interactions in Quincke Rollers

The following description is based on a microscopic model describing the dynamics of a population of colloidal rollers due to Quincke rotation. The direct interactions are detailed in the following section, and are captured in the force $\mathbf{F}_i$ in Eq. A.3. Here we consider the alignment terms. The equations of motion for the ith self-propelled particle are given by the following Langevin equation, where for the rotational case we have rewritten the version in the main text to explicitly consider the effective alignment interaction.

$$\dot{\mathbf{r}}_i = \frac{D_t}{k_B T}[\mathbf{F}_i + f^p\hat{\mathbf{P}}_i] + \sqrt{2D_t}\boldsymbol{\xi}_i^t \tag{A.3}$$

and

$$\dot{\theta}_i = -\frac{D_r}{k_B T}\frac{\partial}{\partial\theta_i}\sum_{j\neq i}\mathscr{R}_\mathrm{align}(\mathbf{r}_{ij},\hat{\mathbf{P}}_i,\hat{\mathbf{P}}_j) + \sqrt{2D_r}\xi_i^r \tag{A.4}$$

where the particle i is subject to a propulsion force of magnitude f^p whose direction changes due to the alignment interaction and noise ξ_i. Note that because the simulations are strictly in 2D, the direction of the dipole $\mathbf{P}$ in Eq. A.4 is that of the rotation, i.e. the direction of self-propulsion, rather than the (3D) induced dipole of the experimental system $\mathbf{P}_\mathrm{exp}$ mentioned above.

Introduced by Caussin *et al.* [4], the effective alignment interaction $\mathscr{R}_{\text{align}}$ reads

$$\mathscr{R}_{\text{align}}(\mathbf{r},\hat{\mathbf{P}}_i,\hat{\mathbf{P}}_j) = -A_1(r)\hat{\mathbf{P}}_i\cdot\hat{\mathbf{P}}_j - A_2(r)\hat{\mathbf{r}}\cdot(\hat{\mathbf{P}}_i-\hat{\mathbf{P}}_j) - A_3(r)\hat{\mathbf{P}}_j\cdot(2\hat{\mathbf{r}}\hat{\mathbf{r}}-\mathbf{I})\cdot\hat{\mathbf{P}}_i \tag{A.5}$$

having $\hat{\mathbf{r}}\equiv\mathbf{r}/r$. The coefficients $A_1(r), A_2(r)$ and $A_3(r)$ incorporate the microscopic parameters, and are given by:

$$A_1(r) = 3\tilde{\mu}_s\frac{\sigma^3}{8r^3}\Theta(r) + 9\left(\frac{\mu_\perp}{\mu_r}-1\right)\left(\mathscr{P}^\infty+\frac{1}{2}\right)\left(1-\frac{E_{\text{Q}}^2}{E_0^2}\right)\frac{\sigma^5}{32r^5}\Theta(r) \tag{A.6. 1}$$

accounting for the short-ranged hydrodynamic interactions and electrostatic couplings that promote the alignment of directions between particles i and j. Here, $\mu_\perp$ and μ_r are the mobility coefficients depending on the liquid viscosity and the distance d between the surface and particle respectively. From the expressions in [303–306] we obtain $\mathscr{P}^\infty = 0.08$, $\tilde{\mu}_s = 11$ and $\mu_\perp/\mu_r = 1.5$.

The electrostatic repulsion and the electro-hydrodynamic interactions coupling are encoded in the $A_2(r)$ and $A_3(r)$ coefficients respectively,

$$A_2(r) = 6\left(\frac{\mu_\perp}{\mu_r}-1\right)\sqrt{\frac{E_0^2}{E_{\text{Q}}^2}-1}\left[\left(\mathscr{P}^\infty+\frac{1}{2}\right)\frac{E_0^2}{E_{\text{Q}}^2}-\chi^\infty\right]\frac{\sigma^4}{16r^4}\Theta(r) \tag{A.6. 2}$$

$$A_3(r) = 2\tilde{\mu_s}\frac{\sigma^2}{4r^2}\frac{\sigma}{2H} + \left[\tilde{\mu}_s\frac{\sigma^3}{8r^3} + 5\left(\frac{\mu_\perp}{\mu_r}-1\right)\left(\mathscr{P}^\infty+\frac{1}{2}\right)\left(1-\frac{E_{\text{Q}}^2}{E_0^2}\right)\frac{\sigma^5}{32r^5}\right]\Theta(r) \tag{A.6.3}$$

where the hydrodynamic and electrostatic couplings are screened over distances proportional to the chamber distance, H = 100 μm. A more detailed description can be found in Refs. [4], and [282]. We estimate such coefficients considering the experimental field intensity under which we observe the active gas phase ($E \geq E_Q$, with $E_Q \approx 8\times10^5\,\text{V}\cdot\text{m}^{-1}$),

and average them over distances $r \in [\sigma, 3\sigma]$. For convenience we approximate the screening function as $\Theta(r) = 1$ if $r \leq H/\pi$ and $\Theta(r) = 0$ otherwise.

Under these assumptions, we obtain

$$A_1 = 0.93 k_B T \tag{A.6.4}$$

$$A_2 = 0.33 k_B T \tag{A.6.5}$$

$$A_3 = 0.48 k_B T \tag{A.6.6}$$

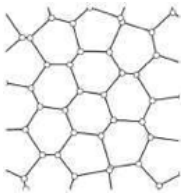

APPENDIX B

The following model is proposed by Mike Allen from discussions about the experimental observations of the Quincke trimers. More details are included in Ref. [367]. For simplicity, to begin with, we assume that the moving particle is a rigid equilateral triangle composed of three Quincke rotors. The motion is of jump–diffusion type, effectively in two dimensions, the processes being as follows.

A jump, which instantaneously rotates the triangle by an angle π about one of the edges, chosen at random, and translates the centre of mass through a distance ℓ perpendicular to the edge. We usually call this a *flip*. The simplest assumption, adopted here, is that successive flips are uncorrelated. In this case, the intervals t_f between successive flips may be sampled from a Poisson process with probability density $\mathscr{P}(t_\mathrm{f}) = \tau^{-1}\exp(-t_\mathrm{f}/\tau)$, defined by the mean interval between flips τ.

Diffusion, specifically centre-of-mass translation with diffusion coefficient D_t, and reorientation about the centre of mass with rotational diffusion coefficient D_r.

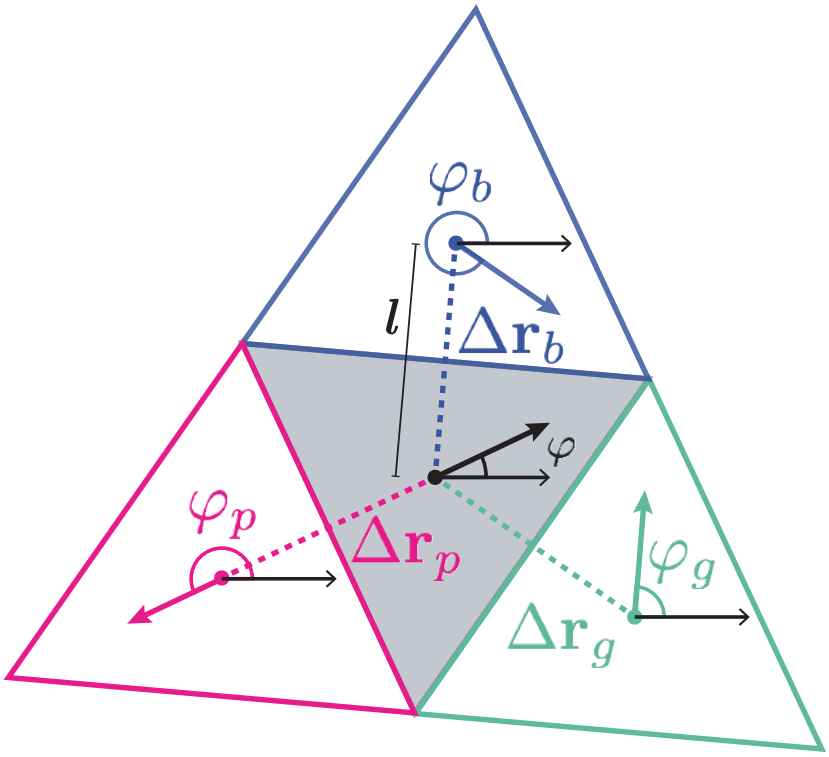

Figure B.1: **Jump-diffusion model.** Geometry of triangle flips. The original triangle is in grey. The coloured, dashed, triangles are obtained by flipping about the corresponding edge. The arrowed double lines indicate the directions of the body-fixed **X** axes. The arrowed single black lines indicate the space-fixed **x** axis, and the angles φ are shown. The single coloured lines indicate the displacements of the centre of mass in each case.

B.1 Jump–diffusion model

Take the centre of mass to lie at $\mathbf{r} = (x, y)$, and the orientation to be defined by Euler angles (φ, θ, ψ); the final angle is always $\psi = 0$. Denote the space-fixed frame by **xyz** and the body-fixed frame by **XYZ**. φ defines the angle between **X** and **x**. θ is the rotation angle about **X** taking values $\theta = 0$ ($\mathbf{Z} = \mathbf{z}$), or $\theta = \pi$ ($\mathbf{Z} = -\mathbf{z}$). The diffusion processes evolve **r** and φ. The flips discontinuously change **r** and both φ and θ. The effect on θ is always $\theta \to \theta + \pi$, and actually, because of the symmetry in this case, it is not necessary to keep track of θ. The effects on **r** and φ must be worked out from the geometry.

B.2 Jump equations

From the figure, it is possible to check the following equations:

$$\Delta\varphi_g = \tfrac{\pi}{3} \qquad \Delta\mathbf{r}_g = \ell\big[\cos(\varphi - \tfrac{\pi}{3}), \sin(\varphi - \tfrac{\pi}{3})\big]$$

$$\Delta\varphi_p = \pi = \tfrac{3\pi}{3} \qquad \Delta\mathbf{r}_p = \ell\big[\cos(\varphi - \pi), \sin(\varphi - \pi)\big]$$

$$\Delta\varphi_b = -\tfrac{\pi}{3} = \tfrac{5\pi}{3} \qquad \Delta\mathbf{r}_b = \ell\big[\cos(\varphi + \tfrac{\pi}{3}), \sin(\varphi + \tfrac{\pi}{3})\big]$$

where $\Delta\varphi_g = \varphi_g - \varphi$ etc. We choose one of these three possible flip cases, randomly. In other words, we randomly choose one out of $\Delta\varphi = \frac{\pi}{3}, \frac{3\pi}{3}, \frac{5\pi}{3}$ and set

$$\Delta\mathbf{r} = \ell\big[\cos(\varphi - \Delta\varphi), \sin(\varphi - \Delta\varphi)\big].$$

Recall that ℓ is the magnitude of the displacement, and is equal to twice the distance between the centre of the triangle and the edges; it is also equal to the distance between the centre of the triangle and the vertices. The side of the triangle is $\sqrt{3}\,\ell$.

B.3 Diffusion equations

Simple diffusion in the absence of external forces, over a time interval Δt, gives

$$\Delta x = \sqrt{2D_\mathrm{t}\Delta t}\,\mathcal{N}_x, \qquad \Delta y = \sqrt{2D_\mathrm{t}\Delta t}\,\mathcal{N}_y, \qquad \Delta\varphi = \sqrt{2D_\mathrm{r}\Delta t}\,\mathcal{N}_\varphi,$$

where $\mathcal{N}_x, \mathcal{N}_y, \mathcal{N}_\varphi$ are independent random numbers chosen from the normal distribution (Gaussian with zero mean and unit variance).

B.4 Units

The problem is defined by the physical parameters ℓ, τ, D_t and D_r. In a simulation program, it is convenient to choose units of length and time, for example so that $\ell = 1$ and $\tau = 1$. This leaves only two dimensionless parameters: the reduced translational diffusion

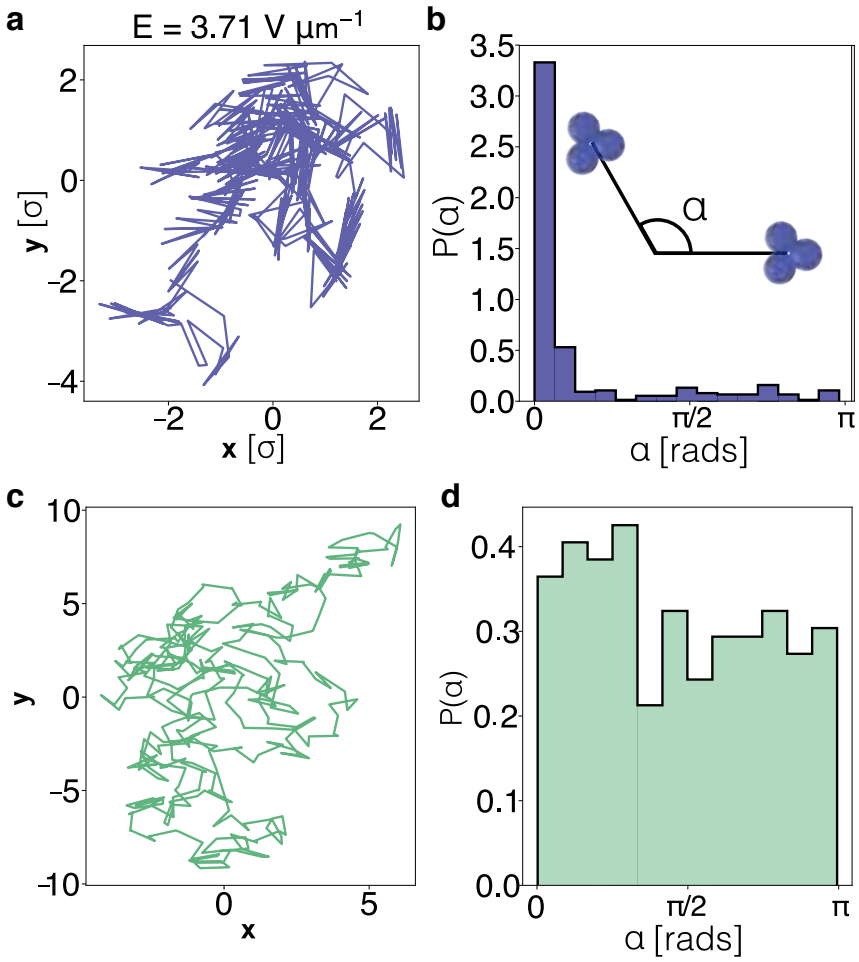

Figure B.2: **Trimer trajectories. a** and **c** are trajectories from experiments and the present model respectively. **b** and **d** show the distribution of the α angles, taken as illustrated by the inset in **b**.

coefficient $D_t^* = D_t\tau/\ell^2$ and the reduced rotational diffusion coefficient $D_r^* = D_r\tau$. The program then produces trajectories in reduced units which are converted back to real units by multiplying x and y by ℓ, and time by τ. Figure B.2 compares two trajectories from experiments sample and the present model. We note the difference between the shape of the trajectories and the distribution of the $alpha$ angles. However, we emphasise that represents a first approximation, and we expect further development of the discrete model.

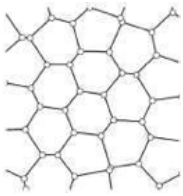

APPENDIX C

C.1 Supplementary Material

Given the very dynamical behaviour of our system, supplementary movies for Chapters 6, 7, and 8 can be accessed by clicking on the link, or alternatively by scanning the following QR code

which redirects to the website in Ref [375]. The movies included in the website are classified as follows:

- Competing interactions for movies corresponding to Chapter 6

- Microgears for results in Chapter 7
- Colloidal molecules for the motion of non-spherical particles described in Chapter 8

C.1.1 Competitive Interaction Movie Details

Supplementary Movie 1

Experimental amoebae phase. Finite-size amoeba clusters displaying collective rotation. The interaction between amoeba aggregates leads to merging, whereas motility induces breaking. Colloids are coloured according to the local ψ_6 indicated by the colourbar. Colloid diameter is $\sigma = 2.92\,\mu$m. Field strength, $E = 1.25E_Q$, Pe = 11, $\phi = 0.11$. Frame acquisition at 180 fps, movie played at 60 fps.

Supplementary Movie 2

Experimental phase transition. Movie shows the experimental phase transition from crystallites to emergent polar bands. Electric strength is rapidly increased from $E = 0.75E_Q$ (Pe ≈ 0) to $E = 3E_Q$, (Pe = 96). Amoebae aggregates emerge as the crystallites become motile. $\phi = 0.072$. Frame acquisition at 180 fps, movie played at 60 fps. Scale bar is $100\,\mu$m.

Supplementary Movie 3

Freezing a band. Transition from polar bands to arrested crystallites. Electric field is rapidly quenched from $E = 3E_Q$, (Pe = 96) to $E = 0.75E_Q$ (Pe ≈ 0). ϕ is 0.072. Frame acquisition at 180 fps, movie played at 60 fps. Scale bar is $100\,\mu$m.

Supplementary Movie 4

Polar band traveling band trough a disorder gas. $E = 3E_Q$, Pe = 96, $\phi = 0.072$. Scale bar is $100\,\mu$m.

Supplementary Movie 5

Onset of banding. Thick bands (of tens of particles) form as particle trajectories undergo alignment. The bands propagate through an isotropic state. Pe = 50 (simulation).

Supplementary Movie 6

Onset of banding. Same data as Supplementary Movie 4, zooming out sequence. Pe = 50 (simulation).

C.1.2 Microgears Movie Details

Supplementary Movie 1

Strong confinement. Movie shows a set of confining regions containing different populations N of rollers. Scale bar is $100\,\mu$m.

Supplementary Movie 2

Rigid rotation. Left: Rotating hexagonal crystallite. The sample consisted of a central roller surrounded by four rotating layers. Scale bar is $5\,\mu$m. Right: Symmetry lines indicate the same angular velocity ω for all the layers. $N = 61$, Pe = 64. Movie recorded at 900 fps, and played at 10 fps.

Supplementary Movie 3

Rigid-slipping rotation.Top left: Microgear at Pe = 90. Scale bar is $5\,\mu$m. Top right. Reference lines show a rigid rotation at the centre, while the outermost layers exhibit a changing behaviour between rigid and slip rotation. Bottom left: The local hexagonal order ψ_6 indicates the rigid body behavior of the central layers, and the changing behaviour between rigid and fluid-like in the exterior. Bottom right: As the layers slip past one another, dislocations appear. However, the rigid behaviour of the centre protects the structure from the propagation of defects towards the centre. $N = 61$. Movie recorded at 900 fps, and played at 10 fps.

Supplementary Movie 4

Slipping-hexagonal rotation. Left panel: Experimental sample at $Pe = 125$. Scale bar is $5\,\mu$m. Middle panel: Reference lines indicate a slip behaviour, with a faster internal rigid rotation. Right panel: The argument of hexagonal order ψ_6 shows sudden changes with the fast sliding of the layers. $N = 61$. Movie recorded at 900 fps, and played at 3 fps.

Supplementary Movie 5

Slip rotation. Top left: Microgear at $Pe = 140$. Scale bar is $5\,\mu$m. Top right. Reference rollers show the full slip behavior of the microgear, and the decoupling of the direction of rotation between the interior and the outermost layer. Bottom left: The local hexagonal order ψ_6 indicates a complete fluid-like behaviour. Bottom right: As the layers slip past one another, dislocations appear and propagate towards the central roller. $N = 61$. Movie recorded at 900 fps, and played at 10 fps.

C.1.3 Colloidal Molecules Movie Details

Supplementary Movie 1

Quincke dumbbells. Left panel: Spinning dumbbells appears at low field strengths. Middle and lefts panels: On increasing field amplitude E, the Quincke dumbbells exhibit circular motion. Scale bar is 50 µm. Movie recorded at 180 fps, and played at 30 fps.

Supplementary Movie 2

Tetramer formation and breaking. Dumbbells featuring circular motion coalesce and form spinning tetramers. Any deviation of the orientations leads to a break off. Scale bar is $10\,\mu$m. Movie recorded at 180 fps, and played at 17 fps.

Supplementary Movie 3

Hexamer formation and break off. A collision between a dumbbell and a previously formed tetramer leads to spinning hexamers. Similar to tetramers, deviations of the

dumbbell orientations promote break off events. Scale bar is 10 μm. Movie recorded at 180 fps, and played at 17 fps.

Supplementary Movie 4

Spinning hexamer. If unperturbed, If unperturbed, hexamers made of three dumbbells exhibit persistent spinning motion. Scale bar is 10 μm. Movie recorded at 180 fps, and played at 17 fps.

Supplementary Movie 5

Jumping trimer. Trimmers exhibit out-of-plane flips and in-plane diffusion. With sufficient electric strength, e.g. $E = 3.71V\,\mu\text{m}^{-1}$, flips become dominant over a preferred direction. Scale bar is 10 μm. Movie recorded at 180 fps, and played at 17 fps.

BIBLIOGRAPHY

[1] M. F. Hsu, E. R. Dufresne, and D. A. Weitz.
Charge stabilization in nonpolar solvents.
Langmuir, 21(11):4881–4887, 2005.

[2] Gerardo E. Pradillo, Hamid Karani, and Petia M. Vlahovska.
Quincke rotor dynamics in confinement: Rolling and hovering.
Soft Matter, 2019.

[3] E. Specht.

[4] Antoine Bricard, Jean-Baptiste Caussin, Nicolas Desreumaux, Olivier Dauchot, and Denis Bartolo.
Emergence of macroscopic directed motion in populations of motile colloids.
Nature, 503(7474):95–98, 2013.

[5] Sriram Ramaswamy.
The Mechanics and Statistics of Active Matter.
Annual Review of Condensed Matter Physics, 1(1):323–345, aug 2010.

[6] Ramin Golestanian and Sriram Ramaswamy.
Active matter.
The European physical journal. E, Soft matter, 36(6):67, 2013.

[7] M C Marchetti, J. F. Joanny, S. Ramaswamy, T. B. Liverpool, J. Prost, Madan Rao, and R. Aditi Simha.
Hydrodynamics of soft active matter.
Reviews of Modern Physics, 85(3):1143–1189, 2013.

[8] András Czirók, Eshel Ben-Jacob, Inon Cohen, and Tamás Vicsek.
Formation of complex bacterial colonies via self-generated vortices.
Physical Review E - Statistical Physics, Plasmas, Fluids, and Related Interdisciplinary Topics, 1996.

[9] Fernando Peruani, Jörn Starruß, Vladimir Jakovljevic, Lotte Søgaard-Andersen, Andreas Deutsch, and Markus Bär.
Collective motion and nonequilibrium cluster formation in colonies of gliding bacteria.
Physical Review Letters, 2012.

[10] A. P. Petroff, X. L. Wu, and A. Libchaber.
Fast-moving bacteria self-organize into active two-dimensional crystals of rotating cells.
Phys. Rev. Lett., 114(15):1–6, 2015.

[11] Cristián Huepe and Maximino Aldana.
Intermittency and clustering in a system of self-driven particles.
Physical Review Letters, 2004.

[12] J. Buhl, D. J.T. Sumpter, I. D. Couzin, J. J. Hale, E. Despland, E. R. Miller, and S. J. Simpson.
From disorder to order in marching locusts.
Science, 2006.

[13] Yingzi Yang, Vincent Marceau, and Gerhard Gompper.
Swarm behavior of self-propelled rods and swimming flagella.
Physical Review E - Statistical, Nonlinear, and Soft Matter Physics, 82(3):1–13, 2010.

[14] Shashi Thutupalli, Ralf Seemann, and Stephan Herminghaus.
Swarming behavior of simple model squirmers.
New Journal of Physics, 13, 2011.

[15] Douglas H. Kelley and Nicholas T. Ouellette.
Emergent dynamics of laboratory insect swarms.
Scientific Reports, 2013.

[16] Marina Sidortsov, Yakov Morgenstern, and Avraham Be'Er.
Role of tumbling in bacterial swarming.
Physical Review E, 96(2):1–7, 2017.

[17] Tamás Vicsek, András Czirók, Eshel Ben-Jacob, Inon Cohen, and Ofer Shochet.
Novel Type of Phase Transition in a System of Self-Driven Particles.
Physical Review Letters, 75(6):1226–1229, aug 1995.

[18] John Toner and Yuhai Tu.
Long-Range Order in a Two-Dimensional Dynamical XYModel: How Birds Fly Together.
Physical Review Letters, 75(23):4326–4329, dec 1995.

[19] J Toner and Y Tu.
Flocks, herds, and schools: A quantitative theory of flocking.
Physical Review E - Statistical Physics, Plasmas, Fluids, and Related Interdisciplinary Topics, 1998.

[20] John Toner, Yuhai Tu, and Sriram Ramaswamy.
Hydrodynamics and phases of flocks, 2005.

[21] John Toner.
Reanalysis of the hydrodynamic theory of fluid, polar-ordered flocks.
Physical Review E - Statistical, Nonlinear, and Soft Matter Physics, 2012.

[22] Tamás Vicsek and Anna Zafeiris.
Collective motion.
Physics Reports, 517(3-4):71–140, aug 2012.

[23] Michele Ballerini, Nicola Cabibbo, Raphael Candelier, Andrea Cavagna, Evaristo Cisbani, Irene Giardina, Alberto Orlandi, Giorgio Parisi, Andrea Procaccini, Massimiliano Viale, and Vladimir Zdravkovic.
Empirical investigation of starling flocks: a benchmark study in collective animal behaviour.
Animal Behaviour, 2008.

[24] Gene F. Mazenko.
Nonequilibrium Statistical Mechanics.
Wiley VCH, 2008.

[25] M. E. Cates.
Diffusive transport without detailed balance in motile bacteria: Does microbiology need statistical physics?
Reports on Progress in Physics, 2012.

[26] Sriram Ramaswamy.
Active matter.
Journal of Statistical Mechanics: Theory and Experiment, 2017(5), 2017.

[27] Clemens Bechinger, Roberto Di Leonardo, Hartmut Löwen, Charles Reichhardt, Giorgio Volpe, and Giovanni Volpe.
Active particles in complex and crowded environments.
Reviews of Modern Physics, 88(4), 2016.

[28] Gandhimohan M. Viswanathan, Marcos G.E. Da Luz, Ernesto P. Raposo, and H. Eugene Stanley.
The physics of foraging: An introduction to random searches and biological encounters.
2011.

[29] Giovanna Di Marzo Serugendo, Noria Foukia, Salima Hassas, Anthony Karageorgos, Soraya Kouadri Mostéfaoui, Orner F. Rana, Mihaela Ulieru, Paul Valckenaers, and Chris Van Aart.
Self-organisation: Paradigms and applications.
In *Lecture Notes in Artificial Intelligence (Subseries of Lecture Notes in Computer Science)*, 2004.

[30] Vito Trianni, Stefano Nolfi, and Marco Dorigo.
Evolution, self-organization and swarm robotics.
In *Swarm Intelligence*. 2008.

[31] Manuele Brambilla, Eliseo Ferrante, Mauro Birattari, and Marco Dorigo.
Swarm robotics: A review from the swarm engineering perspective.
Swarm Intelligence, 2013.

[32] Joseph Wang and Wei Gao.
Nano/microscale motors: Biomedical opportunities and challenges.
ACS Nano, 6(7):5745–5751, 2012.

[33] Marco Tarantola, Tim Meyer, Christoph F. Schmidt, and Wolfram Hubertus Zimmermann.
Physics meets medicine - At the heart of active matter.
Progress in Biophysics and Molecular Biology, 144:1–2, 2019.

[34] H. P. Zhang, A. Be'er, E.-L. Florin, and H. L. Swinney.
Collective motion and density fluctuations in bacterial colonies.
Proceedings of the National Academy of Sciences, 107(31):13626–13630, 2010.

[35] A. Einstein.
Über die von der molekularkinetischen Theorie der Wärme geforderte Bewegung von in ruhenden Flüssigkeiten suspendierten Teilchen.
Annalen der Physik, 1905.

[36] Jörn Dunkel and Peter Hänggi.
Relativistic Brownian motion, 2009.

[37] G. E. Uhlenbeck and L. S. Ornstein.
On the theory of the Brownian motion.
Physical Review, 1930.

[38] P. M. Chaikin and T. C. Lubensky.
Principles of Condensed Matter Physics.
Cambridge University Press, 1995.

[39] Edward M Purcell.
The efficiency of propulsion by a rotating flagellum.
Biophysics, 94(October):11307–11311, 1997.

[40] R. A.L. Jones.
Soft condensed matter.
European Journal of Physics, 23(6), 2002.

[41] U. Erdmann, W. Ebeling, L. Schimansky-Geier, and F. Schweitzer.
Brownian particles far from equilibrium.
European Physical Journal B, 2000.

[42] O. Steuernagel, W. Ebeling, and V. Calenbuhr.
An elementary model for directed active motion.
Chaos, Solitons & Fractals, 4(10):1917–1930, 1994.

[43] Lutz Schimansky-Geier, Michaela Mieth, Helge Rosé, and Horst Malchow.
Structure formation by active Brownian particles.
Physics Letters A, 207(3-4):140–146, 1995.

[44] Frank Schweitzer, Werner Ebeling, and Benno Tilch.
Complex motion of brownian particles with energy depots.
Physical Review Letters, 80(23):5044–5047, 1998.

[45] Pawel Romanczuk and Lutz Schimansky-Geier.
Brownian motion with active fluctuations.
Physical Review Letters, 106(23):1–4, 2011.

[46] P. Romanczuk, M. Bär, W. Ebeling, B. Lindner, and L. Schimansky-Geier.
Active Brownian particles: From individual to collective stochastic dynamics: From individual to collective stochastic dynamics, 2012.

[47] Fernando Peruani and Luis G. Morelli.
Self-propelled particles with fluctuating speed and direction of motion in two dimensions.
Physical Review Letters, 99(1):1–4, 2007.

[48] Howard C. Berg and Douglas A. Brown.
Chemotaxis in Escherichia coli analysed by three-dimensional tracking.
Nature, 1972.

[49] Howard C. Berg and Linda Turner.
Movement of microorganisms in viscous environments [12], 1979.

[50] Howard C. Berg.
Motile Behavior of Bacteria.
Physics Today, 53(1):24–29, 2000.

[51] D. M. Woolley.
Motility of spermatozoa at surfaces.
Reproduction, 2003.

[52] Ingmar H. Riedel, Karsten Kruse, and Jonathon Howard.
Biophysics: A self-organized vortex array of hydrodynamically entrained sperm cells.
Science, 2005.

[53] H. Machemer.
Ciliary activity and the origin of metachrony in Paramecium: effects of increased viscosity.

Journal of Experimental Biology, 1972.

[54] J. R. Blake and M. A. Sleigh.
Mechanics of ciliary locomotion, 1974.

[55] James Lighthill.
Flagellar Hydrodynamics.
SIAM Review, 1976.

[56] E M Purcell.
Life at Low Reynolds Number.
Am. J. Phys., 45:3–11, 1977.

[57] Gavin E. Murphy, Jared R. Leadbetter, and Grant J. Jensen.
In situ structure of the complete Treponema primitia flagellar motor.
Nature, 442(7106):1062–1064, 2006.

[58] Eric Lauga and Raymond E. Goldstein.
Dance of the microswimmers.
Physics Today, 2012.

[59] J. Elgeti, R. G. Winkler, and G. Gompper.
Physics of microswimmers - Single particle motion and collective behavior: A review.
Reports on Progress in Physics, 2015.

[60] M. J. Lighthill.
On the squirming motion of nearly spherical deformable bodies through liquids at very small reynolds numbers.
Communications on Pure and Applied Mathematics, 1952.

[61] Takuji Ishikawa, M. P. Simmonds, and T. J. Pedley.
Hydrodynamic interaction of two swimming model micro-organisms.
Journal of Fluid Mechanics, 2006.

[62] Eric Lauga and Thomas R. Powers.
The hydrodynamics of swimming microorganisms.
Reports on Progress in Physics, 72(9), 2009.

[63] Andreas Zöttl and Holger Stark.
Emergent behavior in active colloids.
Journal of Physics: Condensed Matter, 28(25):253001, 2016.

[64] J. Anderson.
Colloid Transport By Interfacial Forces.
Annual Review of Fluid Mechanics, 1989.

[65] Matthew T Downton and Holger Stark.
Simulation of a model microswimmer.
Journal of Physics: Condensed Matter, 21(20):204101, 2009.

[66] Ingo O. Götze and Gerhard Gompper.
Mesoscale simulations of hydrodynamic squirmer interactions.
Physical Review E - Statistical, Nonlinear, and Soft Matter Physics, 82(4):1–9, 2010.

[67] Knut Drescher, Raymond E. Goldstein, Nicolas Michel, Marco Polin, and Idan Tuval.
Direct measurement of the flow field around swimming microorganisms.
Physical Review Letters, 105(16):1–4, 2010.

[68] Jeffrey S. Guasto, Karl A. Johnson, and J. P. Gollub.
Oscillatory flows induced by microorganisms swimming in two dimensions.
Physical Review Letters, 105(16):18–21, 2010.

[69] F. Alarcón and I. Pagonabarraga.
Spontaneous aggregation and global polar ordering in squirmer suspensions.
Journal of Molecular Liquids, 2013.

[70] Giorgio Pessot, Hartmut Löwen, and Andreas M. Menzel.
Binary pusher–puller mixtures of active microswimmers and their collective behaviour.
Molecular Physics, 116(21-22):3401–3408, 2018.

[71] D. Saintillan.
The Dilute Rheology of Swimming Suspensions: A Simple Kinetic Model.
Experimental Mechanics, 50(9):1275–1281, nov 2010.

[72] David Saintillan and Michael J. Shelley.
Active suspensions and their nonlinear models.
Comptes Rendus Physique, 14(6):497–517, jun 2013.

[73] Salima Rafaï, Levan Jibuti, and Philippe Peyla.
Effective viscosity of microswimmer suspensions.
Physical Review Letters, 104(9):1–4, 2010.

[74] Andrey Sokolov and Igor S. Aranson.
Reduction of viscosity in suspension of swimming bacteria.
Physical Review Letters, 103(14):2–5, 2009.

[75] M. E. Cates, S. M. Fielding, D. Marenduzzo, E. Orlandini, and J. M. Yeomans.
Shearing active gels close to the isotropic-nematic transition.
Physical Review Letters, 2008.

[76] Luca Giomi, Tanniemola B. Liverpool, and M. Cristina Marchetti.
Sheared active fluids: Thickening, thinning, and vanishing viscosity.
Physical Review E - Statistical, Nonlinear, and Soft Matter Physics, 2010.

[77] S. M. Fielding, D. Marenduzzo, and M. E. Cates.
Nonlinear dynamics and rheology of active fluids: Simulations in two dimensions.
Physical Review E - Statistical, Nonlinear, and Soft Matter Physics, 2011.

[78] M. E. Cates and J. Tailleur.
When are active Brownian particles and run-and-tumble particles equivalent? Consequences for motility-induced phase separation.
Epl, 101(2), 2013.

[79] J. Tailleur and M. E. Cates.
Statistical mechanics of interacting run-and-tumble bacteria.
Physical Review Letters, 100(21):3–6, 2008.

[80] Michael E. Cates and Julien Tailleur.
Motility-Induced Phase Separation.
Annual Review of Condensed Matter Physics, 6(1):219–244, mar 2015.

[81] A. P. Solon, M. E. Cates, and J. Tailleur.
Active brownian particles and run-and-tumble particles: A comparative study.
European Physical Journal: Special Topics, 224(7):1231–1262, 2015.

[82] A. Ivlev, H Löwen, G. E. Morfill, and C. P. Royall.
Complex Plasmas and Colloidal Dispersions: Particle-resolved Studies of Classical Liquids and Solids.
World Scientific Publishing Co., Singapore Scientific, 2012.

[83] Daniela J. Kraft, Raphael Wittkowski, Borge Ten Hagen, Kazem V. Edmond, David J. Pine, and Hartmut Löwen.
Brownian motion and the hydrodynamic friction tensor for colloidal particles of complex shape.
Physical Review E - Statistical, Nonlinear, and Soft Matter Physics, 2013.

[84] Borge Ten Hagen, Raphael Wittkowski, Daisuke Takagi, Felix Kümmel, Clemens Bechinger, and Hartmut Löwen.
Can the self-propulsion of anisotropic microswimmers be described by using forces and torques?
Journal of Physics Condensed Matter, 27(19), 2015.

[85] Sven Van Teeffelen and Hartmut Löwen.
Dynamics of a Brownian circle swimmer.
Physical Review E - Statistical, Nonlinear, and Soft Matter Physics, 78(2):2–5, 2008.

[86] Felix Kümmel, Borge Ten Hagen, Raphael Wittkowski, Ivo Buttinoni, Ralf Eichhorn, Giovanni Volpe, Hartmut Löwen, and Clemens Bechinger.
Circular motion of asymmetric self-propelling particles.
Physical Review Letters, 2013.

[87] Raphael Wittkowski and Hartmut Löwen.
Self-propelled Brownian spinning top: Dynamics of a biaxial swimmer at low Reynolds numbers.
Physical Review E - Statistical, Nonlinear, and Soft Matter Physics, 85(2):1–12, 2012.

[88] Hsuan Yi Chen and Kwan Tai Leung.
Rotating states of self-propelling particles in two dimensions.
Physical Review E - Statistical, Nonlinear, and Soft Matter Physics, 73(5):1–9, 2006.

[89] Gabriel S. Redner, Michael F. Hagan, and Aparna Baskaran.
Structure and dynamics of a phase-separating active colloidal fluid.
Physical Review Letters, 110(5):1–5, 2013.

[90] Yaouen Fily, Silke Henkes, and M. Cristina Marchetti.
Freezing and phase separation of self-propelled disks.
Soft Matter, 10(13):2132–2140, 2014.

[91] H. H. Wensink and H. Löwen.
Aggregation of self-propelled colloidal rods near confining walls.
Physical Review E - Statistical, Nonlinear, and Soft Matter Physics, 78(3):20–23, 2008.

[92] Jens Elgeti and Gerhard Gompper.
Wall accumulation of self-propelled spheres.
Epl, 101(4), 2013.

[93] Xingbo Yang, M. Lisa Manning, and M. Cristina Marchetti.
Aggregation and segregation of confined active particles.
Soft Matter, 10(34):6477–6484, 2014.

[94] Mihaela Enculescu and Holger Stark.
Active colloidal suspensions exhibit polar order under gravity.
Physical Review Letters, 2011.

[95] Zhengjia Wang, Hsuan Yi Chen, Yu Jane Sheng, and Heng Kwong Tsao.
Diffusion, sedimentation equilibrium, and harmonic trapping of run-and-tumble nanoswimmers.
Soft Matter, 10(18):3209–3217, 2014.

[96] Walter F. Paxton, Paul T. Baker, Timothy R. Kline, Yang Wang, Thomas E. Mallouk, and Ayusman Sen.
Catalytically induced electrokinetics for motors and micropumps.
Journal of the American Chemical Society, 128(46):14881–14888, 2006.

[97] Aidan Brown and Wilson Poon.
Ionic effects in self-propelled Pt-coated Janus swimmers.
Soft Matter, 10(22):4016–4027, 2014.

[98] I. Theurkauff, C. Cottin-Bizonne, J. Palacci, C. Ybert, and L. Bocquet.
Dynamic clustering in active colloidal suspensions with chemical signaling.
Physical Review Letters, 108(26):1–5, 2012.

[99] Pernille Rørth.
Collective Cell Migration.
Annual Review of Cell and Developmental Biology, 2009.

[100] Kevin Warburton and John Lazarus.
Tendency-distance models of social cohesion in animal groups.
Journal of Theoretical Biology, 1991.

[101] G Nicolis and I Prigogine.
Self-organization in non-equilibrium systems.
Wiley, 1977.

[102] Camazine, S, Deneubourg, JL, Franks, NR, Sneyd, J, Theraulaz, G, and Camazine, S, Deneubourg, JL, Franks, NR, Sneyd, J, Theraulaz, G, and Bonabeau, E.
Self-organization in biological systems.
Princeton University Press, 2001.

[103] D. J.T. Sumpter.
The principles of collective animal behaviour.
Philosophical Transactions of the Royal Society B: Biological Sciences, 361(1465), 2006.

[104] M. Ballerini, N. Cabibbo, R. Candelier, A. Cavagna, E. Cisbani, I. Giardina, V. Lecomte, A. Orlandi, G. Parisi, A. Procaccini, M. Viale, and V. Zdravkovic.
Interaction ruling animal collective behavior depends on topological rather than metric distance: Evidence from a field study.
Proceedings of the National Academy of Sciences of the United States of America, 2008.

[105] Andrea Cavagna, Alessio Cimarelli, Irene Giardina, Giorgio Parisi, Raffaele Santagati, Fabio Stefanini, and M. Viale.
Scale-free correlations in starling flocks.
Proceedings of the National Academy of Sciences, 107(26):11865–11870, 2010.

[106] Iain D. Couzin, Jens Krause, Richard James, Graeme D. Ruxton, and Nigel R. Franks.
Collective memory and spatial sorting in animal groups.
Journal of Theoretical Biology, 2002.

[107] Francesco Ginelli and Hugues Chaté.
Relevance of metric-free interactions in flocking phenomena.
Physical Review Letters, 105(16):1–4, 2010.

[108] Fernando Peruani, Andreas Deutsch, and Markus Bär.
Nonequilibrium clustering of self-propelled rods.
Physical Review E - Statistical, Nonlinear, and Soft Matter Physics, 2006.

[109] Sandrine Ngo, Anton Peshkov, Igor S. Aranson, Eric Bertin, Francesco Ginelli, and Hugues Chaté.
Large-scale chaos and fluctuations in active nematics.
Physical Review Letters, 113(3):1–6, 2014.

[110] Irene Giardina.
Collective behavior in animal groups: Theoretical models and empirical studies.
HFSP Journal, 2008.

[111] Francesco Ginelli, Fernando Peruani, Markus Bär, and Hugues Chaté.
Large-scale collective properties of self-propelled rods.
Physical Review Letters, 104(18):1–4, 2010.

[112] Craig W. Reynolds.
Flocks, herds and schools: A distributed behavioral model.
In *Proceedings of the 14th annual conference on Computer graphics and interactive techniques - SIGGRAPH '87*, volume 21, pages 25–34, New York, New York, USA, 1987. ACM Press.

[113] Francesco Ginelli.
The Physics of the Vicsek Model.
European Physical Journal: Special Topics, 225(11-12):2099–2117, nov 2015.

[114] Guillaume Grégoire and Hugues Chaté.
Onset of Collective and Cohesive Motion.
Physical Review Letters, 92(2):025702, jan 2004.

[115] Hugues Chaté, Francesco Ginelli, Guillaume Grégoire, and Franck Raynaud.
Collective motion of self-propelled particles interacting without cohesion.
Physical Review E, 77(4):046113, apr 2008.

[116] N. D. Mermin and H. Wagner.
Absence of ferromagnetism or antiferromagnetism in one- or two-dimensional isotropic Heisenberg models.
Physical Review Letters, 1966.

[117] P. C. Hohenberg.
Existence of long-range order in one and two dimensions.
Physical Review, 1967.

[118] Aparna Baskaran and M. Cristina Marchetti.
Hydrodynamics of self-propelled hard rods.
Physical Review E - Statistical, Nonlinear, and Soft Matter Physics, 77(1):1–9, 2008.

[119] M. Aldana, V. Dossetti, C. Huepe, V. M. Kenkre, and H. Larralde.
Phase transitions in systems of self-propelled agents and related network models.
Physical Review Letters, 2007.

[120] M. Aldana, H. Larralde, and B. Vázquez.
On the emergence of collective order in swarming systems: A recent debate.
International Journal of Modern Physics B, 2009.

[121] Gabriel Baglietto and Ezequiel V. Albano.
Nature of the order-disorder transition in the Vicsek model for the collective motion of self-propelled particles.
Physical Review E - Statistical, Nonlinear, and Soft Matter Physics, 2009.

[122] Tamás Vicsek, András Czirók, Illés J. Farkas, and Dirk Helbing.
Application of statistical mechanics to collective motion in biology.
Physica A: Statistical Mechanics and its Applications, 1999.

[123] O. J. O'Loan and M. R. Evans.
Alternating steady state in one-dimensional flocking.
Journal of Physics A: Mathematical and General, 1999.

[124] A. P. Solon and J. Tailleur.
Revisiting the Flocking Transition Using Active Spins.
Physical Review Letters, 111(7):078101, aug 2013.

[125] Anton Peshkov, Sandrine Ngo, Eric Bertin, Hugues Chaté, and Francesco Ginelli.
Continuous theory of active matter systems with metric-free interactions.
Physical Review Letters, 109(9):1–6, 2012.

[126] Aparna Baskaran and M. Cristina Marchetti.
Enhanced diffusion and ordering of self-propelled rods.
Physical Review Letters, 101(26):1–4, 2008.

[127] Aparna Baskaran and Cristina M. Marchetti.
Nonequilibrium statistical mechanics of self-propelled hard rods.
Journal of Statistical Mechanics: Theory and Experiment, 2010.

[128] D. Grossman, I. S. Aranson, and E. Ben Jacob.
Emergence of agent swarm migration and vortex formation through inelastic collisions.
New Journal of Physics, 2008.

[129] Eric Bertin, Michel Droz, and Guillaume Grégoire.
Boltzmann and hydrodynamic description for self-propelled particles.
Physical Review E, 74(2):022101, aug 2006.

[130] Thomas Ihle.
Kinetic theory of flocking: Derivation of hydrodynamic equations.
Physical Review E - Statistical, Nonlinear, and Soft Matter Physics, 83(3):1–4, 2011.

[131] Ernst Ising.
Beitrag zur Theorie des Ferromagnetismus.
Zeitschrift für Physik, 1925.

[132] Alexandre P. Solon, Hugues Chaté, and Julien Tailleur.
From Phase to Microphase Separation in Flocking Models: The Essential Role of Nonequilibrium Fluctuations.
Physical Review Letters, 114(6):068101, feb 2015.

[133] Jean-Baptiste Caussin, Alexandre Solon, Anton Peshkov, Hugues Chaté, Thierry Dauxois, Julien Tailleur, Vincenzo Vitelli, and Denis Bartolo.
Emergent Spatial Structures in Flocking Models: A Dynamical System Insight.
Physical Review Letters, 112(14):148102, 2014.

[134] Eric Bertin, Michel Droz, and Guillaume Grégoire.
Hydrodynamic equations for self-propelled particles: Microscopic derivation and stability analysis.
Journal of Physics A: Mathematical and Theoretical, 42(44), 2009.

[135] Anton Peshkov, Igor S. Aranson, Eric Bertin, Hugues Chaté, and Francesco Ginelli.
Nonlinear field equations for aligning self-propelled rods.
Physical Review Letters, 109(26):1–5, 2012.

[136] Eric Bertin, Hugues Chaté, Francesco Ginelli, Shradha Mishra, Anton Peshkov, and Sriram Ramaswamy.
Mesoscopic theory for fluctuating active nematics.
New Journal of Physics, 15, 2013.

[137] Florian Thüroff, Christoph A. Weber, and Erwin Frey.
Critical assessment of the boltzmann approach to active systems.
Physical Review Letters, 111(19):1–5, 2013.

[138] A. Peshkov, E. Bertin, F. Ginelli, and H. Chaté.
Boltzmann-Ginzburg-Landau approach for continuous descriptions of generic Vicsek-like models.
European Physical Journal: Special Topics, 223(7):1315–1344, 2014.

[139] Florian Thüroff, Christoph A. Weber, and Erwin Frey.
Numerical treatment of the boltzmann equation for self-propelled particle systems.
Physical Review X, 4(4):1–23, 2014.

[140] S. Ramaswamy, R. Aditi Simha, and J. Toner.
Active nematics on a substrate: Giant number fluctuations and long-time tails.
Europhysics Letters, 62(2):196–202, 2003.

[141] Xia Qing Shi and Yu Qiang Ma.
Topological structure dynamics revealing collective evolution in active nematics.
Nature Communications, 2013.

[142] Luca Giomi and Antonio Desimone.
Spontaneous division and motility in active nematic droplets.
Physical Review Letters, 112(14):1–5, 2014.

[143] Luca Giomi.
Geometry and topology of Turbulence in active nematics.
Physical Review X, 5(3):1–11, 2015.

[144] K. Kruse, J. F. Joanny, F. Jülicher, J. Prost, and K. Sekimoto.
Asters, Vortices, and Rotating Spirals in Active Gels of Polar Filaments.
Physical Review Letters, 92(7):1–4, 2004.

[145] J. F. Joanny, F. Jülicher, K. Kruse, and J. Prost.
Hydrodynamic theory for multi-component active polar gels.
New Journal of Physics, 9, 2007.

[146] J. Prost, F. Jülicher, and J. F. Joanny.
Active gel physics.
Nature Physics, 11(2):111–117, 2015.

[147] Francis G. Woodhouse and Raymond E. Goldstein.
Spontaneous circulation of confined active suspensions.
Physical Review Letters, 2012.

[148] Hugo Wioland, Francis G. Woodhouse, Jörn Dunkel, John O. Kessler, and Raymond E. Goldstein.
Confinement stabilizes a bacterial suspension into a spiral vortex.
Physical Review Letters, 2013.

[149] Andrea Cairoli, Rainer Klages, and Adrian Baule.
Weak galilean invariance as a selection principle for coarse-grained diffusive models.
Proceedings of the National Academy of Sciences of the United States of America, 2018.

[150] András Czirók, H. Eugene Stanley, and Tamás Vicsek.
Spontaneously ordered motion of self-propelled particles.
Journal of Physics A: Mathematical and General, 1997.

[151] A. P. Solon and J. Tailleur.
Flocking with discrete symmetry: The two-dimensional active Ising model.
Physical Review E - Statistical, Nonlinear, and Soft Matter Physics, 92(4):1–18, 2015.

[152] V. Narayan, S. Ramaswamy, and N. Menon.
Long-Lived Giant Number Fluctuations in a Swarming Granular Nematic.
Science, 317(5834):105–108, jul 2007.

[153] Julien Deseigne, Olivier Dauchot, and Hugues Chaté.
Collective motion of vibrated polar disks.
Physical Review Letters, 105(9):1–4, 2010.

[154] Volker Schaller and Andreas R. Bausch.
Topological defects and density fluctuations in collectively moving systems.
Proceedings of the National Academy of Sciences of the United States of America, 110(12):4488–4493, 2013.

[155] Alexandre P. Solon, Jean Baptiste Caussin, Denis Bartolo, Hugues Chaté, and Julien Tailleur.
Pattern formation in flocking models: A hydrodynamic description.
Physical Review E - Statistical, Nonlinear, and Soft Matter Physics, 92(6):1–18, 2015.

[156] Arvind Gopinath, Michael F. Hagan, M. Cristina Marchetti, and Aparna Baskaran.
Dynamical self-regulation in self-propelled particle flows.
Physical Review E - Statistical, Nonlinear, and Soft Matter Physics, 85(6):1–8, 2012.

[157] Thomas Ihle.
Invasion-wave-induced first-order phase transition in systems of active particles.
Physical Review E - Statistical, Nonlinear, and Soft Matter Physics, 2013.

[158] Jean Baptiste Caussin and Denis Bartolo.
Braiding a flock: Winding statistics of interacting flying spins.
Physical Review Letters, 2015.

[159] Volker Schaller, Christoph Weber, Christine Semmrich, Erwin Frey, and Andreas R. Bausch.
Polar patterns of driven filaments.
Nature, 467(7311):73–77, 2010.

[160] C. A. Weber, T. Hanke, J. Deseigne, S. Léonard, O. Dauchot, E. Frey, and H. Chaté.
Long-range ordering of vibrated polar disks.
Physical Review Letters, 110(20):1–5, 2013.

[161] F. Peruani, A. Deutsch, and M. Bär.
A mean-field theory for self-propelled particles interacting by velocity alignment mechanisms.
In *European Physical Journal: Special Topics*, 2008.

[162] Hugues Chaté, Francesco Ginelli, and Raúl Montagne.
Simple model for active nematics: Quasi-long-range order and giant fluctuations.
Physical Review Letters, 96(18):1–4, 2006.

[163] Yaouen Fily and M. Cristina Marchetti.
Athermal phase separation of self-propelled particles with no alignment.
Physical Review Letters, 108(23):1–5, 2012.

[164] Julian Bialké, Hartmut Löwen, and Thomas Speck.
Microscopic theory for the phase separation of self-propelled repulsive disks.
Epl, 103(3), 2013.

[165] D Levis and L Berthier.
Clustering and heterogeneous dynamics in a kinetic Monte Carlo model of self-propelled hard disks.
Phys. Rev. E, 89:62301, 2014.

[166] Joakim Stenhammar, Adriano Tiribocchi, Rosalind J. Allen, Davide Marenduzzo, and Michael E. Cates.
Continuum theory of phase separation kinetics for active brownian particles.
Physical Review Letters, 111(14):1–5, 2013.

[167] A. P. Solon, Y. Fily, A. Baskaran, M. E. Cates, Y. Kafri, M. Kardar, and J. Tailleur.
Pressure is not a state function for generic active fluids.
Nature Physics, 11(8):673–678, 2015.

[168] Andreas Zöttl and Holger Stark.
Hydrodynamics Determines Collective Motion and Phase Behavior of Active Colloids in Quasi-Two-Dimensional Confinement.
Physical Review Letters, 112(11):118101, mar 2014.

[169] Thomas Speck, Julian Bialké, Andreas M. Menzel, and Hartmut Löwen.

Effective Cahn-Hilliard Equation for the Phase Separation of Active Brownian Particles.
Physical Review Letters, 112(21):218304, may 2014.

[170] Gabriel S. Redner, Caleb G. Wagner, Aparna Baskaran, and Michael F. Hagan.
Classical Nucleation Theory Description of Active Colloid Assembly.
Physical Review Letters, 117(14):1–7, 2016.

[171] Samuel R. McCandlish, Aparna Baskaran, and Michael F. Hagan.
Spontaneous segregation of self-propelled particles with different motilities.
Soft Matter, 8(8):2527–2534, 2012.

[172] Simon N. Weber, Christoph A. Weber, and Erwin Frey.
Binary Mixtures of Particles with Different Diffusivities Demix.
Physical Review Letters, 116(5):1–5, 2016.

[173] Joakim Stenhammar, Raphael Wittkowski, Davide Marenduzzo, and Michael E. Cates.
Activity-induced phase separation and self-assembly in mixtures of active and passive particles.
Physical Review Letters, 114(1):1–5, 2015.

[174] Joakim Stenhammar, Davide Marenduzzo, Rosalind J. Allen, and Michael E. Cates.
Phase behaviour of active Brownian particles: the role of dimensionality.
Soft Matter, 10(10):1489–1499, 2014.

[175] Adam Wysocki, Roland G Winkler, and Gerhard Gompper.
Cooperative Motion of Active Brownian Spheres in Three-Dimensional Dense Suspensions.
EPL (Europhysics Letters), 105(4):48004, feb 2013.

[176] Ricard Matas-Navarro, Ramin Golestanian, Tanniemola B. Liverpool, and Suzanne M. Fielding.
Hydrodynamic suppression of phase separation in active suspensions.
Physical Review E - Statistical, Nonlinear, and Soft Matter Physics, 90(3):1–9, 2014.

[177] Gabriel S. Redner, Aparna Baskaran, and Michael F. Hagan.
Reentrant phase behavior in active colloids with attraction.
Physical Review E - Statistical, Nonlinear, and Soft Matter Physics, 88(1):1–5, 2013.

[178] Silke Henkes, Yaouen Fily, and M. Cristina Marchetti.
Active jamming: Self-propelled soft particles at high density.
Physical Review E - Statistical, Nonlinear, and Soft Matter Physics, 84(4):84–87, 2011.

[179] Thomas W. Lion and Rosalind J. Allen.
Osmosis with active solutes.
Epl, 106(3), 2014.

[180] S C Takatori, W Yan, and J F Brady.
Swim pressure: Stress generation in active matter.
Physical Review Letters, 113(2):1–5, 2014.

[181] Raphael Wittkowski, Adriano Tiribocchi, Joakim Stenhammar, Rosalind J. Allen, Davide Marenduzzo, and Michael E. Cates.
Scalar ϕ 4 field theory for active-particle phase separation.
Nature Communications, 2014.

[182] S. A. Mallory, A. Šarić, C. Valeriani, and A. Cacciuto.
Anomalous thermomechanical properties of a self-propelled colloidal fluid.
Physical Review E - Statistical, Nonlinear, and Soft Matter Physics, 89(5):1–7, 2014.

[183] S C Takatori and J F Brady.
Towards a thermodynamics of active matter.
Physical Review E - Statistical, Nonlinear, and Soft Matter Physics, 91(3):1–7, 2015.

[184] Félix Ginot, Isaac Theurkauff, Demian Levis, Christophe Ybert, Lydéric Bocquet, Ludovic Berthier, and Cécile Cottin-Bizonne.
Nonequilibrium equation of state in suspensions of active colloids.
Physical Review X, 5(1):1–8, 2015.

[185] Ran Ni, Martien A. Cohen Stuart, and Peter G Bolhuis.
Tunable long range forces mediated by self-propelled colloidal hard spheres.
Physical Review Letters, 114(1):1–5, 2015.

[186] Alexandre P. Solon, Joakim Stenhammar, Raphael Wittkowski, Mehran Kardar, Yariv Kafri, Michael E. Cates, and Julien Tailleur.
Pressure and phase equilibria in interacting active Brownian spheres.
Physical Review Letters, 114(19):1–6, 2015.

[187] Pasquale Digregorio, Demian Levis, Antonio Suma, Leticia F. Cugliandolo, Giuseppe Gonnella, and Ignacio Pagonabarraga.
Full Phase Diagram of Active Brownian Disks: From Melting to Motility-Induced Phase Separation.
Physical Review Letters, 2018.

[188] J. M. Kosterlitz and D. J. Thouless.
Ordering, metastability and phase transitions in two-dimensional systems.
Journal of Physics C: Solid State Physics, 1973.

[189] B. I. Halperin and David R. Nelson.
Theory of Two-Dimensional melting.
Physical Review Letters, 1978.

[190] A. P. Young.
Melting and the vector Coulomb gas in two dimensions.
Physical Review B, 1979.

[191] E. P. Bernard and W. Krauth.
Two-step melting in two dimensions: First-order liquid-hexatic transition.
Phys. Rev. Lett., 107:155704, Oct 2011.

[192] Sebastian C. Kapfer and Werner Krauth.
Two-dimensional melting: From liquid-hexatic coexistence to continuous transitions.
Physical Review Letters, 114(3):1–5, 2015.

[193] Alice L. Thorneywork, Joshua L. Abbott, Dirk G.A.L. A. L. Aarts, and Roel P.A. A. Dullens.
Two-Dimensional Melting of Colloidal Hard Spheres.
Physical Review Letters, 118(15):1–5, apr 2017.

[194] David Richard, Hartmut Löwen, and Thomas Speck.
Nucleation pathway and kinetics of phase-separating active Brownian particles.
Soft Matter, 2016.

[195] Julian Bialké, Jonathan T. Siebert, Hartmut Löwen, and Thomas Speck.
Negative Interfacial Tension in Phase-Separated Active Brownian Particles.
Physical Review Letters, 115(9):1–5, 2015.

[196] Walter F. Paxton, Kevin C. Kistler, Christine C. Olmeda, Ayusman Sen, Sarah K. St. Angelo, Yanyan Cao, Thomas E. Mallouk, Paul E. Lammert, and Vincent H. Crespi.
Catalytic nanomotors: Autonomous movement of striped nanorods.
Journal of the American Chemical Society, 2004.

[197] Walter F. Paxton, Ayusman Sen, and Thomas E. Mallouk.
Motility of catalytic nanoparticles through self-generated forces.
Chemistry - A European Journal, 2005.

[198] Jonathan R. Howse, Richard A.L. Jones, Anthony J. Ryan, Tim Gough, Reza Vafabakhsh, and Ramin Golestanian.
Self-Motile Colloidal Particles: From Directed Propulsion to Random Walk.
Physical Review Letters, 2007.

[199] Rawiwan Laocharoensuk, Jared Burdick, and Joseph Wang.
Carbon-nanotube-induced acceleration of catalytic nanomotors.
ACS Nano, 2008.

[200] Stephen J. Ebbens and Jonathan R. Howse.
In pursuit of propulsion at the nanoscale, 2010.

[201] Rémi Dreyfus, Jean Baudry, Marcus L. Roper, Marc Fermigier, Howard A. Stone, and Jérôme Bibette.
Microscopic artificial swimmers.
Nature, 2005.

[202] D. Zerrouki, J. Baudry, D. Pine, P. Chaikin, and J. Bibette.
Chiral colloidal clusters.
Nature, 455(7211):380–382, 2008.

[203] Ambarish Ghost and Peer Fischer.
Controlled propulsion of artificial magnetic nanostructured propellers.
Nano Letters, 2009.

[204] Li Zhang, Jake J. Abbott, Lixin Dong, Bradley E. Kratochvil, Dominik Bell, and Bradley J. Nelson.
Artificial bacterial flagella: Fabrication and magnetic control.
Applied Physics Letters, 2009.

[205] Jennifer Galanis, Daniel Harries, Dan L. Sackett, Wolfgang Losert, and Ralph Nossal.
Spontaneous patterning of confined granular rods.
Physical Review Letters, 96(2):5–8, 2006.

[206] Arshad Kudrolli.
Concentration dependent diffusion of self-propelled rods.
Physical Review Letters, 104(8):1–4, 2010.

[207] Daizou Yamada, Tsuyoshi Hondou, and Masaki Sano.
Coherent dynamics of an asymmetric particle in a vertically vibrating bed.
Physical Review E - Statistical Physics, Plasmas, Fluids, and Related Interdisciplinary Topics, 67(4):4, 2003.

[208] Arshad Kudrolli, Geoffroy Lumay, Dmitri Volfson, and Lev S. Tsimring.
Swarming and swirling in self-propelled polar granular rods.
Physical Review Letters, 100(5):2–5, 2008.

[209] Igor S. Aranson, Dmitri Volfson, and Lev S. Tsimring.
Swirling motion in a system of vibrated elongated particles.
Physical Review E - Statistical, Nonlinear, and Soft Matter Physics, 75(5):1–9, 2007.

[210] Khanh Dang Nguyen Thu Lam, Michael Schindler, and Olivier Dauchot.
Self-propelled hard disks: Implicit alignment and transition to collective motion.
New Journal of Physics, 2015.

[211] G. Briand and O. Dauchot.
Crystallization of Self-Propelled Hard Discs.
Phys. Rev. Lett., 117(9):1–5, 2016.

[212] Guillaume Briand, Michael Schindler, and Olivier Dauchot.
Spontaneously Flowing Crystal of Self-Propelled Particles.
Physical Review Letters, 2018.

[213] G. Junot, G. Briand, R. Ledesma-Alonso, and O. Dauchot.
Active versus Passive Hard Disks against a Membrane: Mechanical Pressure and Instability.
Physical Review Letters, 119(2):1–5, 2017.

[214] Julien Deseigne, Sébastien Léonard, Olivier Dauchot, and Hugues Chaté.
Vibrated polar disks: Spontaneous motion, binary collisions, and collective dynamics.
Soft Matter, 8(20):5629–5639, 2012.

[215] Nitin Kumar, Harsh Soni, Sriram Ramaswamy, and A. K. Sood.
Flocking at a distance in active granular matter.
Nature Communications, 5, 2014.

[216] Y. Nakaseko and M. Yanagida.
Cytoskeleton in the cell cycle.
Nature, 412(6844):291–292, 2001.

[217] J Howard and RL Clark.
Mechanics of Motor Proteins and the Cytoskeleton.
Applied Mechanics Reviews, 2002.

[218] F. J. Nédélec, T. Surrey, A. C. Maggs, and S. Leibler.
Self-organization of microtubules and motors.
Nature, 1997.

[219] Tanniemola B. Liverpool.
Anomalous fluctuations of active polar filaments.
Physical Review E - Statistical Physics, Plasmas, Fluids, and Related Interdisciplinary Topics, 67(3):5, 2003.

[220] Volker Schaller, Christoph A. Weber, Benjamin Hammerich, Erwin Frey, and Andreas R. Bausch.
Frozen steady states in active systems.
Proceedings of the National Academy of Sciences of the United States of America, 108(48):19183–19188, 2011.

[221] Tim Sanchez, Daniel T. N. Chen, Stephen J. DeCamp, Michael Heymann, and Zvonimir Dogic.

Spontaneous motion in hierarchically assembled active matter.
Nature, 491(7424):431–434, 2012.

[222] Yutaka Sumino, Ken H. Nagai, Yuji Shitaka, Dan Tanaka, Kenichi Yoshikawa, Hugues Chaté, and Kazuhiro Oiwa.
Large-scale vortex lattice emerging from collectively moving microtubules.
Nature, 483(7390):448–452, 2012.

[223] Felix C. Keber, Etienne Loiseau, Tim Sanchez, Stephen J. DeCamp, Luca Giomi, Mark J. Bowick, M. Cristina Marchetti, Zvonimir Dogic, and Andreas R. Bausch.
Topology and dynamics of active nematic vesicles.
Science, 2014.

[224] P. Guillamat, J. Ignés-Mullol, and F. Sagués.
Taming active turbulence with patterned soft interfaces.
Nature Communications, 8(1):1–8, 2017.

[225] J. Urzay, A. Doostmohammadi, and J. M. Yeomans.
Multi-scale statistics of turbulence motorized by active matter.
Journal of Fluid Mechanics, 822:762–773, 2017.

[226] Berta Martínez-Prat, Jordi Ignés-Mullol, Jaume Casademunt, and Francesc Sagués.
Selection mechanism at the onset of active turbulence.
Nature Physics, 15(4):362–366, 2019.

[227] Christoph A. Weber, Volker Schaller, Andreas R. Bausch, and Erwin Frey.
Nucleation-induced transition to collective motion in active systems.
Physical Review E - Statistical, Nonlinear, and Soft Matter Physics, 2012.

[228] S C Glotzer and M J Solomon.
Anisotropy of building blocks and their assembly into complex structures.
Nature Mater., 6:557–562, 2007.

[229] S Sacanna, W T M Irvine, P M Chaikin, and D J Pine.
Lock and key colloids.
Nature, 464:575–578, 2010.

[230] P. N. Pusey and W van Megen.
Phase behaviour of concentrated suspensions of nearly hard colloidal spheres.
Nature, 320(6060):340–342, 1986.

[231] C P Royall, W C K Poon, and E R Weeks.
In search of colloidal hard spheres.
Soft Matter, 9:17–27, 2013.

[232] S. Auer and D. Frenkel.
Prediction of absolute crystal-nucleation rate in hard-sphere colloids.
Nature, 2001.

[233] Anand Yethiraj and Alfons van Blaaderen.
A colloidal model system with an interaction tunable from hard sphere to soft and dipolar.
Nature, 421(6922):513–517, 2003.

[234] M E Leunissen, C G Christova, A.-P. Hyninnen, C P Royall, A I Campbell, A Imhof, M Dijkstra, R van Roij, and A van Blaaderen.
Ionic colloidal crystals of oppositely charged particles.
Nature, 437:235–240, 2005.

[235] J Taffs, S R Williams, H Tanaka, and C P Royall.
Structure and Dynamics in the Crystallisation of Nearly Hard Spheres.
ArXiV:cond-mat, 2012.

[236] W van Megen, P N Pusey, and P Bartlett.
Phase behavior of dispersions of hard spherical particles.
Phase Transitions, 21(2-4):207–227, 1990.

[237] Eric R. Weeks, J. C. Crocker, Andrew C. Levitt, Andrew Schofield, and D. A. Weitz.
Three-dimensional direct imaging of structural relaxation near the colloidal glass transition.
Science, 2000.

[238] Willem K. Kegel.
Direct observation of dynamical heterogeneities in colloidal hard-sphere suspensions.
Science, 2000.

[239] C. Patrick Royall, Stephen R. Williams, Takehiro Ohtsuka, and Hajime Tanaka.
Direct observation of a local structural mechanism for dynamic arrest.
Nature Materials, 2008.

[240] Rustem F. Ismagilov, Alexander Schwartz, Ned Bowden, and George M. Whitesides.
Autonomous movement and self-assembly.
Angewandte Chemie - International Edition, 2002.

[241] R. Golestanian, T. B. Liverpool, and A. Ajdari.
Designing phoretic micro- and nano-swimmers.
New Journal of Physics, 9, 2007.

[242] Andreas Walther and Axel H.E. Müller.
Janus particles: Synthesis, self-assembly, physical properties, and applications, 2013.

[243] Marco Lattuada and T. Alan Hatton.
Synthesis, properties and applications of Janus nanoparticles.
Nano Today, 6(3):286–308, 2011.

[244] Luigi Carbone and P. Davide Cozzoli.
Colloidal heterostructured nanocrystals: Synthesis and growth mechanisms.
Nano Today, 2010.

[245] Claire Vilain, Frédéric Goettmann, Audrey Moores, Pascal Le Floch, and Clément Sanchez.
Study of metal nanoparticles stabilised by mixed ligand shell: A striking blue shift of the surface-plasmon band evidencing the formation of Janus nanoparticles.
Journal of Materials Chemistry, 2007.

[246] Shashi Thutupalli, Delphine Geyer, Rajesh Singh, Ronojoy Adhikari, and Howard A Stone.
Flow-induced phase separation of active particles is controlled by boundary conditions.
115(21):5403–5408, 2018.

[247] M. Schmitt and H. Stark.
Swimming active droplet: A theoretical analysis.
EPL, 2013.

[248] Ziane Izri, Marjolein N. Van Der Linden, Sébastien Michelin, and Olivier Dauchot.
Self-propulsion of pure water droplets by spontaneous marangoni-stress-driven motion.
Physical Review Letters, 113(24):1–5, 2014.

[249] Claudio Maggi, Filippo Saglimbeni, Michele Dipalo, Francesco De Angelis, and Roberto Di Leonardo.
Micromotors with asymmetric shape that efficiently convert light into work by thermocapillary effects.
Nature Communications, 6:7855, 2015.

[250] Ivo Buttinoni, Julian Bialké, Felix Kümmel, Hartmut Löwen, Clemens Bechinger, and Thomas Speck.
Dynamical Clustering and Phase Separation in Suspensions of Self-Propelled Colloidal Particles.
Physical Review Letters, 110(23):238301, jun 2013.

[251] Jeremie Palacci, Stefano Sacanna, Asher Preska Steinberg, David J Pine, and Paul M Chaikin.
Living Crystals of Light-Activated Colloidal Surfers.
Science, 339(6122):936–940, 2013.

[252] Marjolein N. Van Der Linden, Lachlan C. Alexander, Dirk G.A.L. Aarts, and Olivier Dauchot.
Interrupted Motility Induced Phase Separation in Aligning Active Colloids.
Physical Review Letters, 123(9):98001, 2019.

[253] Jérémie Palacci, Cécile Cottin-Bizonne, Christophe Ybert, and Lydéric Bocquet.
Sedimentation and effective temperature of active colloidal suspensions.
Physical Review Letters, 105(8):1–4, 2010.

[254] Ramin Golestanian, Tanniemola B. Liverpool, and Armand Ajdari.
Propulsion of a molecular machine by asymmetric distribution of reaction products.
Physical Review Letters, 94(22):1–4, 2005.

[255] Jeffrey L. Moran and Jonathan D. Posner.
Electrokinetic locomotion due to reaction-induced charge auto-electrophoresis.
Journal of Fluid Mechanics, 2011.

[256] Xing Ma, Anita Jannasch, Urban Raphael Albrecht, Kersten Hahn, Albert Miguel-López, Erik Schäffer, and Samuel Sánchez.
Enzyme-Powered Hollow Mesoporous Janus Nanomotors.
Nano Letters, 2015.

[257] Daisuke Takagi, Jérémie Palacci, Adam B. Braunschweig, Michael J. Shelley, and Jun Zhang.
Hydrodynamic capture of microswimmers into sphere-bound orbits.
Soft Matter, 10(11):1784–1789, 2014.

[258] Sébastien Fournier-Bidoz, André C. Arsenault, Ian Manners, and Geoffrey A. Ozin.
Synthetic self-propelled nanorotors.
Chemical Communications, 2005.

[259] Qian Chen, Jonathan K. Whitmer, Shan Jiang, Sung Chul Bae, Erik Luijten, and Steve Granick.
Supracolloidal reaction kinetics of janus spheres.
Science, 331(6014):199–202, 2011.

[260] Benno Liebchen and Hartmut Löwen.
Which interactions dominate in active colloids?
Journal of Chemical Physics, 150(6), 2019.

[261] F. Ginot, I. Theurkauff, F. Detcheverry, C. Ybert, and C. Cottin-Bizonne.
Aggregation-fragmentation and individual dynamics of active clusters.
Nature Communications, 9(1), 2018.

[262] Hong Ren Jiang, Natsuhiko Yoshinaga, and Masaki Sano.
Active motion of a Janus particle by self-thermophoresis in a defocused laser beam.
Physical Review Letters, 105(26):1–4, 2010.

[263] Klaus Kroy, Dipanjan Chakraborty, and Frank Cichos.
Hot microswimmers.
European Physical Journal: Special Topics, 225(11-12):2207–2225, 2016.

[264] Utsab Khadka, Viktor Holubec, Haw Yang, and Frank Cichos.
Active particles bound by information flows.
Nature Communications, 9(1):1–9, 2018.

[265] Giovanni Volpe, Ivo Buttinoni, Dominik Vogt, Hans-Jürgen Kümmerer, and Clemens Bechinger.
Microswimmers in patterned environments.
Soft Matter, 7(19):8810, 2011.

[266] Ivo Buttinoni, Giovanni Volpe, Felix Kümmel, Giorgio Volpe, and Clemens Bechinger.
Active Brownian motion tunable by light.
Journal of Physics Condensed Matter, 2012.

[267] Sela Samin and René Van Roij.
Self-Propulsion Mechanism of Active Janus Particles in Near-Critical Binary Mixtures.
Physical Review Letters, 2015.

[268] Alois Würger.
Self-Diffusiophoresis of Janus Particles in Near-Critical Mixtures.
Physical Review Letters, 2015.

[269] Falko Schmidt, Benno Liebchen, Hartmut Löwen, and Giovanni Volpe.
Light-controlled assembly of active colloidal molecules.
Journal of Chemical Physics, 150(9), 2019.

[270] Erik Gauger and Holger Stark.
Numerical study of a microscopic artificial swimmer.
Physical Review E - Statistical, Nonlinear, and Soft Matter Physics, 2006.

[271] Fernando Martinez-Pedrero, Antonio Ortiz-Ambriz, Ignacio Pagonabarraga, and Pietro Tierno.
Colloidal Microworms Propelling via a Cooperative Hydrodynamic Conveyor Belt.
Physical Review Letters, 115(3):1–5, 2015.

[272] Jing Yan, Sung Chul Bae, and Steve Granick.
Colloidal superstructures programmed into magnetic janus particles.
Advanced Materials, 27(5):874–879, 2015.

[273] J. Yan, S. C. Bae, and S. Granick.
Rotating crystals of magnetic Janus colloids.
Soft Matter, 11(1):147–153, 2015.

[274] Andreas Kaiser, Alexey Snezhko, and Igor S. Aranson.
Flocking ferromagnetic colloids.
Science Advances, 3(2):1–11, 2017.

[275] Michelle Driscoll, Blaise Delmotte, Mena Youssef, Stefano Sacanna, Aleksandar Donev, and Paul Chaikin.
Unstable fronts and motile structures formed by microrollers.
Nature Physics, 13(4):375–379, 2017.

[276] Vishal Soni, Ephraim S. Bililign, Sofia Magkiriadou, Stefano Sacanna, Denis Bartolo, Michael J. Shelley, and William T.M. Irvine.
The odd free surface flows of a colloidal chiral fluid.
Nature Physics, 15(November), 2019.

[277] Debarghya Banerjee, Anton Souslov, Alexander G. Abanov, and Vincenzo Vitelli.
Odd viscosity in chiral active fluids.
Nature Communications, 8(1):1–12, 2017.

[278] Anton Souslov, Benjamin C. Van Zuiden, Denis Bartolo, and Vincenzo Vitelli.
Topological sound in active-liquid metamaterials.
Nature Physics, 13(11):1091–1094, 2017.

[279] Sumit Gangwal, Olivier J. Cayre, Martin Z. Bazant, and Orlin D. Velev.
Induced-charge electrophoresis of metallodielectric particles.
Physical Review Letters, 100(5):1–4, 2008.

[280] Jing Yan, Ming Han, Jie Zhang, Cong Xu, Erik Luijten, and Steve Granick.
Reconfiguring active particles by electrostatic imbalance.
Nature Materials, 15(10):1095–1099, 2016.

[281] Hugues Chaté Xia-qing Shi.
Self-Propelled Rods: Linking Alignment-Dominated and Repulsion-Dominated Active Matter.
arXiv Condensed Matter, 2018.

[282] Antoine Bricard, Jean-Baptiste-Caussin, Debasish Das, Charles Savoie, Vijayakumar Chikkadi, Kyohei Shitara, Oleksandr Chepizhko, Fernando Peruani, David Saintillan, and Denis Bartolo.
Emergent vortices in populations of colloidal rollers.
Nature Communications, 6(May):1–8, 2015.

[283] Delphine Geyer, David Martin, Julien Tailleur, and Denis Bartolo.
Freezing a Flock: Motility-Induced Phase Separation in Polar Active Liquids.
Physical Review X, 9(3):31043, 2019.

[284] G. Quincke.
Ueber Rotationen im constanten electrischen Felde.
Ann. der Phys. und Chemie, 295(11):417–486, 1896.

[285] J T Wan, K W Yu, and G Q Gu.
Relaxation of surface charge on rotating dielectric spheres: Implications on dynamic electrorheological effects.
Physical review. E, Statistical, nonlinear, and soft matter physics, 64(6 Pt 1):061501, 2001.

[286] J R Melcher and G I Taylor.
Electrohydrodynamics: A Review of the Role of Interfacial Shear Stresses.
Annual Review of Fluid Mechanics, 1969.

[287] Thomas B. Jones.
Quincke Rotation of Spheres.
IEEE Transactions on Industry Applications, IA-20(4):845–849, 1984.

[288] I Turcu.
Electric field induced rotation of spheres.
Journal of Physics A: Mathematical and General, 20:3301–3307, 1999.

[289] Yu Dolinsky and T. Elperin.
Dipole interaction of the Quincke rotating particles.
Physical Review E - Statistical, Nonlinear, and Soft Matter Physics, 85(2):1–8, 2012.

[290] Debasish Das and David Saintillan.
Electrohydrodynamic interaction of spherical particles under Quincke rotation.
Phys. Rev. E, 87(4):1–14, 2013.

[291] François Peters, Laurent Lobry, and Elisabeth Lemaire.
Experimental observation of Lorenz chaos in the Quincke rotor dynamics.
Chaos: An Interdisciplinary Journal of Nonlinear Science, 15(1):013102, 2005.

[292] Sonja Krause and Preeti Chandratreya.
Electrorotation of deformable fluid droplets.
Journal of Colloid and Interface Science, 206(1):10–18, 1998.

[293] Jong-Wook Ha and Seung-Man Yang.
Electrohydrodynamics and electrorotation of a drop with fluid less conductive than that of the ambient fluid.
Physics of Fluids, 12(4):764–772, 2000.

[294] Paul F. Salipante and Petia M. Vlahovska.
Electrohydrodynamics of drops in strong uniform dc electric fields.
Physics of Fluids, 22(11), 2010.

[295] Paul F. Salipante and Petia M. Vlahovska.
Electrohydrodynamic rotations of a viscous droplet.
Physical Review E - Statistical, Nonlinear, and Soft Matter Physics, 88(4):1–7, 2013.

[296] Debasish Das and David Saintillan.
Electrohydrodynamics of viscous drops in strong electric fields: Numerical simulations.
2017.

[297] L. Lobry and E. Lemaire.
Viscosity decrease induced by a DC electric field in a suspension.
Journal of Electrostatics, 47(1-2):61–69, 1999.

[298] E. Lemaire, L. Lobry, and N. Pannacci.
Flow rate increased by electrorotation in a capillary.
Journal of Electrostatics, 64(7-9):586–590, 2006.

[299] Nicolas Pannacci, Elisabeth Lemaire, and Laurent Lobry.
Rheology and structure of a suspension of particles subjected to Quincke rotation.
Rheologica Acta, 2007.

[300] Alexandre Morin and Denis Bartolo.
Flowing Active Liquids in a Pipe: Hysteretic Response of Polar Flocks to External Fields.
Physical Review X, 8(2):21037, 2018.

[301] N. Pannacci, L. Lobry, and E. Lemaire.
How insulating particles increase the conductivity of a suspension.
Physical Review Letters, 99(9):2–5, 2007.

[302] N. Pannacci, E. Lemaire, and L. Lobry.
DC conductivity of a suspension of insulating particles with internal rotation.
The European Physical Journal E, 28(4):411–417, 2009.

[303] A.J. Goldman, R.G. Cox, and H. Brenner.
Slow viscous motion of a sphere parallel to a plane wall—I Motion through a quiescent fluid.
Chem. Eng. Sci., 22(4):637–651, apr 1967.

[304] A.J. Goldman, R.G. Cox, and H. Brenner.
Slow viscous motion of a sphere parallel to a plane wall—II Motion through a quiescent fluid.
Chem. Eng. Sci., 22(4):637–651, 1967.

[305] M. E. O'Neill and K. Stewartson.
On the slow motion of a sphere parallel to a nearby plane wall.
J. Fluid Mech., 27(04):705, 1967.

[306] Qianlong Liu and Andrea Prosperetti.
Wall effects on a rotating sphere.
J. Fluid Mech., 657:1–21, aug 2010.

[307] Delphine Geyer, Alexandre Morin, and Denis Bartolo.
Sounds and hydrodynamics of polar active fluids, 2018.

[308] Alexandre Morin, Nicolas Desreumaux, Jean-Baptiste Caussin, and Denis Bartolo.
Distortion and destruction of colloidal flocks in disordered environments.
Nature Physics, 13(1):63–67, 2016.

[309] Alexandre Morin, David Lopes Cardozo, Vijayakumar Chikkadi, and Denis Bartolo.
Diffusion, subdiffusion, and localization of active colloids in random post lattices.
Physical Review E, 96(4):042611, 2017.

[310] Shi Qing Lu, Bing Yue Zhang, Zhi Chao Zhang, Yan Shi, and Tian Hui Zhang.
Pair aligning improved motility of Quincke rollers.
Soft Matter, 14(24):5092–5097, 2018.

[311] Allison P. Berke, Linda Turner, Howard C. Berg, and Eric Lauga.
Hydrodynamic attraction of swimming microorganisms by surfaces.
Physical Review Letters, 2008.

[312] Hamid Karani, Gerardo E. Pradillo, and Petia M. Vlahovska.
Tuning the Random Walk of Active Colloids: From Individual Run-And-Tumble to Dynamic Clustering.
Physical Review Letters, 123(20):208002, 2019.

[313] W. Poon.
PHYSICS: Colloids as Big Atoms.
Science, 304(5672):830–831, 2004.

[314] C P Royall and S R Williams.
The role of local structure in dynamical arrest.
Phys. Rep., 560:1, 2015.

[315] Ian Williams, Erdal C. Oğuz, Robert L. Jack, Paul Bartlett, Hartmut Löwen, and C. Patrick Royall.
The effect of boundary adaptivity on hexagonal ordering and bistability in circularly confined quasi hard discs.
The Journal of Chemical Physics, 140(10):104907, mar 2014.

[316] Y. Mao, M. E. Cates, and H. N.W. Lekkerkerker.
Depletion force in colloidal systems.
Physica A: Statistical Mechanics and its Applications, 1995.

[317] John D. Weeks, David Chandler, and Hans C. Andersen.
Role of repulsive forces in determining the equilibrium structure of simple liquids.
The Journal of Chemical Physics, 1971.

[318] G. Seth Roberts, Rodrigo Sanchez, Roger Kemp, Tiffany Wood, and Paul Bartlett.
Electrostatic charging of nonpolar colloids by reverse micelles.
Langmuir, 24(13):6530–6541, 2008.

[319] G. Seth Roberts, Tiffany A. Wood, William J. Frith, and Paul Bartlett.
Direct measurement of the effective charge in nonpolar suspensions by optical tracking of single particles.
Journal of Chemical Physics, 126(19), 2007.

[320] Roger Kemp, Rodrigo Sanchez, Kevin J. Mutch, and Paul Bartlett.
Nanoparticle charge control in nonpolar liquids: Insights from small-angle neutron scattering and microelectrophoresis.
Langmuir, 26(10):6967–6976, 2010.

[321] Yuri Solomentsev, Marcel Böhmer, and John L. Anderson.
Particle Clustering and Pattern Formation during Electrophoretic Deposition: A Hydrodynamic Model.
Langmuir, 13(23):6058–6068, 1997.

[322] Syun-Ru Yeh, Michael Seul, and Boris I. Shraiman.
Assembly of ordered colloidal aggregrates by electric-field-induced fluid flow.
386(6620):57–59, 1997.

[323] M. Trau, D. A. Saville, and I. A. Aksay.
Field-Induced Layering of Colloidal Crystals.
Science, 272(5262):706–709, 1996.

[324] Dennis C. Prieve, Paul J. Sides, and Christopher L. Wirth.
2-D assembly of colloidal particles on a planar electrode.
Current Opinion in Colloid and Interface Science, 15(3):160–174, 2010.

[325] François Nadal, Françoise Argoul, Patrick Hanusse, Bernard Pouligny, and Armand Ajdari.
Electrically induced interactions between colloidal particles in the vicinity of a conducting plane.
Physical Review E - Statistical, Nonlinear, and Soft Matter Physics, 65(6):1–8, 2002.

[326] W. D. Ristenpart, P. Jiang, M. A. Slowik, C. Punckt, D. A. Saville, and I. A. Aksay.
Electrohydrodynamic flow and colloidal patterning near inhomogeneities on electrodes.
Langmuir, 24(21):12172–12180, 2008.

[327] Ke-Qin Zhang and Xiang Y Liu.
In situ observation of colloidal monolayer nucleation driven by an alternating electric field.
Nature, 429(6993):739–743, 2004.

[328] W. D. Ristenpart, I. A. Aksay, and D. A. Saville.
Assembly of colloidal aggregates by electrohydrodynamic flow: Kinetic experiments and scaling analysis.
Physical Review E - Statistical, Nonlinear, and Soft Matter Physics, 69(2 1):1–8, 2004.

[329] Yu Liu, Janaky Narayanan, and Xiang Yang Liu.
Colloidal phase transition driven by alternating electric field.
Journal of Chemical Physics, 124(12), 2006.

[330] Ke-Qin Zhang and Xiang Y. Liu.
Two Scenarios for Colloidal Phase Transitions.
Physical Review Letters, 96(10):105701, 2006.

[331] C. S. Dutcher, T. J. Woehl, N. H. Talken, and W. D. Ristenpart.
Hexatic-to-disorder transition in colloidal crystals near electrodes: Rapid annealing of polycrystalline domains.
Physical Review Letters, 111(12):1–5, 2013.

[332] L. Antl, J. W. Goodwin, R. D. Hill, R. H. Ottewill, S. M. Owens, S. Papworth, and J. A. Waters.
The preparation of poly(methyl methacrylate) latices in non-aqueous media.
Colloids and Surfaces, 1986.

[333] Songbo Ni, Jessica Leemann, Ivo Buttinoni, Lucio Isa, and Heiko Wolf.
Programmable colloidal molecules from sequential capillarity-assisted particle assembly.
Science Advances, 2(4):1–8, 2016.

[334] Songbo Ni, Emanuele Marini, Ivo Buttinoni, Heiko Wolf, and Lucio Isa.
Hybrid colloidal microswimmers through sequential capillary assembly.
Soft Matter, 13(23):4252–4259, 2017.

[335] Vinothan N. Manoharan, Mark T. Elsesser, and David J. Pine.
Dense packing and symmetry in small clusters of microspheres.
Science, 2003.

[336] Bart De Nijs, Simone Dussi, Frank Smallenburg, Johannes D. Meeldijk, Dirk J. Groenendijk, Laura Filion, Arnout Imhof, Alfons Van Blaaderen, and Marjolein Dijkstra.
Entropy-driven formation of large icosahedral colloidal clusters by spherical confinement.
Nature Materials, 14(1):56–60, 2015.

[337] Sunil K. Sainis, Jason W. Merrill, and Eric R. Dufresne.
Electrostatic interactions of colloidal particles at vanishing ionic strength.
Langmuir, 24(23):13334–13337, 2008.

[338] W C K Poon, E R Weeks, and C P Royall.
On measuring colloidal volume fractions.
Soft Matter, 8(1):21–30, 2012.

[339] Tine Curk, Anouk De Hoogh, Francisco J. Martinez-Veracoechea, Erika Eiser, Daan Frenkel, Jure Dobnikar, and Mirjam E. Leunissen.
Layering, freezing, and re-entrant melting of hard spheres in soft confinement.
Physical Review E - Statistical, Nonlinear, and Soft Matter Physics, 2012.

[340] Benjamin D. Hamilton, Jeong Myeong Ha, Marc A. Hillmyer, and Michael D. Ward.
Manipulating crystal growth and polymorphism by confinement in nanoscale crystallization chambers.
Accounts of Chemical Research, 2012.

[341] Stephen E. Donnelly, Robert C. Birtcher, Charles W. Allen, Ian Morrison, Kazuo Furuya, Minghui Song, Kazutaka Mitsuishi, and Ulrich Dahmen.
Ordering in a fluid inert gas confined by flat surfaces.
Science, 2002.

[342] F. Ramiro-Manzano, E. Bonet, I. Rodriguez, and F. Meseguer.
Layering transitions in confined colloidal crystals: The hcp-like phase.
Physical Review E - Statistical, Nonlinear, and Soft Matter Physics, 76(5):2–5, 2007.

[343] Enkeleida Lushi, Hugo Wioland, and Raymond E. Goldstein.
Fluid flows created by swimming bacteria drive self-organization in confined suspensions.
Proceedings of the National Academy of Sciences of the United States of America, 111(27):9733–9738, 2014.

[344] Kun Ta Wu, Jean Bernard Hishamunda, Daniel T.N. Chen, Stephen J. DeCamp, Ya Wen Chang, Alberto Fernández-Nieves, Seth Fraden, and Zvonimir Dogic.
Transition from turbulent to coherent flows in confined three-dimensional active fluids.
Science, 355(6331), 2017.

[345] Benjamin C. van Zuiden, Jayson Paulose, William T. M. Irvine, Denis Bartolo, and Vincenzo Vitelli.
Spatiotemporal order and emergent edge currents in active spinner materials.
Proceedings of the National Academy of Sciences, 113(46):12919–12924, 2016.

[346] I. Williams, E. C. Oğuz, T. Speck, P. Bartlett, H. Löwen, and C. P. Royall.
Transmission of torque at the nanoscale.
Nature Physics, 12:98—103, 2016.

[347] J Crocker and D Grier.
Methods of Digital Video Microscopy for Colloidal Studies.

J. Colloid Interface Sci., 179(1):298–310, 1996.

[348] J. Perrin and D.L. Hammick.
Atoms.
D. Van Nostrand Company, 1916.

[349] Mathieu Leocmach and Hajime Tanaka.
A novel particle tracking method with individual particle size measurement and its application to ordering in glassy hard sphere colloids.
Soft Matter, 9(5):1447–1457, 2013.

[350] H Tanaka, T Kawasaki, H Shintani, and K Watanabe.
Critical-like behaviour of glass-forming liquids.
Nature Mater., 9:324–331, 2010.

[351] Roberto Cerbino and Veronique Trappe.
Differential dynamic microscopy: Probing wave vector dependent dynamics with a microscope.
Physical Review Letters, 100(18):1–4, 2008.

[352] Sophie Ramananarivo, Etienne Ducrot, and Jeremie Palacci.
Activity-controlled annealing of colloidal monolayers.
Nature Communications, 10(1), 2019.

[353] Ethayaraja Mani and Hartmut Löwen.
Effect of self-propulsion on equilibrium clustering.
Physical Review E - Statistical, Nonlinear, and Soft Matter Physics, 92(3):1–7, 2015.

[354] Andreas M. Menzel and Hartmut Löwen.
Traveling and resting crystals in active systems.
Physical Review Letters, 110(5):1–5, 2013.

[355] Zaiyi Shen, Alois Würger, and Juho S. Lintuvuori.
Hydrodynamic self-assembly of active colloids: chiral spinners and dynamic crystals.
Soft Matter, 2019.

[356] A. J. Archer and N. B. Wilding.
Phase behavior of a fluid with competing attractive and repulsive interactions.
Phys. Rev. E, 76:031501, 2007.

[357] Christoph A. Weber, Christopher Bock, and Erwin Frey.
Defect-mediated phase transitions in active soft matter.
Physical Review Letters, 112(16):1–5, 2014.

[358] J. Eggers, J. R. Lister, and Stone H. A.
Coalescence of liquid drops.
J. Fluid Mech., 401:293–310, 1999.

[359] Z. T. Németh and H. Löwen.
Freezing in finite systems: Hard discs in circular cavities.
Journal of Physics Condensed Matter, 10(28):6189–6204, 1998.

[360] C. Alba-Simionesco, B. Coasne, G. Dosseh, G. Dudziak, K. E. Gubbins, R. Radhakrishnan, and M. Sliwinska-Bartkowiak.
Effects of confinement on freezing and melting, 2006.

[361] D. Wilms, P. Virnau, S. Sengupta, and K. Binder.
Langevin dynamics simulations of a two-dimensional colloidal crystal under confinement and shear.
Physical Review E - Statistical, Nonlinear, and Soft Matter Physics, 85(6):1–10, 2012.

[362] Claudio Maggi, Juliane Simmchen, Filippo Saglimbeni, Jaideep Katuri, Michele Dipalo, Francesco De Angelis, Samuel Sanchez, and Roberto Di Leonardo.
Self-Assembly of Micromachining Systems Powered by Janus Micromotors.
Small, 12(4):446–451, 2016.

[363] R. Di Leonardo, L Angelani, G Ruocco, V Iebba, M P Conte, S Schippa, F. De Angelis, F Mecarini, and E. Di Fabrizio.
A bacterial ratchet motor.
Proceedings of the National Academy of Sciences, 107(21), 2009.

[364] Gaszton Vizsnyiczai, Giacomo Frangipane, Claudio Maggi, Filippo Saglimbeni, Silvio Bianchi, and Roberto Di Leonardo.
Light controlled 3D micromotors powered by bacteria.
Nature Communications, 8(May):1–7, 2017.

[365] Antoine Aubret, Mena Youssef, Stefano Sacanna, and Jérémie Palacci.
Targeted assembly and synchronization of self-spinning microgears.
Nature Physics, 2018.

[366] Thomas Bohlein, Jules Mikhael, and Clemens Bechinger.
Observation of kinks and antikinks in colloidal monolayers driven across ordered surfaces.
Nature Materials, 11(2):126–130, 2012.

[367] Michael Allen.
Trajectory generator for quincke trimers, url: https://github.com/michael-p-allen/quincke-trimers, 2020.

[368] A. v. Blaaderen.
CHEMISTRY: Colloidal Molecules and Beyond.
Science, 301(5632):470–471, jul 2003.

[369] Ran Niu, Thomas Palberg, and Thomas Speck.
Self-Assembly of Colloidal Molecules due to Self-Generated Flow.
Physical Review Letters, 119(2):1–5, 2017.

[370] Hartmut Löwen.
Active colloidal molecules.
Epl, 121(5), 2018.

[371] Rodrigo Soto and Ramin Golestanian.
Self-assembly of active colloidal molecules with dynamic function.
Physical Review E - Statistical, Nonlinear, and Soft Matter Physics, 2015.

[372] Quentin Brosseau, Gregory Hickey, and Petia M. Vlahovska.
Electrohydrodynamic Quincke rotation of a prolate ellipsoid.
Phys. Rev. Fluids, 2(January):014101, 2016.

[373] Debasish Das and Eric Lauga.
Active particles powered by quincke rotation in a bulk fluid.
Physical Review Letters, 122(19):194503, 2019.

[374] N. Narinder, Clemens Bechinger, and Juan Ruben Gomez-Solano.
Memory-Induced Transition from a Persistent Random Walk to Circular Motion for Achiral Microswimmers.
Physical Review Letters, 2018.

[375] Personal website, url: www.mauleonamieva.com.